

Charge Transport and Breakdown Physics in Liquid/Solid Insulation Systems

by

Jouya Jadidian

B.Sc., University of Tehran (2006)

M.Sc., University of Tehran (2008)

Submitted to the Department of Electrical Engineering and Computer Science in partial
fulfillment of the requirements for the degree of

Doctor of Philosophy

at the

MASSACHUSETTS INSTITUTE OF TECHNOLOGY

June 2013

© Massachusetts Institute of Technology, MMXIII. All rights reserved.

Author _____
Department of Electrical Engineering and Computer Science
May 20, 2013

Certified by _____
Markus Zahn
Thomas and Gerd Perkins Professor of Electrical Engineering
Thesis Supervisor

Accepted by _____
Leslie A. Kolodziejcki
Chairman, Department Committee on Graduate Students

Charge Transport and Breakdown Physics in Liquid/Solid Insulation Systems

by Jouya Jadidian

Submitted to the Department of Electrical Engineering and Computer Science
in partial fulfillment of the requirements for the degree of

Doctor of Philosophy

Liquid dielectrics provide superior electrical breakdown strength and heat transfer capability, especially when used in combination with liquid-immersed solid dielectrics. Over the past half-century, there has been extensive research characterizing “streamers” in order to prevent them, as they are the main origins of electrical breakdown in liquid dielectrics. Streamers are conductive structures that form in regions of liquid dielectrics that are over-stressed by intense electric fields. Streamers can transform to surface flashovers when they reach any liquid-immersed solid insulation. Surface flashovers usually propagate faster and further than streamers in similar electric field intensity. Charge generation and transport is crucially important in liquid dielectric breakdown, since without the presence of the electric charge and its ability to migrate in the liquid dielectric volume and on the interface of liquid/solid dielectrics, streamers and surface flashovers are unable to develop.

In this thesis, we develop a finite element method transport model in one, two and three-dimensional geometries to help understand the complicated dynamics of electric charge transport and streamer breakdown in liquid dielectrics. This electrohydrodynamic model clarifies many of the mechanisms behind streamer/surface flashover formation, propagation and branching in typical liquid/solid dielectric composite systems. Several key mechanisms have been identified and added to the transport model of streamers, such as effects of electric field intensity on the ionization potential of liquid dielectric molecules and electron velocity saturation, which make the modeling results more realistic. In addition to improving the understanding of electrical breakdown physics in liquid-based insulation systems, a significant effort is made throughout this thesis research to enhance the stability, convergence, speed and accuracy of the model, making it a convenient and reliable tool for designing high voltage components that contain pure liquid dielectrics, nanofluids and liquid immersed insulation systems. This model, for the first time, is able to treat any given electrode shape and gap distance as well as any applied voltage waveform with accurate results, which provides a convenient preliminary way to verify the performance of an insulation system in terms of breakdown voltage, time to breakdown, electric field intensity distribution and ionization level. The model precision is validated through experimental records, analytical solutions and alternative modeling approaches wherever available. Specifically, we verify our one-dimensional numerical results with exact analytical solutions, and our two and three-dimensional modeling results with experimental data found in the literature or provided by ABB Corporate Research, Sweden. The streamer initiation voltages, number of streamer branches, breakdown voltages and currents are in excellent agreement with the experimental data compared to the prior theoretical research on liquid breakdown physics. Identical results obtained using a finite volume method also confirm the correctness of the finite element approach used in this thesis. The presented model can be employed to search for novel configurations of liquid immersed insulation systems including nanofluids and liquid/solid composite systems.

Thesis Supervisor: Markus Zahn

Title: Thomas and Gerd Perkins Professor of Electrical Engineering

ACKNOWLEDGEMENT

I have really enjoyed my MIT life. I have had a unique advisor, Professor Markus Zahn, who has treated me like his own son. I am profoundly grateful to him for sharing his knowledge and experience with me, for his encouragement and friendship during the course of my PhD research. I have learned so many invaluable things from him beyond the scope of graduate studies.

I also appreciate insightful comments of my thesis committee members, Professors Jeffrey Lang and Luca Daniel, at the defense and at our committee and individual meetings, which helped me take one step back and look at the big picture of my thesis research.

I am truly indebted to members of the ABB Corporate Research team in Västerås, Sweden, with whom I worked closely on this project: Dr. Nils Lavesson, Dr. Ola Widlund and Dr. Karl Borg, who provided technical advice, constructive criticism and encouragement. I would like to acknowledge the ABB Corporation for the financial and technical support of this research.

I am thankful to my friends and colleagues at the Laboratory for Electromagnetic and Electronic Systems for many discussions and their company: Dr. Shahriar Khushrushahi, Dr. George Hwang, Mohammad Araghchini, Uzoma Orji, Samantha Gunter, Samuel Chang, Wei Li, Richard Zhang, Juan Antonio, Jiankang Wang, Wardah Inam and Seungbum Lim. My warm appreciation is due to Janet Fischer and Dimonika Bray and all other MIT administrative staff, who always had time for helping me out, no matter how busy they were.

The work that resulted in this thesis began long before I arrived at MIT. The preparation for my PhD studies has to be traced back to my several years at the High Voltage Laboratory of the University of Tehran. I particularly would like to thank my former advisors, Professors Hossein Mohseni, Kaveh Niayesh and Amir Abbas Shayegani and all my colleagues at this lab, many of whom are now spread around the world. I especially would like to pay tribute to a wonderful friend and an outstanding scholar, Jamal Shakeri, who regrettably succumbed to cancer.

This thesis is dedicated to my parents, Marzieh and Abbas, who have always been concerned about my education. They gave me a rare name, a pure Persian word, which means a person who is ravenous to search out the causes of things: a researcher. As far back as I can remember, I have marveled at their selection: my name is the best gift I have ever received. They enthusiastically started teaching their four-year-old son reading and basic arithmetic, and now I sincerely believe whatever I have achieved is their accomplishment too. I also dedicate this thesis to my sister, Darya, who will soon be graduating with her undergraduate degree. Although it has been extremely difficult for all of us to be apart, they have embraced the separation with patience, only for the sake of my well-being and success.

I would like to express my sincere gratitude to my best friend and my wife, Sepideh, for her unconditional love and unwavering faith throughout the years of college and graduate school. She has been astonishingly strong and a steady source of confidence in difficulties we both have faced. I hope I will be able to return the favor, her technical comments and endless support, during the remainder of her PhD research at Tufts University.

1. Introduction	29
1.1. Charge Generation and Transport in Liquid Dielectrics Leading to Streamer Formation and Electrical Breakdown	30
1.2. Analysis and Modeling of Streamer Development in Liquid-Solid Insulation Systems	31
1.2.1. <i>One-Dimensional Analysis of Charge Transport in Liquid-Solid Composite Dielectric Systems</i>	33
1.2.2. <i>Two-Dimensional Axisymmetric Modeling of Single Column Streamer</i>	33
1.2.3. <i>Two-Dimensional Modeling of Breakdown Phenomena</i>	34
1.2.4. <i>Modeling of Surface Flashover on Liquid Immersed Dielectrics</i>	34
1.2.5. <i>Fully Three-Dimensional Modeling of Streamer Branching</i>	35
1.3. Main Contributions of Thesis	35
1.4. Thesis Outline	41
2. Pre-breakdown Mechanisms in Transformer Oil-Based Insulation Systems	43
2.1. Streamer Initiation, Propagation and Branching in Transformer Oil	43
2.2. Interactions of Streamers Initiated in Transformer Oil with Adjacent Solid and Gaseous Dielectrics	46
2.3. Effects of Additives on Breakdown in Transformer Oil	48
2.3.1. <i>Different Hydrocarbon Molecules in Transformer oil</i>	48
2.3.2. <i>Nanoparticle Additives and Microparticle Contaminations</i>	50

3. Numerical Simulation Problem Posing/Approach	53
3.1. Introduction to COMSOL Multiphysics Modeling of Streamer/Surface Flashover	53
3.2. Problem Posing Elements	53
3.2.1. <i>Simulation Geometry</i>	54
3.2.2. <i>Governing Equations</i>	54
3.2.3. <i>Boundary Conditions</i>	55
3.2.4. <i>Stabilization Techniques</i>	55
3.2.5. <i>Meshing Policies and Mesh Element Definitions</i>	57
3.2.6. <i>Numerical Solvers</i>	59
4. One-dimensional Analysis and Modeling of Unipolar Charge Transport in Liquid-Solid Composite Dielectric Systems	63
4.1. Migration of Unipolar Charge Carrier Transport between Cartesian, Cylindrical and Spherical Electrodes in Liquid-Only Systems	64
4.2. Migration-Ohmic Analysis of Charge Transport in a Series Liquid-Solid Dielectric System with Linear Charge Injection from a Planar Electrode	64
4.2.1. <i>Governing Equations and Linear Charge Injection</i>	65
4.3. Migration-Ohmic Analysis of Space Charge Limited Injection and Transport in a Series Liquid-Solid Dielectric System	73
4.3.1. <i>Cartesian Electrode Geometry</i>	73
4.3.2. <i>Coaxial Cylindrical Electrode Geometry</i>	77
4.3.3. <i>Concentric Spherical Electrode Geometry</i>	82
4.4. Comparison of Analytical Solutions and Modeling Results	87
4.5. Summary	91
5. Two-dimensional Electrohydrodynamic Modeling of Streamer Initiation and Propagation in Dielectric Liquids	93

5.1. Electrode Geometries and Gap Distances	94
5.2. Governing Equations	95
5.3. Charge Carrier Characteristics	97
5.3.1 <i>Ionization Mechanisms</i>	97
5.3.2 <i>Recombination of Charge Species</i>	100
5.3.3 <i>Electric Field Dependent Electron Mobility</i>	102
5.3.4 <i>Temperature Dependent Electron and Ion Mobilities</i>	104
5.4. Boundary Conditions	104
5.5. Breakdown Stages in Liquid Dielectrics	105
5.5.1 <i>Streamer Initiation: Effects of Applied Voltage Parameters</i>	107
5.5.2 <i>Streamer Initiation: Effects of Electrode Geometries</i>	123
5.5.3 <i>Streamer Acceleration due to Re-ignition from Needle Electrode</i>	126
5.5.4 <i>Breakdown Completion: Effects of Gap Distance and Electrode Geometries on Full Breakdown</i>	131
5.6. Summary	138
6. Three-dimensional Electrohydrodynamic Modeling of Streamer Development and Branching in Dielectric Liquids	139
6.1. Spatial Inhomogeneities: Stochastic Origins of Branching	139
6.1.1 <i>Visible Macro-Inhomogeneities</i>	140
6.1.2 <i>Stochastic Micro-Inhomogeneities</i>	140
6.2. Three-Dimensional Modeling of Streamer Initiation and Branching	141
6.3. Numerical Implementation of Stochastic Inhomogeneities	144
6.4. Modeling Results: Streamer Stochastic Branching Driven by Micro-Inhomogeneities	146
6.5. Geometry of Streamer Head: Deterministic Causes of Branching	161

6.6. Summary	167
7. Surface Flashover Formation and Growth on Liquid Immersed Dielectrics	169
7.1. Streamer Interaction with Perpendicular and Parallel Liquid Immersed Dielectric Interfaces	170
7.2. Surface Flashover Development on a Parallel Liquid Immersed Dielectric Interface	176
7.1.1 <i>Liquid Immersed Dielectrics with Greater Permittivity than the Liquid (Pressboard in transformer oil)</i>	177
7.1.2 <i>Liquid Immersed Dielectrics with about the Same Permittivity as the Liquid (PTFE in transformer oil)</i>	178
7.1.3 <i>Liquid Immersed Dielectrics with Smaller Permittivity than the Liquid (SF₆ in transformer oil)</i>	179
7.3. Surface Flashover Development on a Perpendicular Liquid Immersed Dielectric Interface	181
7.3.1 <i>Liquid Immersed Dielectrics with Greater Permittivity than the Liquid (Pressboard in transformer oil)</i>	183
7.3.2 Liquid Immersed Dielectrics with about the Same Permittivity as the Liquid (PTFE in transformer oil)	185
7.3.3 Liquid Immersed Dielectrics with Smaller Permittivity than the Liquid (SF ₆ in transformer oil)	185
7.4. Sanity Checks	190
7.5. Summary	196
8. Concluding Remarks and Suggestions for Future Work	199
8.1. Streamer Initiation	199
8.2. Streamer Propagation	200
8.3. Streamer Branching	200
8.4. Streamer Interaction with Immersed Dielectrics	201

8.5. Streamer Branching	202
8.6. Sanity Checks	203
8.7. Future Work	203
Appendices:	207
A1. Optimized Combination of Artificial Diffusion Stabilization Techniques for Finite Element Modeling of Drift Dominated Transport of Charge Carriers	207
A2. Optimal Mesh Element Density Distribution for Streamer Development Finite Element Modeling	209
A3. Simple Illustration of the Physical Differences between Positive and Negative Streamer Formation in Dielectric Liquids	217
A4. Implementation of Stochastic Inhomogeneities	218
A5. Other Numerical Simulation Methods for Streamer Development Modeling	220
Bibliography	223

List of Figures

- 1.1. Streamer velocity plotted versus applied voltage peak as modeling obtained in this thesis (red square symbols), modeling results of others (green symbols) and experimental data found in the literature (blue symbols) for different electrode gap distances. The gap distances are labeled on the respective curves. Experimental data are taken from different references (■ [2], ● [4], * [6], ★ [7], ◆ [18], ▲ [60], and * [106]). The green symbols show the modeling results O’Sullivan [23] (◀) and Hwang [25] (▶). 36
- 1.2. Streamer velocity plotted versus applied voltage peak as modeling obtained in this thesis (red square symbols), modeling results of others (green symbols) and experimental data found in the literature (blue symbols) for different electrode gap distances. The gap distances are labeled on the respective curves. Experimental data are taken from different references (■ [2], ● [4], * [6], ◆ [18]). There is no prior modeling results on negative streamers. 37
- 1.3. Maximum pre-breakdown current plotted for different electrode gap distances. Red square symbols show the modeling results of this thesis and blue symbols show the experimental data found in the literature. Each pair of data is labeled with the associated applied voltage peak. Experimental data are taken from different references (■ [2], ◆ [18], ▶ [60], and * [106]). 38
- 1.4. Experimental data for a 6 mm gap (●), a 20 mm gap (▼), and a 50 mm gap (★), all obtained from [16]. Modeling results for a 6 mm gap distance (■). The solid curve, which is fitted to the modeling results, is $V_i = 10^{2.2} \sqrt{r_t}$, where r_t is the positive electrode tip radius in millimeters and the initiation voltage, V_i , is in kilovolts. 38
- 1.5. Modeling results (red symbols), obtained in this thesis, and experimental records (blue symbols), found in the literature, for breakdown voltages of different needle-sphere electrode gap distances. The model does not include statistical factors affecting the streamer formation and propagation. Therefore, the calculated value for the definite breakdown voltage by the model, is roughly two times greater than the 50% breakdown voltage which is determined after numerous experiments. Experimental data are taken from different references (■ [2], ● [4], * [6], ★ [7], ◆ [18]). 39
- 1.6. Modeling results (red bars), obtained in this thesis, and experimental records (blue symbols), found in the literature, for number of active streamer branches emanating from a streamer node right after the branching, plotted versus the ratio of applied voltage peak over initiation voltage. Initiation voltage is mainly a function of the needle electrode tip radius. The model does not include statistical

factors affecting the streamer formation and propagation. Experimental data are taken from different references (■[2], ●[4], ★[7], ◆[18], ▲[60], and * [106]). 40

2.1. (a): A positive streamer and (b): a negative streamer formed in the 5 mm gap under different applied voltages (+26 kV and -52 kV). Filamentary structure of the positive streamer can be clearly distinguished from the thick and bushy shape of the negative streamer. The luminous plasma generated inside the channel formed by a negative streamer is also quite bulkier. The shock waves seen around the negative streamer supports the idea of formation of an appreciable gas volume inside the negative streamer channel [8,18]. 44

2.2. (a) Time-integrated and (b-i) time resolved images of a streamer branching during a positive/negative streamer conversion in 600 mbar artificial air. (j): A negative pulse of 35 kV is applied to the needle electrode (70 μm tip radius) for about 100 ns, followed by a positive voltage pulse for 150 ns, which creates positive streamers that run over the surface of the nearly spherical previously formed negative discharge. This is particularly interesting since it reveals that filamentary positive streamers and bubble shaped negative streamers can interchange during a discharge [56]. 45

2.3. (Left) Single phase transformer windings covered by pressboard layers and (Right): Single phase high voltage transformer windings and bushing wound with pressboard layers ready for immersing in transformer oil. Courtesy of High Voltage Laboratory, University of Tehran, used with permission. 47

2.4. Surface flashover development (a): within a polytetrafluoroethylene (PTFE) bore [60] and (b,c): plate perpendicular to the streamer propagation direction [60,61]. 47

2.5. Time to breakdown (left) and average streamer velocity (right) versus applied voltage peak provided by ABB Corporate Research in two different transformer oils for the needle-sphere geometry detailed in IEC Standard 60897 [66]. Positive and negative breakdown voltages of mineral oil types A and B are listed below:

Transformer Oil	Positive Breakdown Voltage	Negative Breakdown Voltage
Type A	105 kV	256 kV
Type B	126 kV	166 kV

49

2.6. Electric field lines for various times after a uniform z-directed electric field is turned on at t=0 around a perfectly conducting spherical nanoparticle of radius R surrounded by transformer oil, and free electrons with uniform charge. The thick electric field lines separate field lines that terminate on the nanoparticle from field lines that go around the particle. The nanoparticles can assist and avoid breakdown by scavenging free electrons by intensifying and weakening the electric field ahead of the positive and negative streamer heads, respectively. 51

3.1. COMSOL framework with different modules and interfaces. These modules can be combined and cascaded to accomplish any complicated modeling task with different aspects [71]. 55

- 3.2. The plots compare the stabilized solution (dashed line) with the reference solution (solid line). a) unstabilized Galerkin formulation, b) stabilized formulation with isotropic diffusion, c) stabilized formulation with streamline anisotropic diffusion, d) stabilized formulation with SUPG diffusion, e) stabilized formulation with SUPG diffusion and crosswind diffusion [71]. 58
- 4.1. Two-region, series planar, liquid-solid dielectric model excited by a time-dependent current source, $I(t)$, with Region I obeying a mobility (μ) conduction law and Region II obeying Ohmic conduction. 65
- 4.2. Nondimensionalized DC voltage $\tilde{V} = V \epsilon_{oil} \mu / (\sigma a^2)$ for various non-dimensional current densities $\tilde{J}_0 = J / J_0$ as a function of non-dimensionalized charge injection coefficient $\tilde{A} = Aa / \epsilon_{oil}$. 68
- 4.3. Space-time domain for the transient one-dimensional model of charge transport in the migration-Ohmic system for planar electrodes. In Region I, the demarcation curve, $x_d(t)$, separates the initial condition problem (Sub-region I₁) from the charge injection problem (Sub-region I₂). The integration paths ζ_1 and ζ_2 in Region I and ξ_1 in Region II, used to calculate terminal voltage are shown for times less than the charge time of flight (t_d) starting at $x=0, t=0$ and ending at $x=a, t=t_d$. Integration paths ζ_3 and ζ_2 in Region I /II are shown for times greater than t_d . 70
- 4.4. Nondimensionalized voltage $\tilde{V} = V \epsilon_{oil} \mu / (\sigma a^2)$ between electrodes for various values of nondimensionalized linear injection coefficient $\tilde{A} = Aa / \epsilon_{oil}$ as a function of nondimensionalized time $\tilde{t} = t \sqrt{\mu J_0 / (a \epsilon_{oil})}$. 72
- 4.5. Two-region, series, oil-pressboard dielectric model for cylindrical electrodes excited by a step current source with Region I (Oil) for $r_i < r < r_m$ obeying a mobility (μ) conduction law and Region II (Pressboard) for $r_m < r < r_o$ obeying Ohmic conduction. 78
- 4.6. Space-time domain for the transient one-dimensional model of charge transport in the migration-Ohmic system for coaxial cylindrical electrodes. In Region I, the demarcation curve, $r_d(t)$, separates the initial condition problem (Sub-region I₁) from the charge injection problem (Sub-region I₂). The integration paths ζ_1 and ζ_2 in Region I and ξ_1 in Region II, used to calculate terminal voltage are shown for times less than the charge time of flight (t_d) starting at $r=r_i, t=0$ and ending at $r=r_m, t=t_d$. Integration paths ζ_3 and ζ_2 in Region I /II are shown for times greater than t_d . 81
- 4.7. Two-region, series, oil-pressboard dielectric model for spherical electrodes excited by a step current source with Region I (Oil) $r_i < r < r_m$ obeying a mobility (μ) conduction law and Region II (Pressboard) $r_m < r < r_0$ obeying Ohmic conduction. 83

- 4.8. Space-time domain for the transient one-dimensional model of charge transport in the migration-ohmic system for concentric spherical electrodes. In Region I, the demarcation curve separates the initial condition problem (Sub-region I₁) from the charge injection problem (Sub-region I₂). The integration paths ζ_1 and ζ_2 in Region I and ξ_1 in Region II, used to calculate terminal voltage are shown for times less than the charge time of flight (t_d) starting at $r=r_i$, $t=0$ and ending at $r=r_m$, $t=t_d$. Integration paths to calculate terminal voltage ζ_3 and ζ_2 in Region I/II are shown for times greater than t_d . 86
- 4.9. Non-dimensionalized voltage $\tilde{V} = V / (\sqrt{2J_s a^3 / (9\mu\epsilon_{oil})} + J_s a / \sigma)$ between electrodes for the three electrode geometries treated in this chapter as a function of non-dimensionalized time $\tilde{t} = t[\mu J_s / (\sigma a)]$ where all parameter values are defined in Table 4.3, and in particular $a=0.0125$ m is the oil region thickness in planar, cylindrical and spherical geometries. 88
- 4.10. Non-dimensionalized steady state electric field $\tilde{E} = E\epsilon_{oil}\mu / (\sigma a)$ between electrodes for different electrode geometries. Non-dimensionalized distance between positive electrode and interfacial surface is defined as $\tilde{s} = s / (2a)$ which is equal to $x/(2a)$ for planar geometry, $r/(2a)-0.5$ for cylindrical geometry and $r/(2a)-0.5$ for spherical geometry. All parameter values are defined in Table 4.3, and in particular $r_i=r_i=a=0.0125$ m is the radius of the interior electrode in cylindrical and spherical geometries respectively. 89
- 4.11. Non-dimensionalized space-time, trajectories for different electrode geometries which show the demarcation curves in planar, cylindrical and spherical geometries. Variable S is the demarcation trajectory x , r , and r given in equations (4.44), (4.62), and (4.82) for planar, cylindrical, and spherical geometries, respectively. Non-dimensionalized distance between the positive electrode and the interfacial surface is defined as $\tilde{s} = S / (2a)$ which is equal to $x/(2a)$ for planar geometry, $r/(2a)-0.5$ for cylindrical geometry and $r/(2a)-0.5$ for spherical geometry as a function of non-dimensionalized time $\tilde{t} = t\sqrt{\mu J_s / (a\epsilon_{oil})}$ where all parameter values are defined in Table 4.3, and in particular $r_i=r_i=a=0.0125$ m is the radius of the interior electrode in cylindrical and spherical geometries, respectively. 89
- 4.12. Nondimensionalized volume charge density in the oil regions $\tilde{\rho} = \rho\sqrt{\mu a / (\epsilon_{oil} J_s)}$ between electrodes for different electrode geometries in steady state. Nondimensionalized distance between the positive electrode and interfacial surface is defined as $\tilde{s} = S / (2a)$ which is equal to $x/(2a)$ for planar geometry, $r/(2a)-0.5$ for cylindrical geometry and $r/(2a)-0.5$ for spherical geometry. 90
- 4.13. Nondimensionalized electric surface charge density at the oil/pressboard interface $\tilde{\sigma}_s = \sigma_s / (J_s \epsilon_{pb} / \sigma - \sqrt{2J_s \epsilon_{oil} a / \mu})$ for planar, cylindrical and spherical geometries as a function of non-dimensionalized time $\tilde{t} = t[\mu J_s / (\sigma a)]$. 90

- 5.1. Needle-sphere electrode chamber dimensions (left) and the actual electrode chamber in laboratory filled with transformer oil (right). This structure is used for experimental studies of streamers at ABB [55-57]. This exact geometry is also used for simulation purposes as described in IEC 60897 standard [66]. The electrodes are 25 mm apart and the radii of curvature of the needle and sphere electrodes are 40 μm and 6.35 mm, respectively. 95
- 5.2. IEC 60060 lightning impulse voltage (non-dimensional, $\tilde{v} = V / V_0$) with rise-time t_r (10% to 90% of peak voltage) versus non-dimensional time, $\tilde{t} = t / \tau_1$ generated with subtracting two exponential functions. 105
- 5.3. Electric field magnitude and lines (right side) and the net charge density and equipotential lines (left side) for a positively applied lightning impulse voltage with 130 kV peak and 100 ns rise-time at $t=155$ ns. No discharges are observed for a 130 kV negatively applied impulse voltage. 108
- 5.4. Electric field magnitude and lines (right side) and the net charge density and equipotential lines (left side) for a positively applied lightning impulse voltage with 200 kV peak and 100 ns rise-time at $t=100$ ns. 109
- 5.5. Electric field magnitude and lines (right side) and the net charge density and equipotential lines (left side) for a positively applied lightning impulse voltage with 400 kV peak and 100 ns rise-time at $t=100$ ns. 110
- 5.6. Electric field magnitude and lines (right side) and the net charge density and equipotential lines (left side) for a positively applied lightning impulse voltage with 400 kV peak and 100 ns rise-time at $t=200$ ns. 111
- 5.7. Electric field magnitude and lines (right side) with the charge density generation rate and equipotential lines (left side) for a negatively applied lightning impulse voltage with -400 kV peak and 1 ns rise-time at $t=5$ ns. 112
- 5.8. Electric field magnitude and lines (right side) with the charge density generation rate and equipotential lines (left side) for a negatively applied lightning impulse voltage with -600 kV peak and 1 ns rise-time at $t=5$ ns. 113
- 5.9. Streamer head average distance from needle tip for positive and negative applied voltages with different peak amplitudes. Positive streamer velocity tends to time increases, while a negative streamer decreases significantly after an initial bubble is formed around the needle. Error-bars show the range of results obtained by each of the artificial streamline diffusions (anisotropic, compensated streamline upwind Petrov-Galerkin and Galerkin least-square methods) to solve the charge continuity equations. The streamer velocity under +400 kV is roughly 2 times greater than +200 kV streamer velocity which is itself two times greater than +130 kV. Dissimilar rise-times for positive and negative streamers are shown to ease comparison between positive and negative streamers with velocities on the same order. 116

- 5.10. Electric field magnitude and lines (right side) and the net charge density and equipotential lines (left side) for a positively applied lightning impulse voltage with +200 kV peak and 50 ns rise-time at $t=70$ ns. 118
- 5.11. Electric field magnitude and lines (right side) and the net charge density and equipotential lines (left side) for a positively applied lightning impulse voltage with +200 kV peak and 10 ns rise-time at $t=8.5$ ns. 119
- 5.12. Electric field magnitude and lines (right side) and the net charge density and equipotential lines (left side) for a positively applied lightning impulse voltage with +200 kV peak and 2 ns rise-time at $t=2$ ns. 120
- 5.13. Volume charge densities and electric field distributions for different positively applied voltage peak amplitudes and rise-times. The pictures are shown for the instant times that the streamer heads travel half a millimeter from the needle tip. Space charge densities are shown as filled contours from $0.5|\rho_{max}|$ (the brightest color) to $|\rho_{max}|$ (the darkest color). Electric field contours are shown as black solid lines from $0.5|E_{max}|$ to $|E_{max}|$. The value of each contour is labeled on the curve as a fraction of $|E_{max}|$. The streamer head curvatures can be compared between streamers formed by (a): 130 kV with 1.2 μ s rise-time: $|E_{max}|=3.1\times 10^8$ V/m , $|\rho_{max}|=4.25\times 10^3$ C/m³; (b): 130 kV with 100 ns rise-time: $|E_{max}|=2.9\times 10^8$ V/m , $|\rho_{max}|=3.94\times 10^3$ C/m³; (c): 200 kV with 1.2 μ s rise-time: $|E_{max}|=2.9\times 10^8$ V/m , $|\rho_{max}|=3.12\times 10^3$ C/m³; (d): 200 kV with 100 ns rise-time: $|E_{max}|=2.8\times 10^8$ V/m , $|\rho_{max}|=2.43\times 10^3$ C/m³; (e): 400 kV with 1.2 μ s rise-time: $|E_{max}|=2.6\times 10^8$ V/m , $|\rho_{max}|=1.54\times 10^3$ C/m³; and (f): 400 kV with 100 ns rise-time $|E_{max}|=2.4\times 10^8$ V/m , $|\rho_{max}|=0.93\times 10^3$ C/m³. 121
- 5.14. Electric field distributions and charge density generation rates for different negatively applied voltage peak amplitudes and rise-times. Space charge density generation rate, G_M are shown as filled contours from $0.5|G_{max}|$ (the brightest color) to $|G_{max}|$ (the darkest color). Electric field contours are shown as black solid lines from $0.5|E_{max}|$ to $|E_{max}|$. The value of each contour is labeled on the curve as a fraction of $|E_{max}|$. The approximate radius of an ionized bubble can be compared between different applied voltage peaks and rise-times: -250 kV with 1ns rise-time (upper right): $|E_{max}|=1.01\times 10^8$ V/m and $|G_{max}|=0.7\times 10^{11}$ Cm⁻³s⁻¹; -400 kV with 1ns rise-time (middle right): $|E_{max}|=1.42\times 10^8$ V/m and $|G_{max}|=1.2\times 10^{11}$ Cm⁻³s⁻¹; -600 kV with 1ns rise-time (bottom right): $|E_{max}|=1.75\times 10^8$ V/m and $|G_{max}|=6.21\times 10^{11}$ Cm⁻³s⁻¹; -400 kV peak with 100 ns rise-time (upper left): $|E_{max}|=0.95\times 10^8$ V/m and $|G_{max}|=0.84\times 10^{11}$ Cm⁻³s⁻¹; and -600 kV peak with 100 ns rise-time (bottom left): $|E_{max}|=1.15\times 10^8$ V/m and $|G_{max}|=1.21\times 10^{11}$ Cm⁻³s⁻¹. 122
- 5.15. Experimental data for a 6 mm gap (●), a 20 mm gap (▼), and a 50 mm gap (★), all obtained from [16]. Modeling results for a 6 mm gap distance (■). The solid curve, which is fitted to the modeling results, is $V_i=10^{2.2}\sqrt{r_t}$, where r_t is the positive electrode tip radius in millimeters and the initiation voltage, V_i , is in kilovolts. 123

- 5.16. A set of different positive needle electrode tip sizes with the same gap distance and applied voltage, which is slightly above the initiation voltage for all of the positive electrode radii of curvature. 124
- 5.17. A set of different grounded tip sizes with the same gap distances and applied voltages. Ionization (high electric field) region is larger at sharper grounded electrodes. 125
- 5.18. Electron velocity models and ionization potential (derived by Density Functional Theory) as functions of electric field intensity, $v_e=v_0|E|/(|E|+E_0)$. The numerical values of parameters of the saturated electron velocity are labeled on the curves and ionization potential constants are set as $A=1.36\times 10^{-18}$ J, $\gamma=1.118\times 10^{-22}$ Jcm^{1/2}V^{-1/2}. Values $v_0=41$ km/s, $E_0=0.1$ MV/cm is used in [2,3]. 126
- 5.19. Electron charge density and flux distributions obtained by the ordinary model with constant electron mobility (left panel) and the ESV model (right panel) under a similar applied voltage with 500 kV peak and 100 ns rise-time. Each panel shows two frames of the streamer, i.e., the stem of the streamer (which attaches to the needle electrode tip) and the streamer head. Both streamer heads are at the same distance from the needle tip, but at slightly different time instants (after 0.6 μ s for the linear model with constant electron mobility and after 0.57 μ s for the ESV model). 127
- 5.20. Charge carrier density (a), flux (b) and electric field distribution (c) obtained from the ESV model approximately 2 mm from the needle electrode tip while the streamer head is 5 mm from the needle tip under an applied voltage with 500 kV and 100 ns rise-time. Due to the electron velocity saturation, the electron and ion charge density do not quite cancel. Therefore, a secondary frontier of electric field is created inside the streamer column. In the case of $E_0=0.1$ MV/cm, this secondary frontier propagates slowly, however, for smaller E_0 , the secondary frontier can propagate much faster and even collide with the main frontier (streamer head front). 128
- 5.21. Electric field distributions in the range of $0.5|E_{\max}|$ as the brightest color to $|E_{\max}|$ as the darkest color for positively applied impulse voltages with 0.1 μ s rise-time and 400 kV peak amplitude. The values of $|E_{\max}|$ at $z=0$, $z=2$ mm and $z=3$ mm are 3.24 MV/cm, 3.46 MV/cm and 3.58 MV/cm (except at $t=0.52$ μ s that is 4.27 MV/cm), respectively. The velocity of the streamer front is approximately doubled after collision. 129
- 5.22. Normalized length of the streamers for different applied voltage amplitudes. Dashed lines show the results of the constant electron mobility model adapted from the reference [48] and the solid lines show the ESV model results. Streamers accelerate abruptly under impulse voltages with higher amplitudes than 400 kV in the ESV model. The sudden acceleration happens exactly when the main and secondary streamer fronts collide. Error-bars show the range of results obtained by each of the artificial streamline diffusions (anisotropic,

- compensated streamline upwind Petrov-Galerkin and Galerkin least-square methods) to solve the charge continuity equations. 130
- 5.23. Minimum applied voltage peak required for reigniting a positive streamer from the needle electrode placed 25 mm from a grounded sphere electrode against saturation electric field, E_0 . For saturation fields above 0.651 MV/cm no re-ignition is observed (applied voltage peaks up to 10 MV are examined). 131
- 5.24. Normalized length of the streamers for different electrode geometries and gap distances at breakdown voltages. Breakdown voltage is the minimum impulse voltage amplitude at which the streamer is able to reach the ground electrode and consequently breakdown occurs. The streamer lengths are fitted with exponential and single term polynomial curves for needle-needle and needle-sphere geometries, respectively. Streamers require higher impulse voltage amplitudes to reach the grounded needle electrodes. The streamer velocity clearly increases when the streamer approaches the grounded electrode at $z=d$. 132
- 5.25. Streamer breakdown in needle-sphere (a, b, c, d) and needle-needle (e, f, g, h) electrode gaps, 10 mm apart. Streamers always emanate from the positive needle and eventually hit the grounded electrode. Electric field distributions are shown in the range of $0.5|E_{\max}|$, as the brightest color to $|E_{\max}|$, as the darkest color for positively applied impulse voltages with $0.1\mu\text{s}$ rise-time and different peak amplitudes. The values of $|E_{\max}|$ (for $0.1 < z < 9.9$ mm) and breakdown time are (a): 3.24 MV/cm, 1.092 μs ; (b): 3.06 MV/cm, 0.564 μs ; (c): 2.98 MV/cm, 0.328 μs ; (d): 2.56 MV/cm, 0.212 μs ; (e): 3.48 MV/cm, 0.244 μs ; (f): 3.47 MV/cm, 0.377 μs ; (g): 3.46 MV/cm, 0.648 μs ; and (h): 3.48 MV/cm, 0.782 μs . The maximum electric field, $|E_{\max}|$, within 0.1 mm of electrodes is about 30% less. The trajectories of streamers are reasonably similar to Figure 5.25 and can be approximately scaled by the applied voltage amplitude (considering the time to breakdown). 134
- 5.26. Grounded electrodes' displacement and conduction currents, through needle-needle and needle-sphere electrodes 10 mm apart at their own breakdown voltages, i.e., 112 kV and 92 kV, respectively. The displacement current rises abruptly just after application of an impulse voltage by the background electric field while conduction currents increase dramatically when the streamer hits the ground electrode at the times corresponding to $z/d=1$ in Figure 5.24 (for $d=10$ mm). The streamer charge influences displacement current indirectly, by changing the electric field distribution inside the gap. However, the effect of the streamer charge on the displacement current is not appreciable since the streamer engages a negligible portion of the electrode surface. An initial rise in the conduction current of needle-needle geometry is due to the intense electric field near the grounded needle that causes an appreciable ionization leading to a limited conduction current (~ 100 mA) until the streamer reaches the grounded needle. 135
- 5.27. Grounded electrodes' total current (conduction plus displacement), through different gaps and geometries at their own breakdown voltages. The current rises dramatically when the streamer hits the ground electrode at the times

corresponding to $z=d$ in Figure 5.24. Displacement current dominates the total current just after application of the impulse voltage. Semi-exponential attenuation of the displacement current suggests that the displacement current decay obeys the dielectric relaxation time dictated by the electrode geometry and dielectric properties. Both the initial magnitude and the decay rate of the displacement current toward the grounded needle electrode are smaller than the sphere electrode. This is consistent with their geometries since the area of the needle surface electrode is ~ 10 times smaller than the sphere electrode surface area. The conduction current dominates the total current as the streamer reaches the grounded electrode that leads to breakdown (dramatic rise of current). 136

5.28. Predicted breakdown voltage for different gap distances. Error-bars show the range of results obtained by each of the artificial streamline diffusions (anisotropic, compensated streamline upwind Petrov-Galerkin and Galerkin least-square methods) to solve the charge continuity equations. 137

6.1. Typical view of positive streamer branching in a liquid dielectric, (a) experimental image of a positive streamer initiated from a needle electrode [16] and, (b): 3-D modeling result of a corresponding case (iso-surface plot of the electric field distribution). The streamer structures are qualitatively similar in experiments and simulations. The fractal structure of the streamer tree in the experimental image makes it possible to compare the modeling result also with other nodes of the tree including the one at the needle electrode tip. 142

6.2. Iso-surface plot of electric field distribution as modeling result of streamer is compared with corresponding experimental image in the inset image. Definite breakdown voltage, U_{DBD} , for the modeling geometry (gap length, $d=25$ mm, and the electrode tip radius, $r_i=40$ μm) is equal to 95 kV. In the experimental data, the applied voltages are expressed in terms of streamer initiation voltage, V_i , and 50% breakdown voltage, U_{BD} , which is the impulse peak at which the dielectric breaks down in half of the discharge tests:

<i>Modeling (peak, rise time)</i>	<i>Experiment (Photography method and applied voltage peak)</i>
2.85 V_i (0.9 U_{DBD}), 1 ns	Streak image of streamer formed by 2.18 V_i (0.33 $U_{50BD}=327$ kV) in a 150 mm gap with $r_i=1$ mm ($U_{50BD}\approx 970$ kV) [13,15]

147

6.3. Iso-surface plot of electric field distribution as modeling result of streamer is compared with corresponding experimental image in the inset image. Definite breakdown voltage, U_{DBD} , for the modeling geometry ($d=25$ mm, $r_i=40$ μm) is equal to 95 kV. In the experimental data, the applied voltages are expressed in terms of streamer initiation voltage, V_i , and 50% breakdown voltage, U_{BD} , which is the impulse peak at which the dielectric breaks down in half of the discharge tests:

<i>Modeling (peak, rise time)</i>	<i>Experiment (Photography method and applied voltage peak)</i>
6 V_i (1.9 U_{DBD}), 100 ns	Streak image of streamer formed by 4.88 V_i (1.57 $U_{50BD}=583$ kV) in a 100 mm gap with $r_i=1$ mm ($U_{50BD}\approx 370$ kV) [13,15]

148

6.4. Iso-surface plot of electric field distribution as modeling result of streamer is compared with corresponding experimental image in the inset image. Definite

breakdown voltage, U_{DBD} , for the modeling geometry ($d=25$ mm, $r_i=40$ μ m) is equal to 95 kV. In the experimental data, the applied voltages are expressed in terms of streamer initiation voltage, V_i , and 50% breakdown voltage, U_{BD} , which is the impulse peak at which the dielectric breaks down in half of the discharge tests:

<i>Modeling (peak, rise time)</i>	<i>Experiment (Photography method and applied voltage peak)</i>
7.66 V_i (2.42 U_{DBD}), 10 ns	Schlieren images of streamer formed by 7.25 V_i (100 kV=5.55 U_{50BD} , 30 ns) in a 2.5 mm gap with $r_i=25$ μ m ($U_{50BD} \approx 18$ kV) [15,18]

149

6.5. Iso-surface plot of electric field distribution as modeling result of streamer is compared with corresponding experimental image in the inset image. Definite breakdown voltage, U_{DBD} , for the modeling geometry ($d=25$ mm, $r_i=40$ μ m) is equal to 95 kV. In the experimental data, the applied voltages are expressed in terms of streamer initiation voltage, V_i , and 50% breakdown voltage, U_{BD} , which is the impulse peak at which the dielectric breaks down in half of the discharge tests:

<i>Modeling (peak, rise time)</i>	<i>Experiment (Photography method and applied voltage peak)</i>
8.66 V_i (2.74 U_{DBD}), 100 ns	Streak images of streamer formed by 8.2 V_i (0.8 $U_{50BD}=24$ kV) in a 3 mm gap with $r_i=5$ μ m ($U_{50BD} \approx 30$ kV) [15,105].

150

6.6. Iso-surface plot of electric field distribution as modeling result of streamer is compared with corresponding experimental image in the inset image. Definite breakdown voltage, U_{DBD} , for the modeling geometry ($d=25$ mm, $r_i=40$ μ m) is equal to 95 kV. In the experimental data, the applied voltages are expressed in terms of streamer initiation voltage, V_i , and 50% breakdown voltage, U_{BD} , which is the impulse peak at which the dielectric breaks down in half of the discharge tests:

<i>Modeling (peak, rise time)</i>	<i>Experiment (Photography method and applied voltage peak)</i>
9 V_i (2.84 U_{DBD}), 10 ns	Schlieren images of streamer formed by 2.77 V_i (47 KV= 1.88 U_{50BD} , 20 ns) in a 5 mm gap with $r_i=25$ μ m ($U_{50BD} \approx 25$ kV) [15,18]

151

6.7. Iso-surface plot of electric field distribution as modeling result of streamer is compared with corresponding experimental image in the inset image. Definite breakdown voltage, U_{DBD} , for the modeling geometry ($d=25$ mm, $r_i=40$ μ m) is equal to 95 kV. In the experimental data, the applied voltages are expressed in terms of streamer initiation voltage, V_i , and 50% breakdown voltage, U_{BD} , which is the impulse peak at which the dielectric breaks down in half of the discharge tests:

<i>Modeling (peak, rise time)</i>	<i>Experiment (Photography method and applied voltage peak)</i>
10 V_i (3.16 U_{DBD}), 100 ns	Schlieren images of streamer formed by 7.25 V_i (5.55 $U_{50BD}=100$ kV, 300 ns) in a 2.5 mm gap with $r_i=25$ μ m ($U_{50BD} \approx 18$ kV) [15,18]

152

6.8. Iso-surface plot of electric field distribution as modeling result of streamer is compared with corresponding experimental image in the inset image. Definite breakdown voltage, U_{DBD} , for the modeling geometry ($d=25$ mm, $r_i=40$ μ m) is equal to 95 kV. In the experimental data, the applied voltages are expressed in terms of streamer initiation voltage, V_i , and 50% breakdown voltage, U_{BD} , which

is the impulse peak at which the dielectric breaks down in half of the discharge tests:

<i>Modeling (peak, rise time)</i>	<i>Experiment (Photography method and applied voltage peak)</i>
10.66 V_i (3.37 U_{DBD}), 100 ns	Shadowgraphy images of streamer formed by 11.1 V_i (5.55 U_{50BD} =100 kV, 1.2 μ s) in a 2.5 mm gap with r_i =30 μ m (U_{50BD} \approx 14 kV) [2,15]

153

- 6.9. Iso-surface plot of electric field distribution as modeling result of streamer is compared with corresponding experimental image in the inset image. Definite breakdown voltage, U_{DBD} , for the modeling geometry ($d=25$ mm, $r_i=40$ μ m) is equal to 95 kV. In the experimental data, the applied voltages are expressed in terms of streamer initiation voltage, V_i , and 50% breakdown voltage, U_{BD} , which is the impulse peak at which the dielectric breaks down in half of the discharge tests:

<i>Modeling (peak, rise time)</i>	<i>Experiment (Photography method and applied voltage peak)</i>
11.33 V_i (3.58 U_{DBD}), 10 ns	Streak images of streamer formed by 10.23 V_i (1.14 U_{50BD} =30 kV) in a 2 mm gap with $r_i=5$ μ m (U_{50BD} \approx 30 kV) [15,105].

154

- 6.10. Iso-surface plot of electric field distribution as modeling result of streamer is compared with corresponding experimental image in the inset image. Definite breakdown voltage, U_{DBD} , for the modeling geometry ($d=25$ mm, $r_i=40$ μ m) is equal to 95 kV. In the experimental data, the applied voltages are expressed in terms of streamer initiation voltage, V_i , and 50% breakdown voltage, U_{BD} , which is the impulse peak at which the dielectric breaks down in half of the discharge tests:

<i>Modeling (peak, rise time)</i>	<i>Experiment (Photography method and applied voltage peak)</i>
12.6 V_i (4 U_{DBD}), 10 ns	Intensifier gate photographs of streamer formed by 13.2 V_i (0.9 U_{50BD} =304 kV) in a 200 mm gap with $r_i=40$ μ m (U_{50BD} \approx 340 kV) [14,15]

155

- 6.11. Iso-surface plot of electric field distribution as modeling result of streamer is compared with corresponding experimental image in the inset image. Definite breakdown voltage, U_{DBD} , for the modeling geometry ($d=25$ mm, $r_i=40$ μ m) is equal to 95 kV. In the experimental data, the applied voltages are expressed in terms of streamer initiation voltage, V_i , and 50% breakdown voltage, U_{BD} , which is the impulse peak at which the dielectric breaks down in half of the discharge tests:

<i>Modeling (peak, rise time)</i>	<i>Experiment (Photography method and applied voltage peak)</i>
15.2 (4.8 U_{DBD}) 10 ns	Intensifier gate photographs of streamer formed by 16 V_i (0.87 U_{50BD} =304 kV) in a 200 mm gap with $r_i=3$ μ m (U_{50BD} \approx 350 kV) [14,15]

156

- 6.12. Iso-surface plot of electric field distribution as modeling result of streamer is compared with corresponding experimental image in the inset image. Definite breakdown voltage, U_{DBD} , for the modeling geometry ($d=25$ mm, $r_i=40$ μ m) is equal to 95 kV. In the experimental data, the applied voltages are expressed in terms of streamer initiation voltage, V_i , and 50% breakdown voltage, U_{BD} , which is the impulse peak at which the dielectric breaks down in half of the discharge tests:

<i>Modeling (peak, rise time)</i>	<i>Experiment (Photography method and applied voltage peak)</i>
15.83 V_i (5 U_{DBD}), 100 ns	Shadowgraphy images of streamer formed by 14.44 V_i (9.28 U_{50BD} = 130 kV, 1.2 μ s) in a 2.5 mm gap with $r_i=30$ μ m (U_{50BD} \approx 14 kV) [2,15]

157

- 6.13. Iso-surface plot of electric field distribution as modeling result of streamer is compared with corresponding experimental image in the inset image. Definite breakdown voltage, U_{DBD} , for the modeling geometry ($d=25$ mm, $r_i=40$ μ m) is equal to 95 kV. In the experimental data, the applied voltages are expressed in terms of streamer initiation voltage, V_i , and 50% breakdown voltage, U_{BD} , which is the impulse peak at which the dielectric breaks down in half of the discharge tests:

<i>Modeling (peak, rise time)</i>	<i>Experiment (Photography method and applied voltage peak)</i>
16.1 (5.1 U_{DBD}), 10 ns	Intensifier gate photographs of streamer formed by 18.62 V_i (1.38 $U_{50BD}=304$ kV) in a 50 mm gap with $r_i=3$ μ m ($U_{50BD}\approx 220$ kV) [14,15]

158

- 6.14. Iso-surface plot of electric field distribution as modeling result of streamer is compared with corresponding experimental image in the inset image. Definite breakdown voltage, U_{DBD} , for the modeling geometry ($d=25$ mm, $r_i=40$ μ m) is equal to 95 kV. In the experimental data, the applied voltages are expressed in terms of streamer initiation voltage, V_i , and 50% breakdown voltage, U_{BD} , which is the impulse peak at which the dielectric breaks down in half of the discharge tests:

<i>Modeling (peak, rise time)</i>	<i>Experiment (Photography method and applied voltage peak)</i>
18.3 V_i (5.8 U_{DBD}), 100 ns	Schlieren images of streamer formed by 20.1 V_i (4.3 $U_{50BD}=28$ kV, 1 μ s) in a 1 mm gap with $r_i=5$ μ m ($U_{50BD}\approx 6.5$ kV) [3,18]

159

- 6.15. Symmetrical streamer branching due to symmetric initial electron disturbance distribution (planes of symmetry are $x=0$ and $y=0$) showing that the numerical instabilities are minor enough to guarantee that the branching occurs due to physical inhomogeneities. The propagation direction of the main streamer column is in $-z$ direction. The left panel shows iso-surface plots of the electric field generated by streamer branching from different view planes (xy, xz and yz plane views).

161

- 6.16. Streamer head configuration defined based on distribution of volume charge density. Three characteristic lengths, r_a , r_b and d are defined based on the distribution of charge density magnitude ($0.5\rho_{max}$ to ρ_{max}) to study the streamer head instability growth, which ultimately cause the branching. Numerical modeling shows that the chance of branching increases as the head curvature ratio $\alpha=r_a/d$ increases. Our previous studies on the 2-D streamer model (Chapter 5) show that increasing either applied voltage peak or applied voltage rate of rise would increase α .

162

- 6.17. Colors show the applied voltage rise-times: black (1 μ s), blue (100 ns), purple (10 ns) and red (1 ns). Marker shapes indicate the applied voltage peaks: 130 kV (*), 200 kV (\star), 250 kV (\bullet), 300 kV (\blacktriangledown), 350 kV (\blacksquare), 400 kV (\blacklozenge), and 500 kV (\times). The points are obtained by taking average from ten different inhomogeneity distributions, but with the same inhomogeneity radius, maximum intensity and density of 5 μ m, 10^4 Cm^{-3} and 10^{11} m^{-3} , respectively.

164

- 6.18. Actual span of data of each normalized characteristic length indicated with error bars. The streamer characteristic lengths are measured from of 280 simulation

cases (10 individual simulations with different inhomogeneities in each case) modeled within the parameter boundaries of $|G_{Mp}| < 10^{10} \text{ Cm}^{-3}\text{s}^{-1}$, $|\rho_p| < 10^4 \text{ Cm}^{-3}$, $C_p = 10^{11} \text{ m}^{-3}$, $1 \mu\text{m} < R_p < 10 \mu\text{m}$. The values shown in Figure 18 are midpoints in each case. Colors show the applied voltage rise-times: black (1 μs), blue (100 ns), purple (10 ns) and red (1 ns). Marker shapes indicate the applied voltage peaks: 130 kV (*), 200 kV (★), 250 kV (●), 300 kV (▼), 350 kV (■), 400 kV (◆), and 500 kV (×). 165






7.1. Efficiency (left) and damage percentage (right) of liquid immersed solid dielectric (spacer) versus, ε_i , the ratio of the liquid permittivity over the solid LID permittivity, for different pressboard materials (different plotted symbols), as reported in [63]. The dielectric efficiency is maximum and the damage on the immersed dielectric is minimum where the permittivities are equal, $\varepsilon_i=1$. 169


7.2. Perpendicular (left) and parallel (right) liquid immersed dielectric (LID) configurations in 25 mm apart needle-sphere electrode geometries. Two bottom panels show closer views of the perpendicular (left) and parallel (right) immersed dielectrics just next to the needle electrodes. Streamers initiate from the positive needle electrode, elongate through the oil bulk and possibly settle on the LID surface as shown by arrows in the bottom panels. The distance of the perpendicular interfacial surface from the needle electrode tip varies in the range of 1- 4 mm and the diameter of the parallel bore varies between 100-400 μm . 172

7.3. Streamer/surface flashover initiation on the perpendicular [panels (a), (b)] and parallel [panels (c), (d)] LID interfaces. The streamer formed in oil emanates from a needle under an impulse voltage with 400 kV peak and 0.1 μs rise-time hits the SF_6 surface [panels (a), (c)] and the pressboard surfaces [panels (b), (d)]. In each panel, the left hand side picture shows the normalized volume charge density (from $0.5|\rho_{max}|$ (the brightest color) to $|\rho_{max}|$ (the darkest color)) and the right hand side picture shows the normalized electric field magnitude (from $0.5|E_{max}|$ to $|E_{max}|$). Values of $|E_{max}|$ and $|\rho_{max}|$ are (a): $|E_{max}|=2.2 \times 10^8 \text{ V/m}$, $|\rho_{max}|=7.71 \times 10^2 \text{ C/m}^3$, (b): $|E_{max}|=2.9 \times 10^8 \text{ V/m}$, $|\rho_{max}|=1.85 \times 10^3 \text{ C/m}^3$, (c): $|E_{max}|=2.8 \times 10^8 \text{ V/m}$, $|\rho_{max}|=2.31 \times 10^3 \text{ C/m}^3$ and (d): $|E_{max}|=3.21 \times 10^8 \text{ V/m}$, $|\rho_{max}|=4.88 \times 10^3 \text{ C/m}^3$ respectively. 173

7.4. Free volume charge in the oil region and its image charge in pressboard region close to the oil immersed barrier interface. The direction and magnitude of the force on the free volume charge caused by permittivity mismatch can be calculated using the method of images [15]. 175

7.5. Intensity and direction difference across the interfacial surface of two dielectrics due to the difference of permittivity. Left side of the figure shows the reason that the electric field magnitude is greater in pressboard region (in absence of surface charge density) and field lines deflect inward when the pressboard permittivity is smaller than the oil. The right hand side shows the reason that opposite is true when the pressboard permittivity is greater than the oil. 175

- 7.6. Electric field distribution for flashovers expanding on the parallel LID surface under positive applied impulse voltage with (a): 200 kV peak and (b,c): 400 kV peak all with 0.1 μ s rise-time. Panels (a) and (b) show surface flashover on PTFE and panel (c) shows surface flashover on a pressboard interface. At all panels, the flashover edge is about 1 mm from the needle tip. 176
- 7.7. Electric field magnitude distribution for parallel pressboard (PB) interface. The streamers are formed by impulse voltages with 130 kV (first row), 200 kV (second row) and 400 kV (third row) peak amplitudes, all with 0.1 μ s rise-time. $E_{\min} \approx 0$ and E_{\max} is given in each panel. E_{\min}  E_{\max} 177
- 7.8. Electric field magnitude distribution for parallel PTFE interface. The streamers are formed by impulse voltages with 130 kV (first row), 200 kV (second row) and 400 kV (third row) peak amplitudes, all with 0.1 μ s rise-time. $E_{\min} \approx 0$ and E_{\max} is given in each panel. E_{\min}  E_{\max} 178
- 7.9. Electric field magnitude distribution for parallel SF₆ interface. The streamers are formed by impulse voltages with 130 kV (first row), 200 kV (second row) and 400 kV (third row) peak amplitudes, all with 0.1 μ s rise-time. $E_{\min} \approx 0$ and E_{\max} is given in each panel. E_{\min}  E_{\max} 180
- 7.10. Surface flashover edge trajectories on the parallel LID surface against time under applied impulse voltage with 130 kV, 200kV and 400 kV peaks and 0.1 μ s rise-time. Purple markers and dashed curves show streamer head positions in oil-only system adapted from ². Time $t=0$ corresponds to the time that streamer reaches the parallel LID interface. Purple dotted curves are fitted polynomial expressions as $1.8 \times 10^{12} t^{1.9}$, $1.7 \times 10^{11} t^{1.7}$ and $2.3 \times 10^9 t^{1.38}$ [mm] for streamers formed by 130 kV, 200 kV and 400kV, respectively in oil-only systems which are valid for $t < 1 \mu$ s. 182
- 7.11. Electric field distributions at the perpendicular interfacial LID surfaces 1 mm from the needle tip for applied voltages with 130 kV (top), 200 kV (middle) and 400 kV (bottom) peaks and 0.1 μ s rise-time. Left panel shows the oil-pressboard interface with size scale of 5 μ m for all three sections. Right panel shows oil-SF₆ interface with size scale of 10 μ m for all three sections. All surface flashover edges are 0.25 mm from the axis of symmetry. Again, it should be noted that the spatial scale of the left column is different from the right column. 183
- 7.12. Electric field magnitude distribution for perpendicular pressboard interface. The streamers are formed by impulse voltages with 130 kV (first row), 200 kV (second row) and 400 kV (third row) peak amplitudes, all with 0.1 μ s rise-time. $E_{\min} \approx 0$ and E_{\max} is given in each panel. E_{\min}  E_{\max} 184
- 7.13. Electric field magnitude distribution for perpendicular PTFE interface. The streamers are formed by impulse voltages with 130 kV (first row), 200 kV (second row) and 400 kV (third row) peak amplitudes, all with 0.1 μ s rise-time. $E_{\min} \approx 0$ and E_{\max} is given in each panel. E_{\min}  E_{\max} 186

- 7.14. Electric field magnitude distribution for perpendicular SF₆ interface. The streamers are formed by impulse voltages with 130 kV (first row), 200 kV (second row) and 400 kV (third row) peak amplitudes, all with 0.1 μs rise-time. E_{min}≈0 and E_{max} is given in each panel.  187
- 7.15. Electric field magnitude distribution for perpendicular LID interfaces. The streamers are formed by impulse voltages with and 130 kV (first row), 200 kV (second row) and 400 kV (third row) peak amplitudes, all with 0.1 μs rise-time. E_{min}≈0 and E_{max} is given in each panel. 187
- 7.16. Surface flashover edge trajectories on the perpendicular LID surface against time for (a): pressboard with ε_r= 4.4 and (b): SF₆ at five bar with ε_r=1.1 (b). “d” is the distance of the perpendicular interface from the needle tip. 189
- 7.17. Normal component (z-direction) electric field distribution at the interfacial surface of oil/pressboard at z=250 μm distance from the needle having 200 kV peak and 100 ns rise-time at t=200 ns. The electric field strength is normalized to 1.2×10⁷ V/m. The tangential component (r-direction) of electric field is continuous across the interface. Three perpendicular 5 μm segments have been chosen (using “cross-sectional plot parameters, line/extrusion”) to plot E_z, and ρ on. Yellow lines show electric field streamlines and white lines show equipotential lines. 191
- 7.18. Normal component (z-direction) electric field distribution on *segment 1* shown in Fig. 7.16 at the oil/pressboard interfacial. The electric field strength is normalized to 1.2×10⁷ V/m. The distance is normalized to 25 mm. 192
- 7.19. Normal component (z-direction) electric field distribution on *segment 2* shown in Fig. 7.16 at the oil/pressboard interfacial surface 250 μm far from the needle having 200 kV peak and 100 ns rise-time at t=200 ns. The electric field strength is normalized to 1.2×10⁷ V/m. The distance is normalized to 25 mm. 192
- 7.20. Normal component (z-direction) electric field distribution on *segment 3* shown in Fig. 7.16 at the oil/pressboard interfacial surface 250 μm far from the needle having 200 kV peak and 100 ns rise-time at t=200 ns. The electric field strength is normalized to 1.2×10⁷ V/m. The distance is normalized to 25 mm. 193
- 7.21. Space charge density on the *segment 1* shown in Fig. 7.16 at the oil/pressboard interfacial surface 250 μm from the needle having 200 kV peak and 100 ns. 193
- 7.22. Space charge density on the *segment 2* shown in Fig. 7.16 at the oil/pressboard interfacial surface 250 μm from the needle having 200 kV peak and 100 ns. 194

- 7.23. Space charge density on the *segment 3* shown in Fig. 7.16 at the oil/pressboard interfacial surface 250 μm from the needle having 200 kV peak and 100 ns. Space charge density is almost zero at this segment. 194
- 7.24. Surface charge density at the oil/pressboard interfacial (shown in Fig. 7.16) surface 250 μm far from the needle having 200 kV peak and 100 ns at different time instants. The harsh oscillations observed in this plot is usual when we are using weak form boundary conditions and streamline artificial diffusion. These fluctuations are minimized using different arbitrary functions and weak constraints. However, these oscillations are inevitable while streamline artificial diffusion is applied. 195
- 7.25. Surface charge density at the oil/pressboard interfacial surface 250 μm from the needle having 200 kV peak and 100 ns rise-time at $t=200$ ns. Fitting is also provided using MATLAB parameters gaussian fit. Dotted data shows the envelops of the raw data and the solid lines show the fitted curve with similar colors for each data. 196
- 8.1. Schematic view of the multiphase model of streamer propagation. There are three distinct physical phases: liquid, gas and plasma. For each phase one would have to solve different sets of equations, which also have to be interrelated. To reduce the number of elements and complexity of the model, one can assume the electric field to be uniformly distributed in the inter-electrode area. 204
- A1. Different streamer propagation mechanisms under two different artificial diffusions: electric field magnitude distribution solved by (left): upwind Petrov-Galerkin diffusion and (right): anisotropic diffusion. The applied voltage peak magnitude to the positive needle is 200 kV and the rise-time is 100 ns. 208
- A2. Off-axis branching in a streamer formed by a positive impulse with 200 kV and 1 ns rise-time still appears even with an extremely fine mesh around the needle (colors and white lines depict electric field and equipotential lines, respectively). 210
- A3. Off-axis branching in a positive streamer formed by a positive impulse with 200 kV and 1 ns rise-time disappears even with a fine mesh over a larger box around the needle (colors and white lines depict electric field and equipotential lines, respectively). 210
- A4. Electric field magnitude (color) and streamlines (white lines) for two different mesh element size distributions under a positively applied voltage (200 kV peak and 100 ns rise-time at time 85 ns). The two simulations are separately computed with the left side plot having a smooth fine mesh while the right side plot has a fine mesh within 40 μm and for the outer area beyond this box it has been freely meshed. Both SD and CWD are applied. 211
- A5. Different cases of element size transformation over space and spatial disturbances that they may produce, (a): critical disturbance over a big jump in element size; (b): negligible

disturbance over a small jump in element size; (c): a gradual rise in element size minimizes the effect of numerical disturbances due to element size variation.	212
A6. Mesh refinement policy in the 3D model in the vicinity of the needle. Mesh refinement data is given in Table A1.	213
A7. Comparison of 3-D model result and 2-D model result for plasma mesh calibration for an applied impulse voltage with 200 kV peak and 100 ns rise-time after 80 ns (2-D model) and 84 ns (3-D model). The maximum electric fields are 3.54 MV/cm (2-D model) and 3.42 MV/cm (3-D model). The streamer heads are at almost equal distances from the needle tip.	214
A8. Comparison of 3-D model result and 2-D model result for plasma mesh calibration for an applied impulse voltage with 200 kV peak and 100 ns rise-time after 80 ns (2-D model) and 84 ns (3-D model). The maximum electric fields are 3.54 MV/cm (2-D model) and 3.36 MV/cm (3-D model). The streamer heads are at almost equal distances from the needle tip.	215
A9. An exemplary mesh selection process for a 2-D axisymmetric modeling. Similar processes have been employed for each cases presented in this thesis.	216
A10. Illustration of a negative streamer (left) and a positive streamer (right) formation and propagation in a needle-plane geometry (which is similar to needle-sphere geometry). As can be seen the negative streamers initiate with wider front due to the lower mobility of the positive ions. Since positive ions are not as effective as electrons to shield the needle electrode electric field, the needle affects a larger space immediately after the voltage is applied to the electrode; therefore the initial ionized region becomes much bulkier than the positive streamers. This eventually leads to lower field enhancement ahead of negative streamers and decreases the average velocity compared to fast positive streamers which always keep their filamentary shape thanks to the highly mobile electrons constantly forming at the ionization zone at the streamer head.	217
A11. The pillbox containing 12 inhomogeneities (red spheres) with 10 μm radius adjacent to the needle electrode. The streamer branching results obtained with these inhomogeneities (an any other sizes above and below 5 μm radius) show less similarity to the experimental images than those modeling images taken from results generated with inhomogeneities with 5 μm radius, suggesting that in practice, the effective inhomogeneities should have an average radius of 5 μm .	219
A12. The pillbox containing 12 inhomogeneities (red spheres) with 5 μm radius adjacent to the needle electrode. The streamer branching results obtained with these inhomogeneities with 5 μm radius, show the maximum resemblance with experimental pictures suggesting that in practice, the effective inhomogeneities should have an average radius of 5 μm .	220

List of Tables

4.1.	Governing Equations of Charge Transport in Liquid/Solid Insulation Systems	64
4.2.	Parameters of dielectric Analysis with Linear Charge Injection Condition in Cartesian Geometry	66
4.3.	Numerical Parameter Values of dielectric Analysis with Space Charge Limited Condition	87
5.1.	Physical Parameters Used in the Streamer/Surface Flashover Model	99
7.1.	Parameters of Investigated Transformer Oil-Immersed Dielectrics	171
A1.	Mesh Data in Figure A6	214
A2.	Numerical Simulation Methods for Streamer Development Modeling	221

Introduction

Each year, an enormous financial investment is made for high-voltage technology all around the world. The main objective of the high voltage industry is to invent, design and manufacture a broad range of devices used in diverse applications and technologies:

- *Aerospace*: charged particle accelerators, compact ultrahigh capacitors and plasma propulsion devices
- *Health and Medical Applications*: capillary electrophoresis, cell separation, spectrometry, X-ray and magnetic resonance imaging devices
- *Defense*: Threat detection, radars, high power microwave generation, and electromagnetic launchers
- *Commercial industries*: Air/water quality testing and filtration, semiconductor manufacturing, lighting, plasma display panels, and pulsed food sterilization
- *Power delivery*: power transmission, transformation, interruption and distribution apparatus.

Therefore, any means to improve the performance or lower the manufacturing/maintenance expenses of high-voltage systems is valuable to industry as well as society whose annual expenditure on energy, medical care, etc. is directly affected by the price of high voltage technology.

Electrical insulation is a vital component of all high-voltage systems [1]. The technology and materials, used for high-voltage electrical insulation, ultimately determine the quality, reliability and final price of a high-voltage device. In general, the insulation materials used in high-voltage technology can be divided into three categories: solid dielectrics (such as silicon rubber, epoxy resin and cross-linked polyethylene), liquid dielectrics (such as mineral oil, silicon oil and natural ester), and gas dielectrics (such as air and SF₆). The dielectric task is to insulate high voltage segments from the low-voltage and grounded components and prevent the entire electric system from breaking down. This is considered as a safety concern too, since low-voltage sections are usually accessible to operators and patients.

Among different types of dielectric materials, liquids have an excellent capability of withstanding extra high voltages while their superior heat transfer efficiency makes liquid-based insulation systems the best choice for compact high voltage devices [2] in which a considerable amount of heat is generated by the high voltage components such as in power transformers and medical imaging devices. To prevent excessive temperature rise, the accumulated heat should somehow

be carried out of the device volume. Usually liquid dielectrics are the only fluid inside the device that can be circulated regularly.

Most liquid dielectrics, which are highly flammable, can trigger a sustaining fire in case of an electrical breakdown. The risk of fire is another main incentive for reducing the volume of the liquid dielectric in high voltage apparatus as failure of bulkier equipment can cause larger fires. Therefore, insulation failure potentially leads to disastrous consequences on environment, industry, financial markets, safety, and health.

Over the past half-century, there have been many scientific investigations devoted to characterizing and understanding of dielectric liquid breakdown, leading to the formation of a large body of literature on the subject [2-27]. A universally accepted breakdown theory does not exist due to the scientific complexity of the liquid-state in high voltage environment and the many different experimental test situations reported in the literature. This thesis aims at addressing this deficiency by comprehensively modeling the important mechanisms that influence the electrodynamic characteristics of electrically stressed dielectric liquids, with and without the presence of immersed solid barriers and microscopic inhomogeneities.

Streamers are the main origins of electric breakdown in liquid dielectrics [2]. Section 1.1 of this chapter describes the streamers formed in liquid dielectrics and introduces the causes of electrical charge generation and transport in a typical liquid dielectric. Charge generation and transport is crucially important in liquid dielectrics, since without the presence of migrating charges in the liquid dielectric, streamers cannot develop. Section 1.2 introduces the methodology of this thesis research to study the physics of streamer formation, propagation and branching in the most used liquid dielectric, transformer oil. The mechanisms of streamer interaction with liquid immersed solid dielectrics, which often result in the formation of surface flashovers, are also briefly addressed in this section. Section 1.3 reviews the key contributions of this thesis research. This chapter concludes with section 1.4, giving an outline of the entire thesis.

1.1 Charge Generation and Transport in Liquid Dielectrics Leading to Streamer Formation and Electrical Breakdown

A dielectric liquid is usually defined as an electrically insulating liquid in which self-dissociation is extremely small and its resistivity is greater than $1 \times 10^9 \Omega\text{-cm}$ [16]. Free electrical charges inside the dielectric liquid, either injected from an external source or generated by different types of ionization play the main role in electrical breakdown. Electrical breakdown in a dielectric liquid occurs when the liquid is bridged from the high voltage electrode to a grounded electrode by highly conductive ionized channels called arcs. Arc formation is the last step in a series of very short-time events on the nanosecond to microsecond timescale, before electric breakdown. Pre-breakdown phenomena, called streamers, are narrow (in transformer oil their thickness varies between a few micrometers to a few millimeters) low-density ionized structures that form in regions of dielectric fluid that are over-stressed by intense electric fields (On the order of 1 MV/cm or higher for transformer oil). Streamers usually propagate with velocities on the order of

~km/s in liquid dielectrics. Once a streamer forms, it tends to elongate, emanating from the point of initiation, typically a sharp high-voltage electrode, and growing towards a point with the lowest potential in the system (usually grounded). When the streamer reaches the grounded electrode, it traces a high conductivity path, which acts like a short circuit between the two electrodes. Therefore, when the streamer reaches the grounded electrode, the current flowing through the arc increases dramatically as the impedance across the gap drops, which completes the electrical breakdown of the dielectric. In liquid and high-pressure gaseous dielectrics, streamers are the main causes of electric breakdown. Streamers in liquid dielectrics mainly consist of ionized plasma and gases. The products remaining in the streamer trace can recombine and dissolve in the fluid unless the voltage source injects too much energy into the channel and forms a burning arc. This means that gaseous and liquid dielectrics can be self-healing after occurrence of streamers unlike solid dielectrics in which any partial electrical discharge causes a permanent insulation damage. The ability of liquid dielectrics to conform to complex geometries and self-heal, along with their high heat transfer capacity leads to their preferred practical use compared to solid and gaseous dielectrics in low frequency (e.g., 50 or 60 Hz power systems) and high frequency (e.g., power modulators and pulsed power systems) applications.

1.2 Analysis and Modeling of Streamer Development in Liquid-Solid Insulation Systems

Over the past several decades the quantity and quality of experimental electrical breakdown research in dielectric liquids in general and in transformer oil in particular has increased significantly. However, one cannot introduce a thorough understanding of streamer physics only based on the present empirical results. There are many hypotheses about streamer development mechanisms, such as different propagation modes for different applied voltage polarities [5,8,13], fractal morphology of streamer trees [17], role of gas bubbles in streamer development [18,19] and multiphase fingering initiated by small signal interfacial waves [20,21], each revealing important characteristics of streamer propagation and branching. Nonetheless, a realistic model of streamer dynamics is still required to understand the primary reasons behind streamer formation, propagation and branching, in which many different processes take part including electrostatics, quantum mechanics, thermodynamics and fluid mechanics.

Many research groups have attempted to model streamer development in different media, especially for gaseous dielectrics such as air and SF₆. They have approached many complex problems in streamer propagation in gases using different density, particle and hybrid models as well as many experimental studies [29-38]. Briels *et al.* accurately measured the diameter and velocity of streamers in air [32]. Niayesh *et al.* demonstrated the role of runaway electrons in a very short delayed breakdown in different electrode geometries through a 2-D axisymmetric modeling [33,38]. Niemayer *et al.* successfully argued that the streamer trees have fractal structures [40] and Babaeva *et al.*, presented a model incorporating macroscopic inhomogeneities in a 2-D axisymmetric model [19]. Nijdam introduced stereo-photography of streamers in air [35]. These works give a first insight on streamer acceleration, branching and dependence on applied voltage, however they cannot explain streamer dynamics in liquids, since different factors govern

the streamer development in liquids. Qian *et al.* proposed a three-carrier continuum model in a simple geometry in a 2-D Cartesian coordinates [39]. However, their model needs much improvement to explain streamer development with an acceptable resolution in complex electrode geometries.

Over the past nine years at MIT, a comprehensive research study has been conducted on streamer initiation driven by molecular ionization and propagation of single column streamers in transformer oil based dielectric liquids using a three-carrier continuum electrohydrodynamic model with COMSOL Multiphysics [23-28,41-53]. Through these years, many important aspects of streamer physics have been identified and explained. O’Sullivan [23] found out that the molecular ionization is the primary mechanism responsible for streamer formation and propagation in liquids rather than other ionization processes [23,24]. He developed a preliminary model of phase conversion (vaporization) inside the propagating streamer column [23,24]. Hwang [25] continued and extended O’Sullivan’s work to explain how adding conductive nanoparticles into transformer oil increases the positive impulse voltage breakdown strength compared to the pure transformer oil [25-27]. Hwang also developed a preliminary model for 2-D streamer propagation in liquid-solid composite dielectric systems [25].

Nevertheless, there are still many other attributes of streamers that remain unexplained such as propagation of negative streamers, effects of the applied voltage peak amplitude and rise-time on streamer development, branching origins, and causes of higher propagation velocity modes of streamers. One of the traditionally interesting goals is the development of a physical model that can predict the breakdown voltage and time to breakdown. The previous works have mostly focused on the initiation stage of streamer, which happens in the vicinity of the needle electrode [23-27]. The aim of this thesis is to develop a more complete model able to answer each of the following questions:

1. Is there an analytical solution for charge transport dynamics in a typical liquid-solid composite dielectric system? Can we relate the physical parameters of the charge transport such as velocity, density and time of flight to circuit parameters like voltage and current?
2. What are the analogies and the differences between positive and negative streamers propagating in liquid dielectrics?
3. How do characteristics of the voltage source, electrode geometries and electrode gap distances affect the streamer velocity, shape and number of streamer branches, breakdown voltage, current and delay?
4. What are the effects of an immersed dielectric in a liquid dielectric on the breakdown process? Do they assist breakdown or can they help prevent it? What are the determining parameters of the immersed dielectric to prevent breakdown?
5. What causes streamers to branch out in a typical liquid dielectric? Are streamer branching origins completely stochastic?

1.2.1 *One-Dimensional Analysis of Charge Transport in Liquid-Solid Composite Dielectric Systems*

To answer question 1 raised in section 1.2, closed form analytical solutions for one-dimensional (1-D) migration-Ohmic unipolar analysis of charge transport phenomena in the series, two-region, oil-pressboard composite dielectric systems are presented in planar, coaxial cylindrical and concentric spherical electrode geometries with a step current source. Different charge injection boundary conditions are applied to these problems to find closed form solutions in the steady state and transients for different physical parameters. Using the method of characteristics the governing partial differential equations are converted into a set of ordinary differential equations that allow analytical solution as a function of time and space for volume and interfacial surface charge densities, charge trajectories in the oil region, and electric field and voltage drop in oil and pressboard regions. Analytical solutions are compared with numerical solutions of identical problems obtained using COMSOL Multiphysics as a way of gaining confidence in the correctness and accuracy of our numerical methods and solutions. Unfortunately, the analytic solution is impossible for more complex 2-D and 3-D geometries.

1.2.2 *Two-dimensional Axisymmetric Modeling of Single Column Streamer*

This thesis extends the two-dimensional (2-D) axisymmetric streamer models of O’Sullivan [23] and Hwang [25] to answer the questions raised in section 1.2. To answer questions 2 and 3, these 2-D models are significantly improved in this thesis research to contain more physics. For instance, the ionization potential of hydrocarbon molecules has been imported to the model presented in this thesis based on the results derived from Density Functional Theory (DFT) [12]. Specifically, dependency of the hydrocarbon molecule ionization potential on the electric field intensity is considered. Electron saturation velocity is also taken into account in the present model. In addition to the added physics into the model, more realistic settings and functions are applied in the model such as standard lightning impulse voltages (exactly the same voltage that is applied in the high-voltage laboratories) instead of Heaviside step functions as used in [25]. This extension makes the results comparable to the experimental measurements.

To eliminate numerical instabilities in the models of [23-28], improved numerical stabilization methods and mesh refinement policies are employed. More consistent stabilization techniques such as upwind streamline and crosswind artificial diffusions have been applied to effectively stabilize the conservation of charge equations for different applied voltage polarities with much broader varieties of peak amplitudes and rise-times. Previous works were unable to consistently stabilize the simulations, resulting in convergence issues and non-physical results [25]. Different combinations of direct and iterative state of the art solvers have been employed as well. Such numerical approaches enable the present model to solve the equations with much greater spatial resolution. Models of O’Sullivan [23] and Hwang [25] accurately describe the positive streamers for a certain positive peak amplitude (130 kV) and rise-time (~10 ns) of applied voltage. Beyond these limits, the models suffer from numerical artifacts and instabilities. In this thesis, simulations are stabilized in such a way that can be generalized easily to any complicated applied voltage

waveform or electrode geometry designed for specific high voltage apparatus such as a power transformer with or without pressboard [41-53].

These improvements to the 2-D axisymmetric model, enabled us to study the effects of different applied voltage polarities, peak amplitudes, rise-times [41,42,48], gap distances [49], electrode geometries [52] and immersed dielectrics [45,50] on streamer development in the most used liquid dielectrics, transformer oil.

1.2.3 *Two-dimensional Modeling of Breakdown Phenomena*

A strong enough sustained over-excitation across the liquid insulation results in a propagating streamer, which eventually bridges the gap between its point of origin at the needle electrode and the opposite sphere electrode that is usually grounded. When this bridge forms, the impedance across the gap drops significantly and an arc may initiate and consequently electrical failure may occur depending on the internal impedance and the power of the voltage source. To model the streamer traveling over a relatively long distance, an extremely efficient mesh refinement policy is required, since in such cases, the high number of mesh elements becomes the modeling bottleneck as the simulation time could be unreasonably high. Through a successful modeling of the complete breakdown process, the streamer velocity over the entire inter-electrode gap has been calculated as well as the flowing current profile until an electrical discharge occurs [49]. This study enables the model to predict the breakdown voltage at any given rise-time and the breakdown lag, which are of extremely important technical interest in the insulation, pulsed power and current interruption applications. According to the results of the complete breakdown modeling, we will answer question 3 raised in section 1.2.

1.2.4 *Modeling of Surface Flashover on Liquid Immersed Dielectrics*

When streamers hit the surface of the liquid immersed dielectric, they transform into surface flashovers creeping on the immersed dielectric interfaces. To determine whether presence of immersed dielectrics, with different permittivities and orientations, assist or help prevent breakdown of liquid dielectrics (to answer question 4 raised in section 1.2), a 2-D axisymmetric model of surface flashover expansion on the interface of the liquid immersed dielectrics is developed [45,50]. Modeling results are presented as flashover shapes, velocities, and distributions of electric field, volume charge density and surface charge density for different liquid-solid and liquid-gas interfaces.

As a typical application, the surface flashover initiation and development on the surfaces of a liquid immersed dielectric is particularly of interest for design of the transformer insulation system, which includes both liquid (transformer oil) and liquid immersed solid dielectrics (pressboard).

1.2.5 Fully Three-Dimensional Modeling of Streamer Branching

Among the other chief characteristics of streamers, which are not fully explained yet, one can mention the causes of streamer branching phenomena, and the effects of the applied voltage and distribution of inhomogeneities on the streamer number of branches, branch velocities and the spatial angle between the branches. A fully three-dimensional streamer model presented in this thesis, shows that the branching as an intrinsic attribute of streamers has both stochastic and deterministic origins, which in some cases make the branching inevitable depending on shape and velocity of the volume charge at the streamer head [51]. Based on the modeling results for streamers propagating in a liquid dielectric, a gauge on the streamer head geometry is introduced that determines whether branching occurs under a given streamer head geometry and specific inhomogeneous perturbation [51]. The model is also able to predict the number of just born branches in case of a branching.

1.3 Main Contributions of Thesis

In this section, the key contributions of the thesis research are reviewed briefly. This thesis introduces a model through which many streamer breakdown characteristics can be accurately predicted. Specifically, for the first time, this thesis presents modeling results for pre-breakdown current, streamer initiation voltage, time to breakdown, initiation voltage, breakdown voltage and number of streamer branches emanating from a streamer node for a wide range of different electrodes, gap geometries, dielectric materials and applied voltages. In addition, this thesis adds many important physics into the existing models of O’Sullivan [23] and Hwang [25], such as electric field dependent ionization potential of hydrocarbon molecules and electric field dependent electron mobility. Using these added features, the model presented in this thesis extends and improves upon the existing modeling results in the literature. Among them, modeling the streamer velocity and shape for different geometries and applied voltages can be mentioned. The results presented in this thesis agree with experimental records in the literature more precisely than the previous models based on which this research is built [23-28]. The detailed results are presented and discussed in the following chapters. Thorough explanations of the modeling approach and discussions of the results are given wherever required throughout this thesis.

In Figure 1.1, the modeling results for streamer velocity obtained in this thesis research are compared with the experimental records found in the literature and the previous modeling work. As can be seen, the model is stable enough to predict the streamer velocity in a much wider range of electrode geometries and applied voltages compared to the prior contributions. The results are also more accurate on the case studies that can be analyzed with previous models. The results plotted in Figure 1.1 are obtained from the two-dimensional model introduced in Chapters 3 and 5.

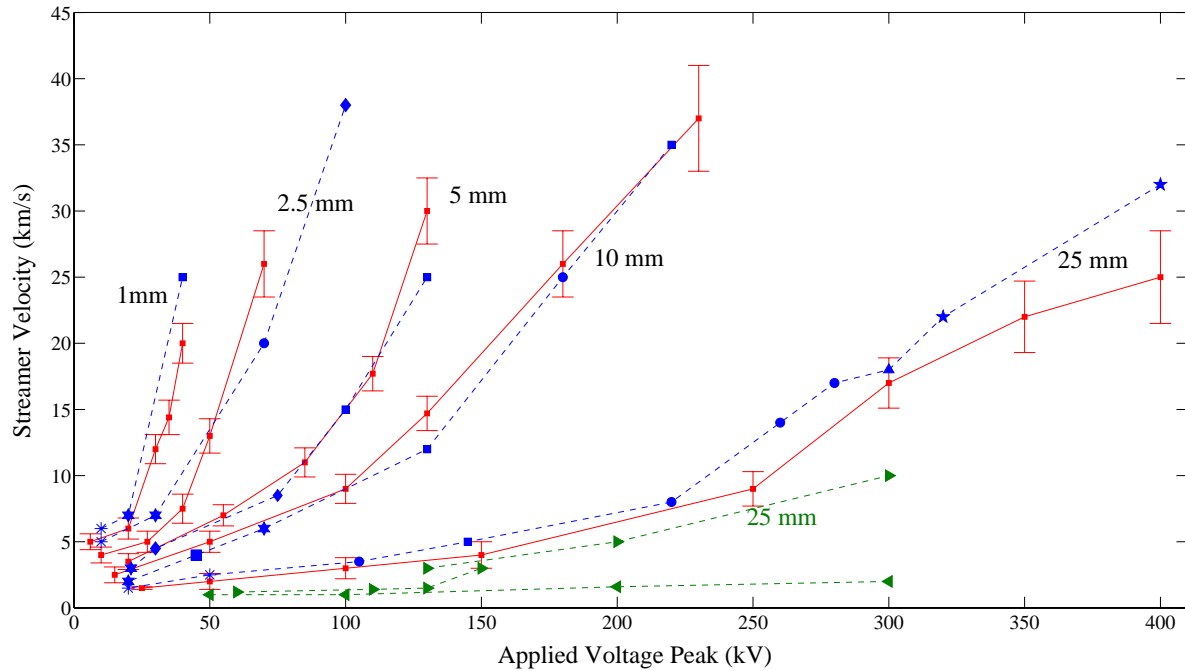


Figure 1.1: Streamer velocity plotted versus applied voltage peak obtained from modeling in this thesis (red square symbols), modeling results of others (green symbols: O'Sullivan [23] (\blacktriangleleft) and Hwang [25] (\blacktriangleright)) and experimental data found in the literature for different electrode gap distances (blue symbols: \blacksquare [2], \bullet [4], \ast [6], \star [7], \blacklozenge [18], \blacktriangle [60], and \ast [106]). The gap distances are labeled on the respective curves. Experimental data are taken from different references.

As can be seen in Figure 1.1, the modeling results presented in this thesis are closer to the experimental measurements than the earlier modeling results of [23,25] which is due to the added physics into the model and also the numerical improvements in the latest versions of the Finite Element Method software, COMSOL Multiphysics used in this thesis research for modeling the streamer development.

An extensive series of modeling results for many different streamer attributes, including positive streamer shape, trajectory and velocity is given and discussed in Chapter 5. Figure 1.2 compares the negative streamer modeling results for streamer velocity with the experimental data found in the literature. Negative streamer propagation modeling results in liquid dielectrics are presented in this thesis for the first time. As can be seen in Figures 1.1 and 1.2, the velocity of negative streamers is appreciably lower than the positive streamers under the same circumstances. The differences between positive and negative streamers will be discussed in length.

In Figures 1.3 and 1.4, the modeling results obtained in this thesis research are compared with the experimental records found in the literature for pre-breakdown current peak, and the minimum voltage required for streamer initiation, respectively. These modeling results are presented in this thesis for the first time to the author's best knowledge. These results are particularly interesting for the ongoing research on the partial discharge (PD) in power apparatus, especially power transformers.

The results plotted in Figures 1.1-1.4 are obtained from the two-dimensional model introduced in Chapters 3 and 5. The modeling results of these figures are extensively discussed in Chapter 5.

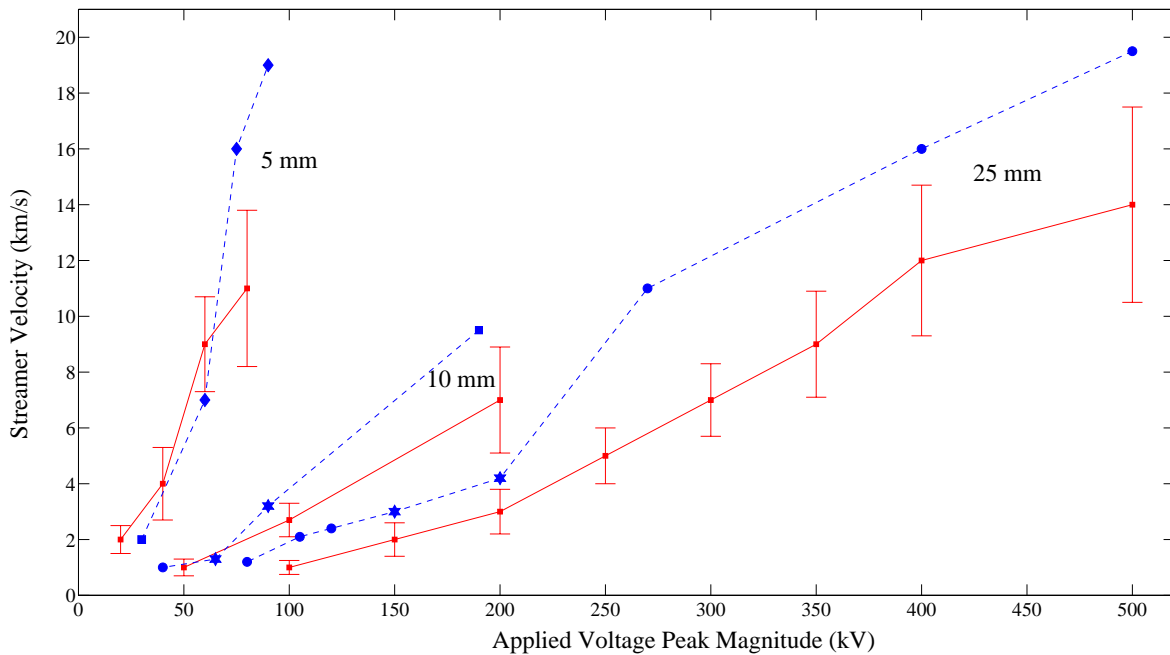


Figure 1.2: Streamer velocity plotted versus applied voltage peak as modeling obtained in this thesis (red square symbols), modeling results of others (green symbols) and experimental data found in the literature (blue symbols) for different electrode gap distances. The gap distances are labeled on the respective curves. Experimental data are taken from different references (■[2], ●[4], * [6], ◆[18]). There is no prior modeling results on negative streamers.

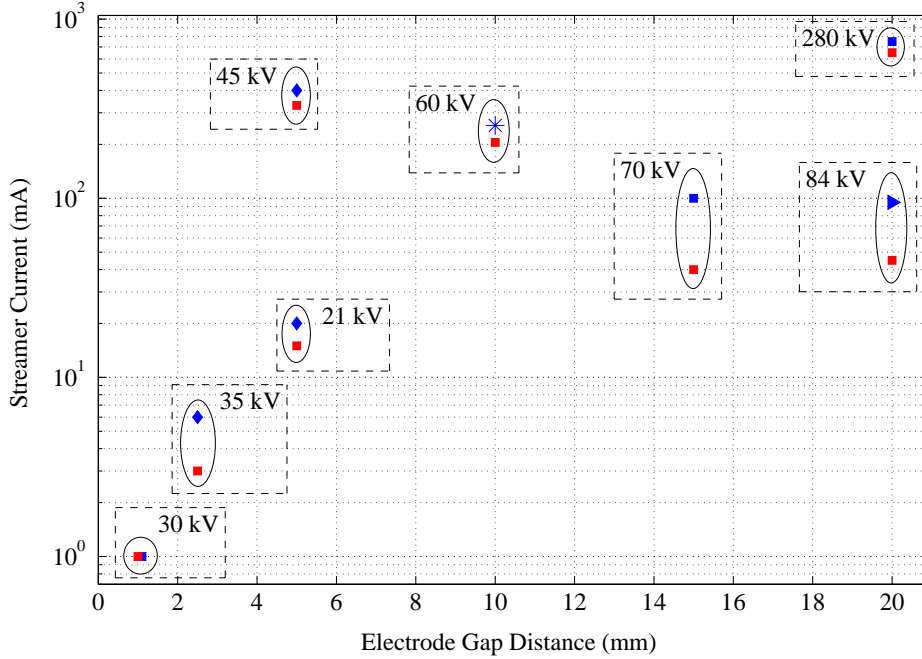


Figure 1.3: Maximum pre-breakdown current plotted for different electrode gap distances. Red square symbols show the modeling results of this thesis and blue symbols show the experimental data found in the literature. Each pair of data is labeled with the associated applied voltage peak. Experimental data are taken from different references (■[2], ◆[18], ►[60], and * [106]).

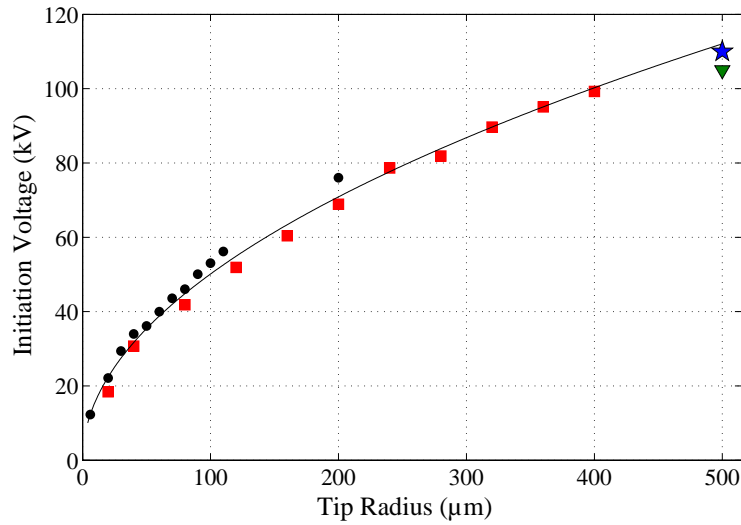


Figure 1.4: Experimental data for initiation voltage of a 6 mm gap (●), a 20 mm gap (▼), and a 50 mm gap (★), all obtained from [15]. Modeling results for a 6 mm gap distance (■). The solid curve, which is fitted to the modeling results, is $V_i = 10^{2.2} \sqrt{r_t}$, where r_t is the positive electrode tip radius in millimeters and the initiation voltage, V_i , is in kilovolts.

Perhaps the most interesting result of this thesis, from the insulation designer's point of view is the prediction of the breakdown voltage of the insulation system. The presented model in Chapter 5 is capable of modeling the streamer flight in entire electrode gap, through which the model can evaluate the breakdown voltage of each electrode gap distance. The computational capacity is the restriction that limits the simulation of the electrode gap length to 10 mm. Prediction of streamer breakdown voltage is a substantial numerical task and this thesis for the first time has incorporated this feature for the liquid dielectrics. Figure 1.5 compares the modeling results with the experimental data found in the literature. As can be seen in this figure, definite breakdown voltage, obtained from the model, is approximately two times greater than the 50% breakdown voltage extracted from the experimental data. In experimental research, since the streamer breakdown is essentially stochastic, the breakdown voltage is expressed in terms of a 50% breakdown voltage, which is the voltage peak at which the dielectric breaks down in half of the discharge tests. The model, however, does not include statistical factors affecting the streamer formation and propagation. Therefore, the calculated value for the definite breakdown voltage by the model is reasonably (almost) two times greater than the 50% breakdown voltage, which is determined after numerous repetitive experiments.

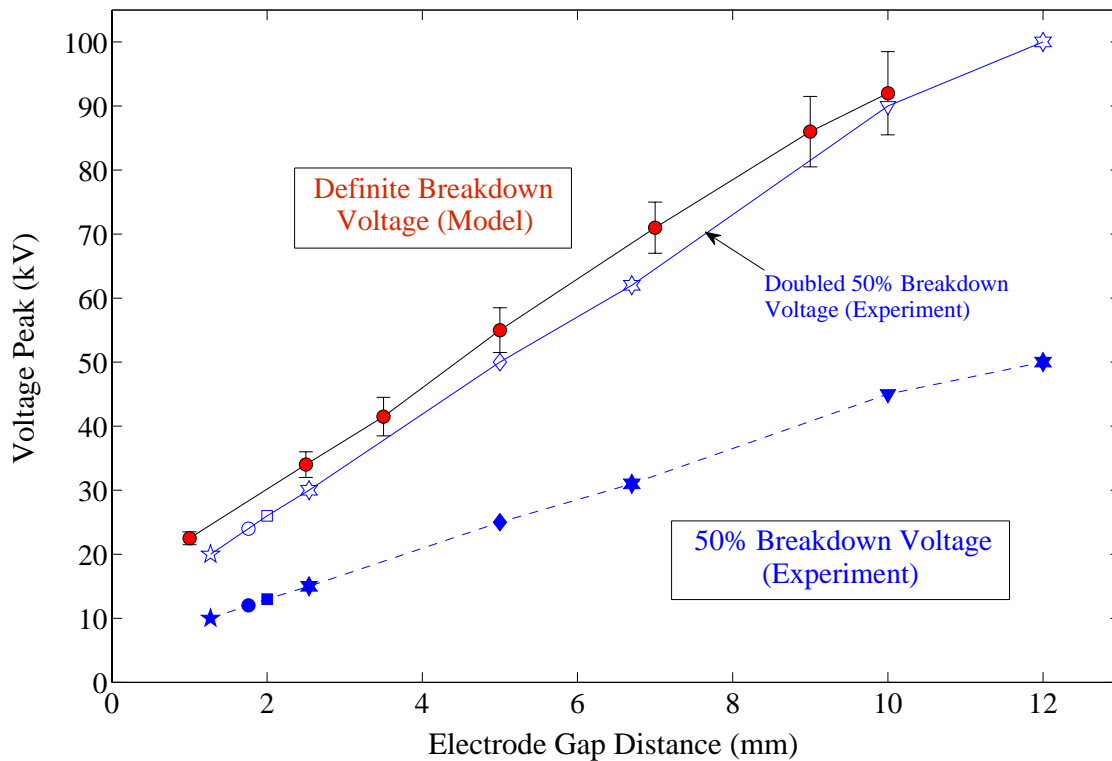


Figure 1.5: Modeling results (red symbols), obtained in this thesis, and experimental data (blue symbols), found in the literature, for breakdown voltages of different needle-sphere electrode gap distances. The model does not include statistical factors affecting the streamer formation and propagation. Therefore, the calculated value for the definite breakdown voltage by the model, is roughly two times greater than the 50% breakdown voltage which is determined after numerous repetitive experiments. Experimental data are taken from different references (■[2], ●[3], ▼[5], ✱[6], ★[7], ◆[18]).

The final goal of this thesis is an ambitious one: three-dimensional modeling of streamer branching. It has been more than 30 years history of various theoretical efforts for understanding the streamer branching which is extremely interesting in many disciplines such as physics, chemistry, mathematics and of course engineering. This thesis investigates both deterministic and stochastic roots of streamer branching. As a conclusion, the streamer tree number of branches is related to the volume charge configuration at the streamer head and the applied voltage amplitude. To be able to assess our modeling results, we have plotted the number of branches obtained from the three-dimensional model in Figure 1.6 alongside the results we have taken from different experimental images found in the literature. The number of active streamer branches is plotted versus applied voltage peak normalized by the streamer initiation voltage, which is mainly a function of electrode tip radius and not the gap distance.

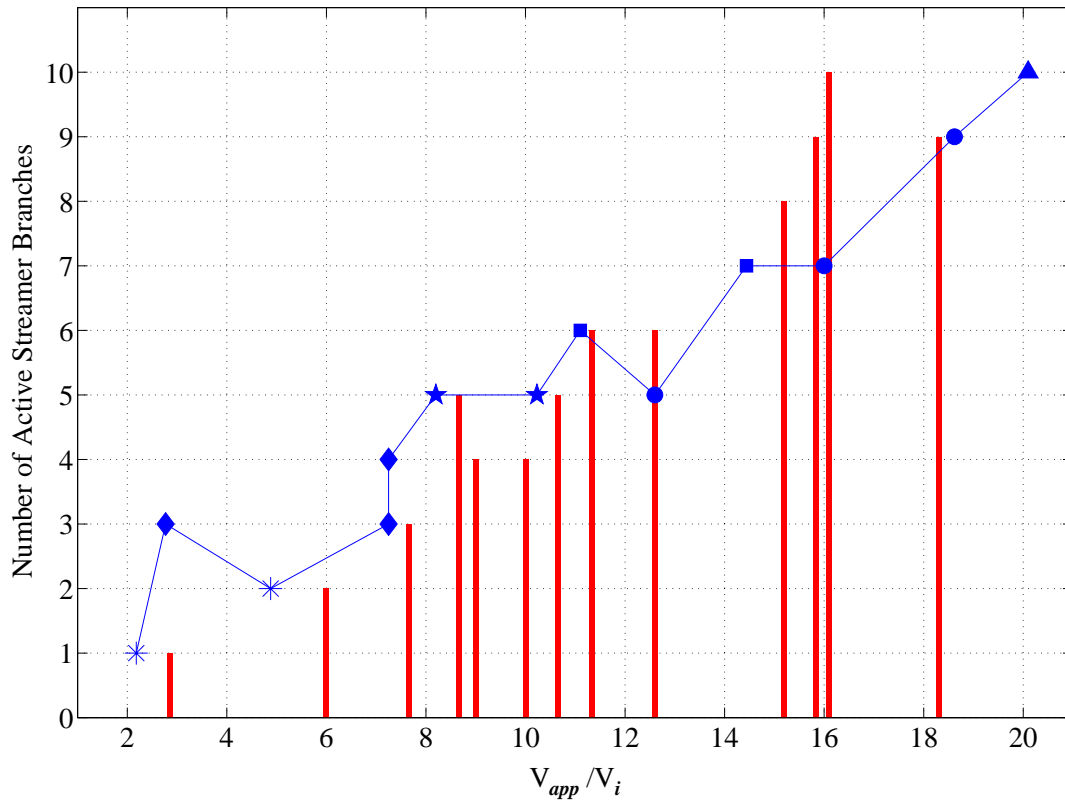


Figure 1.6: Modeling results (red bars), obtained in this thesis, and experimental data (blue symbols), found in the literature, for the number of active streamer branches emanating from a streamer node right after the branching, plotted versus the ratio of applied voltage peak over initiation voltage. Initiation voltage is mainly a function of the needle electrode tip radius. The model does not include statistical factors affecting the streamer formation and propagation. Experimental data are taken from different references (■[2], ●[4], ★[7], ♦[18], ▲[60], and * [106]). More details are provided about both modeling and experimental data in Chapter 6.

The presented modeling results in this thesis generally help us take a further step in understanding streamer breakdown in dielectric liquids. The agreement between modeling results and the experiments shown in Figures 1.1-1.6 indicates that the presented model is a promising tool for both streamer research and industrial design of liquid dielectric based insulation systems. The model itself can be regarded as a contribution from both numerical modeling and physical points of view.

1.4 Thesis Outline

To study the charge transport mechanisms and streamer physics in this thesis, the first priority is given to the analytical approach. Unfortunately, analytical solution is only available for single polarity charge in simple one-dimensional electrode geometries. Therefore, for complete modeling of streamers in standard electrode geometries, our second priority, the numerical modeling tools, are employed to find a solution that satisfies both governing equations and boundary conditions. In addition to transformer oil-only systems, insulation systems involving solid dielectrics immersed in transformer oil are also modeled to understand the effects of barriers with different materials and different surface orientations on the streamer development. Furthermore, a fully 3-D stochastic streamer model is presented which explains the stochastic and deterministic causes of streamer branching in liquid dielectrics.

The remainder of this thesis is organized with Chapter 2 describing the underlying mechanisms of streamer development in transformer oil-based insulations systems. In this chapter, the current knowledge about the causes of streamer formation, propagation and branching is reviewed. In addition, in this chapter we also analyze applications of the immersed dielectrics, like pressboard, and different types of additives, such as various types of oil molecules and conductive nanoparticles in transformer oil.

Chapter 3 in full detail gives the governing equations, boundary conditions, key parameters and characteristics used in the model. In particular, we describe the simulation geometries, implementation of governing equations and boundary conditions in COMSOL Multiphysics, numerical stabilization techniques and solvers, meshing policies and mesh element definitions. Using information given in this chapter, one should be able to rebuild the model from scratch to reproduce identical results.

One-dimensional analysis of unipolar charge transport in different Cartesian, cylindrical and spherical coordinates is presented in Chapter 4. Detailed solutions in steady-state and transient form, obtained by the method of characteristics, are discussed with complete explanation and illustrations. At the end of this chapter, analytical solutions are compared with identical problems simulated in COMSOL Multiphysics as a confirmation of modeling methods and results.

Two-dimensional axisymmetric modeling results of streamer initiation and propagation in transformer oil are presented in Chapter 5. Some of these results are compared with earlier modeling and experimental works to make sure that the modeling results are accurate.

Chapter 6 explains the streamer branching phenomena in transformer oil using the results of a three-dimensional model of streamer development. Stochastic and deterministic origins of streamer branching are identified by detailed comparison of modeling results and experimental images of streamer trees under many different conditions. Numerical implementation of the 3-D streamer model incorporating stochastic microscopic inhomogeneities is also described in this chapter. As compared in Chapter 6, obtained 3-D structures of streamer trees from the model agree qualitatively and quantitatively with corresponding experimental images found in the literature.

Surface flashover formation and expansion on liquid immersed dielectrics are discussed using the modeling results in Chapter 7. Different immersed dielectric permittivities and orientations are examined in a 2-D axisymmetric liquid/solid model, and the results are qualitatively explained using the method of images in this chapter.

This thesis concludes in Chapter 8 with a summary of the key findings and suggested future work to deepen the understanding of breakdown in dielectric liquids.

A few appendices are presented at the end of this thesis, which are useful for reproducing the results of the thesis and establishing a solid background for the continuing future modeling work. A list of the references cited in this thesis is given afterwards.

Pre-breakdown Mechanisms in Transformer Oil-Based Insulation Systems

Many experimental results have been reported on streamer development in high-voltage-stressed transformer oil [2-18], none can lead to a complete theory of breakdown. These empirical records in the literature give insights into the potential mechanisms behind streamer formation and ultimately to electrical breakdown in dielectric liquids, in general, and in transformer oil, in particular. This chapter details important streamer characteristics when it elongates in transformer oil and interacts with immersed dielectrics and additives in transformer oil. Based upon the mechanisms introduced in this chapter, a generalized physical model of electrical breakdown in liquid dielectrics will be developed and used throughout this thesis.

2.1 Streamer Initiation, Propagation and Branching in Transformer Oil

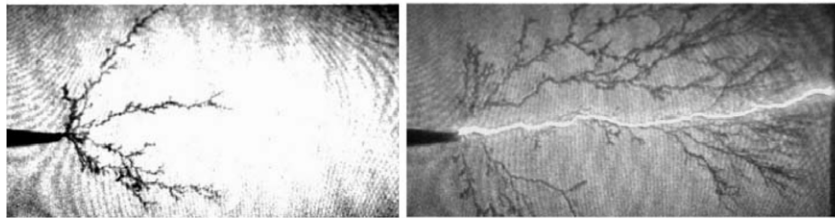
There are a number of mechanisms suggested in the literature for streamer initiation, propagation and branching. All these mechanisms share the central concept that generation of space charge (either by injection from the electrodes or ionization of the oil molecules), acceleration of highly mobile electrons, and spatial inhomogeneities are critical to streamer formation, propagation and branching, respectively.

The extent of the streamer development depends on physicochemical properties of the liquid dielectric [25], electrode geometries [15,51], gap distance [9,14,51] and the nature and strength of the electrical excitation [15,48,53]. In transformer oil, experimental evidence shows that streamers emanating from an electrode holding the positive potential (anode) generally have filamentary structures and tend to initiate at lower applied voltages than streamers initiating from a negative voltage electrode (cathode) for the same electrode geometries and gap distances⁴ [49]. Furthermore, for the same voltage magnitude, positive streamers propagate faster and further than their negative counterparts [48]. As a result, positive streamers, which are more common in nature⁵, constitute a greater risk to oil-insulated systems than do negative streamers. Figure 2.1 shows a positive streamer and a negative streamer formed in the similar geometry (5 mm gap) under different applied voltages. As a rule of thumb, the breakdown voltage magnitude for a positively applied voltage (anode-initiated streamer) is about half of the voltage magnitude

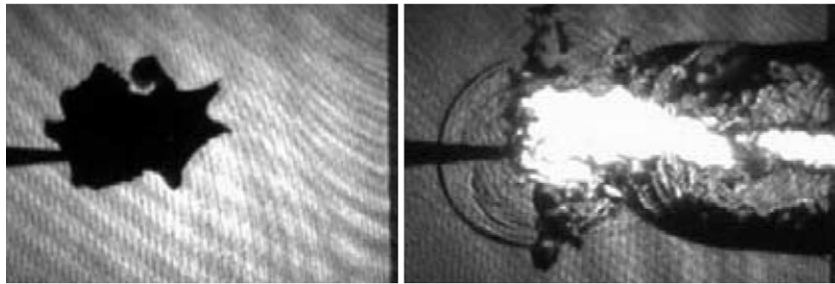
⁴ Streamers initiated from the positive electrode (anode initiated streamers) are called positive streamers, and streamers initiated from the negative electrode (cathode initiated streamers) are called negative streamers.

⁵ Positive lightning strokes that hit power equipment are more common (90% of the strokes are positive) [54]. Nevertheless, negative streamers cannot be neglected since these strokes can generate travelling waves, which can pick up any high amplitude, polarity and steep wave front depending on the transmission line length and characteristics [54].

required for a breakdown under a negatively applied voltage (anode-initiated streamer). In addition, the streamer breakdown is clearly sensitive to the background pressure of the liquid when a negative voltage is applied to the needle electrode, which suggests that in negative breakdown. Unlike positive breakdown, a significant amount of gas is generated inside the streamer channel, also known as bubbles [8,18,19]. The appearance of shockwaves in images taken by [8,18] around negative streamers supports the idea of phase conversion in negative streamers.



(a): Positive Streamer



(b): Negative Streamer

Figure 2.1: (a): A positive streamer and (b): a negative streamer formed in the 5 mm gap under different applied voltages (+26 kV and -47 kV). Filamentary structure of the positive streamer can be clearly distinguished from the thick and bushy shape of the negative streamer. The luminous plasma generated inside the channel formed by a negative streamer is also quite bulkier. The shock waves seen around the negative streamer supports the idea of formation of an appreciable gas volume inside the negative streamer channel [8,18]. The propagation velocities of positive and negative streamers are 1.43 km/s and 0.83 km/s, respectively [18].

As can be seen in Figure 2.1, both positive and negative streamers branch out in liquid dielectrics just like other dielectric media. Branching is an essential element of streamer discharge that requires a finite perturbation [19,29]. Such perturbations in transformer oil can be inherited from an inhomogeneous initial state, (such as an initial electron density fluctuation) [28-37,51], macroscopic external perturbations (such as dust particles, air bubbles, water drops, or other macroscopic objects) [19], and/or spatial variation of oil molecule types and molecule orientations [27,28].

Several theories have been suggested for causes of streamer branching. Many effective approaches have been also employed to analyze the dynamics of streamer branching, such as fractal morphology of streamer trees [17,40], conformal mapping [30], electro-hydrodynamic

modeling with or without cylindrical symmetry [19,31,39], macroscopic inhomogeneities in bulk liquid [19], realistic fluctuations of discrete electrons [29], slow branching in deterministic fluid models [31], multiphase fingering driven by small signal interfacial waves [20,21]; each revealing important aspects of streamer branching. However, a comprehensive quantitative understanding of the branching phenomena is yet to appear.

From a theoretical point of view, streamers can branch in fully deterministic models through Laplacian instability that resembles the underlying mechanism of viscous finger branching in a two-fluid Hele-Shaw flow [21]. Such instabilities can develop when the volume charge layer ahead of the streamer head is much thinner than the streamer head radius of curvature. In extreme case of a planar ionization front, an infinitesimally small perturbation is sufficient to trigger a branching instability, but for an elongating streamer head with a finite head radius of curvature, only perturbations larger than a certain threshold can grow into a self-sustaining branch structure at the streamer head [29]. Due to the strongly nonlinear nature of streamer dynamics, small fluctuations can be amplified by strong electric fields and significantly alter the propagation path of a streamer. Branching is probably the most noticeable visual attribute of streamers not only in transformer oil and liquid dielectrics, but also in all other dielectrics such as different solid and gaseous dielectrics. For instance, Figure 2.2 shows an interesting case of streamer branching, in which positive streamer branches develop from the remainder of the charges left from an initially formed negative streamer in artificial air. The applied voltage, which is a combination of negative and positive pulses (Fig. 2.2 (j)), forms a bubble-shaped negative streamer (appreciably similar to negative streamers in transformer oil as we will discuss more in Chapter 5) that eventually converts to multiple positive streamer branches.

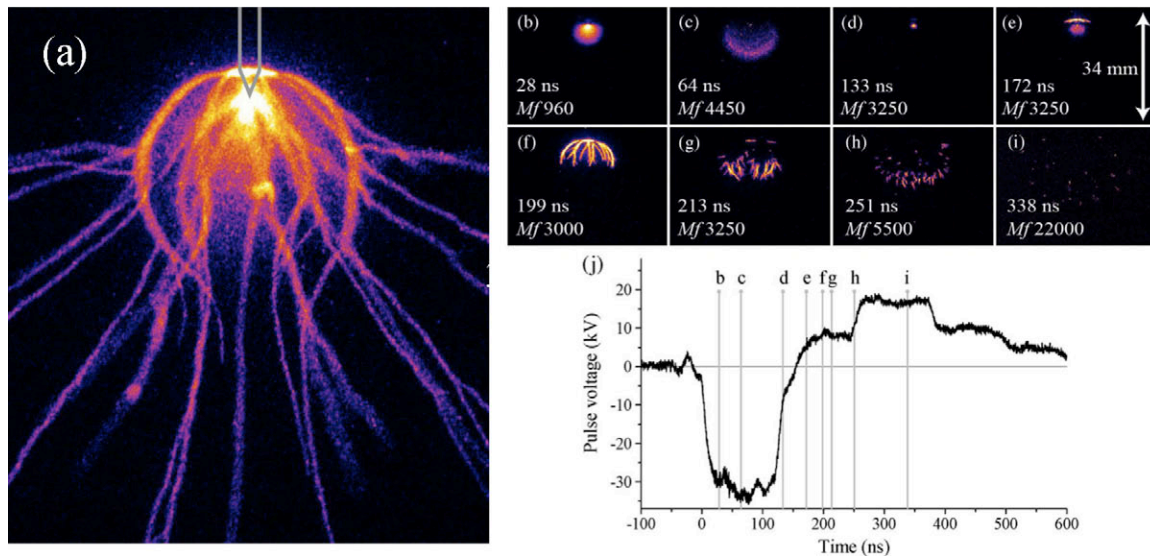


Figure 2.2: (a) Time-integrated and (b-i) time resolved images of a streamer branching during a positive/negative streamer conversion in 600 mbar artificial air. (j): A negative pulse of 35 kV is applied to the needle electrode ($70 \mu\text{m}$ tip radius) for about 100 ns, followed by a positive voltage pulse for 150 ns, which creates positive streamers that run over the surface of the nearly spherical previously formed negative discharge. This is particularly interesting since it reveals that filamentary positive streamers and bubble shaped negative streamers can interchange during a discharge [36].

2.2 Interactions of Streamers Initiated in Transformer Oil with Adjacent Solid and Gaseous Dielectrics

High-voltage equipment is often composed of several different dielectric materials for improved insulating and thermal characteristics. For example, a large portion of a power transformer's insulation capability is based on solid insulation materials such as high-quality, thick cellulose paper and boards, known as transformer-board or pressboard [57,58]. The breakdown voltage of transformer oil over small gaps (millimeters) is remarkably high (several tens of kilovolts). However, the insulation properties of transformer oil-only in large gaps are not satisfactory. The breakdown voltage will improve in the large gaps if transformer oil is used in combination with solid barriers (usually pressboards) [57]. Pressboards have high dielectric strength, good mechanical properties, long lifetime, and are compatible with transformer oil making them good choices for liquid/solid-insulated transformers. The composite transformer oil/pressboard system is generally designed to increase the insulation strength of the transformer against partial discharge, streamers and most importantly electrical breakdown.

Since a pressboard is essentially cellulose paper, which tends to absorb moisture, it has to be carefully dried. Cellulose materials used in pressboards are made from slow growing types of woods that have high-density long fibers. These cellulose long fibers and their high-density lead to durability and high dielectric strength of the oil immersed pressboard [57]. In processing cellulose to be used in an oil-filled transformer, it must be dried and oil impregnated in vacuum. Any moisture content remaining in the pressboard can decrease the dielectric strength and accelerate aging [57]. Oil impregnation of the cellulose, performed under vacuum at elevated temperatures, ensures that the tiny air bubbles between the individual fibers are filled with oil. These air bubbles could easily cause partial discharges if the bubbles were not replaced with oil. Further information regarding cellulose insulation can be found in IEC 60554-3 for cellulose paper and IEC 60641-3 for pressboard [58,59]. Figure 2.3 shows a single-phase transformer with its windings and bushing covered with pressboards ready for oil impregnation. All of the visible brown materials in this figure, which cover the windings and the bushing, are made of different pressboard layers.

Streamer propagation in transformer oil is greatly affected, in general, by the presence of pressboard and, in particular, by two critical characteristics of it: 1) the orientation of the oil-pressboard interface and 2) the permittivity difference between oil and pressboard. To study the permittivity difference and interface orientation of immersed dielectrics, in this thesis, we have selected immersed dielectric materials with higher and lower permittivities than oil placed in either parallel or perpendicular orientations with respect to the original propagation direction of the streamer. Figure 2.4 shows some experimental images for streamer/surface flashover conversion on the parallel (a cylindrical bore shown in part (a)) and perpendicular (horizontal plates shown in parts (b-c)) pressboards immersed in transformer oil.

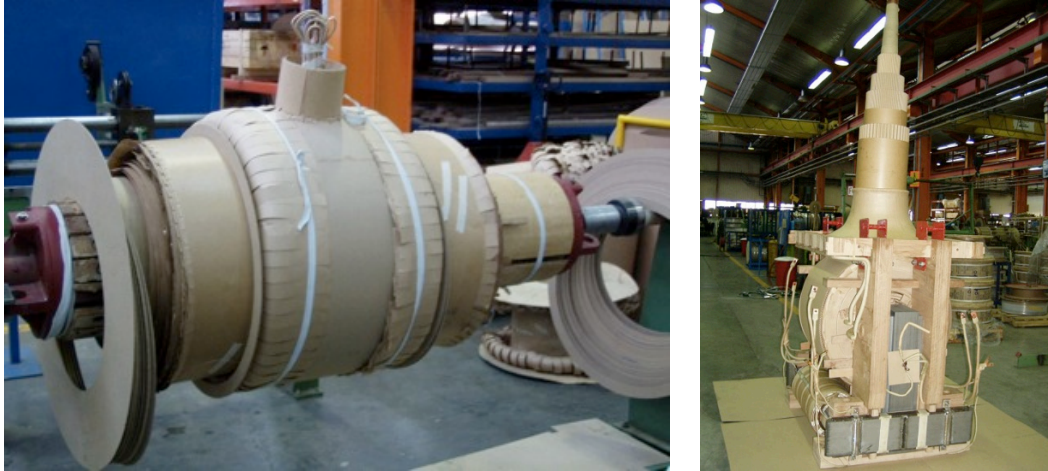


Figure 2.3: (Left) Single-phase transformer windings covered by pressboard layers and (Right): Single-phase high voltage transformer windings and bushing covered with pressboard layers ready for immersing in transformer oil [Courtesy of High Voltage Laboratory, University of Tehran, used with permission].

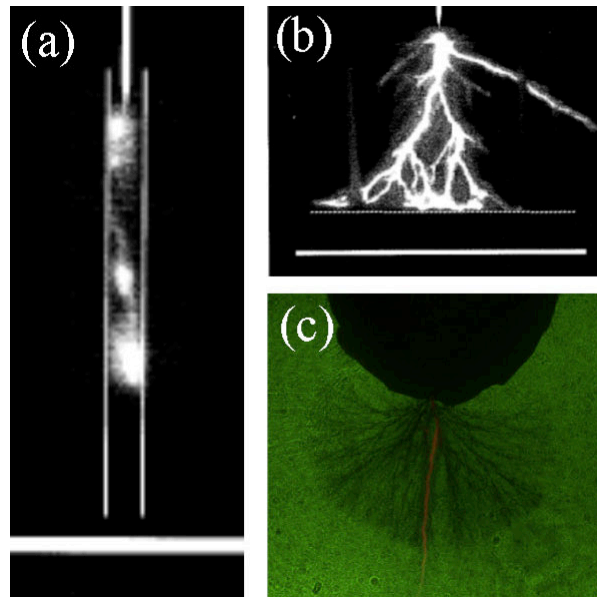


Figure 2.4: Surface flashover development (a): within a polytetrafluoroethylene (PTFE) bore [10] and (b,c): plate perpendicular to the streamer propagation direction [10,61].

It has been reported that low permittivity insulating solids, such as polyethylene and polypropylene, which have relative permittivities of 2.1–2.3 and almost match that of oil, result in higher flashover breakdown voltages for the impulse and 60 Hz excitations [62]. On the other hand, experimental evidence shows that a permittivity mismatch (regardless of which permittivity is greater), such as that of oil and pressboard, assists flashover propagation and enhance surface irregularities [63].

In other works [10,111], the researchers observed that the presence of pressboard spacer objects in oil gave way to large field enhancement due to the permittivity mismatch. Therefore, it was postulated that the field enhancement led to the reduction of the breakdown voltage in an oil-pressboard system compared to an oil-only system. They too were able to show that by utilizing solid materials with relative permittivities comparable to transformer oil, the breakdown voltage appreciably improves compared to the oil-pressboard system.

The reported impact of permittivity differences between oil and pressboard shows that it is a source of major concern for insulation designers. There have also been several patents that address this issue by innovative techniques to reduce the permittivity of pressboard, such that it becomes closer to that of the transformer oil [112,113]. In Chapter 7 of this thesis, based on the modeling results and the method of images [64], we explain and discuss the reasons behind such experimental observations.

2.3 Effects of Additives on Breakdown in Transformer Oil

Many of streamer characteristics are explained through effects of different transformer molecule types and additives. Three charge generation mechanisms of field-, impact-, and photo-ionizations, which play vital roles in streamer development, completely rely on the type and percentage of oil molecules and additives. In a typical transformer oil, it has been shown that the field ionization dramatically increases and becomes the dominant mechanism of charge generation at electric field magnitudes above ~ 1 MV/m [23]. At such levels of electric field intensity, the amount of the volume charge inside the electrode gap is high enough to initiate streamers depending on the electric field direction and electrode gap geometry. Above the minimum voltage for streamer formation, increasing the applied voltage magnitude interestingly does not increase the electric field magnitude inside the oil gap. Instead, an increase in applied voltage amplitude significantly affects the streamer behavior. Different hydrocarbon molecules in transformer oil play a key role in abrupt changes of streamer velocity as the applied voltage amplitude increases [27,28,48,53].

2.3.1 *Different Hydrocarbon Molecules in Transformer oil*

One of the most important streamer characteristics that can be related to the oil additives is the average velocity of streamer propagation [25-28]. Hwang *et al.* have related the transition between streamer modes and oil molecule types [25,27,28]. Distinct classification of streamer modes in transformer oil is based on clear differences in their propagation velocities under different amplitudes of IEC lightning impulse (1.2 μ s rise-time, 50 μ s fall-time) voltage excitations. The higher the magnitude of applied impulse voltage, the higher the streamer mode, and the higher the average streamer propagation velocity. According to [25,27,28], the streamer velocity and shape change dramatically as the applied voltage magnitude increases, although the results do not fully satisfy the 2-D cylindrical symmetry.

Transformer oil is a mixture of different hydrocarbon molecule types including paraffinics, naphthenics and aromatics with controlled percentage of each. To elucidate the role of each hydrocarbon molecule type, researchers have tried to strip away some of the complexity by focusing on pure hydrocarbon liquids by adding controlled amounts of specific additives to study their affects on pre-breakdown phenomena [25,27]. Hwang has compared the properties of streamers propagating in transformer oil with different percentages of each hydrocarbon molecule type [27].

Biller [65] hypothesized that for heterogeneous liquid dielectrics, slow mode streamers are linked to the ionization of “easily ionizable” molecules, while the faster modes are caused by the ionization of main “ordinary” molecules. In the context of transformer oil, the “easily ionizable” species are equivalent to aromatic molecules, which have lower ionization energies [12,25] and lower number density [25,27] than the naphthenic and paraffinic molecules. Ionization of the low concentration aromatic molecules in transformer oil leads to the propagation of streamers with velocities on the order of 1 km/s. The “ordinary” molecules are the main naphthenic and paraffinic hydrocarbons that comprise the majority of transformer oil [25]. As the applied voltage increases, the ionization of the main hydrocarbon molecules in transformer oil, high concentration naphthenic/paraffinic molecules, dominates producing high electric field levels and space charge at the streamer tip, which results in higher modes of streamer propagation [25]. Figure 2.5 shows the streamer average velocity under different applied voltages. Occurrence of different modes is common between different dielectric liquids, however, the voltages at which the transition between modes happens is quite sensitive to the composition and amount of the additives.

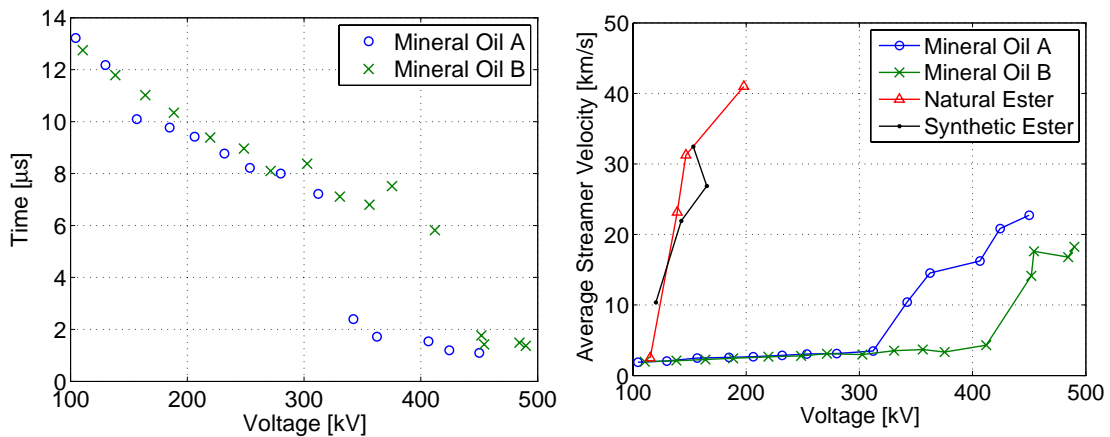


Figure 2.5: Time to breakdown (left) and average streamer velocity (right) versus applied voltage peak provided by ABB Corporate Research in two different transformer oils for the needle-sphere geometry detailed in IEC Standard 60897 [66]. Positive and negative breakdown voltages of mineral oil types A and B are listed below:

Transformer Oil	Positive Breakdown Voltage	Negative Breakdown Voltage
Type A	105 kV	256 kV
Type B	126 kV	166 kV

2.3.2 *Nanoparticle Additives and Microparticle Contaminations*

An interesting research, focused on enhancing transformer oil's electrical and thermal characteristics, is the use of nanotechnology in transformer oil to accelerate cooling of transformer core and coils, simultaneously with increasing the breakdown voltage of the liquid dielectric. In this way, nanoparticle suspensions of a conductive magnetic material (e.g., Fe_3O_4) have been added into the transformer oil [67-70]. This mixture is called a nanofluid. Extensive discussion of heat transfer improvements made by the nanoparticles can be found in [68-70]. Although this approach may defy the conventional wisdom due to the high conductivity of the nanoparticles, the past measurements have shown that such nanofluids have substantially higher positive voltage breakdown levels with slower positive streamer velocities than that of pure transformer oil [25,68-70]. Specifically, it has been shown that floating conductive nanoparticles in transformer oil can lower the positive streamer velocity [25,26]. This paradoxical superior electric field breakdown performance compared to that of pure oil is due to the electron charging of the nanoparticles that convert high mobility electrons generated by field ionization to slow negatively charged nanoparticles carrying trapped electrons with effective mobility reduction by a factor of about $\sim 10^5$ [2-25].

When conductive nanoparticles are added to transformer oil, they effectively trap free electrons, which results in a significant velocity decrease for positive streamers and a velocity increase for negative streamers. Positive streamer's higher propagation speed and positive impulse's higher rate of occurrence in nature offers that the suspending nanoparticles improve high voltage performance and reliability of the transformer oil based nanofluids. Electrical breakdown testing of magnetite nanofluid shows that for positive streamers the breakdown voltage was almost twice that of the base oils during lightning impulse tests while the negative breakdown voltage is up to 15% lower than pure transformer oil breakdown voltage [23,25,70].

The main reason for these changes in positive and negative breakdown voltages is that the free electrons captured by the floating nanoparticles cannot contribute to the streamer propagation and charge transport, since the charged nanoparticles are much less mobile than the electrons. Therefore, fewer electrons are available for streamer development, which means that the velocities of positive and negative streamers would be lower and higher, respectively. This is particularly significant because slower positive streamers and faster negative streamers require more and less time, respectively, to traverse the gap between electrodes to lead to the breakdown. This allows more and less times for the applied positive and negative impulse voltages, respectively, to be extinguished. The results found by Segal *et al.* [67-70] were in direct conflict with conventional wisdom and experience regarding the breakdown of dielectric liquids, where the presence of conducting particulate matter in a dielectric liquid was expected to decrease its breakdown strength. On the other hand, negative impulse voltages cause lower performance of nanofluids since less free electrons lead to thinner initial negative streamer column, which allows for a higher electric field enhancement ahead of the streamer. Therefore, the presence of conducting nanoparticles helps negative streamers propagate faster, meaning that the negative breakdown voltage is reduced in nanofluids compared to the pure transformer oil. The difference between the effect of floating conductive nanoparticles on positive and negative streamers can

also be explained using the analysis performed by Hwang *et al.* [25,26] shown in Figure 2.6. This figure shows how charging a perfectly conducting sphere with surrounding electrons changes the configuration of electric field lines within the liquid dielectric. Charged nanoparticles (with free mobile electrons) make the electric field ahead of positive streamers weaker. In the case that a negative voltage is applied to the needle electrode, the electric field ahead of the negative streamers intensifies. The reason is that the negative streamers propagate in opposite direction electric field.

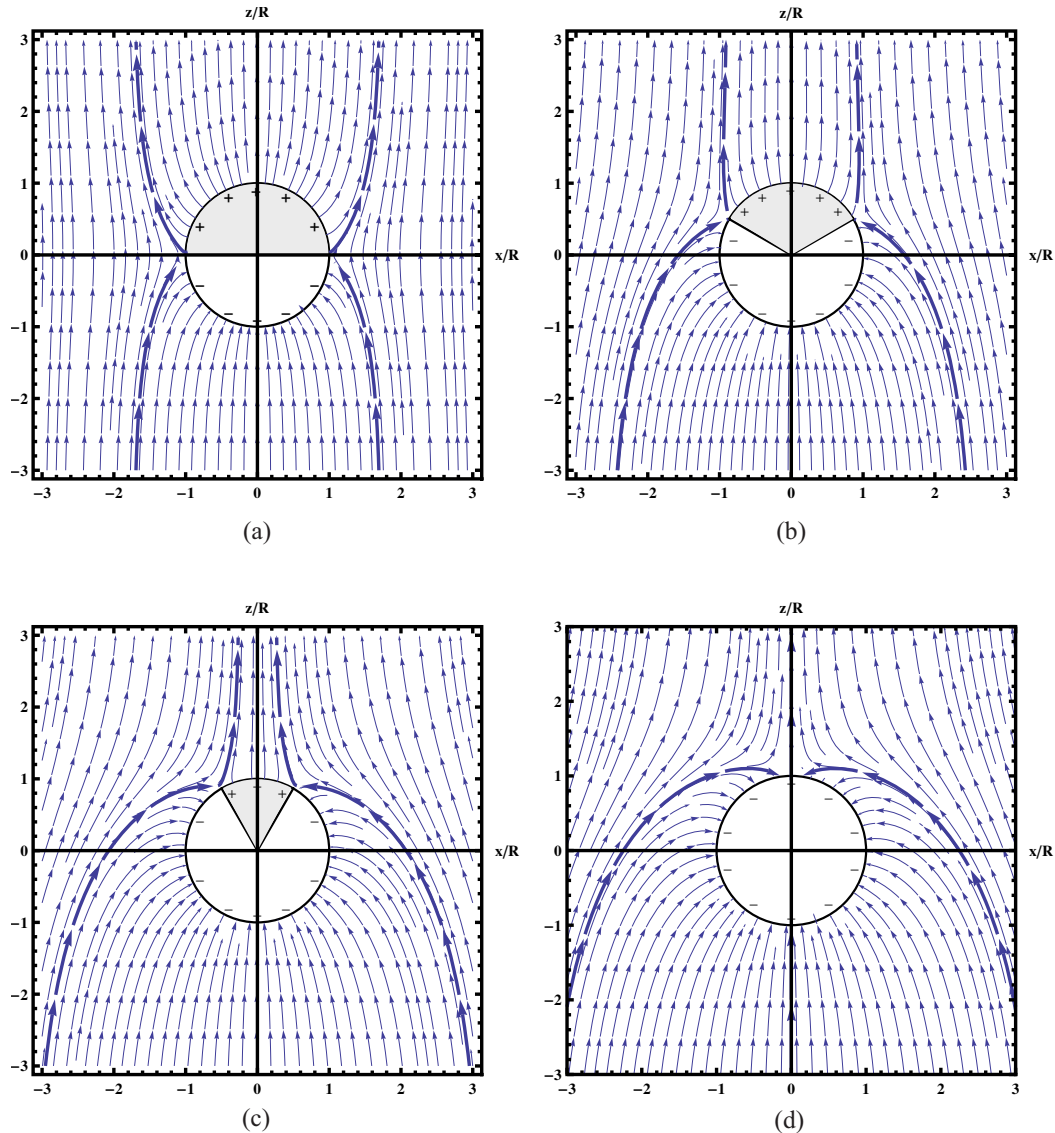


Figure 2.6: Electric field lines for various times after a uniform z -directed electric field is turned on at $t=0$ around a perfectly conducting spherical nanoparticle of radius R surrounded by transformer oil, and free electrons with uniform charge. The thick electric field lines separate field lines that terminate on the nanoparticle from field lines that go around the particle. The suspending nanoparticles can assist and avoid breakdown by scavenging the free electrons and intensifying and weakening the electric field ahead of the negative and positive streamer heads, respectively.

Figure 2.6 can be used to explain the nanoparticle effects on propagation of both positive and negative streamers. Positive streamers propagating in the direction of electric field lines (bottom to top in Figure 2.6) observe an electric field intensity reduction, right in the space beyond an individual charged nanoparticle in their path. Negative streamers, however are propagating in the opposite direction of the electric field lines (top to bottom in Figure 2.6) and observe an electric field enhancement right in the space after they pass an individual charged nanoparticle. These electric field intensity reduction and enhancement are responsible for charged nanoparticle effects on decreasing positive streamer velocities and increasing negative streamer velocities, which consequently affect the breakdown voltages as well.

Numerical Simulation Problem Posing/Approach

Before discussing any streamer model in detail, it is essential to introduce the simulation tool that can effectively solve such multiphysics problems. Most of the simulation work and model solutions presented in this thesis is performed using a commercial finite element method (FEM) simulation package, COMSOL Multiphysics, which as the name suggests, is a simulation tool capable of solving multiphysics problems. This feature makes COMSOL a suitable choice for modeling streamer initiation and growth due to the required coupling of electrodynamic, thermodynamic and fluid-dynamic processes. In this section, we describe the basic steps to build a COMSOL model to be solved in a timely manner.

3.1 Introduction to COMSOL Multiphysics Modeling of Streamer/Surface Flashover

The implementation and subsequent simulation of a streamer model using COMSOL is quite straightforward and can be done in five simple steps. The first step is the selection of the spatial dimension for which the simulation will take place and the mathematical equations that make up the model using COMSOL's Model Navigator [71]. The simulation geometry is then defined along with the subdomain and boundary settings for each of the model equations. The geometry is then meshed, the model is solved and finally, the results of the simulation are post-processed. This chapter presents the way our streamer model (or any other similar model) should be set up and solved in COMSOL Multiphysics 4.3a (which is quite similar to the older versions of the software). The accuracy of COMSOL in streamer modeling was tested in this thesis and in O'Sullivan's work [23] by solving problems with known analytical solutions using COMSOL and comparing the results with these solutions. This comparative analysis, the results of which are published in [46,72,73], shows that the method implemented in COMSOL Multiphysics is capable of generating very accurate numerical solutions. In addition, results of our FEM modeling have been compared to the results obtained from a finite volume method (FVM) software, OpenFoam, and results are in reasonable agreement [74].

3.2 Problem Posing Elements

To model the streamers, many COMSOL modules should be selected and carefully tuned with accurate parameter definitions and realistic boundary conditions. Before then, however, the

simulation geometry and the boundary conditions should be chosen in a way that the modeling results can be compared with previous models and experiments. Apart from these physical issues, any numerical effort has to answer two challenging questions. One, is there any quicker or more accurate technique (e.g., meshing scheme and solver) that can be employed? Two, how can we be sure that the results are trustworthy (verification)? This chapter presents the essential steps we have taken in this thesis to make our model faster and more accurate. Using the features introduced in this chapter, we have significantly improved and optimized our model. More details of the streamer model and verifying evidence of accuracy for the obtained results are also given in the following chapters.

3.2.1 *Simulation Geometry*

Before selecting the relevant governing equations for the model, the simulation geometry must be defined. COMSOL provides users with a range of CAD tools for geometry modeling purposes. Some of these CAD tools are provided with a livelink [71] in which both COMSOL and CAD tools can run simultaneously. One of these powerful tools is Solidwork [71], which is especially helpful for three-dimensional (3-D) simulation geometries. In addition to these external tools, the COMSOL package allows for drawing new geometries as well as the importation of geometries from stand alone CAD packages. All the streamer simulations presented in this thesis use a simulation geometry imported from an external source. A 3-D CAD representation of this geometry, studied in Chapter 6, was built inside COMSOL Multiphysics using its own “revolve” and “extrusion” functions. This 3-D representation was used for all 3-D studies carried out as a part of this thesis. In addition to the traditional Cartesian 1-D, 2-D and 3-D geometries, COMSOL supports a very useful axisymmetric space dimension that enables us to model the essentially 3-D phenomena of streamer development using the axial symmetry approximation with a much faster pace.

3.2.2 *Governing Equations*

Once the simulation geometry has been drawn/imported into COMSOL, the subdomain and the boundary settings for the model equations must be specified by selecting each of the model equations and entering the appropriate parameter values and expressions into each module’s settings dialogue boxes. The details of these subdomain and boundary settings will be discussed further in later sections of this chapter. The first and foremost question is which modules are required to accomplish the modeling task having the governing equations. The software covers a vast variety of modules as shown in Figure 3.1. Even if the physics/governing equations cannot be found in this list, it can be implemented based upon the Partial Differential Equation (PDE) module embedded in the Multiphysics core of the software, which possesses the general forms of PDEs and appropriate boundary conditions.

COMSOL Multiphysics®						
Electrical Modules	Mechanical Modules	Fluid Modules	Chemical Modules	Multipurpose	Interfacing Modules (LiveLink™)	
AC/DC	Heat Transfer	CFD	Chemical Reaction	Optimization	MATLAB	Excel®
RF	Structural Mechanics	Microfluidics	Batteries & Fuel Cells	Material Library	CAD Import	ECAD Import Module
MEMS	Nonlinear Structural Mechanics	Subsurface Flow	Electro-deposition	Particle Tracing Module	SolidWorks®	Space Claim®
Plasma	Geomechanics	Pipe Flow	Corrosion		Inventor®	AutoCAD®
	Fatigue		Chemical Transport		Creo®	Pro/ENGINEER®
	Acoustics				Solid Edge®	CATIA®VS

Figure 3.1: COMSOL framework with different modules and interfaces. These modules can be combined and cascaded to accomplish any complicated modeling task with different aspects [71]. The highlighted modules have been used in this thesis.

3.2.3 Boundary Conditions

Probably the trickiest part of setting a model is defining the correct boundary conditions. Each problem imposes its own specific boundary conditions and sometimes it is not provided in COMSOL by default. For these cases, usage of functions and codes written using MATLAB syntax is crucially useful (COMSOL and MATLAB share almost the same syntax). Apart from these cases, the software collects all the common equations and boundary conditions formulated by the physics interfaces into one large system of PDE boundary conditions, which can be easily set up.

3.2.4 Stabilization Techniques

Several techniques for handling numerical instabilities (usually raised by transport equations) without the need for mesh refinement are available in COMSOL Multiphysics. Commonly, different stabilization techniques add some terms into the transport equations. These terms introduce a numerical diffusion (also known as artificial diffusion, artificial viscosity or numerical viscosity, etc.) that stabilizes the solution. Such stabilizations are divided into two categories, inconsistent and consistent [71]. A consistent stabilization method adds numerical diffusion in such a way that solution of the problem with numerical diffusion is also an exact

solution of the original equation without the excessive terms. In other words, a consistent stabilization method gives less numerical diffusion the closer the numerical solution comes to the exact solution. An inconsistent stabilization method, on the other hand, adds numerical diffusion in such a way that an exact solution of the resulting equation is not necessarily a solution to the problem with numerical diffusion. In other words, an inconsistent method adds a certain amount of diffusion independently of how close the numerical approximate solution is to the exact solution.

Adding isotropic diffusion, as an example of inconsistent stabilization techniques, is equivalent to adding an extra term into the equation, which changes the essence of the problem [71]. Therefore, a solution obtained with isotropic diffusion might not be satisfactory in all cases. Nonetheless, the added diffusion definitely dampens the effects of numerical oscillations and impedes their propagation to the other parts of the finite element system. Isotropic diffusion has not been used in obtaining results reported in this thesis. However, it has been helpful in the preliminary stages of the modeling where no solution was yet available.

Streamline diffusion (SD) and Crosswind diffusion (CWD) are the most popular types of consistent stabilization techniques. Most application modes that support streamline diffusion support one or several of the following three types:

- Anisotropic diffusion (implemented only in COMSOL 3.5a)
- Streamline upwind Petrov-Galerkin (SUPG)
- Galerkin least-squares (GLS)

Anisotropic diffusion is a direct refinement of the isotropic diffusion method described above. In many cases, there is no need for any artificial diffusion in the direction orthogonal to the field direction. It is therefore possible to modify the system to a form that only adds artificial diffusion in the direction of the flow (the streamline direction). Analogous to the case of isotropic artificial diffusion, a problem stabilized with anisotropic diffusion is not identical to the original problem. In fact, the exact solution to the original equations does not solve the stabilized problem. However, the errors introduced by the anisotropic artificial diffusion are far less serious than the ones created by isotropic artificial diffusion.

The Streamline upwind Petrov-Galerkin method is a consistent method, which means that it does not perturb the original transport equation. A model that converges with this method can be considered to be a solution to the discrete counterpart of the original equation. It is closely related to upwinding schemes in finite difference and finite volume methods. SUPG can be shown to add a smaller amount of stability than anisotropic diffusion [71]. It can be shown that the accuracy of SUPG is better than anisotropic diffusion even at anisotropic diffusion's best performance.

Galerkin least-squares (GLS) is a more advanced version of SUPG, with which it shares many features. GLS, for example, is also a consistent method and has the same order of accuracy as SUPG. Compared to Galerkin least-squares (GLS), SUPG is, on the one hand, less sophisticated and thereby less stabilizing; on the other hand, SUPG involves fewer discrete terms and is therefore computationally less expensive [75].

All types of streamline diffusion introduce artificial diffusion in the streamline direction. This is often enough to obtain a smooth numerical solution provided that the exact solution of the original equation does not contain any discontinuities. At sharp gradients, however, undershoots and overshoots can occur in the numerical solutions. Crosswind diffusion addresses these spurious oscillations by adding diffusion orthogonal to the streamline direction, that is, in the crosswind direction [76].

Most crosswind diffusion methods are consistent; that is, they do not alter the equation. The most efficient methods are nonlinear [76,77]. This means that the discrete equation system becomes nonlinear even if the original equation is linear, which can increase the computational cost.

COMSOL recommends using crosswind diffusion if it is important to avoid undershoots or overshoots [71]. Typical examples are concentrations that must not become negative and mass fractions that must not be greater than one [78]. Codina [76] presents a comprehensive review of most of the existing crosswind diffusion methods.

Figure 3.2 displays and compares the effects of different types of stabilization techniques with the exact solution of a given transport equation (the generic scalar convection-diffusion transport equation):

$$\frac{\partial u}{\partial t} + \beta \cdot \nabla u = \nabla \cdot (c \nabla u) + F \quad (3.1)$$

The case, in which no artificial diffusion is applied, is also shown in Figure 3.2. The solution closely follows the reference solution away from the boundary layers, but at the boundary layers, oscillations occur. This is a typical behavior for streamline diffusion: the solution becomes smooth and exact in the regions away from the boundaries, but can contain oscillations at sharp gradients.

3.2.5 Meshing Policies and Mesh Element Definitions

The effective meshing of the simulation geometry is a crucial step in any simulation process. The simulation geometry must be meshed in a manner that minimizes the solution error and the simulation time at the same time, which in some cases turns out to be difficult. Many simulation geometries are such that an acceptable solution accuracy can be achieved from reasonably coarse meshes. Unfortunately, this is not always the case. Geometries with vastly differing feature sizes, such as the needle/sphere geometry that was used during the course of this thesis, often require fine meshes, particularly if significant dynamics are expected to exist in the regions surrounding the small features. Since significant dynamics do occur near the tip of the needle electrode during streamer simulations, the meshing of the needle/sphere simulation geometry proved to be challenging. Unstructured meshes were used for all the simulations being discussed in this thesis. The number of mesh elements in the unstructured mesh is determined from the shape of the simulation geometry and the settings in the mesh parameters.

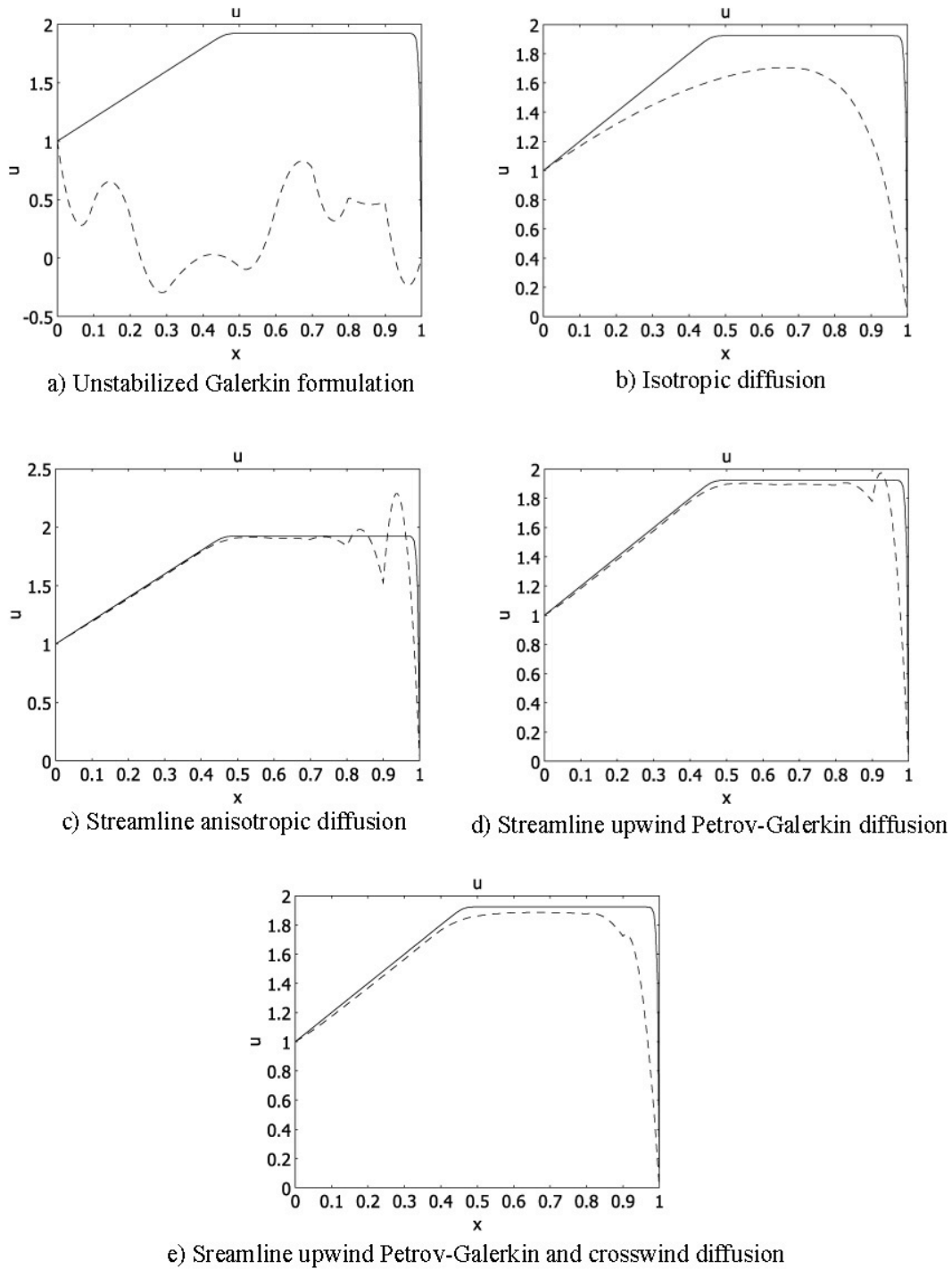


Figure 3.2: The plots compare the stabilized solution (dashed line) with the reference solution (solid line). a) unstabilized Galerkin formulation, b) stabilized formulation with isotropic diffusion, c) stabilized formulation with streamline anisotropic diffusion, d) stabilized formulation with SUPG diffusion, e) stabilized formulation with SUPG diffusion and crosswind diffusion [71].

The COMSOL meshing tool allows a range of settings to be varied, which can lead to the generation of a more suitable mesh than would be generated by the default meshing settings. Imposing such conditions on specific boundaries for example allows for the generation of meshes, which are dense in the regions where significant dynamics are expected, thus ensuring accuracy, while at the same time sparse in the other regions, thus reducing the computational load.

COMSOL has recently added a feature called physics-controlled mesh in the sequence type list in the setting window of a mesh node using which COMSOL Multiphysics creates a mesh that is adapted to the chosen physics settings in the model. In this type of meshing, COMSOL still lets the user to modify the overall element scheme and size of the physics-induced mesh such as selecting a different element size setting in the element size list. If one changes the physics settings in the model and rebuilds the meshing sequence, COMSOL Multiphysics creates a new mesh adapted to the new physics settings. We greatly benefited from this feature in this thesis [71].

Another interesting feature embedded in the COMSOL meshing environment is adaptive mesh refinement. In this feature, the user determines the maximum number of elements and maximum number of refinements. If the number of elements exceeds this number, the solver will stop even if it has not reached the number specified in the maximum number of refinements field [71].

The moving mesh feature is also provided by COMSOL Multiphysics. This attribute feature adds automatic remeshing whenever and wherever required [71]. Automatic remeshing can be added together with the Time-Dependent Solver operation feature. It can be used along with the Moving Mesh interface to assure a satisfactory mesh quality throughout the simulation. Detailed explanations about the mesh implementation in this thesis research are given in Appendix A2.

3.2.6 Numerical Solvers

Once the simulation geometry is imported, the equation settings are specified and the meshing is complete, all that remains to be done is to solve the model and examine the results. Solving a model with COMSOL involves selecting an appropriate solver for the set of partial differential equations, which make up the model. Streamers are dynamic structures; therefore a time-dependent solver is required to solve a streamer model. COMSOL provides many time-dependent solvers that can solve both linear and nonlinear PDE problems. COMSOL allows the selection of a number of linear system solvers. Some of these are direct solvers, while others are iterative solvers. All the solvers break down each problem into the solution of one or several linear systems of equations. Priority is usually with direct solvers, however, the decision to use a direct or iterative solver is ultimately driven by solution time and memory requirements as large numerical problems may easily make the computer out of memory, or cause very slow solution (long time to finish the simulation). The direct solvers solve a linear system by Gaussian elimination, which is a stable and reliable process well suited for ill-conditioned systems. This reduces the need for tuning the solver and as a result, direct solvers are more efficient for solving 1-D and 2-D problems. The use of direct solvers with 3-D problems often demands unreasonably

large memory resources and therefore the iterative solvers are generally preferred for 3-D problems. Six linear system solvers are available for solving the time-dependent problems.

Three direct and three iterative linear solver systems are implemented in COMSOL Multiphysics, each suitable for solving particular problems. It might be straight forward to recommend one of these solvers for a problem having one module; however, when the number of modules exceeds three, it becomes quite tricky to decide which direct solver is more effective before trying all of them. Before introducing the streamer/surface flashover model and their optimum solvers, a brief description of each COMSOL solver is given in this section.

There are three major direct linear solvers embedded in COMSOL Multiphysics:

1) Usually the default solver in most of the problems solved in COMSOL is a parallel sparse direct linear solver, MUMPS (MULTifrontal Massively Parallel sparse direct Solver) [79], which works on general systems of the form $Ax = b$. MUMPS uses several reordering algorithms to permute the columns and thereby to minimize the fill-ins. This solver is multithreaded on platforms that support multithreading and also supports solving on distributed memory architectures through the use of MPI [71,79]. This solver also includes out-of-core capabilities. The MUMPS out-of-core solver stores the LU factors on the hard drive. This minimizes the internal memory usage. The cost is longer solution times because it takes a longer time to read and write to the hard disk than using the internal memory. One can specify the temporary directory where MUMPS stores the LU factors using the *-tmpdir* switch [79]. The LU factors are stored as blocks on the hard drive. The MUMPS code was originally written in F90 [79].

2) The parallel sparse direct linear solver PARDISO also works on general systems of the form $Ax = b$. In order to improve the sequential and parallel sparse numerical factorization performance, the solver algorithms are based on a Level-3 BLAS update [71,80], and they exploit pipelining parallelism with a combination of left-looking and right-looking supernode techniques [71,80]. PARDISO is multithreaded on platforms that support multithreading. On distributed memory architectures, the solver settings are changed to corresponding MUMPS settings if needed. The code is written in C and Fortran. COMSOL Multiphysics uses the PARDISO version developed by Olaf Schenk and collaborators [80], which is included with Intel MKL (Intel Math Kernel Library). To avoid pivoting, PARDISO uses a pivot perturbation strategy that tests the magnitude of the potential pivot against a constant threshold. The perturbation strategy is not as robust as ordinary pivoting. In order to improve the solution time, PARDISO uses iterative refinements [71,80]. PARDISO also includes out-of-core capabilities. The PARDISO out-of-core solver stores the LU factors on the hard drive. This minimizes the internal memory usage. The price is longer solution times because it takes again a longer time to read and write to disk. One can specify the temporary directory where PARDISO stores the LU factors using the *-tmpdir* switch; see the COMSOL Multiphysics Installation and Operations Guide for further details. The LU factors are stored as blocks on the hard drive [71,80].

3) The SPOOLES (SParse Object Oriented Linear Equations Solver) also works on general systems of the form $Ax = b$ using the multifrontal method and direct LU factorization of the sparse matrix A [81]. When the matrix A is symmetric or Hermitian, the solver uses an LDLT

version of the algorithm, which saves half the memory [71]. SPOOLES uses several reordering algorithms to permute the columns and thereby minimize the fill-ins. This solver is multithreaded on platforms that support multithreading and also supports solving on distributed memory architectures through the use of MPI [81]. The code is written in C [81]. COMSOL Multiphysics uses SPOOLES version 2.2 developed by Cleve Ashcraft and collaborators [71,81].

All these three linear system solvers above work on general sparse linear systems of the form $Ax = b$ and use LU factorization on the matrix A to compute the solution x . In doing so, they use a reordering algorithm that permutes the columns of A to minimize the number of nonzeros in the L and U factors. Popular reordering algorithms include Minimum degree, Nested dissection, and Multisection. The solvers MUMPS and SPOOLES run distributed when running COMSOL in distributed mode (on clusters, for example). All linear system solvers benefit from shared memory parallelism (multicore processors, for example); however, MUMPS do so to a slightly lesser extent than PARDISO and SPOOLES [71,79-81].

Three major iterative direct solvers in COMSOL multiphysics are

1) The GMRES Iterative system solver uses the restarted Generalized Minimum RESidual method [71] is an iterative method for general linear systems of the form $Ax = b$. For fast convergence it is important to use an appropriate preconditioner. The value in the number of iterations before restart field in the general section of the settings window for the iterative node specifies the number of iterations the solver performs until it restarts (the default is 50). There is no guarantee that a restarted GMRES converges for a small restart value. A larger restart value increases the robustness of the interactive procedure, but it also increases the memory use and the computational time. For large problems, the computational cost is often very large to produce a preconditioner of such a high quality that the termination criteria are fulfilled for a small number of iterations and for a small restart value. For those problems, it is often advantageous to set up a preconditioner with a somewhat lower quality and instead increase the restart value or iterate more steps. Doing so typically increases the condition number for the preconditioned system, so an increase in the error-estimate factor might be needed as well. Two slightly different versions of GMRES are available in COMSOL Multiphysics. The difference between these two versions is whether left or right preconditioning is used [71]. The default choice is left preconditioning. Normally, the two versions of GMRES have similar convergence behavior [71,82]. However, if the preconditioner is ill-conditioned, there will be differences in the behavior.

2) The FGMRES Iterative Solver uses the restarted Flexible Generalized Minimum RESidual method [71]. The solver is a variant of the GMRES solver that can handle a wider class of preconditioners in a robust way [71]. One can, for example, use any iterative solver as a preconditioner for FGMRES. The downside with this method is that it uses twice as much memory as GMRES for the same value in the number of iterations before restart field. FGMRES uses right preconditioning and therefore has the same convergence criterion as right-preconditioned GMRES. If FGMRES is used together with a constant preconditioner such as the Incomplete LU preconditioner, then the FGMRES solver will be identical to the right preconditioned GMRES solver.

3) The Conjugate Gradients Iterative Solver uses the conjugate gradients iterative method [71]. It is an iterative method for linear systems of the form $Ax = b$ where the matrix A is positive definite and symmetric (Hermitian). Sometimes the solver also works when the matrix is not positive definite, especially if it is close to positive definite. This solver uses less memory and is often faster than the GMRES solver, but it applies to a restricted set of models. For fast convergence it is important to use an appropriate preconditioner, which should be positive definite and Hermitian/symmetric. Select the preconditioning type from the Preconditioning list. The default choice is left preconditioning. For the conjugate gradient method this choice only affects the convergence criterion and not the algorithm itself.

The iterative solver iterates until a relative tolerance is fulfilled. The user specifies this tolerance in the relative error field of the operation feature that this attribute belongs to. The solvers that require less memory and computational time per iteration typically are less robust and not applicable to all problem types. The tolerance settings can have an important impact on the accuracy of the solution. When the solution for the value of a particular variable is larger than the tolerance values, the error will be small; however, if the solution is less than the tolerance values, the error in the solution will be large. Therefore, when it comes to setting the tolerance values it is important to have a prior knowledge of the scale of the solution.

The physics interface selects a default linear system solver that usually is appropriate for the problem type, at least for single-physics models. If the default solver does not perform well, COMSOL recommends reviewing the following guidelines to choose the appropriate linear system solver [71]:

- 1 Try the PARDISO direct solver.
- 2 Try the MUMPS direct solver.
- 3 If the solver still runs out of memory or is too slow, use one of the iterative solvers GMRES, FGMRES, or BiCGStab. Select a preconditioner according to the guidelines in the section about the iterative solver.
- 4 If the system is positive definite and real symmetric or Hermitian, try the conjugate gradients iterative solver, which is more memory-efficient and sometimes faster than GMRES, FGMRES, and BiCGStab. Select a symmetric preconditioner. Try the SPOLES direct solver. It often uses less memory but is less numerically stable and is also slower.
- 5 The attribute feature handles settings for iterative linear system solvers. You can use the Iterative node together with operation features such as the Eigenvalue Solver, Stationary Solver, and Time-Dependent Solver.
- 6 An alternative to the iterative linear system solvers is given by direct linear system solvers, which are handled via the direct attribute feature. Although several attribute features for solving linear systems can be attached to an operation feature, only one can be active at a given time.

Implementation of all these solvers can be found in the COMSOL reference guide [71] under the topic of “solver algorithms.”

One-dimensional Analysis and Modeling of Unipolar Charge Transport in Liquid-Solid Composite Dielectric Systems

To gain confidence in the COMSOL streamer modeling, the unipolar charge carrier transport is analytically solved in different one-dimensional (1-D) Cartesian, cylindrical and spherical geometries and the solutions are compared with COMSOL modeling results of the same problem. Specifically, 1-D migration-Ohmic unipolar charge transport in series, two-region, oil-pressboard composite dielectric systems are analytically solved in planar, coaxial cylindrical and concentric spherical electrode geometries with a step current source. Space charge limited and linear injection conditions are applied as the boundary condition on the electrode surface in transformer oil. The method of characteristics is used to convert the governing partial differential equations into a set of ordinary differential equations that allows for expressing analytical solutions as functions of time and space for volume and interfacial surface charge densities, electric field and voltage drop in oil, and pressboard regions. Charge trajectories in the oil region are also obtained using the method of characteristics in different coordinates. Comparison of analytical solutions with COMSOL Multiphysics numerical modeling results confirms the correctness and high accuracy of our numerical solutions.

Apart from the verification of our modeling approach, results of this chapter are the base on which we build the ultimate 2-D asymmetric model of multipolar charge transport (streamer/surface flashover) in liquid/solid composite dielectric systems in Chapter 7. Power transformers, transmission cables, and other high voltage equipment often utilize liquid-solid composite dielectric systems such as transformer oil-pressboard. Such composite dielectric systems constitute the major insulation solutions used to improve the insulation and cooling capabilities of high voltage equipment [57]. Experimental evidence has shown that pre-breakdown phenomena in liquid-solid insulation systems often differ from liquid-only systems [1]. Therefore, the ability to model and understand charge injection, transport and interface charge accumulation is of great importance.

The governing partial differential equations in time and space for a step current source are converted into a set of ordinary differential equations in the moving charge's reference frame using the method of characteristics and solved for different boundary conditions. The space charge limited boundary condition is often used in semiconductor applications. In this thesis, we have applied this injection boundary condition along with linear charge injection to two-region series oil/pressboard planar, cylindrical and spherical geometries with a step current source. The liquid dielectric (oil) is assumed to have unipolar ion conduction described by a constant mobility μ , while the solid dielectric (pressboard) is modeled by an Ohmic conductivity σ , with zero volume charge density. The results give charge density and charge trajectories in the oil region,

and the electric field distribution as a function of time and space in both oil and pressboard regions. The terminal voltage and surface charge density at the oil/pressboard interface are calculated as a function of time. Most of the analysis yields closed-form expressions, which are in good agreement with numerical simulations. The general form of governing equations in oil and pressboard (pb) regions are listed Table 4.1.

Table 4.1: Governing equations of charge transport in liquid/solid insulation systems

	Liquid Region (Oil)	Solid Region (Pressboard)
Gauss' law	$\nabla \cdot (\epsilon_{oil} \vec{E}_{oil}) = \rho$	$\nabla \cdot (\epsilon_{pb} \vec{E}_{pb}) = 0$
Conservation of charge	$\nabla \cdot \vec{J}_{oil} + \frac{\partial \rho}{\partial t} = 0$	$\nabla \cdot \vec{J}_{pb} = 0$
Migration/Conduction Equations	$\vec{J}_{oil} = \rho \mu \vec{E}_{oil}$	$\vec{J}_{pb} = \sigma \vec{E}_{pb}$

4.1 Migration of Unipolar Charge Carrier between Cartesian, Cylindrical and Spherical Electrodes in Liquid-Only Systems

A one-dimensional transient analysis of unipolar charge injection and transport in a single dielectric region between two planar electrodes stressed by an applied step voltage was first presented in [7-9]. In these publications, exact solutions are obtained for the transient behavior of the bulk electric-field and space-charge density distributions and for the terminal current-voltage (I-V) time dependence. The analysis is generalized to handle any initial and boundary conditions for any terminal constraints or excitations. This chapter extends the closed-form single region results to two-region series planar, cylindrical, and spherical geometries that model a liquid/solid lossy dielectric system such as transformer oil/pressboard.

4.2 Migration-Ohmic Analysis of Charge Transport in a Series Liquid-Solid Dielectric System with Linear Charge Injection from a Planar Electrode

This section extends the closed-form solutions of [84,85] obtained for single region migration problem to a two-region series planar geometry that models a liquid/solid lossy dielectric system such as transformer oil/pressboard composite dielectric system used in power transformers.

The governing partial differential equations of Table 4.1 are converted into a set of ordinary differential equations in the moving charge’s reference frame using the method of characteristics and solved with the linear charge injection constitutive law where the injected positive charge density from the positive electrode at $x=0$ is proportional to electrode electric field. In the previous studies [23,25], the analysis was confined to space-charge-limited injection, whereby the electric field at the charge injecting electrode is zero while the charge density is infinite keeping the injection current finite. In this thesis, we have generalized this injection boundary condition to a linear injection law such that the electric field at the charge-injecting electrode can be non-zero.

The liquid dielectric is assumed to have unipolar ion conduction described by a constant mobility, while the solid dielectric is modeled by ohmic conduction. The results give charge density and charge trajectories in the liquid region, and the electric field distribution as a function of time and space in both regions. The terminal voltage and surface charge density at the liquid/solid interface are calculated as functions of time. Most of the analysis yields closed-form expressions, which are in excellent agreement with numerical simulations [72,73].

4.2.1 Governing Equations and Linear Charge Injection

A one-dimensional migration-Ohmic model, where all quantities only depend on coordinate x and time t , describes the charge transport phenomena in a planar series two-region liquid-solid geometry shown in Fig. 1. Region I represents a transformer oil region with positive charge mobility, μ , and dielectric permittivity, $\epsilon_I = \epsilon_{oil}$, while Region II represents a pressboard region with Ohmic conductivity, σ , and dielectric permittivity, $\epsilon_{II} = \epsilon_{pb}$. For the transient analysis, we excite the system with step terminal current $I(t) = J_0 S u(t)$ at $t=0$, where $I(t \leq 0) = 0$ and $I(t \geq 0) = J_0 S$ where J_0 is the terminal current per unit electrode area S . It is assumed that only the positive electrode at $x=0$ injects positive volume charge into the system. This charge travels from Region I into Region II passing through the interface at $x=a$, where surface charge can accumulate at the interface. In this model, we have selected representative numerical values in Table 4.2 for transformer oil and pressboard.

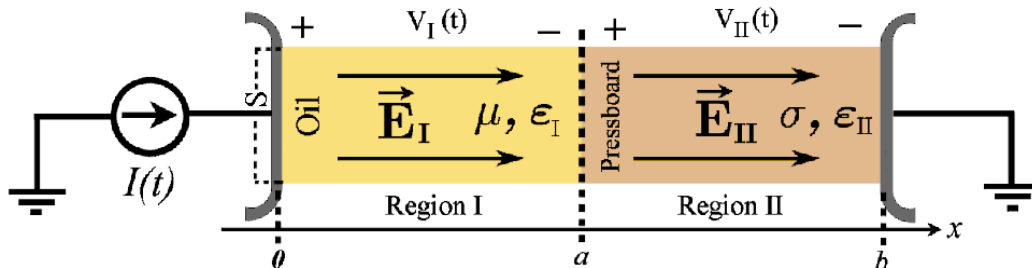


Figure 4.1: Two-region, series planar, liquid-solid dielectric model excited by a time-dependent current source, $I(t)$, with Region I obeying a mobility (μ) conduction law and Region II obeying Ohmic conduction.

Table 4.2: Parameters of dielectric analysis with linear charge injection condition in Cartesian geometry

<i>Parameter</i>	<i>Symbol</i>	<i>Value</i>
Permittivity of Region I (Oil)	$\epsilon_{oil} = \epsilon_I$	$2 \times 10^{-11} \text{ Fm}^{-1}$
Permittivity of Region II (Pressboard)	$\epsilon_{pb} = \epsilon_{II}$	$4 \times 10^{-11} \text{ Fm}^{-1}$
Positive Ion Mobility in Region I (Oil)	μ	$10^{-9} \text{ m}^2 \text{V}^{-1} \text{s}^{-1}$
Conductivity of Region II (Pressboard)	σ	$3 \times 10^{-12} \text{ } \Omega^{-1} \text{m}^{-1}$
Applied Current Density	$J_0 = I_0/S$	10^{-7} Am^{-2}
Region I Thickness	a	0.0125 m
Total Thickness (Region I and Region II)	b	0.025 m

In this one-dimensional geometry, the electric field and current density in both regions are only in the x direction. Gauss' law and conservation of charge can be written for the one-dimensional (x -direction) system in oil region as:

$$\epsilon_{oil} \frac{\partial E_{oil}(x,t)}{\partial x} = \rho(x,t), \quad (4.1)$$

$$\frac{\partial J_{oil}(x,t)}{\partial x} + \frac{\partial \rho(x,t)}{\partial t} = 0. \quad (4.2)$$

The boundary conditions for the electric field and current density at the interfacial surface $x=a$ are:

$$\epsilon_{pb} E_{pb}(x=a_+,t) - \epsilon_{oil} E_{oil}(x=a_-,t) = \sigma_s(t), \quad (4.3)$$

$$J_{pb}(x=a_+,t) - J_{oil}(x=a_-,t) + \frac{\partial \sigma_s(t)}{\partial t} = 0. \quad (4.4)$$

where $J_{oil}(x,t) = \rho(x,t)\mu E_{oil}(x,t)$ is the migration current density in Region I, $J_{pb}(t) = \sigma E_{pb}(t)$ is the ohmic current density in Region II and $\sigma_s(t)$ is the surface charge density at the interface ($x=a$). Since the electric field is conservative (i.e., $\nabla \times \vec{E} = 0$) in both regions, the voltage drop between the electrodes is:

$$V(t) = V_I(t) + V_{II}(t) = V_{oil}(t) + V_{pb}(t) = \int_0^a E_{oil}(x,t) dx + \int_a^b E_{pb}(x,t) dx. \quad (4.5)$$

At the positive electrode ($x=0$), the positive charge carriers are injected into oil (Region I) via the assumed linear injection law:

$$\rho(x=0,t) = \epsilon_{oil} \partial E_{oil}(x,t) / \partial x |_{x=0} = A E_{oil}(x=0,t), \quad (4.6)$$

where A is the charge injection coefficient. Using equations (4.1) and (4.2), the total migration and displacement current densities in Region I are:

$$J_0(t) = \mu\rho(x,t)E_{oil}(x,t) + \varepsilon_{oil} \frac{\partial E_{oil}(x,t)}{\partial t}. \quad (4.7)$$

where $J_0(t)=I_0(t)/S$ is the current source I_0 per unit electrode area S for $t \geq 0_+$. In Region II, the total Ohmic and displacement current density is only a function of time and not space:

$$J_0(t) = \sigma E_{pb}(t) + \varepsilon_{pb} \frac{\partial E_{pb}(t)}{\partial t}. \quad (4.8)$$

In the steady-state ($t \rightarrow \infty$), the total current densities, $J_{oil}(x,t)$ and $J_{pb}(x,t)$ are constant. Hence, from equations (4.7) and (4.8):

$$J_0 = \mu\varepsilon_{oil} E_{oil} \frac{dE_{oil}}{dx} = \sigma E_{pb} \Rightarrow J_0 = \frac{d}{dx} \left(\frac{1}{2} \varepsilon_{oil} \mu E_{oil}^2 \right) = \sigma E_{pb}. \quad (4.9)$$

Using equation (4.6), as a charge boundary condition at $x=0$, we obtain:

$$E_I = \sqrt{\frac{J_0}{\mu} \left(\frac{2x}{\varepsilon_{oil}} + \frac{1}{A} \right)}, \quad E_{pb} = J_0 / \sigma. \quad (4.10)$$

From equations (4.5) and (4.10), the terminal voltage is:

$$V = \frac{2}{3} \sqrt{\frac{2J_0}{\varepsilon_{oil}\mu}} \left[\left(a + \frac{\varepsilon_{oil}}{2A} \right)^{3/2} - \left(\frac{\varepsilon_{oil}}{2A} \right)^{3/2} \right] + \frac{J_0}{\sigma} (b-a) \quad (4.11)$$

Figure 4.2 plots the non-dimensional steady-state terminal voltage $\tilde{V} = V\varepsilon_{oil}\mu / (\sigma a^2)$ versus non-dimensional charge injection coefficient $\tilde{A} = Aa / \varepsilon_{oil}$ for different values of non-dimensional applied current density $\tilde{J}_0 = J_0\varepsilon_{oil}\mu / (a\sigma^2)$.

Equation (4.11) is rewritten to solve for the current density as a function of voltage in equation (4.12):

$$J_0 = \left[\frac{\sigma}{6(b-a)\sqrt{\varepsilon_{oil}\mu}} \left(\left(\frac{\varepsilon_{oil}}{A} \right)^{3/2} - \left(2a + \frac{\varepsilon_{oil}}{A} \right)^{3/2} + \left(\left(\frac{\varepsilon_{oil}}{A} \right)^{3/2} - \left(2a + \frac{\varepsilon_{oil}}{A} \right)^{3/2} \right)^2 + 36 \frac{\varepsilon_{oil}\mu}{\sigma} (b-a)V \right)^{1/2} \right]^2. \quad (4.12)$$

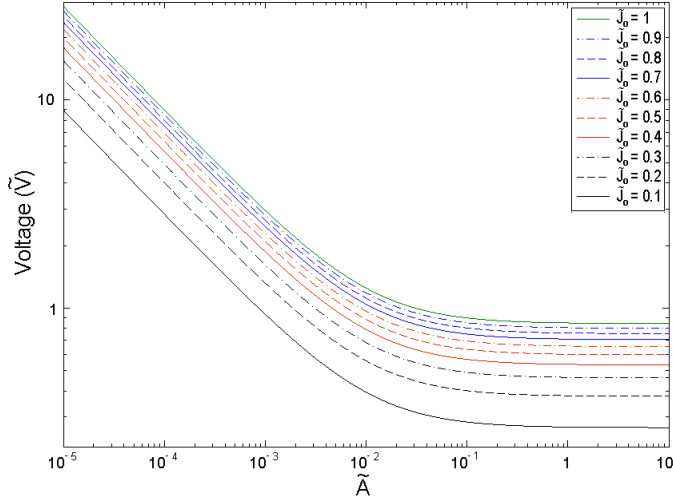


Figure 4.2: Nondimensionalized DC voltage $\tilde{V} = V\epsilon_{oil}\mu / (\sigma a^2)$ for various non-dimensional current densities $\tilde{J}_0 = J / J_0$ as a function of non-dimensionalized charge injection coefficient $\tilde{A} = Aa / \epsilon_{oil}$.

From equation (4.10), the steady-state charge density in the liquid region (Region I) is found using Gauss' law:

$$\rho(x) = \epsilon_{oil} \frac{dE_{oil}}{dx} = \sqrt{J_0 / \left(\mu \left(\frac{2x}{\epsilon_{oil}} + \frac{1}{A} \right) \right)}. \quad (4.13)$$

The surface charge density σ_s on the interfacial surface $x=a$ is found from equation (4.3):

$$\sigma_s = \epsilon_{pb} J_0 / \sigma - \sqrt{J_0 \epsilon_{oil} (2a + \epsilon_{oil} / A) / \mu}. \quad (4.14)$$

The special case of space charge limited injection, as presented in [2], occurs when A is assumed to be infinitely large, so that the electric field at $x=0$ goes to zero, i.e., $E(x=0) \rightarrow 0$. For this special case, the electric field, terminal voltage, current density, charge density and surface charge in equations (4.10-4.14), respectively, agree with the results of [25].

Due to the step current source in Fig. 4.1, the transient analysis results in both migration/ohmic conduction and displacement currents (equations (4.7) and (4.8)). We assume an initially unexcited system with a linear charge injection law, given by equation (4.6), at $x=0$. From equations (4.2), (4.6) and (4.8), the current densities in Regions I and II are equal to $J_0(t)$. Also, since E_{II} only depends on time and not position, the charge density in Region II is zero, i.e., $\rho_{pb} = \epsilon_{pb} \partial E_{pb} / \partial x = 0$.

The solution of electric field in Region I can be obtained from the total derivative of the electric field in the reference frame of the moving charge, which is:

$$\frac{dE_{oil}}{dt} = \frac{\partial E_{oil}}{\partial t} + \frac{dx}{dt} \cdot \frac{\partial E_{oil}}{\partial x} = \frac{J_0}{\epsilon_{oil}} \quad \text{on} \quad \frac{dx}{dt} = \mu E_{oil}. \quad (4.15)$$

Using the method of characteristics, a general solution method for hyperbolic partial differential equations, the electric field along a charge trajectory is obtained by integrating equation (4.15):

$$E_{oil}(x, t) = \frac{J_0}{\epsilon_{oil}}(t - t_0) + E_{oil}(x_0, t_0). \quad (4.16)$$

Since $dx/dt = \mu E_l$, the charge trajectory position x in Region I is obtained by integrating equation (4.16):

$$x(t) = \frac{J_0 \mu}{2\epsilon_{oil}}(t - t_0)^2 + \mu E_{oil}(x_0, t_0)(t - t_0) + x_0, \quad (4.17)$$

where x_0 is the starting position of a trajectory at time, $t=t_0$. Using the method of characteristics with equation (4.2), the differential equation which describes the charge density along the trajectories is:

$$\frac{\partial \rho}{\partial t} + \mu E_{oil} \frac{\partial \rho}{\partial x} + \frac{\mu}{\epsilon_{oil}} \rho^2 = \frac{d\rho}{dt} + \frac{\mu}{\epsilon_{oil}} \rho^2 = 0 \quad \text{on} \quad \frac{dx}{dt} = \mu E_{oil}. \quad (4.18)$$

By solving the ordinary differential equation in equation (4.18), the volume charge density in Region I is:

$$\rho(t) = \frac{\epsilon_{oil} \rho(x_0, t_0)}{\epsilon_{oil} + \mu \rho(x_0, t_0)(t - t_0)} \quad \text{on} \quad \frac{dx}{dt} = \mu E_{oil}, \quad (4.19)$$

where $\rho(x_0, t_0)$ is the charge density at the starting point of a trajectory at $x=x_0$, $t=t_0$. Figure 4.3 shows the results in the space-time domain for the charge transport transient model. Injected charge in Region I travels on specific trajectories (like the solid black curve shown in Fig. 4.3) until they reach the interfacial surface at $x=a$.

In Sub-region I_1 (the area which is labeled as “initial condition problem” in Figure 4.3), the charge density is zero, since it has been assumed that there is no initial volume charge at $t=0$. With zero initial charge density, $\rho(x_0, t_0=0)=0$, the charge density $\rho(t)$ given by equation (4.19) remains zero for its entire trajectory. As a result, the electric field, $E_{oil}(t)$, for Sub-region I_1 is merely a function of time and not position. Conversely, after positive charge is injected from the positive electrode for $t_0>0$, in Sub-region I_2 , the charge density, $\rho(x=0, t=t_0)$, is non-zero and the electric field and the charge density are functions of space and time.

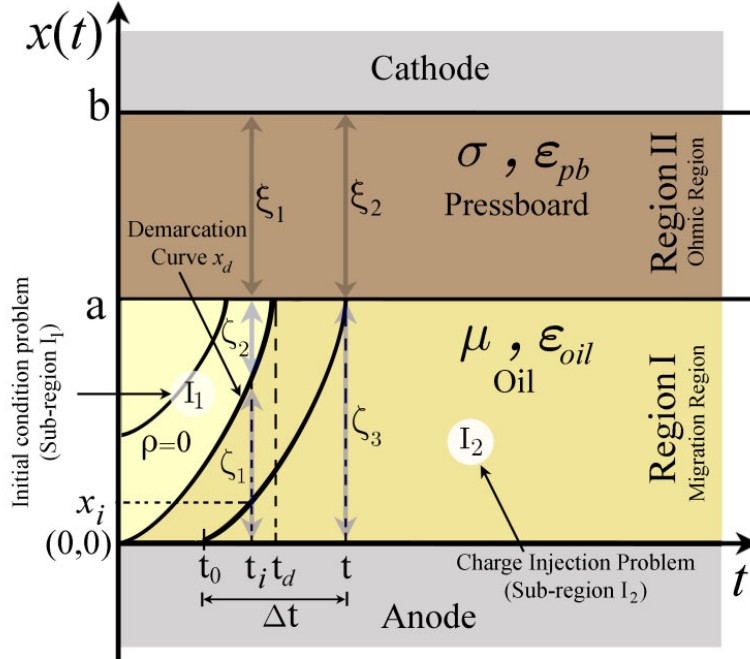


Figure 4.3: Space-time domain for the transient one-dimensional model of charge transport in the migration-Ohmic system for planar electrodes. In Region I, the demarcation curve, $x_d(t)$, separates the initial condition problem (Sub-region I₁) from the charge injection problem (Sub-region I₂). The integration paths ζ_1 and ζ_2 in Region I and ξ_1 in Region II, used to calculate terminal voltage are shown for times less than the charge time of flight (t_d) starting at $x=0, t=0$ and ending at $x=a, t=t_d$. Integration paths ζ_3 and ξ_2 in Region I/II are shown for times greater than t_d .

The demarcation curve, $x_d(t)$, in Figure 4.3, given by equation (4.17) with $x_0=0, t_0=0$, separates Sub-regions I₁ and I₂. Along this charge trajectory the electric field is given by equation (4.16) with $E_{oil}(x_0=0, t_0=0)=0$. To the right of the demarcation curve (Sub-region I₂) we have positive charge trajectories emanating from $(x_0=0, t_0>0)$. Thus, for the demarcation curve $x_d(t)$ and other charge trajectories in Sub-region I₁, the electric field is obtained from equation (4.16) with $E_{oil}(x_0, t_0=0)=0$. The electric field at $t=0$ is zero, since no charge is yet injected into Region I. The demarcation curve is characterized by equation (4.17) with $x_0=0, t_0=0$ and $E_t(x_0=0, t_0=0)=0$. The demarcation time, t_d , is the charge time of flight, where $x_d(t=t_d)=a$ with $t_0=0$:

$$t_d = \sqrt{\frac{2\epsilon_{oil}a}{\mu J_0}}. \quad (4.20)$$

To obtain the electric field in Sub-region I₂ at any arbitrary point in the space-time domain, such as (x_i, t_i) in Figure 4.3, we first need to determine $E_{oil}(x=0, t=t_0)$ to serve as an initial condition. The electric field at $x=0$ is the solution of equation (4.7):

$$\mu A E_{oil}^2(x=0, t) + \epsilon_{oil} \partial E_{oil}(x=0, t) / \partial t = J_0, \quad (4.21)$$

which has the solution:

$$E_I(x=0,t) = \sqrt{\frac{J_0}{\mu A}} \tanh\left(\sqrt{\mu A J_0} \frac{t}{\epsilon_{oil}}\right). \quad (4.22)$$

As a check, for the space charge limited case ($A \rightarrow \infty$), the electric field at $x=0$ must be zero to keep the current density J_0 finite [84,85], which is satisfied by equation (4.22). Having determined the electric field at the positive charge injecting electrode at $x=0$, for all values of starting time t_0 in equation (4.22), the electric field for any point in Region I in space and time is derived from equation (4.16). Also, we can obtain the trajectory characteristics for unipolar charge emanating from the charge injecting electrode ($x_0=0$) at $t=t_0$ via equations (4.17) and (4.22). However, the equations for electric field and charge trajectories are not complete since t_0 , or equivalently $\Delta t = t - t_0$, is not known for arbitrary values of x and t in Region I. Fortunately, by solving the quadratic equation of equation (4.17) for Δt when $x=a$, two possible solutions exist. Taking into consideration that Δt must always be positive, the correct solution is:

$$\Delta t = t - t_0 = \frac{\epsilon_{oil}}{J_0} \left[\sqrt{E_{oil}^2(x=0,t_0) + \frac{2J_0}{\mu\epsilon_{oil}}a} - E_{oil}(x=0,t_0) \right]. \quad (4.23)$$

To determine the voltage across the two regions we need to integrate the electric field over $0 < x < b$, as shown by equation (4.5). However, we must first obtain the electric field at any arbitrary point, (x_i, t_i) in Sub-region I₂, which requires $E_{oil}(x=0,t_0)$ from equation (4.22). To obtain $E_{oil}(x=0,t_0)$, the initial time, t_0 , needs to be determined for any x_i and t_i from equation (4.23), which is a non-linear equation. Since, no algebraic solution is available for t_0 and $\Delta t = t - t_0$ (Fig 4.3) in terms of any arbitrary point x_i and t_i , it is not possible to determine E_{oil} at any point in the space-time domain. Nonetheless, using equation (4.7), which is rewritten here as:

$$\epsilon_{oil} \frac{\partial E_{oil}}{\partial t} + \mu \rho E_{oil} = \epsilon_{oil} \frac{\partial E_{oil}}{\partial t} + \frac{\partial}{\partial x} \left(\frac{1}{2} \mu \epsilon_{oil} E_{oil}^2 \right) = J_0 \quad (4.24)$$

and by deriving the electric field at $x=a$ and $x=0$ we are still able to find the voltage across the Region I. By integrating x from x_1 to x_2 at a fixed time in equation (4.24) we obtain:

$$\frac{dV_{oil}}{dt} + \frac{1}{2} \mu \left(E_{oil}^2(x=a,t) - E_{oil}^2(x=0,t) \right) = \frac{J_0 a}{\epsilon_{oil}}. \quad (4.25)$$

For $t < t_d$, integration path of electric field should include ζ_1 and ζ_2 in respective Sub-regions I₂ and I₁ (Fig. 3) which can be also obtained from equation (4.16) and (4.25).

For $t > t_d$, the integration path ζ_3 is entirely in Sub-region I₂ (Fig. 3). Thus, the voltage drop across Region I for $t > t_d$ can be found using equations (4.22) and (4.25).

Now that the electric field is known in Sub-region I₁, we merely need the electric field at $x=a$ and $x=0$ for any time to find $V_{oil}(t)$. In other words, we need t_0 or equivalently Δt to find the voltage drop across Region I. To solve the nonlinear equation in equation (4.23) for Δt , we have applied both the Gauss-Newton and Levenberg-Marquardt algorithms, which give nearly identical results.

Solving for the electric field in Region II is more straightforward. From equation (4.8) with $J_{pb}(t)=\sigma E_{pb}(t)$ the electric field is:

$$E_{pb} = \frac{J_0}{\sigma}(1 - e^{-t/\tau}), \quad \tau = \frac{\epsilon_{pb}}{\sigma}. \quad (4.26)$$

By integrating $V_I(t)$ in equation (4.25) along ζ_1 and ζ_2 for $t < t_d$ and along ζ_3 for $t > t_d$, we have the voltage drop across Region I for any time. Also from equation (4.26), $V_{pb}(t)$ is found by integrating the electric field over space in Region II from $x=a$ to $x=b$. Adding $V_{oil}(t)$ and $V_{pb}(t)$ gives the total voltage drop versus time, which is given by equation (4.27). As a check, for the space-charge limited injection case when $A \rightarrow \infty$, equation (4.27) agrees with the results of [2] since according to equations (4.20) and (4.23), $A \rightarrow \infty$ results in $\Delta t \rightarrow t_d$. Figure 4.4 shows the voltage dynamics across both regions for different values of linear injection coefficient A . As can be seen in this figure, for $\tilde{A} = Aa / \epsilon_{oil}$ greater than 1, the voltage of the system is essentially equal to the space-charge limited injection solution ($\tilde{A} \rightarrow \infty$).

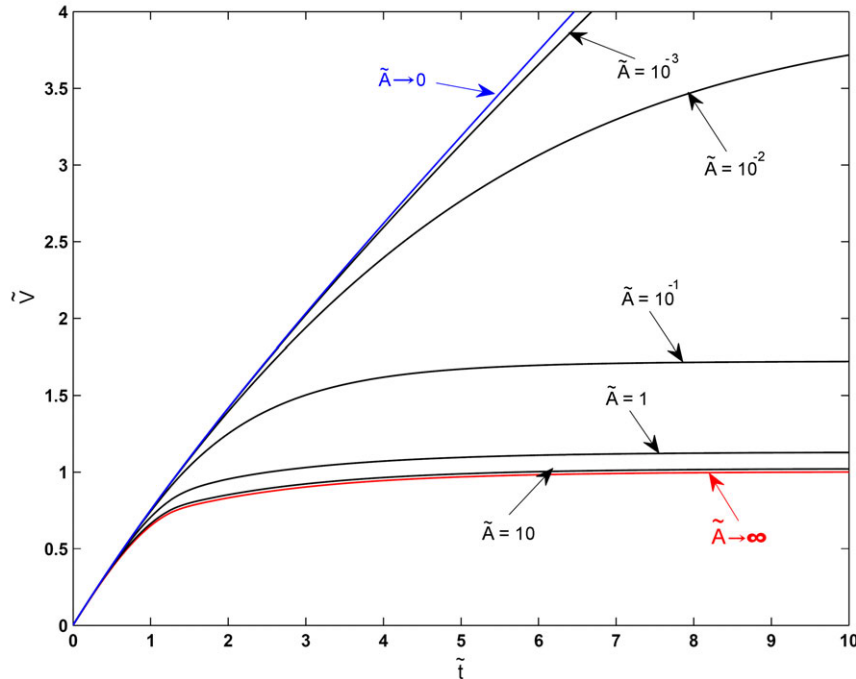


Figure 4.4: Nondimensionalized voltage $\tilde{V} = V\epsilon_{oil}\mu / (\sigma a^2)$ between electrodes for various values of nondimensionalized linear injection coefficient $\tilde{A} = Aa / \epsilon_{oil}$ as a function of nondimensionalized time $\tilde{t} = t\sqrt{\mu J_0 / (a\epsilon_{oil})}$.

$$V(t) = \begin{cases} \frac{J_0 a}{\epsilon_{oil}} t - \frac{\mu J_0^2}{6\epsilon_{oil}^2} t^3 + \frac{J_0}{2A} t - \frac{\epsilon_{oil}}{2A} \sqrt{\frac{J_0}{\mu A}} \tanh\left(\sqrt{\mu A J_0} \frac{t}{\epsilon_{oil}}\right) + \frac{J_0(b-a)}{\sigma} (1 - e^{-t/\tau}) & 0 \leq t \leq t_d \\ J_0(t-t_0) \left[\frac{a}{\epsilon_{oil}} - \frac{1}{2A} \tanh^2\left(\sqrt{\mu A J_0} \frac{t_0}{\epsilon_{oil}}\right) \right] - \frac{\mu J_0^2}{6\epsilon_{oil}^2} (t-t_0)^3 - \frac{J_0}{\epsilon_{oil}} \sqrt{\frac{\mu J_0}{A}} \tanh\left(\sqrt{\mu A J_0} \frac{t_0}{\epsilon_{oil}}\right) \frac{(t-t_0)^2}{2} & t \geq t_d \\ + \frac{J_0}{2A} (t-t_0) - \frac{\epsilon_{oil}}{2A} \sqrt{\frac{J_0}{\mu A}} \left(\tanh\left(\sqrt{\mu A J_0} \frac{t}{\epsilon_{oil}}\right) - \tanh\left(\sqrt{\mu A J_0} \frac{t_0}{\epsilon_{oil}}\right) \right) + \frac{J_0(b-a)}{\sigma} (1 - e^{-t/\tau}) & \end{cases} \quad (4.27)$$

4.3 Migration-Ohmic Analysis of Space Charge Limited Injection and Transport in a Series Liquid-Solid Dielectric System

Space charge limited injection is a boundary condition on the charge-emitting electrode placed inside the liquid dielectric (oil). According to this condition, the injected charge density from the electrode is infinite so that the electric field at the charge-injecting electrode is zero keeping the injection current finite. In this section, the two-region liquid/solid charge transport problem is solved for Cartesian, cylindrical and spherical coordinates. These three different coordinates cover many practical geometries in insulation industry, therefore the solutions of this section can be useful in practice as well.

4.3.1 Cartesian Electrode Geometry

Similarly the one-dimensional migration-Ohmic equation set can be applied for space charge limited injection in the series two-region oil liquid-pressboard solid planar geometry shown in Figure 4.1. The only difference is the boundary condition on the positive electrode. At the positive electrode ($x=0$), the positive charge carriers are injected into Region I via the assumed space charge limited condition where $\rho(x=0,t)=\infty$ requires that $E_{oil}(x=0,t)=0$ so that J_{oil} remains finite:

$$\rho(x=0,t) = J_{oil} / [\mu E_{oil}(x=0,t)] = \infty \rightarrow E_{oil}(x=0,t) = 0 \quad (4.28)$$

The total migration and displacement current densities in Region I are:

$$J_{oil}(t) = \mu \rho(x,t) E_{oil}(x,t) + \epsilon_{oil} \frac{\partial E_{oil}(x,t)}{\partial t} = J_s(t) = \frac{I_s(t)}{A} \quad (4.29)$$

where $J_s(t)=I_s(t)/A$ is the current source I_s per unit electrode area A for $t \geq 0_+$. In Region II, the total Ohmic and displacement current density in the pressboard is only a function of time and not position:

$$J_{pb}(t) = \sigma E_{pb}(t) + \epsilon_{pb} \frac{\partial E_{pb}(t)}{\partial t} = J_s(t) \quad (4.30)$$

In the steady-state ($t \rightarrow \infty$), $J_{oil}(x)=J_{pb}(x)=I_s/S$. Hence, from equations (4.29) and (4.30):

$$J_{oil} = J_{pb} = \mu \epsilon_{oil} E_{oil}(x) \frac{dE_{oil}(x)}{dx} = \frac{d}{dx} \left(\frac{1}{2} \epsilon_{oil} \mu E_{oil}^2(x) \right) = \sigma E_{pb} = J_s = I_s / A \quad (4.31)$$

Using equation (4.15), $E_{oil}(x=0,t)=0$ as a boundary condition at $x=0$, we obtain from equation (4.31):

$$E_{oil}(x) = \sqrt{\frac{2xJ_s}{\mu \epsilon_{oil}}}, \quad E_{pb} = \frac{J_s}{\sigma} \quad (4.32)$$

The steady state terminal voltage is:

$$V = \frac{2}{3} \sqrt{\frac{2J_s}{\epsilon_{oil} \mu}} a^{3/2} + \frac{J_s}{\sigma} (b-a) \quad (4.33)$$

Equation (4.33) is rewritten to solve for the current density as a function of voltage:

$$J_s = \left[\frac{\sqrt{8\sigma^2 a^3 + 36\epsilon_{oil} \mu (b-a)V} - \sqrt{8\sigma^2 a^3}}{6(b-a)\sqrt{\epsilon_{oil} \mu}} \right]^2 \quad (4.34)$$

From equation (4.32), the steady-state charge density in the oil region (Region I) is found using Gauss' law:

$$\rho(x) = \epsilon_{oil} \frac{dE_{oil}(x)}{dx} = \sqrt{\frac{\epsilon_{oil} J_s}{2\mu x}} \quad (4.35)$$

The surface charge density σ_s on the interfacial surface $x=a$ is

$$\sigma_s = \epsilon_{pb} J_s / \sigma - \sqrt{2J_s \epsilon_{oil} a / \mu}. \quad (4.36)$$

For space charge limited injection, the electric field, terminal voltage, current density, charge density and surface charge in equations (4.32-4.36), respectively are plotted in section 4.4.

Due to the step current source in Figure 4.1, the transient analysis results in both migration/ohmic conduction and displacement currents (equations (4.29) and (4.30)). We assume an initially unexcited system with space charge limited injection, given by Eq. (15), at $x=0$. From equations (4.29) and (4.30), the total current densities in Regions I and II are equal to $J_s(t)$. Also, since $E_{pb}(t)$ only depends on time and not position, the charge density in Region II is zero, i.e., $\rho_{pb} = \varepsilon_{pb} \partial E_{pb} / \partial x = 0$.

The solution for the electric field in Region I is obtained from the total derivative of the electric field in the reference frame of the moving charge:

$$\frac{dE_{oil}(x,t)}{dt} = \frac{\partial E_{oil}(x,t)}{\partial t} + \frac{dx}{dt} \frac{\partial E_{oil}(x,t)}{\partial x} = \frac{J_s}{\varepsilon_I} \quad \text{on} \quad \frac{dx}{dt} = \mu E_{oil}(x,t) \quad (4.37)$$

Using the method of characteristics [7-9], a general solution method for hyperbolic partial differential equations, the electric field along a charge trajectory is obtained by integrating equation (4.37):

$$E_{oil}(x,t) = \frac{J_s}{\varepsilon_{oil}}(t-t_0) + \underbrace{E_{oil}(x_0,t_0)}_0 = \frac{J_s}{\varepsilon_{oil}}(t-t_0) \quad \text{on} \quad \frac{dx}{dt} = \mu E_{oil}(x,t) \quad (4.38)$$

where J_s is constant for $t > 0$ and $E_{oil}(x=0,t) = E_{oil}(x,t=0) = 0$. Since $dx/dt = \mu E_{oil}(x,t)$, the charge trajectory position x in Region I is obtained by integrating equation (4.38):

$$x(t) = \frac{J_s \mu}{2 \varepsilon_{oil}} (t-t_0)^2 + x_0 \quad (4.39)$$

where $0 \leq x_0 \leq a$ is the starting position of a trajectory at $t_0 = 0$, and $x_0 = 0$ for $t = t_0 \geq 0$. The differential equation which describes the charge density along the trajectories is:

$$\frac{\partial \rho(x,t)}{\partial t} + \mu E_{oil}(x,t) \frac{\partial \rho(x,t)}{\partial x} + \frac{\mu}{\varepsilon_{oil}} \rho(x,t)^2 = 0 \quad (4.40)$$

Using the method of characteristics, equation (4.40) is rewritten as:

$$\frac{d\rho(x,t)}{dt} = \frac{\partial \rho(x,t)}{\partial t} + \frac{dx}{dt} \frac{\partial \rho(x,t)}{\partial x} = -\frac{\mu}{\varepsilon_{oil}} \rho(x,t)^2 \quad \text{on} \quad \frac{dx}{dt} = \mu E_{oil}(x,t) \quad (4.41)$$

The general solution of the ordinary differential equation in equation (4.41), for the volume charge density in Region I is:

$$\rho(t) = \frac{\rho(x_0, t_0)}{1 + \frac{\mu\rho(x_0, t_0)(t - t_0)}{\epsilon_{oil}}} \quad \text{on } \frac{dx}{dt} = \mu E_{oil}(x, t) \quad (4.42)$$

where $\rho(x_0, t_0)$ is the charge density at the starting point of a trajectory at $x=x_0$, $t=t_0$. For the initial condition in sub-region I₁ of Figure 4.3, $\rho(x_0, t_0=0)=0$. Thus in Sub-region I₁ (the area which is labeled as “initial condition problem” in Figure 4.3), the charge density is zero, $\rho(x, t=0)=0$, since it has been assumed that there is no initial volume charge at $t=0$. With zero initial charge density, $\rho(x_0, t_0=0)=0$, the charge density $\rho(t)$ given by equation (4.42) remains zero for its entire trajectory. As a result of equation (4.10), with $\rho(x, t)=0$, the electric field, $E_{oil}(t)$, for Sub-region I₁ is merely a function of time and not position.

Conversely, after positive charge is injected from the $x=0$ positive electrode at $x=0$ for $t_0>0$, in Sub-region I₂, the charge density, $\rho(x=0, t=t_0) = \infty$ for space charge limited injection and the injected charge density is a function of space and time:

$$\rho(t) = \frac{\epsilon_{oil}}{\mu(t - t_0)} \quad \text{on } \frac{dx}{dt} = \mu E_{oil}, \quad (4.43)$$

Figure 4.3 shows the result (demarcation curve) in the space-time domain for the charge transport transient model. Injected charge in sub-Region I₂ travels on specific trajectories (like solid black curve at $t=t_0$ in that figure) until they reach the interfacial surface at $x=a$.

The demarcation curve, $x_d(t)$ in Figure 4.3, given by equation (4.39) with $x_0=0$, $t_0=0$, separates Sub-regions I₁ and I₂. Along this charge trajectory the electric field is given by equation (4.38) with $t_0=0$, $E_{oil}=J_s t/\epsilon_{oil}$. To the right of the demarcation curve (Sub-region I₂) we have positive charge trajectories emanating from $(x_0=0, t_0>0)$. Thus, for the demarcation curve $x_d(t)$ and other charge trajectories in Sub-region I₁, the electric field is obtained from equation (4.38) with $t_0=0$. The electric field at $t=0$ is zero, since no charge is yet injected into Region I. The demarcation curve is characterized by equation (4.39) with $x_0=0$, $t_0=0$ and $E_{oil}(x_0=0, t_0=0)=0$. The demarcation time, t_d , is the charge time of flight, where $x_d(t=t_d)=a$ with $t_0=0$:

$$x_d(t) = \frac{\mu J_s}{2\epsilon_{oil}} t^2, \quad t_d = \sqrt{\frac{2\epsilon_{oil} a}{\mu J_s}} \quad (4.44)$$

To obtain the electric field in Sub-region I₂ at any arbitrary point in the space-time domain, such as (x_i, t_i) in Fig. 4.3, the space charge limited condition, $E_{oil}(x=0, t=t_0) = 0$, serves as an initial condition.

For $t < t_d$, the integration path of electric field for calculation of the voltage drop across Region I should include ζ_1 and ζ_2 in Sub-regions I₂ and I₁ (Figure 4.3). For $t > t_d$, the integration path ζ_3 is entirely in Sub-region I₂. Thus, the voltage drop across Regions I and II for $t < t_d$ can be found by

integration paths ζ_1 and ζ_2 in Region I and ξ_1 in Region II; and for $t > t_d$ the integration paths are ζ_3 in Region I and ξ_2 in Region II (Figure 4.3).

Solving for the electric field in Region II is more straightforward. From equation (4.30) the electric field in the pressboard region is:

$$E_{pb}(t) = \frac{J_s}{\sigma}(1 - e^{-t/\tau}), \quad \tau = \frac{\epsilon_{pb}}{\sigma}. \quad (4.45)$$

where we used the initial condition, $E_{pb}(t=0)=0$. Therefore, the interfacial surface charge density is:

$$\sigma_s = \begin{cases} J_s [\tau(1 - e^{-t/\tau}) - t] & 0 \leq t \leq t_d \\ J_s [\tau(1 - e^{-t/\tau}) - t_d] & t \geq t_d \end{cases} \quad (4.46)$$

By integrating $E_{oil}(t)$ in equation (4.38) along ζ_1 and ζ_2 (Fig. 4.3) for $t < t_d$ and along ζ_3 for $t > t_d$, we have the voltage drop $V_{oil}(t)$ across Region I for any time. Also from equation (4.45), $V_{pb}(t)$ is found by integrating the electric field $E_{pb}(t)$ over space in Region II from $x=a$ to $x=b$. Adding $V_{oil}(t)$ and $V_{pb}(t)$ from equations (4.32) and (4.45) gives the total voltage drop versus time, which is given by equation (4.47):

$$V(t) = \begin{cases} \frac{J_s a}{\epsilon_{oil}} t - \frac{\mu J_s^2}{6 \epsilon_{oil}^2} t^3 + \frac{J_s (b-a)}{\sigma} (1 - e^{-t/\tau}) & 0 \leq t < t_d \\ \frac{2}{3} \sqrt{\frac{2 J_s a^3}{\epsilon_{oil} \mu}} + \frac{J_s (b-a)}{\sigma} (1 - e^{-t/\tau}) & t \geq t_d \end{cases} \quad (4.47)$$

4.3.2 Coaxial Cylindrical Electrode Geometry

We consider the cylindrical coaxial geometry in Figure 4.5, where the inner electrode at $r=r_i$ is a source of ions with mobility μ in the oil region ($r_i < r < r_m$) and the electric field is purely radial. We assume all physical parameters to be constant and consider only one-dimensional variations with the radial coordinate r , so that the current and electric field are only in the radial direction. The general governing equations in oil and pressboard regions are the same as equations (4.1-4.3) in cylindrical geometry.

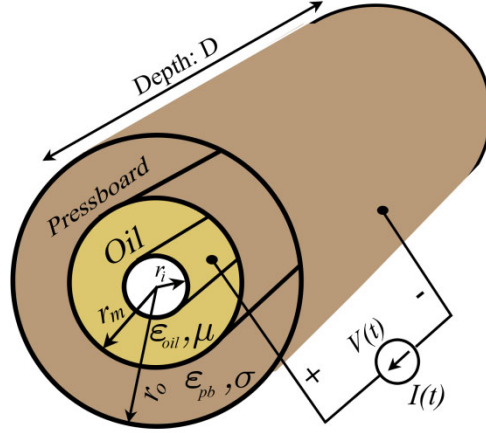


Figure 4.5: Two-region, series, oil-pressboard dielectric model for cylindrical electrodes excited by a step current source with Region I (Oil) for $r_i < r < r_m$ obeying a mobility (μ) conduction law and Region II (Pressboard) for $r_m < r < r_o$ obeying Ohmic conduction.

Again, an infinite amount of charge is available at the charge emitting ($r=r_i$) electrode for space charge limited injection, so the emitter electric field at $r=r_i$ must be zero to keep the current finite.

For steady-state ($t \rightarrow \infty$), the total current $I(t) = 2\pi r D J_r(r)$ is constant. From equations (4.1-4.3) in cylindrical coordinates, the charge density is

$$\rho(r) = \epsilon_{oil} \frac{1}{r} \frac{\partial(rE_{oil}(r))}{\partial r} \quad (4.48)$$

Using equations (4.2), (4.3) and (4.48):

$$J_s(r) = \frac{\epsilon_{oil}\mu}{r} E_{oil}(r) \frac{\partial(rE_{oil}(r))}{\partial r} = \frac{\epsilon_{oil}\mu}{2r^2} \frac{d(rE_{oil}(r))^2}{dr} = \frac{I_s}{2\pi D r} \quad (4.49)$$

By solving equation (4.49), with space charge limited injection, $E_{oil}(r_i) = 0$, the electric field in the liquid region is:

$$E_{oil}(r) = \sqrt{\frac{I_s}{2\pi\epsilon_{oil}\mu D} \left(1 - \frac{r_i^2}{r^2}\right)} \quad (4.50)$$

Hence, using equation (4.48), the total steady-state charge density is then:

$$\rho(r) = \sqrt{\frac{\epsilon_{oil} I_s}{2\pi\mu D (r^2 - r_i^2)}} \quad (4.51)$$

The electric field in the pressboard (Region II) is:

$$J_s(r) = \sigma E_{pb}(r) = \frac{I_s}{2\pi D r} \Rightarrow E_{pb}(r) = \frac{I_s}{2\pi\sigma D r} \quad (4.52)$$

Integrating the electric-field distribution over r in both regions using the integral solution in Region I, $r_i < r < r_m$:

$$\int_r^1 \frac{1}{r} \sqrt{r^2 - r_i^2} dr = \left[\sqrt{r^2 - r_i^2} - r_i \cos^{-1}\left(\frac{r_i}{r}\right) \right] \quad (4.53)$$

yields the steady-state voltage across both regions as:

$$V = \sqrt{\frac{I_s}{2\pi\epsilon_{oil}\mu D}} \left[\sqrt{r_m^2 - r_i^2} - r_i \cos^{-1}\left(\frac{r_i}{r_m}\right) \right] + \frac{I_s \ln(r_o / r_m)}{2\pi\sigma D} \quad (4.54)$$

Due to the step current source in Figure 4.5, the transient analysis results in both migration/Ohmic conduction and displacement currents.

We again assume an initially unexcited system with space charge limited conditions at $r=r_i$. Hence, the radial current densities in Regions I and II are equal to $J_s(t)$. Also, since the charge density in the pressboard region is zero, the electric field in the pressboard region, $E_{pb}(t)$, depends on time and position as $1/r$:

$$J_s(r,t) = \frac{\mu\epsilon_{oil}}{r} E_{oil}(r,t) \frac{\partial(rE_{oil}(r,t))}{\partial r} + \epsilon_{oil} \frac{\partial E_{oil}(r,t)}{\partial t} = \sigma E_{pb}(t) + \epsilon_{pb} \frac{\partial E_{pb}(t)}{\partial t} = \frac{I_s}{2\pi D r} \quad t > 0 \quad (4.55)$$

To solve for the time dependent charge density in the oil region, based on equations (4.1-4.3), we have:

$$\frac{1}{r} \left[\rho(r,t) \frac{\partial}{\partial r} (r\mu E_{oil}(r,t)) + r\mu E_{oil}(r,t) \frac{\partial \rho(r,t)}{\partial r} \right] + \frac{\partial \rho(r,t)}{\partial t} = 0 \quad (4.56)$$

which can be reduced to:

$$\frac{\mu\rho(r,t)^2}{\epsilon_{oil}} + \mu E_{oil}(r,t) \frac{\partial \rho(r,t)}{\partial r} + \frac{\partial \rho(r,t)}{\partial t} = 0 \quad (4.57)$$

According to the method of characteristics, equation (4.57) can be rewritten as a pair of ordinary differential equations:

$$\frac{d\rho(r,t)}{dt} = \frac{\partial\rho(r,t)}{\partial t} + \frac{dr}{dt} \frac{\partial\rho(r,t)}{\partial r} = -\frac{\mu\rho(r,t)^2}{\epsilon_{oil}} \quad \text{on } \frac{dr}{dt} = \mu E_{oil}(r,t) \quad (4.58)$$

The cylindrical differential equation for charge density is identical to the analogous planar geometry equation in equation (4.40) and so has solutions from equations (4.41) and (4.42) and Figure 4.6:

$$\rho(t) = \begin{cases} 0 & \text{Sub-region I}_1 \\ \frac{\epsilon_{oil}}{\mu(t-t_0)} & \text{Sub-region I}_2 \end{cases} \quad \text{on } \frac{dr}{dt} = \mu E_{oil}(r,t) \quad (4.59)$$

Again, from equations (4.2), (4.48) and (4.55), we have an ordinary differential equation for electric field in the oil regions I₁ and I₂ for which using the method of characteristics gives:

$$\frac{d(rE_{oil}(r,t))}{dt} = \frac{I_s}{2\pi\epsilon_{oil}D} \quad \text{on } \frac{dr}{dt} = \mu E_{oil}(r,t) \quad (4.60)$$

with charge trajectories:

$$r(t)^2 = \begin{cases} \frac{\mu I_s}{2\pi\epsilon_{oil}D} t^2 + r_s^2, 0 \leq t \leq t_d, r_d(t) \leq r \leq r_m & \text{(Sub-region I}_1\text{)} \\ \frac{\mu I_s}{2\pi\epsilon_{oil}D} (t-t_0)^2 + r_i^2, t \geq t_0, r_i \leq r \leq r_m & \text{(Sub-region I}_2\text{)} \end{cases} \quad (4.61)$$

Note again that the demarcation curve, $r_d(t)$ is the charge trajectory that separates the initial condition problem from the charge injection problem which starts from $r=r_i$ at $t_0=0$ in equation (4.61). By solving equation (4.61) we obtain similar regions and sub-regions as the planar geometry in Fig. 4, but now for cylindrical geometry as shown in Figure 4.6. The demarcation curve $r_d(t)$ and time of flight t_d for cylindrical electrodes shown in Figure 4.6 is:

$$r_d(t) = \sqrt{\frac{\mu I_s}{2\pi\epsilon_{oil}D} t^2 + r_i^2}, \quad t_d = \sqrt{\frac{2\pi\epsilon_{oil}D}{\mu I_s} (r_m^2 - r_i^2)} \quad (4.62)$$

The electric field in sub-region I₁ above the demarcation curve, where $\rho=0$ is:

$$E_{oil}(r,t) = \frac{I_s t}{2\pi\epsilon_{oil}D r} \quad \text{on } r(t)^2 = \frac{\mu I_s}{2\pi\epsilon_{oil}D} t^2 + r_s^2, r_i < r_s < r_m \quad (4.63)$$

where r_s is the starting point of a charge trajectory between r_i and r_m at $t=0$. In sub-region I₂, where $\rho=\epsilon_{oil}/[\mu(t-t_0)]$ we have:

$$E_{oil}(r,t) = \frac{I_s(t-t_0)}{2\pi\epsilon_{oil}Dr} \text{ on } r(t)^2 = \frac{\mu I_s}{2\pi\epsilon_{oil}D}(t-t_0)^2 + r_i^2. \quad (4.64)$$

where the trajectories start at $r=r_i$ and $t=t_0$.

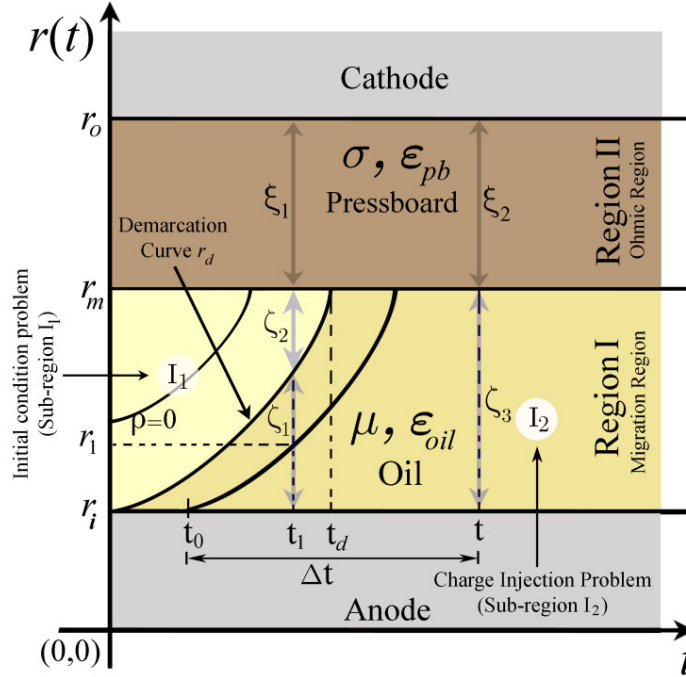


Figure 4.6: Space-time domain for the transient one-dimensional model of charge transport in the migration-Ohmic system for coaxial cylindrical electrodes. In Region I, the demarcation curve, $r_d(t)$, separates the initial condition problem (Sub-region I₁) from the charge injection problem (Sub-region I₂). The integration paths ζ_1 and ζ_2 in Region I and ξ_1 in Region II, used to calculate terminal voltage are shown for times less than the charge time of flight (t_d) starting at $r=r_i$, $t=0$ and ending at $r=r_m$, $t=t_d$. Integration paths ζ_3 and ξ_2 in Region I/II are shown for times greater than t_d .

Solving for the electric field in Region II is more straightforward. By solving the differential equation of the last term in equation (4.55) in cylindrical geometry (analogous to equation (4.30) for planar geometry), the electric field in the pressboard region is:

$$E_{pb}(t) = \frac{I_s}{2\pi\sigma Dr}(1 - e^{-t/\tau}), \quad \tau = \frac{\epsilon_{pb}}{\sigma}. \quad (4.65)$$

To find the interfacial surface charge density we use the boundary condition at $r=r_m$:

$$\epsilon_{pb}E_{pb}(r=r_{m+},t) - \epsilon_{oil}E_{oil}(r=r_{m-},t) = \sigma_s(t) \quad (4.66)$$

which yields:

$$\sigma_s(t) = \begin{cases} \frac{I_s}{2\pi D r_m} [\tau(1 - e^{-t/\tau}) - t] & 0 \leq t < t_d \\ \frac{I_s}{2\pi D r_m} [\tau(1 - e^{-t/\tau}) - t_d] & t \geq t_d \end{cases} \quad (4.67)$$

where t_d is given in equation (4.49).

Again, integrating the electric-field distributions over r in both regions using the identity of equation (4.53) yields the transient voltage across regions as

$$V(t) = \begin{cases} \frac{I_s t}{2\pi \epsilon_{oil} D} \ln\left(\frac{r_m}{r_d(t)}\right) + \sqrt{\frac{I_s}{2\pi \epsilon_{oil} \mu D}} \left[\sqrt{r_d^2(t) - r_i^2} - r_i \cos^{-1}\left(\frac{r_i}{r_d(t)}\right) \right] + \frac{I_s \ln(r_o / r_m)}{2\pi D \sigma} (1 - e^{-t/\tau}) & 0 \leq t \leq t_d \\ \sqrt{\frac{I_s}{2\pi \epsilon_{oil} \mu D}} \left[\sqrt{r_m^2 - r_i^2} - r_i \cos^{-1}\left(\frac{r_i}{r_m}\right) \right] + \frac{I_s \ln(r_o / r_m)}{2\pi D \sigma} (1 - e^{-t/\tau}) & t \geq t_d \end{cases} \quad (4.68)$$

where the demarcation curve $r_d(t)$ is given in equation (4.62).

4.3.3 Concentric Spherical Electrode Geometry

Throughout this chapter, a lower case roman r is used for spherical radial coordinates while an italicized r is used for cylindrical radial coordinates. We consider the spherical geometry in Figure 4.7, where the inner electrode at $r=r_i$ is a source of ions with mobility μ in the oil region ($r_i < r < r_m$) and the electric field is purely radial. We assume all physical parameters to be constant and consider only one-dimensional variations with the radial coordinate r , so that the current and electric field are only in the radial direction. The general equations are assumed to be the same as equations (4.1-4.3), but in spherical geometry. Again, an infinite amount of charge is available at the charge emitting ($r=r_i$) electrode, so that the emitter electric field at $r=r_i$ must be zero to keep the current finite.

In the steady-state ($t \rightarrow \infty$), the total current $I(t) = 4\pi r^2 J_r(r)$ is constant. From equations (4.1-4.3) in spherical coordinates, the charge density is only in the oil region (Region I in Figure 4.8):

$$\rho(r, t) = \epsilon_{oil} \frac{1}{r^2} \frac{\partial(r^2 E_{oil}(r, t))}{\partial r} \quad r_i < r < r_m \quad (4.69)$$

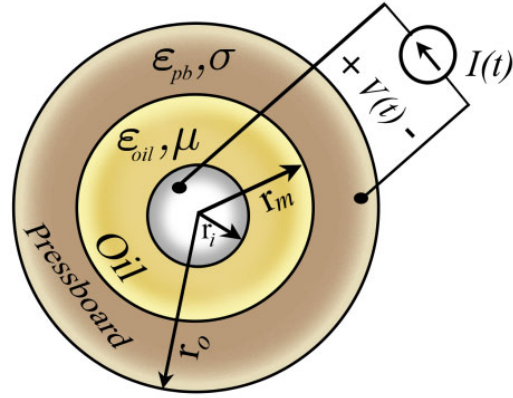


Figure 4.7: Two-region, series, oil-pressboard dielectric model for spherical electrodes excited by a step current source with Region I (Oil) $r_i < r < r_m$ obeying a mobility (μ) conduction law and Region II (Pressboard) $r_m < r < r_o$ obeying Ohmic conduction.

Using equations of Table 4.1:

$$J_s(r) = \rho(r)\mu E_{oil}(r) = \frac{\epsilon_{oil}\mu}{r^2} E_{oil} \frac{\partial(r^2 E_{oil}(r))}{\partial r} = \frac{I_s}{4\pi r^2}, \quad r_i < r < r_m \quad (4.70)$$

By solving equation (4.70), with space charge limited injection, $E_{oil}(r_i)=0$, the steady state electric field in the oil region is:

$$E_{oil}(r) = \sqrt{\frac{I_s}{6\pi\epsilon_{oil}\mu} \left(\frac{r^3 - r_i^3}{r^4} \right)}, \quad r_i < r < r_m \quad (4.71)$$

Hence, using equation (4.70), the steady state charge density is then:

$$\rho(r) = \frac{I_s}{4\pi\mu r^2 E_{oil}(r)} = \sqrt{\frac{3\epsilon_{oil} I_s}{8\pi\mu (r^3 - r_i^3)}} \quad (4.72)$$

and the electric field in the pressboard region (Region II) in Figure 4.8 is:

$$J_s = \sigma E_{pb}(r) = \frac{I_s}{4\pi r^2} \Rightarrow E_{pb}(r) = \frac{I_s}{4\pi\sigma r^2} \quad (4.73)$$

Due to the step current source in Figure 4.7, the transient analysis results in both migration/Ohmic conduction and displacement currents:

$$J_s(t) = \frac{I_s}{4\pi r^2} = \frac{\mu\epsilon_{oil}}{r^2} E_{oil}(r,t) \frac{\partial(r^2 E_{oil}(r,t))}{\partial r} + \epsilon_{oil} \frac{\partial E_{oil}(r,t)}{\partial t} = \sigma E_{pb}(r,t) + \epsilon_{pb} \frac{\partial E_{pb}(r,t)}{\partial t} \quad (4.74)$$

We again assume an initially unexcited system with space charge limited injection at $r=r_i$. Hence, the current densities in Regions I and II are equal to $J_s(t)$. Also, since the electric field in the pressboard region, $E_{pb}(r,t)$, only depends on time and radial position as $1/r^2$, the charge density in Region II is zero. To solve for the charge density in the oil region (Region I), based on equations (4.1-4.3) in spherical coordinates (Figure 4.7), we have:

$$\frac{1}{r^2} \left[\rho(r,t) \frac{\partial}{\partial r^2} (r^2 \mu E_{oil}(r,t)) + r \mu E_{oil}(r,t) \frac{\partial \rho(r,t)}{\partial r} + \frac{\partial \rho(r,t)}{\partial t} \right] = 0 \quad (4.75)$$

which reduces to:

$$\frac{\mu \rho(r,t)^2}{\epsilon_{oil}} + \mu E_{oil}(r,t) \frac{\partial \rho(r,t)}{\partial r} + \frac{\partial \rho(r,t)}{\partial t} = 0 \quad (4.76)$$

According to the method of characteristics, equation (4.76) can be rewritten as a pair of ordinary differential equations:

$$\frac{d\rho(r,t)}{dt} = \frac{\partial \rho(r,t)}{\partial t} + \frac{dr}{dt} \frac{\partial \rho(r,t)}{\partial r} = -\frac{\mu \rho(r,t)^2}{\epsilon_{oil}} \quad \text{on} \quad \frac{dr}{dt} = \mu E_{oil}(r,t) \quad (4.77)$$

Considering boundary conditions of zero volume charge at $t=0$ and space charge limited charge injection at $r=r_i$, the distribution of charge density is of identical form as planar and cylindrical geometries given by equations (4.42), (4.43) and (4.59):

$$\rho(t) = \begin{cases} 0 & \text{Sub-region } I_1 \\ \frac{\epsilon_{oil}}{\mu(t-t_0)} & \text{Sub-region } I_2 \end{cases} \quad \text{on} \quad \frac{dr}{dt} = \mu E_{oil}(r,t) \quad (4.78)$$

Again, from equations (4.2), (4.69) and (4.74), we find an ordinary differential equation in terms of electric field in the oil region using the method of characteristics:

$$\frac{d(r^2 E_{oil})}{dt} = \frac{I_s}{4\pi \epsilon_{oil}} \quad \text{on} \quad \frac{dr}{dt} = \mu E_{oil} \quad (4.79)$$

The electric field and charge trajectories are then:

$$E_{oil}(r,t) = \frac{I_s t}{4\pi\epsilon_{oil} r^2} \quad \text{on} \quad r^3 = \frac{3\mu I_s}{8\pi\epsilon_{oil}} t^2 + r_s^3, \quad r_i \leq r_s \leq r_m \quad \text{in Sub-Region I}_1 : 0 \leq t \leq t_d, r_d(t) \leq r \leq r_m \quad (4.80)$$

$$E_{oil}(r,t) = \frac{I_s (t-t_0)}{4\pi\epsilon_{oil} r^2} \quad \text{on} \quad r^3 = \frac{3\mu I_s}{8\pi\epsilon_{oil}} (t-t_0)^2 + r_i^3, \quad \text{in Sub-Region I}_2 : t \geq t_0, r_i \leq r \leq r_m \quad (4.81)$$

The demarcation curve, $r_d(t)$ and time of flight t_d for spherical electrodes shown in Figure 4.8 are:

$$r_d(t) = \left[\frac{3\mu I_s}{8\pi\epsilon_{oil}} t^2 + r_i^3 \right]^{1/3}, \quad r_i \leq r \leq r_m \quad (4.82)$$

$$t_d = \sqrt{\frac{8\pi\epsilon_{oil}}{3\mu I_s} (r_m^3 - r_i^3)} \quad (4.83)$$

The demarcation curve as shown in Fig. 8 for spherical geometry is the charge trajectory that separates the initial condition problem from the charge injection problem that starts from $r=r_i$ at $t=0$ in equation (4.80). By solving equations (4.79)-(4.81) we have similar regions and sub-regions as in Figure 4.3 and 4.6 as shown in Figure 4.8 for spherical geometry. Above the demarcation curve (I_1), where $\rho=0$ at $t_0=0$ we have:

$$E_{oil}(r,t) = \frac{I_s t}{4\pi\epsilon_{oil} r^2} \quad \text{on} \quad r(t)^3 = \frac{3\mu I_s}{8\pi\epsilon_{oil}} t^2 + r_s^3 \quad \text{Sub-Region I}_1 \quad (4.84)$$

where r_s is the starting position with $r_i < r < r_m$ at $t_0=0$. In sub-region I_2 , where $\rho = \epsilon_{oil} [\mu(t-t_0)]$ we have:

$$E_{oil}(r,t) = \frac{I_s (t-t_0)}{4\pi\epsilon_{oil} r^2} \quad \text{on} \quad r(t)^3 = \frac{3\mu I_s}{8\pi\epsilon_{oil}} (t-t_0)^2 + r_i^3 \quad \text{Sub-region I}_2 \quad (4.85)$$

By solving equation (4.74) in spherical geometry (analogous to equation (4.30) for planar geometry and equation (4.55) for cylindrical geometry), the electric field in the pressboard region is:

$$E_{pb}(t) = \frac{I_s}{4\pi\sigma r^2} (1 - e^{-t/\tau}), \quad \tau = \frac{\epsilon_{pb}}{\sigma}, \quad \text{Region II} \quad (4.86)$$

To find the interfacial surface charge density at $r=r_m$ we have:

$$\varepsilon_{pb} E_{pb}(r = r_{m+}, t) - \varepsilon_{oil} E_{oil}(r = r_{m-}, t) = \sigma_s(t) \quad (4.87)$$

which yields:

$$\sigma_s(t) = \begin{cases} \frac{I_s}{4\pi r_m^2} [\tau(1 - e^{-t/\tau}) - t] & 0 \leq t < t_d \\ \frac{I_s}{4\pi r_m^2} [\tau(1 - e^{-t/\tau}) - t_d] & t \geq t_d \end{cases} \quad (4.88)$$

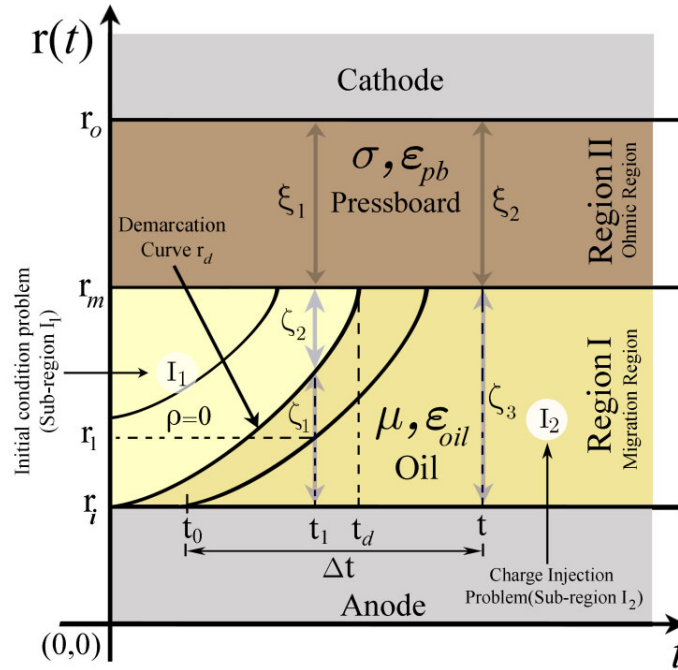


Figure 4.8: Space-time domain for the transient one-dimensional model of charge transport in the migration-ohmic system for concentric spherical electrodes. In Region I, the demarcation curve separates the initial condition problem (Sub-region I₁) from the charge injection problem (Sub-region I₂). The integration paths ζ_1 and ζ_2 in Region I and ξ_1 in Region II, used to calculate terminal voltage are shown for times less than the charge time of flight (t_d) starting at $r=r_i$, $t=0$ and ending at $r=r_m$, $t=t_d$. Integration paths to calculate terminal voltage ζ_3 and ξ_2 in Region I/II are shown for times greater than t_d .

To find the voltage across Region I, we have to evaluate the integral:

$$f(r) = \int_{r_i}^r \frac{\sqrt{r^3 - r_i^3}}{r^2} dr \quad (4.89)$$

which we evaluate by numerical methods in Section 4.4.

4.4 Comparing Analytical Solutions and Modeling Results in Different Coordinates

The first goal of this chapter is to give some simple analytical solutions, which enable us to check the accuracy of our computer models with one-dimensional planar, cylindrical and spherical electrode geometries. The analytical approach and closed form solutions for planar, cylindrical and spherical electrode geometries were presented in sections 4.2-4.4. In this section, we present and compare some simple analytical and numerical solutions from previous sections. Numerical results of COMSOL Multiphysics applied to the same one-dimensional electrode geometries are compared with closed form solutions in this chapter. The analytical and numerical COMSOL results are in excellent agreement being at worst within 0.01% for COMSOL solved spherical geometry transients and at best within 10^{-10} % for COMSOL solved steady-state planar solutions.

In this section, we present plots of some analytical solutions from the previous sections as well as some numerical results in spherical geometry. In the model, we have selected representative values in Table 4.3 for transformer oil and pressboard with the space charge limited condition.

Figure 4.9 shows the transient voltages of planar and cylindrical geometries which have been obtained analytically in equations (4.47) and (4.68). The voltage for spherical geometry was obtained using numerical integration methods to evaluate the integral of equation (4.89).

Table 4.3: Numerical parameter values of dielectric analysis with space charge limited condition

<i>Parameter</i>	<i>Symbol</i>	<i>Value</i>
Permittivity of oil region	ϵ_{oil}	$2 \times 10^{-11} \text{ Fm}^{-1}$
Permittivity of pressboard region	ϵ_{pb}	$4 \times 10^{-11} \text{ Fm}^{-1}$
Positive ion mobility in oil	μ	$10^{-9} \text{ m}^2 \text{V}^{-1} \text{ s}^{-1}$
Conductivity of pressboard region	σ	$3 \times 10^{-12} \text{ } \Omega^{-1} \text{ m}^{-1}$
Planar geometry interfaces	a, b	0.0125 m, 0.025 m
Cylindrical geometry interfaces	r_i, r_m, r_o, D	0.0125 m, 0.025 m, 0.0375 m, 0.05 m
Spherical geometry interfaces	r_i, r_m, r_o	0.0125 m, 0.025 m, 0.0375 m
Current density at positive electrode	J_s	$2.5 \times 10^{-7} \text{ Am}^{-2}$

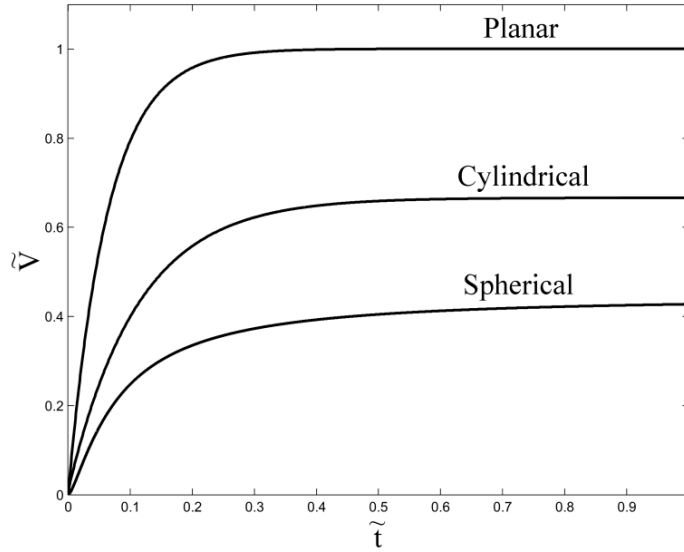


Figure 4.9: Non-dimensionalized voltage $\tilde{V} = V / (\sqrt{2J_s a^3 / (9\mu\epsilon_{oil})} + J_s a / \sigma)$ between electrodes for the three electrode geometries treated in this chapter as a function of non-dimensionalized time $\tilde{t} = t[\mu J_s / (\sigma a)]$ where all parameter values are defined in Table 4.3, and in particular $a=0.0125$ m is the oil region thickness in planar, cylindrical and spherical geometries.

Figure 4.10 shows the steady state electric field versus position in both oil and press-board regions of planar, cylindrical and spherical geometries. This graph is shown with a logarithmic scale on the vertical axis. The jump in electric field at the interface between oil and pressboard materials at $\tilde{S}=0.5$ is due to both the discontinuity in dielectric constants and due to the steady state surface charge distribution.

Figure 4.11 shows the demarcation curves in the space-time domain in the oil region which separates the initial condition problem (Sub-region I_1 in Figs. 4.4, 4.6 and 4.8) from the charge injection problem (Sub-region I_2 in Figs. 4.4, 4.6 and 4.8) for planar, cylindrical and spherical geometries.

Figure 4.12 shows the steady state volume charge density versus position in the oil regions of planar, cylindrical and spherical geometries.

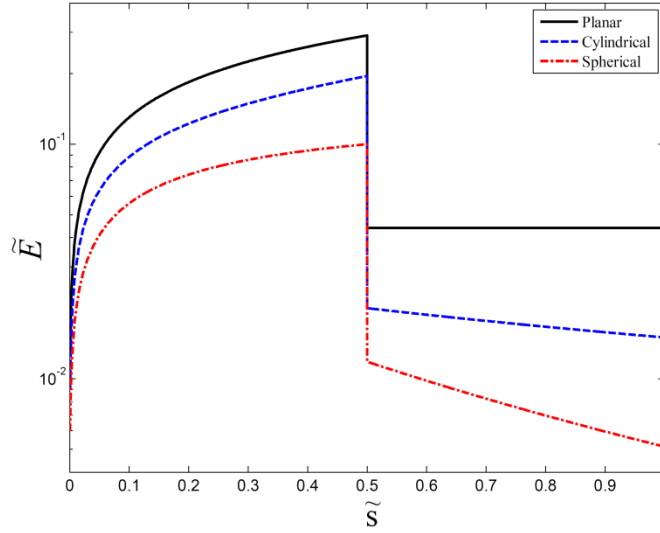


Figure 4.10: Non-dimensionalized steady state electric field $\tilde{E} = E\epsilon_{oil}\mu/(\sigma a)$ between electrodes for different electrode geometries. Non-dimensionalized distance between positive electrode and interfacial surface is defined as $\tilde{s} = s/(2a)$ which is equal to $x/(2a)$ for planar geometry, $r/(2a)-0.5$ for cylindrical geometry and $r/(2a)-0.5$ for spherical geometry. All parameter values are defined in Table 4.3, and in particular $r_i=r_i=a=0.0125$ m is the radius of the interior electrode in cylindrical and spherical geometries respectively.

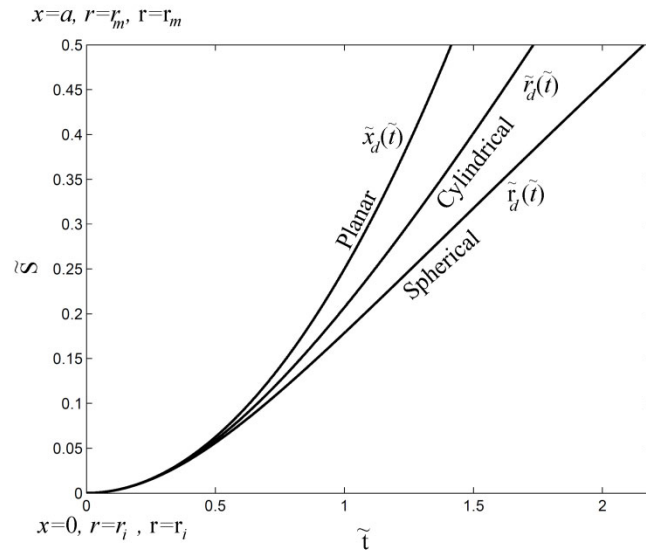


Figure 4.11: Non-dimensionalized space-time, trajectories for different electrode geometries which show the demarcation curves in planar, cylindrical and spherical geometries. Variable S is the demarcation trajectory x , r , and r given in equations (4.44), (4.62), and (4.82) for planar, cylindrical, and spherical geometries, respectively. Non-dimensionalized distance between the positive electrode and the interfacial surface is defined as $\tilde{s} = s/(2a)$ which is equal to $x/(2a)$ for planar geometry, $r/(2a)-0.5$ for cylindrical geometry and $r/(2a)-0.5$ for spherical geometry as a function of non-dimensionalized time $\tilde{t} = t\sqrt{\mu J_s / (a\epsilon_{oil})}$ where all parameter values are defined in Table 4.3, and in particular $r_i=r_i=a=0.0125$ m is the radius of the interior electrode in cylindrical and spherical geometries, respectively.

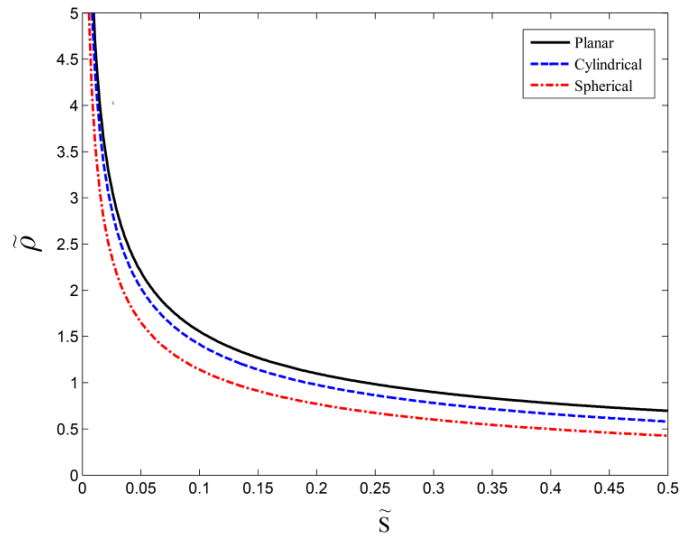


Figure 4.12: Nondimensionalized volume charge density in the oil regions $\tilde{\rho} = \rho\sqrt{\mu a / (\epsilon_{oil} J_s)}$ between electrodes for different electrode geometries in steady state. Nondimensionalized distance between the positive electrode and interfacial surface is defined as $\tilde{S} = S / (2a)$ which is equal to $x / (2a)$ for planar geometry, $r / (2a) - 0.5$ for cylindrical geometry and $r / (2a) - 0.5$ for spherical geometry.

Figure 4.13 shows the transient interfacial surface charge density of planar, cylindrical and spherical geometries which have been obtained analytically in equations (4.46), (4.67) and (4.88), respectively.

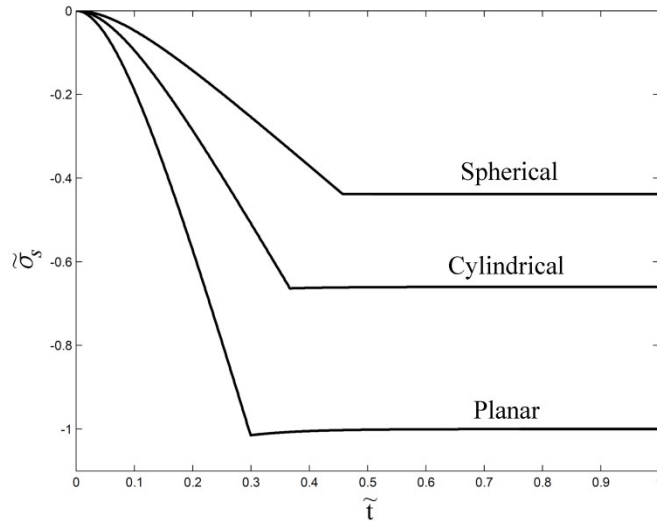


Figure 4.13: Nondimensionalized electric surface charge density at the oil/pressboard interface $\tilde{\sigma}_s = \sigma_s / (J_s \epsilon_{pb} / \sigma - \sqrt{2 J_s \epsilon_{oil} a / \mu})$ for planar, cylindrical and spherical geometries as a function of nondimensionalized time $\tilde{t} = t [\mu J_s / (\sigma a)]$.

We have also performed some numerical simulations using COMSOL Multiphysics to confirm analytical solutions we obtained in this chapter for planar, cylindrical and spherical electrode geometries. The model assumes charge migration in the oil region and Ohmic conduction in the pressboard region. We have applied the COMSOL electro-quasi-static module with convection and diffusion modules of COMSOL for solving charge migration conduction in oil using equations shown in Table 4.1. For the Ohmic pressboard region, we have used the in-plane electric currents module of COMSOL to solve equation shown in Table 4.1. Proper boundary conditions have been employed to exactly match with those assumptions we have taken in our analyses. The numerical results closely match with analytical solutions with error less than 0.01 percent.

4.5 Summary

One-dimensional migration-Ohmic unipolar analysis of the charge transport phenomena has been presented in this chapter. Oil-pressboard composite dielectric systems have been analyzed in planar, coaxial cylindrical and concentric spherical electrode geometries with a step current source. Space charge limited injection and linear injection problems have been solved in the steady-state and transient using the method of characteristics, which converts the governing partial differential equations into a set of ordinary differential equations. Application of this method allowed us to analytically solve for volume and interfacial surface charge densities, charge trajectories in the oil region, and electric field as functions of time and space.

Analytical solutions are compared with some COMSOL Multiphysics numerical solutions as a way of gaining confidence in the correctness and accuracy of our numerical solutions.

Two-dimensional Electrohydrodynamic Modeling of Streamer Initiation and Propagation in Dielectric Liquids

Electrical breakdown modeling has been proven to be a complex task particularly in liquid dielectrics, not only due to the multidisciplinary nature of dielectric breakdown, which involves electrodynamics, collision physics, fluid mechanics, and thermodynamics, but also because of numerous different ionization mechanisms (e.g., field ionization, impact ionization, thermal ionization and photo-ionization), charge carriers, and injection processes [2,23,25,87,88]. Over the years, a set of multiphysics equations has been refined for streamer modeling in liquid dielectrics [23-25,39,41-53]. Unfortunately, analytical solutions for these equations are not available especially in complicated electrode geometries [72,73,84,85]. Therefore, an efficient multiphysics numerical model will significantly assist us to better interpret and understand the breakdown process. Since it is impossible to incorporate all of the influential dynamics into the breakdown model (even if they were all identified), the priority is given to the essential processes. Specifically, we have focused on the most important factors in the breakdown of transformer oil, (a): ionization potential of hydrocarbon molecules (field ionization) [48], (b): charge injection mechanisms (from needle electrode) [23,92], (c): field and temperature dependent charge carrier mobilities [2], (d): electrode geometries and gap distances [49], and (e): applied voltage characteristics (e.g., peak, rise-time and fall-time) [48].

The simplest geometry for modeling the formation and propagation of a single column streamer is the 2-D axisymmetric (cylindrical) geometry. The axisymmetric model presented in this chapter has revealed many underlying mechanisms of streamer initiation, propagation, and final breakdown. Nevertheless, many of the streamer attributes cannot be explained through a symmetric model. The streamer branching, for instance, is essentially a nonsymmetrical phenomenon that should be described by a robust three-dimensional model (Chapter 6) that is usually computationally expensive. This chapter describes required underlying physics and the governing equations to build a 2-D axisymmetric streamer model. The model equations have been solved numerically using the finite element software package, COMSOL Multiphysics [71]. The implementation of the model in COMSOL Multiphysics is presented along with the modeling results obtained in this thesis research. The basic structure of the two-dimensional (2D) axisymmetric model developed in this chapter is essentially analogous to those used in [23], [25]; however, several key improvements have been made in the present version of the model, including:

- Lightning impulse voltages (based on the IEC standard definition [86]) have been applied instead of Heaviside step functions used in [23], [25] to make the results comparable to the experimental records.

- Effects of the electric field on the hydrocarbon molecules ionization potential and electron mobility are taken into account based on the results derived from quantum chemistry theories [11,12,93,94].
- More consistent stabilization techniques have been applied to solve the conservation of charge equations for each charge carrier [71-78].
- Different combinations of direct and iterative solvers have been employed which enables the model to solve the equations with much greater spatial resolution [79-83].

This chapter is organized with Section 5.1 describing the simulation geometry including the gap distances and the electrode shapes. Governing equations, charge carrier characteristics and the boundary equations of the electro-thermal hydrodynamic model are given in sections 5.2 through 5.4. Section 5.5 gives the results of 2-D streamer modeling for different electrode shapes, gap distances, applied voltage polarities and peak amplitudes under different streamer initiation, propagation and breakdown stages. The axisymmetric model described in this chapter has also been extended to model the three-dimensional streamer branching in Chapter 6 and the streamer interactions with liquid immersed conductive and non-conducting walls in Chapter 7.

5.1 Electrode Geometries and Gap Distances

Maximum effort in this thesis has been made to enable the numerical modeling results to be compared with identical experimental measurements by the ABB, Sweden and from the literature. The first step is to choose a standard electrode gap geometry. The best-known electrode geometry is a needle-sphere electrode geometry defined by IEC 60897, entitled, “Methods for the determination of the lightning impulse breakdown voltage of insulating liquids” [66] as shown in Figure 5.1 filled with transformer oil.

Since the electric field intensity near the electrode surface is higher around the sharp points (such as the needle electrode tip) because of their smaller radius of curvature, the electrodes are defined by the IEC 60897 in such a way that the streamer always initiates from the needle electrode regardless of the applied voltage polarity. Therefore, if streamer breakdown occurs, the spherical electrode (usually grounded) eventually collects at least on of the streamers initiated from the sharp needle electrode.

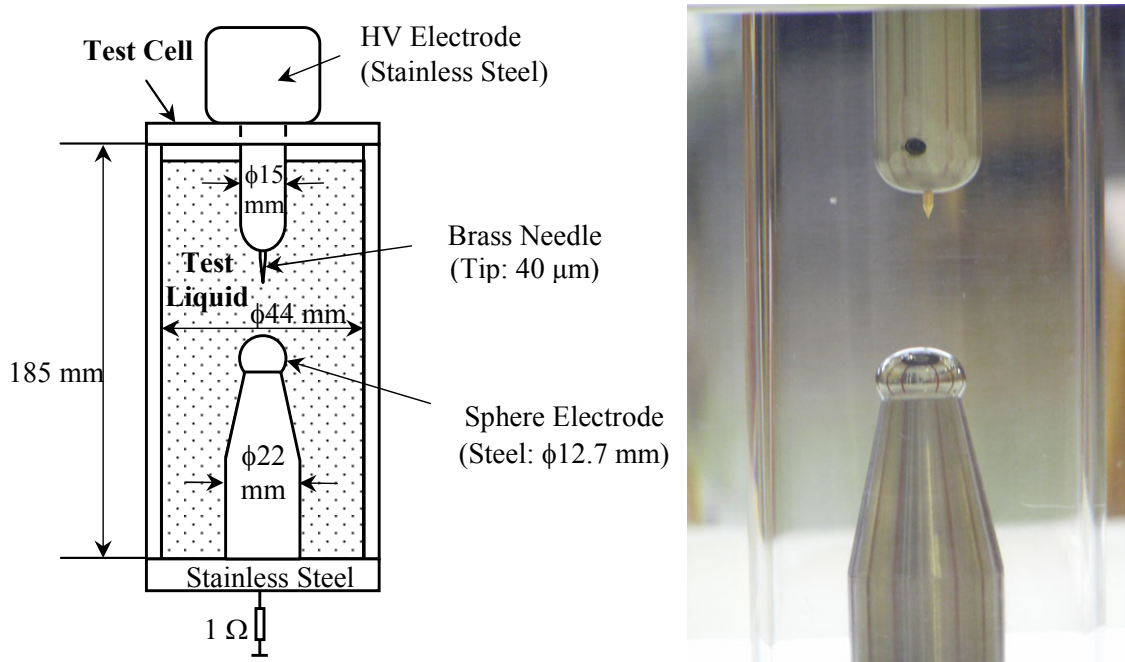


Figure 5.1: Needle-sphere electrode chamber dimensions (left) and the actual electrode chamber in laboratory filled with transformer oil (right). This structure is used for experimental studies of streamers at ABB [55-57]. This exact geometry is also used for simulation purposes as described in IEC 60897 standard [66]. The electrodes are 25 mm apart and the radii of curvature of the needle and sphere electrodes are 40 μm and 6.35 mm, respectively.

5.2 Governing Equations

Every quantity in this thesis is assumed to be in local thermodynamic equilibrium having definite values. A three-carrier continuum model is utilized to account for the charge generation, recombination, and transport mechanisms. The governing equations are based on the drift-dominated charge continuity equations (5.1)-(5.3) for positive ion (ρ_p), negative ion (ρ_n) and electron (ρ_e) charge densities, coupled through Gauss' law and charge migration equation (5.4). Application of convection-dominated form of the continuity equations means that the diffusion terms are neglected for each charge carrier. The thermal diffusion equation (5.5) is included to model temperature variations (T) and gas formation in oil. The effect of phase transitions that normally occur within the streamer are neglected. The negative ion and electron charge densities, ρ_n and ρ_e , are both negative quantities [48] in the governing equations.

$$\frac{\partial \rho_p}{\partial t} + \nabla \cdot (\rho_p \mu_p \vec{E}) = G_F(|\vec{E}|) + \frac{\rho_p \rho_e R_{pe}}{q} + \frac{\rho_p \rho_n R_{pn}}{q} \quad (5.1)$$

$$\frac{\partial \rho_n}{\partial t} - \nabla \cdot (\rho_n \mu_n \vec{E}) = \frac{\rho_e}{\tau_a} - \frac{\rho_p \rho_n R_{pn}}{q} \quad (5.2)$$

$$\frac{\partial \rho_e}{\partial t} - \nabla \cdot (\rho_e \mu_e \vec{E}) = -G_F(|\vec{E}|) - \frac{\rho_p \rho_e R_{pe}}{q} - \frac{\rho_e}{\tau_a} \quad (5.3)$$

$$\nabla \cdot (\varepsilon \vec{E}) = \rho_p + \rho_e + \rho_n, \vec{J} = (\mu_p \rho_p - \mu_e \rho_e - \mu_n \rho_n) \vec{E} \quad (5.4)$$

$$\frac{\partial T}{\partial t} + v \cdot \nabla T = \frac{1}{\rho_l c_v} (k_T \nabla^2 T + \vec{E} \cdot \vec{J}) \quad (5.5)$$

where v , ε , k_T , c_v , and ρ_l are the oil's velocity, permittivity (2.2 ε_0), thermal conductivity, specific heat, and mass density, respectively. The numerical values of model coefficients are given in Table 5.1 for transformer oil. On the microsecond time scales of interest for streamer formation, the oil's velocity is negligible, i.e., $v = 0$. In addition, q is the magnitude of electronic charge, and E is the local electric field. The parameters μ_p , μ_n , and μ_e are the mobilities of the positive ions, negative ions, and electrons, respectively. R_{pn} , R_{pe} are the ion-ion and ion-electron recombination coefficients obtained from the Langevin relationship and τ_a is the electron attachment time constant, respectively.

Since diffusion of the charged species is assumed to be negligible in equations (5.1-5.3), we have solved the conservative form of the general convection and diffusion equations with triangular quartic elements. Numerical solutions of the charge continuity equations usually exhibit harsh oscillations given that the exact solutions are smooth and continuous. These spurious oscillations are caused by numerical instabilities [71,76]. To avoid these severe local oscillations that exist in the number density of charged species of the previous model [23,24], which has been solved using only the artificial anisotropic streamline diffusion (AISD) formulation for the scalar convection-diffusion equation, nonlinear crosswind diffusion (CWD) has been applied as an artificial diffusion stabilizer in addition to different types of streamline diffusions (SDs) such as (anisotropic, compensated streamline upwind Petrov-Galerkin (SUPG) and Galerkin least-square methods) to solve the charge continuity equations. It has been shown in [76] that CWD is less over-diffusive than other discontinuity-capturing techniques and leads to a better numerical behavior, while it is computationally expensive due to its non-linear nature [76]. On the other hand, SD techniques effectively stabilize the system and accelerate the solution. We have applied both SD and CWD at the same time to optimally stabilize the numerical solution. Both artificial diffusion techniques are tuned to balance a tradeoff between removing nonphysical local oscillations (due to SD) and excessively smooth results just next to the walls (due to CWD). An average has been taken whenever any discrepancy is observed between results of different SD techniques mentioned above.

5.3 Charge Carrier Characteristics

Free electrons along with positive and negative ions constitute the main charge carriers in the liquid electrics. Charge carrier characteristics, such as mobility and generation mechanisms, chiefly determine the behavior of the dielectric while it is exposed to extremely intense electric fields. Unfortunately, these characteristics are not fully known. Lack of knowledge of charge carrier parameters are probably the main weak point of the model built in this thesis research.

This section summarizes the current knowledge of charge carrier characteristics, including ionization and recombination mechanisms and carrier mobilities.

5.3.1 Ionization mechanisms

The complex nature and structure of liquids has inhibited the development of a comprehensive liquid state theory. Rather, scientists have derived models and understanding of the basic processes in liquids by utilizing theories from both the solid-state [87] or compressed gas-state [88].

In regards to the modeling and understanding of breakdown phenomena in liquids, the modeling of the liquid as a compressed gas most often prevails with scientists taking concepts from gas discharge physics [88]. This inherently has to do with the development of a low-density gaseous-phase during streamer formation and the ease in which the transition between gas and liquid phases occurs with varying temperature and pressure [89]. However, streamers in liquids show several phenomenological similarities to electrical trees in solids and the comparison of liquids and amorphous solids has found some promising results [90]. Therefore, a study of streamer formation based solely upon considering the liquid as a solid or gas would be a narrow minded endeavor. Appropriately, three different mechanisms that find their origins from both solid-state and gas discharge theory and lead to an increase in the free charge carrier concentration in the liquid state when it is electrically over-stressed are discussed in detail. The mechanisms are electric field dependent molecular ionization (field ionization), impact ionization and photo-ionization.

Electric field enhanced ionic dissociation or the Onsager effect [114] is another charge generation mechanism hypothesized by researchers to drive streamer development. It is a process that occurs in a dielectric liquid whereupon neutral ion-pairs dissociate to form free positive and negative ions under an applied field. It has been used to describe electrical conduction in non-polar liquids such as transformer oil by several authors [96,115,116]. O'Sullivan et al. [25,51] showed that electric field enhanced ionic dissociation is also unlikely to be the key catalyst to streamer

development in transformer oil because appreciable dissociation of ions and current density occur only in the region close to the high voltage electrode.

O'Sullivan [] and Hwang [25] have shown that in liquid dielectrics in general and in transformer oil in particular, field ionization is the dominant generation process of charge carriers. For in depth study of the contribution of the impact ionization and photo ionization refer to O'Sullivan [23] and Hwang [25].

The field ionization process provides the generation term in equations (5.1), (5.3) and plays a key role in describing streamer dynamics. In spite of the recombination terms that are defined by constants, the field ionization charge density rate source term, G_M , is modeled using the Zener model of electron tunneling in solids [11]:

$$G_M(|\vec{E}|) = \frac{q^2 n_0 a |\vec{E}|}{h} \exp\left(-\frac{\pi^2 m^* a \Delta^2}{qh^2 |\vec{E}|}\right) \quad (5.6)$$

All parameter values as listed in Table 5.1 are consistent with those used in [5], [6] except electric field dependent ionization potential, which has been derived by Density Functional Theory (DFT) [12]. Smalø *et al.* have used DFT to find out the effect of the intense electric field on the ionization energy of hydrocarbons [7]. The ionization energy for the different aromatic, naphthenic and paraffinic hydrocarbon molecules are derived and fitted by linear regression. The final result of DFT is that the constant ionization potential in equation (5.6), Δ , should be replaced by an electric field dependent ionization potential, $\text{IP}(|\vec{E}|)$:

$$G_F(|\vec{E}|) = \frac{q^2 n_0 a |\vec{E}|}{h} \exp\left(-\frac{\pi^2 m^* a \text{IP}(\vec{E})^2}{qh^2 |\vec{E}|}\right) \quad (5.7)$$

There are several implementations of the field dependent ionization potential of hydrocarbon molecule. One of the simplest representations is in the form of equation (5.8).

$$\text{IP}(\vec{E}) = \Delta_0 - \gamma \sqrt{|\vec{E}|} \quad (5.8)$$

By importing the electric field dependent ionization potential function derived by DFT (equation (5.8)) into equation (5.7), we have:

$$G_F(|\vec{E}|) = \frac{q^2 n_0 a |\vec{E}|}{h} \exp\left(-\frac{\pi^2 m^* a}{qh^2} \left(\frac{\Delta_0}{\sqrt{|\vec{E}|}} - \gamma\right)^2\right) \quad (5.9)$$

Application of the generation term in the form of equation (5.9) enables the model to describe the negative streamers and positive streamers formed by positive and negative extra high voltages ($\geq 200\text{kV}$) [48]. Representative parameter values for the ionization potential function are listed in Table 5.1 as well as other parameters used to solve governing equations (5.1-5.6).

Table 5.1: Physical parameters used in the streamer/surface flashover model

<i>Symbol</i>	<i>Parameter</i>	<i>Value</i>	<i>Reference</i>
n_0	Number density of ionizable species	$1 \times 10^{23} \text{ m}^{-3}$	[25,65]
a	Molecular separation distance	$3.0 \times 10^{-10} \text{ m}$	[23,25,39]
m^*	Effective electron mass	$0.1 \times m_e = 9.1 \times 10^{-32} \text{ kg}$	[25,94]
Δ_0	Ionization potential function parameter	$1.36 \times 10^{-18} \text{ J}$,	[12,93,94]
γ	Ionization potential function parameter	$1.118 \times 10^{-22} \text{ Jcm}^{1/2}\text{V}^{-1/2}$	[12,93,94]
R_{pn}, R_{pe}	Ion-ion and ion-electron recombination rates	$1.64 \times 10^{-17} \text{ m}^3\text{s}^{-1}$	[11,25]
μ_p, μ_n	Positive and negative ion mobilities	$10^{-9} \text{ m}^2\text{V}^{-1}\text{s}^{-1}$	[11,25]
μ_e	Electron mobility	$10^{-4} \text{ m}^2\text{V}^{-1}\text{s}^{-1}$	[11,25,94]
c_v	Specific heat	$1.7 \times 10^3 \text{ Jkg}^{-1}\text{K}^{-1}$	[2,25]
ρ_l	Oil mass density	880 kgm^{-3}	[11]
k_T	Oil thermal conductivity	$0.13 \text{ Wm}^{-1}\text{K}^{-1}$	[2,11]
q	Electronic charge	$1.602 \times 10^{-19} \text{ C}$	[64]
τ_a	electron attachment time constant	200 ns	[25,39]
h	Planck's constant	$6.626068 \times 10^{-34} \text{ m}^2\text{kgs}^{-1}$	[64]

Models that use generation term in equation (5.6) with constant ionization potential, $IP=A_0$ [23,25] are not able to describe positive streamers formed by extra high voltages (above +200 kV) and negative streamers within the 2-D axisymmetric geometry [23,25,28]. The application of DFT in the generation term in the form of equation (5.9) enables the model to describe the negative streamers as well as positive streamers formed by extremely high voltages [41-53]. Representative parameter values for the ionization potential function are also included in Table 5.1, as well as other parameters used to solve the governing equations (5.1-5.9). Consistent boundary conditions have been applied to the streamer model [48].

5.3.2 Recombination of Charged Species

Streamer development is carried out by free electrons and ions in the dielectric liquid. Interaction of these free charge carriers with each other and the surrounding media opens up the possibility of recombination between electrons and positive ions and neutral species. Even different kinds of ions with opposite electric charge polarity can recombine to produce neutral molecules. The recombination terms usually act against the generation term to reduce the available number of charge carriers by recombining them and turning them into neutral molecules. Electrons also recombine with neutral molecules to generate negative ions. Nevertheless, this exceptional case of recombination is not modeled by recombination constants. Instead, an electron attachment time constant describes the process, which results in generation of negative ions.

In the model described in this thesis, the ion-ion and ion-electron recombination coefficients, obtained from the Langevin relationship are assumed equal, $R_{pn}=R_{pe}=q(\mu_p+\mu_n)/\varepsilon$ [5], since using the Langevin relationship for the ion-electron recombination rate leads to overestimation []. The Langevin recombination relationship is a diffusion limited process and valid for situations where the electric field levels are low to moderate and the recombining species are of similar physical scale. To compensate for the reduction in the recombination cross-section caused by high electric field levels, we have used the Langevin recombination term for ion-ion recombination to model ion/electron recombination. This approach effectively compensates for the reduction in the recombination cross-section by reducing the apparent electron mobility.

As a chemical reaction, recombination rate depends upon the spatial distribution of the reactants [32]. The recombination of electrons or negative ions with positive ions can be described as

$$\frac{d\rho_{\pm}}{dt} = -R_{\pm}\rho_{\pm}^2 \quad (5.10)$$

where R_{\pm} is the recombination rate constant, with units (m^3/s) and ρ_{\pm} is the number density of positive and negative species. The recombination rate constant R_{\pm} is related to the diffusion coefficients of the species, D_{\pm} as:

$$R_{\pm} = 4\pi(D_{+} + D_{-})(r_{+} + r_{-}) \quad (5.11)$$

where r_+ and r_- are the reaction radii of the charge carriers. The diffusion coefficients are related to low field mobilities by the Nernst-Einstein equation as follows:

$$\frac{D_{\pm}}{\mu_{\pm}} = \frac{kT}{q} \quad (5.12)$$

where k is the Boltzmann constant, T is the temperature in Kelvin and q is the magnitude of an electron charge. Plugging equation (5.12) into equation (5.11) yields the following expression:

$$R_{\pm} = 4\pi \frac{kT}{q} (\mu_+ + \mu_-)(r_+ + r_-) \quad (5.13)$$

Recombination between two charge carriers is considered to be inevitable when the carriers get within a distance $r = r_+ + r_-$ apart. This distance r is the distance when the coulomb force of attraction between the charge carriers equals the liquid's thermal energy kT :

$$r = \frac{q^2}{4\pi\epsilon kT} \quad (5.14)$$

Substituting Equation (5.14) into Equation (5.13) yields the following expression for R_{\pm} :

$$R_{\pm} = \frac{q(\mu_+ + \mu_-)}{\epsilon} \quad (5.15)$$

This mobility dependent expression for the recombination rate coefficient R_{\pm} , is often referred to as the Langevin recombination coefficient. When modeling streamer formation and growth in a dielectric liquid, Langevin recombination is implemented as a bulk sink term in the charge continuity equations for the positive and negative free charge carriers.

The Langevin recombination theory is a diffusion based ion recombination theory and as such it is only strictly valid for situations where the electric field levels are low to moderate and the recombining species are of similar physical scale [32]. It has been shown that the Langevin recombination model overestimates the rate of ion/electron recombination in liquids at low to moderate electric field levels [33, 34]. No data exists in the literature regarding ion/electron recombination rates at the electric field levels encountered during streamer initiation and growth ($1 \times 10^8 - 1 \times 10^9$ (V/m)); however by carrying out some simple analysis it is possible to see that the Langevin theory would greatly overestimate the recombination rate.

The Langevin's recombination theory is based on the concept of recombination cross-sections. The radius of the recombination cross section for an electron and a positive ion is related to the energy of the free electron as:

$$r_{cs} = \frac{e^2}{4\pi\epsilon kT_{he}} \quad (5.16)$$

where the term kT_{he} is the energy of the "hot" electron moving through the liquid under the influence of the strong electric field. Electrons generated during streamer formation have energies on the order of several electron-volts [32]. This contrasts with ions, whose low-mobility results in them only having energies on the order of mill-electron-volts. Using equation 5.16, the recombination cross-section of an electron with an energy of 3 eV and that of an ion with an energy of 25 meV can be calculated to approximately be: 1.25×10^{-19} and 1.25×10^{-15} (m²) respectively. This means that the recombination cross-section for a highly energized electron with a positive ion is a factor of 1×10^4 smaller than the recombination cross-section for two ions.

In addition to recombination, electrons also combine with neutral molecules to form negative ions. This process is modeled as an electron attachment time constant. In very pure hydrocarbon liquids, energetic electrons have attenuation lengths on the order of several centimeters, meaning that an electron can be expected to travel for several centimeters in the liquid from the point where it was formed before it attaches to a neutral molecule to form a negative ion [100]. In commercial dielectric liquids, the attenuation length will be shorter due to higher levels of impurities in the liquid [25].

The attachment time constant is simply the quotient of the electron attenuation length and the electron velocity. A representative set of numbers for such a calculation are an electron attenuation length λ_a of 1 mm, an electron mobility μ_e of 1×10^{-4} m²V⁻¹s⁻¹ and an electric field strength of 5×10^7 V/m. These numbers give an attachment time τ_a of:

$$\tau_a = \frac{\lambda_a}{\mu_e |E|} = 200 \text{ ns} \quad (5.17)$$

which corresponds with values found in the literature [25,101]. Although attachment undoubtedly takes place during streamer growth in dielectric liquids, its impact on the overall streamer propagation process is reasonably small due to the fact that attachment processes take place on a longer time scale than important dynamics such as the separation of positive ions and electrons in the ionization zone at a streamer's tip [25].

5.3.3 Electric Field Dependent Electron Mobility

The constant values of mobilities in the older versions of the model, listed in Table 5.1, are taken from [11]. In this thesis, causes of positive streamer acceleration are rationalized by saturation of

the electron velocity at extremely high divergent electric fields. Such findings explain the abrupt jump in the streamer velocity under extra-high voltages (i.e., above 400 kV for needle-sphere electrodes 25-mm apart), traditionally known as higher modes of positive streamers. The model that uses a nonlinear electric field dependent electron velocity describes the streamer velocity more accurately when compared to the experimental data in the literature.

Electron Saturation Velocity (ESV) is the maximum velocity an electron attains in the presence of very high electric fields. The ESV is a fundamental parameter in the design of semiconductor devices especially field effect transistors [95]. In liquid dielectrics, electrons normally move at an average drift velocity proportional to the electric field intensity they experience temporally [96]. The proportionality constant, mobility of the carrier, is known to be a dielectric property [97,98]. However, as the electric field in a liquid dielectric increases above ~ 0.01 MV/cm, the mobility of the electrons starts to decrease, the transverse component of electron diffusion coefficient becomes greater than the longitudinal component due to raising the backscattering rate, and the average electron energy particularly ahead of the ionization front eventually limits the electron velocity in the direction of the electric field [97]. For intense electric fields above ~ 1 MV/cm, the drift velocity becomes almost constant and independent of electric field intensity, transverse and longitudinal components of the electron diffusion coefficient do not effectively contribute to the electron average velocity (both become smaller than ~ 10 cm²/s) [96-99]. At extremely high electric fields above ~ 10 MV/cm, electrons gain more energy from the field than they can transfer to the neutral molecules of the liquid, and become runaways. The velocity of the runaway electrons is not equilibrated [96,97]. Typical ESV in transformer oil is on the order of $\sim 1 \times 10^6$ cm/s that occurs at electric field strengths on the order of ~ 1 MV/cm or higher [96]. Both the saturation field and the saturation velocity of all materials including transformer oil strongly depend on impurities, chain/crystal defects and temperature [96]. If the two electrodes between which the electrons move are much smaller than the Debye length (mean free path), hot electron effects (velocity overshoots) can be observed [97-99].

The dependencies of mobilities on the electric field (ESV model) [97] are taken into account. Runaway and hot electron effects are not incorporated in the model, since appearance of such phenomena is unlikely for applied voltages up to 400 kV (the maximum electric field does not reach above ~ 10 MV/cm). The ESV is modeled as a rational function of electric field intensity that is adopted from semiconductor models [39,96]. The constant mobility model anticipates slower and faster electrons at lower and higher fields than 4 MV/cm, respectively, compared to the ESV model. Constant mobility of electron, which is derived from measurements performed only at intense uniform electric fields [95] has been also used for low electric fields and highly divergent fields in the previous versions of the model [48] due to the lack of a comprehensive experimental record. The results of the ESV model match the empirical data of higher mode streamers in the literature more accurately than the constant mobility model. Therefore, we argue that the ESV model describes the electron behavior at applied voltages above 400 kV more accurately. Most of the results reported in this chapter are obtained by the constant mobility model with values listed in chapter 5.1. The ESV model is applied wherever stated in this thesis.

5.3.4 Temperature Dependent Electron and Ion Mobilities

The dependencies of mobilities on the temperature [2] (due to lower viscosity of the the fluid at higher temperatures) are taken into account. This dependency is described by the Einstein relation (kinetic theory) [2]. All of the parameter values of the Einstein relation for transformer oil are taken from [2].

5.4 Boundary Conditions

Consistent boundary conditions have been applied to the streamer model. First of all, to unify all the research efforts in liquid discharge physics, standard electrode geometries, and standard applied impulse voltages have been defined by the International Electrotechnical Commission (IEC), as shown in Figure 5.1. In addition, IEC has defined the impulse applied voltage which can be generated with Marx generators in typical high voltage laboratories. Positive and negative IEC standard impulse voltages with a broad range of applied voltage peak amplitudes (spanning from initiation peak voltage to acceleration peak voltage) and rise-times (from a few nano-seconds to a few micro-seconds) have been studied for different gap distances and electrode shapes. Specifically, the potential of the sphere electrode is set to the ground. The needle electrode potential is defined using two subtracting exponential voltages to create the standard lightning impulse voltage according to IEC 600060-1 [86] as:

$$V_{impulse} = KV_0 \left(e^{-\frac{t}{\tau_1}} - e^{-\frac{t}{\tau_2}} \right) \quad (5.18)$$

where K is a non-dimensional compensation factor to determine the polarity of impulse voltage and to keep the peak amplitude of the impulse exactly equal to V_0 , since in general, the maximum value of subtraction of two exponential functions is not generally 1.

The top, bottom and side insulating (transparent) walls shown in Figure 5.1 have been assigned to have zero normal displacement field components (i.e., $\vec{n} \cdot \vec{D} = 0$). This boundary condition acts like a continuity equation, which means no terminating walls are felt by electric field lines across the walls. The electrode boundary conditions along the charge transport continuity equations are convective fluxes for all species, while insulating wall boundaries are assigned to have no flux of any species. All boundaries are set to zero normal thermal diffusive flux (i.e., $\vec{n} \cdot \vec{\nabla} T = 0$) making the approximation that the system is adiabatic on the timescales of interest [23,25,48].

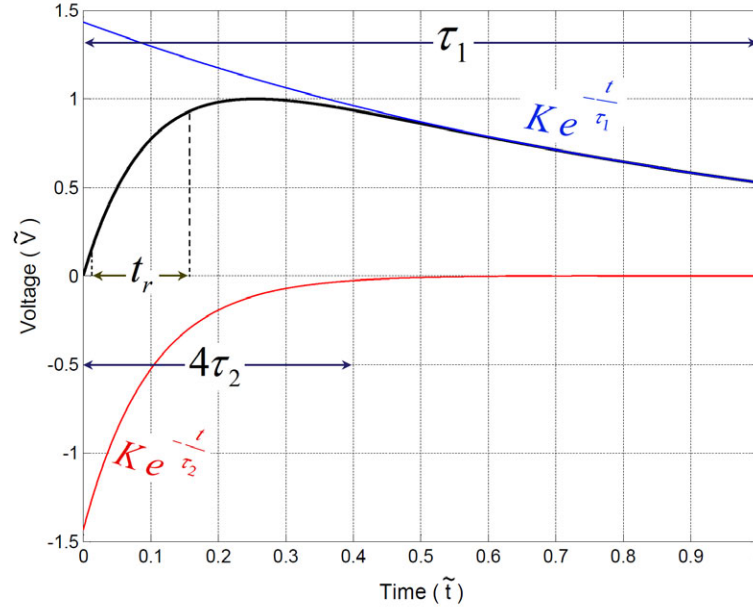


Figure 5.2: IEC 60060 lightning impulse voltage (non-dimensional, $\tilde{V} = V/V_0$) with rise-time t_r (10% to 90% of peak voltage) versus non-dimensional time, $\tilde{t} = t/\tau_1$ generated with subtracting two exponential functions.

5.5 Breakdown Stages in Liquid Dielectrics

We have divided the entire streamer breakdown process into three distinct stages: initiation, propagation and final stage of breakdown. These stages are defined based on the position of the streamer head. During the initiation stage, the streamer emanates from the needle electrode and travels a few millimeters. The streamer stays in the propagation stage until it reaches the second electrode. The breakdown completes when the streamer hits the second electrode (final breakdown stage). From the modeling point of view, after the initiation stage, the model requires a significant amount of computational capacity. In this section (5.5), we discuss these stages separately.

The extent of a streamer development depends upon many factors including both the nature of the dielectric liquid (i.e., chemical composition) and the applied electrical excitation (i.e., magnitude, duration, rise time, polarity, etc.). Hwang has addressed some of the transformer oil characteristics that affect the streamer breakdown [25-28]. Transformer oil is not a pure liquid hydrocarbon, but is a mixture of many different naphthenic, paraffinic, and aromatic molecules with a complex molecular structure, which makes it difficult to characterize many parameters, such as electron mobility, number of ionizable species and ionization potential. The electric field

dependent molecular ionization is the key mechanism for streamer development in transformer oil. Except for the ionization potential function, we have imported the rest of the parameters into the model using simple assumptions with no or weak experimental records [23,25,48]. Firstly, there is multiple evidence indicating that effective electron mass, m^* is a function of electric field while we have imported a constant value for zero electric field due to the lack of a reference [100,101]. It is fairly complicated to derive a function for the effective mass of free electrons [94], which is not in the scope of this thesis. Secondly, the number of the ionizable species, n_0 , is not precisely known for different situations of transformer oil. The previous works have assumed empirical constant values for n_0 [23,25]. The model results indicate that there is a semi-linear relation between numbers of ionizable species, n_0 , and the streamer velocity. The number of ionizable species, n_0 , has been simply increased to model higher modes of positive streamers in [25], however, as discussed in 5.5.3, the 3rd mode positive streamer velocity only rises an order of magnitude when the streamer reaches about 8~10 mm from the needle tip. Therefore, it seems that n_0 should be a function of electric field intensity itself, which is not known to the best of the author's knowledge. The third important parameter, which is not known precisely, is the electron mobility. The value, shown in Table 5.1 for electron mobility is derived from Walden's rule, which assumes the electron is a spherical particle and uses a classical electron radius, R_e known as the Lorentz radius [5]. However, as described in sections 5.3.3 and 5.3.4, dependence of particle mobilities on the bulk oil temperature and electric field intensity are taken into account [2]. Temperature dependent mobility of charge carriers, applied to the model, has significantly increased the negative streamer velocity [48]. The temperatures obtained in the model for streamer core, indicate that a gas (vapor) phase develops underneath the streamer crust due to collisions. The model does not cover the ionization process in the gas phase. Future studies should include impact ionization in the gas phase as well as the phase conversion in the liquid bulk [102, 103] to better model the pre-breakdown mechanisms behind the streamer propagation. Therefore, the exact parameters describing the actual behavior of the hydrocarbon molecules in the pre-breakdown stage are not fully known and there is still much work remaining to be done on the characteristics of the transfer oil molecule under electrical and thermal stresses.

Simulation results reported in this chapter indicate that negative streamers demand higher peak voltages to initiate from a needle electrode. Also, bushy negative streamers initially occupy larger volume around the needle electrode compared to the filamentary positive streamers. An initial ionized body formed by negatively applied impulse voltage propagates slower due to the lower electric field enhancement ahead of the ionized region. When the ionized body grows a few millimeters from the negative needle, the 2-D axisymmetric model fails to track the physical velocity of the negative streamer, since in spite of positive streamers, experiments confirm that the negative streamers cannot propagate in a stable single on-axis streamer column and the formation of the off-axis branches are inevitable for negative streamer propagation beyond a few millimeters. Branching phenomena must be studied in a computationally expensive full 3-D model, which is in the scope of this continuing research. Including the electric field dependence of ionization potential derived using DFT [12, 93, 94] enables the presented model to physically describe the higher streamer velocity and streamer column diameter under higher applied voltages. The model confirms that higher mode velocities do not take place until the streamer travels beyond 8~10 millimeters from the needle electrode as already observed in experiments [2].

Our model also indicates that the applied voltages with smaller rise-times form thicker streamer columns in liquid dielectrics, while applied voltages with longer rise-times create thinner streamers. Such effects have been reported from experiments on the streamer formed in gaseous media. The molecular structure and behavior of liquids is more complex than gases and solids and even in the purest liquids, there exists trace amounts of impurities that make it difficult to isolate the mechanisms behind electrical breakdown. In particular, transformer oil is a mixture of many different aromatic, naphthenic, and paraffinic molecules with complex molecular structures. The major weak point of the presented model is the lack of data about effective electron mass, electron mobility and the number of ionizable species in electrically stressed transformer oil.

5.5.1 *Streamer Initiation: Effects of Applied Voltage Parameters*

Mechanisms behind the streamer initiation caused by standard positive and negative impulse voltages with different peak amplitudes and rise-times have been investigated in this section using the 2-D axisymmetric EHD model. It has been experimentally observed that streamer initiation characteristics are strongly dependent on the voltage polarity and peak amplitude [41-53]. In the case of transformer oil, experimental evidence has shown that streamers emanating from a positive electrode tend to initiate at lower applied voltages and propagate faster and further than negative streamers [8,13,41-53]. A few streamer propagation modes have been identified for lightning impulse voltage excitations depending on the peak amplitude of the excitation voltage. For instance, the 2nd mode positive streamers initiate at the breakdown voltage, which denotes 50% probability of breakdown, while the 3rd mode initiates at the acceleration voltage (roughly two times greater than 50% breakdown voltage) where the streamer propagation velocity rises dramatically [104]. Average propagation velocities for 2nd and 3rd mode streamers are on the order of 1 km/s and 10 km/s respectively [25,104]. In the literature, the 1st mode of positive streamers is often ignored as it has a low probability of leading to breakdown [25,28]. Similar modes have been identified for negative streamers depending on applied voltage magnitude [28,104]. Simulation results clearly show the effects of applied voltage peak for both polarities. Figure 5.3 shows a filamentary positive streamer formed by an applied voltage with +130 kV peak and 100 ns rise-time at $t=155$ ns. The initiation velocity and diameter of this streamer are clearly less than a positive streamer formed by an applied voltage with +200 kV peak and 100 ns rise-time shown at $t=100$ ns in Figure 5.4. The effect of the applied voltage peak is even more evident in Figure 5.5 showing a higher mode positive streamer formed by an applied voltage with +400 kV peak and 100 ns rise-time shown at $t=100$ ns. The average velocity of +400 kV is approximately greater by factors of 4 and 2 than +200 kV and +130 kV respectively. In addition, it can be seen in these figures that higher applied voltages create thicker positive streamers [48].

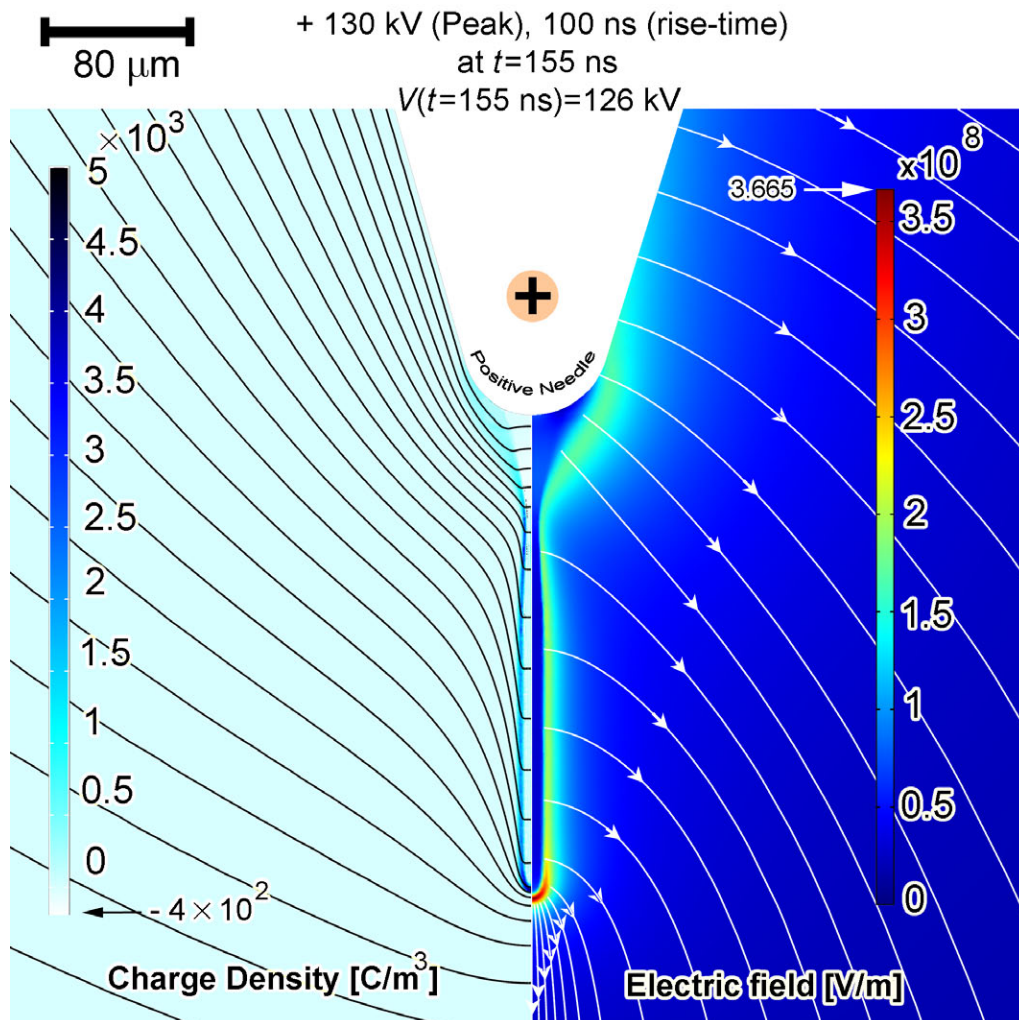


Figure 5.3: Electric field magnitude and lines (right side) and the net charge density and equipotential lines (left side) for a positively applied lightning impulse voltage with 130 kV peak and 100 ns rise-time at $t=155$ ns. No discharges are observed for a 130 kV negatively applied impulse voltage.

Positive streamers formed by +130 kV and +200 kV impulse voltages (shown in Figures 5.3 and 5.4) almost reach their eventual diameters after the streamer head travels about 250 μm from the positive needle tip. However, it takes a relatively longer time for a +400 kV streamer to attain its ultimate diameter as shown after 100 ns and 200 ns in Figures 5.5 and 5.6, respectively. In Figure 5.6, the variation of the streamer diameter formed by +400 kV is almost damped in 1 mm from the needle electrode tip (after 200 ns). Therefore, it takes longer times and distances for streamers formed by higher voltage peak amplitudes to stabilize. We will further discuss the positive streamer diameters in this section.

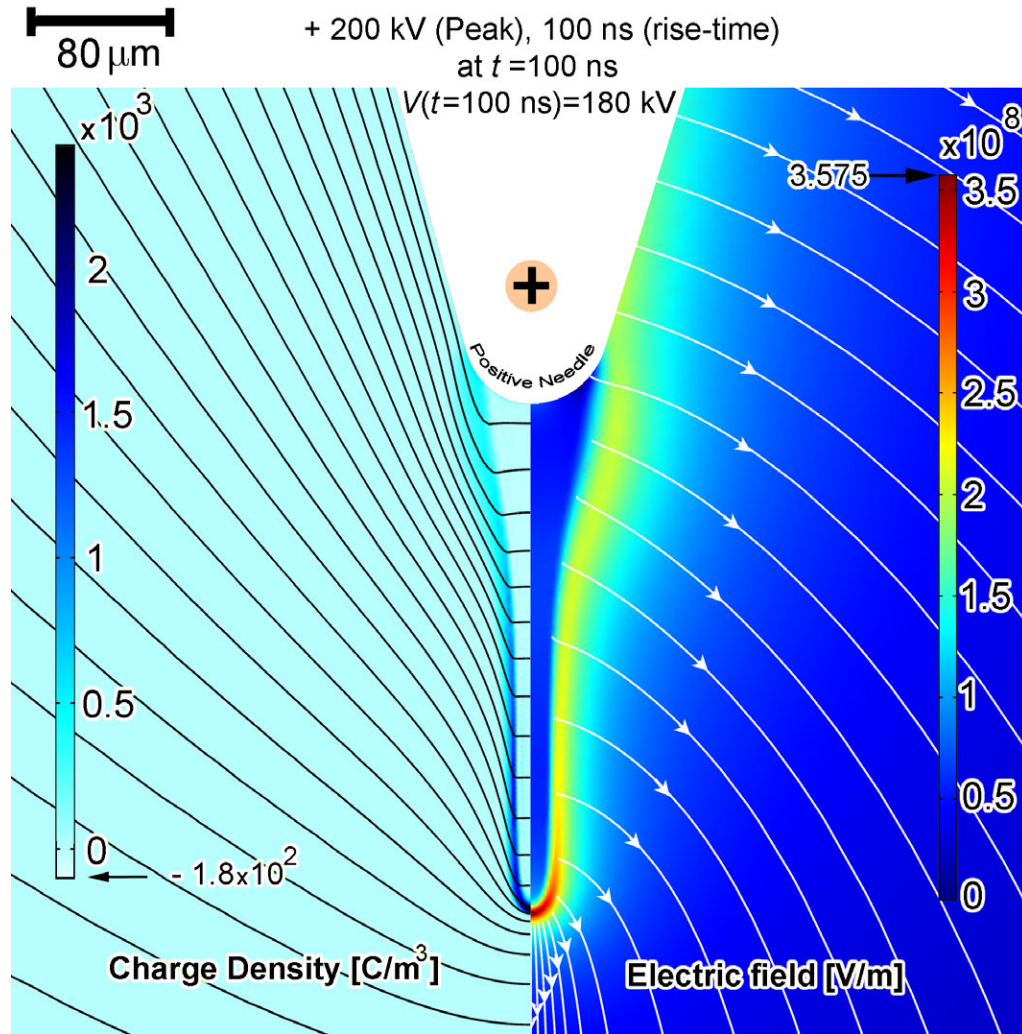


Figure 5.4: Electric field magnitude and lines (right side) and the net charge density and equipotential lines (left side) for a positively applied lightning impulse voltage with 200 kV peak and 100 ns rise-time at $t=100$ ns.

Comparing Figures 5.3, 5.4 and 5.5 indicates that the stabilized thickness of streamers and streamer head radius of curvature grow as the applied voltage peak increases. In addition, streamers formed by higher voltages carry higher total charge at relatively higher velocity. As shown in Chapter 6, higher charge density at wider streamer heads will increase the chance instability growths at the streamer heads if inhomogeneities disturb the cylindrical symmetry. Therefore, the fact that the higher applied voltage peaks generate higher number of streamer branches is also due to the dependency of charge density configuration at the streamer head on the applied voltage peak as shown in Figures 5.2-5.5.

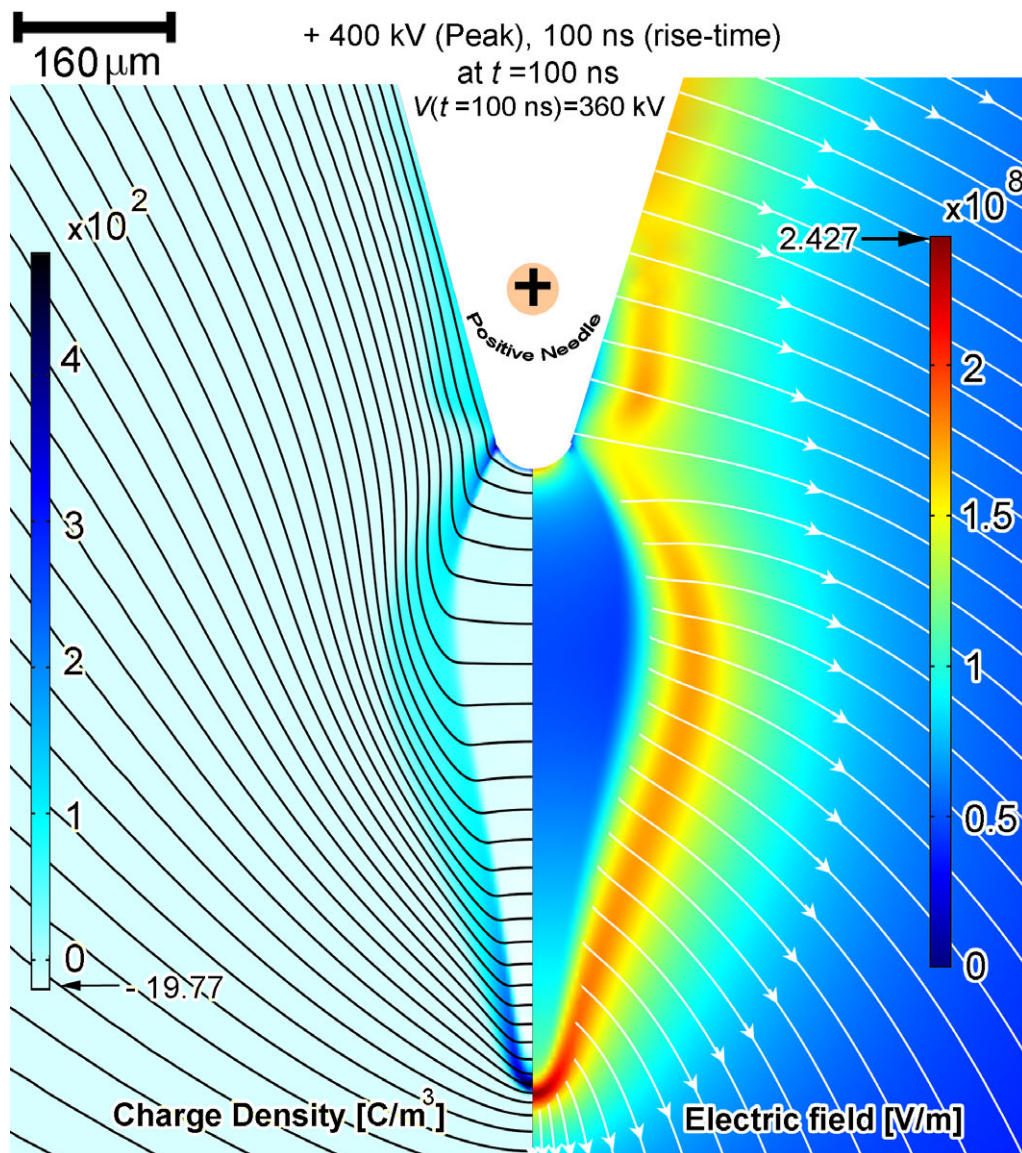


Figure 5.5: Electric field magnitude and lines (right side) and the net charge density and equipotential lines (left side) for a positively applied lightning impulse voltage with 400 kV peak and 100 ns rise-time at $t=100$ ns.

It should be noted here that the optimal stabilization techniques to study the shape of the streamers in the 2-D axisymmetric model is combination of crosswind diffusion (CWD) and compensated streamline upwind Petrov-Galerkin (SUPG) streamline diffusions to solve the charge continuity equations. Particular application of artificial anisotropic streamline diffusion (AISD) as the only stabilizer should be avoided although it increases the simulation speed [23,25], since it leads in an oversimplification, which results in an ignorance of streamer column diameter dynamics over time and space as can be seen in Figure 5.6 for instance.

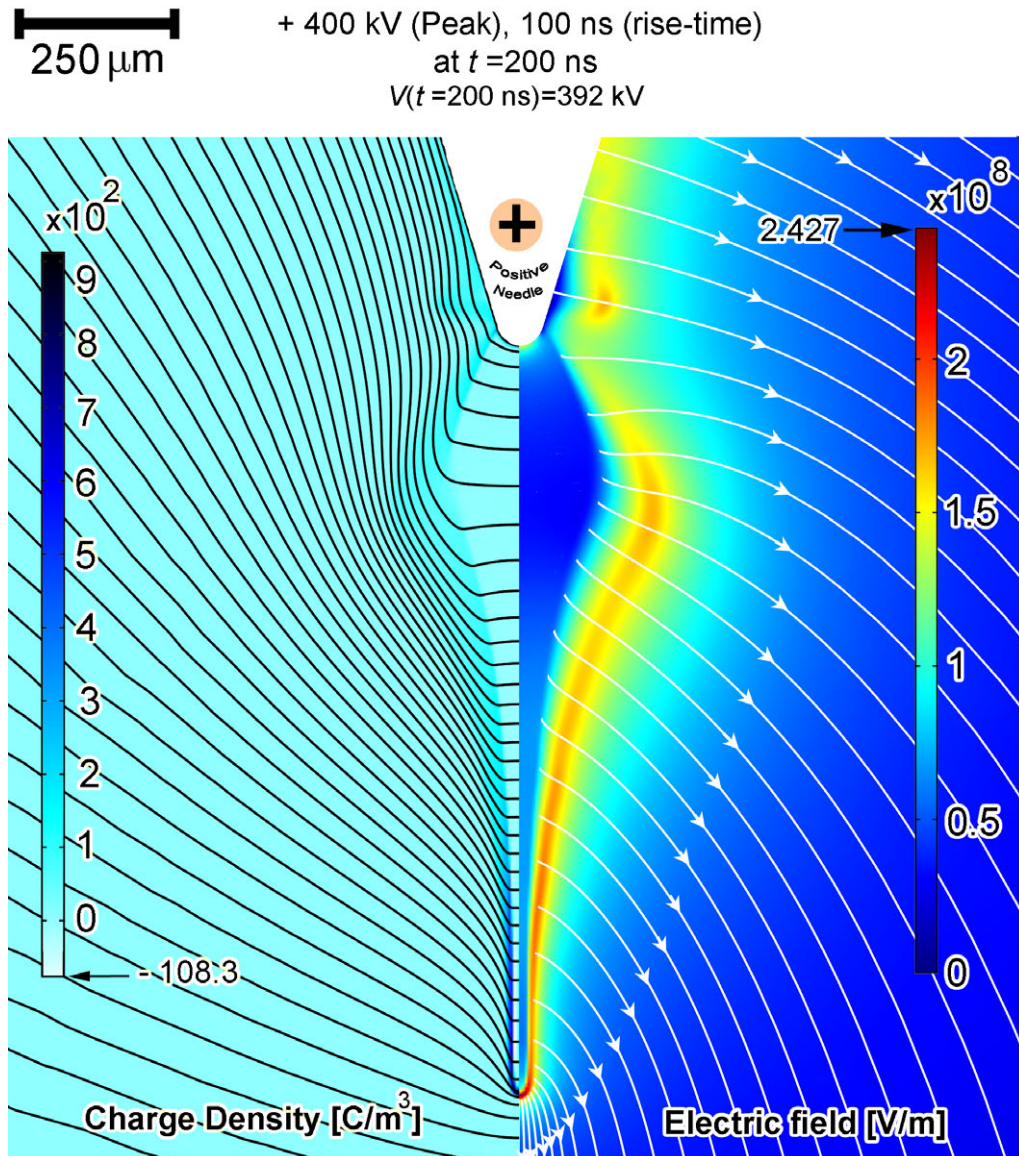


Figure 5.6: Electric field magnitude and lines (right side) and the net charge density and equipotential lines (left side) for a positively applied lightning impulse voltage with 400 kV peak and 100 ns rise-time at $t = 200$ ns.

In spite of filamentary positive streamers, negative streamers form in a bushy shape as shown in Figures 5.7 and 5.8. The negative streamer produced by an impulse with -400 kV peak and 1 ns rise-time grows in both axial and radial directions to build an ionized bubble in the vicinity of the negative needle. Such a bushy configuration of the net charge density significantly shields the intense electric field, which leads to a significant drop in the streamer velocity after the streamer front travels about half a millimeter from the needle tip. The negative streamers cannot initiate in a filamentary shape, since the opposing electric field formed by stationary ions slows down the

electrons; while in positive streamers, sluggish positive ions assists the electric field amplification ahead of the streamer, which accelerates the filamentary streamer even at a few millimeters from the needle tip.

Increasing the applied voltage peak amplitude affects negative streamer shape and the velocity of negative streamers fairly similar to the positive counterparts. Figure 5.8 shows a negative streamer formed by an applied voltage with -600 kV and 1 ns rise-time. Comparing Figures 5.7 and 5.8 clarifies that higher voltages create a bulkier ionized bubble, which grows faster, and further in both axial and radial directions.

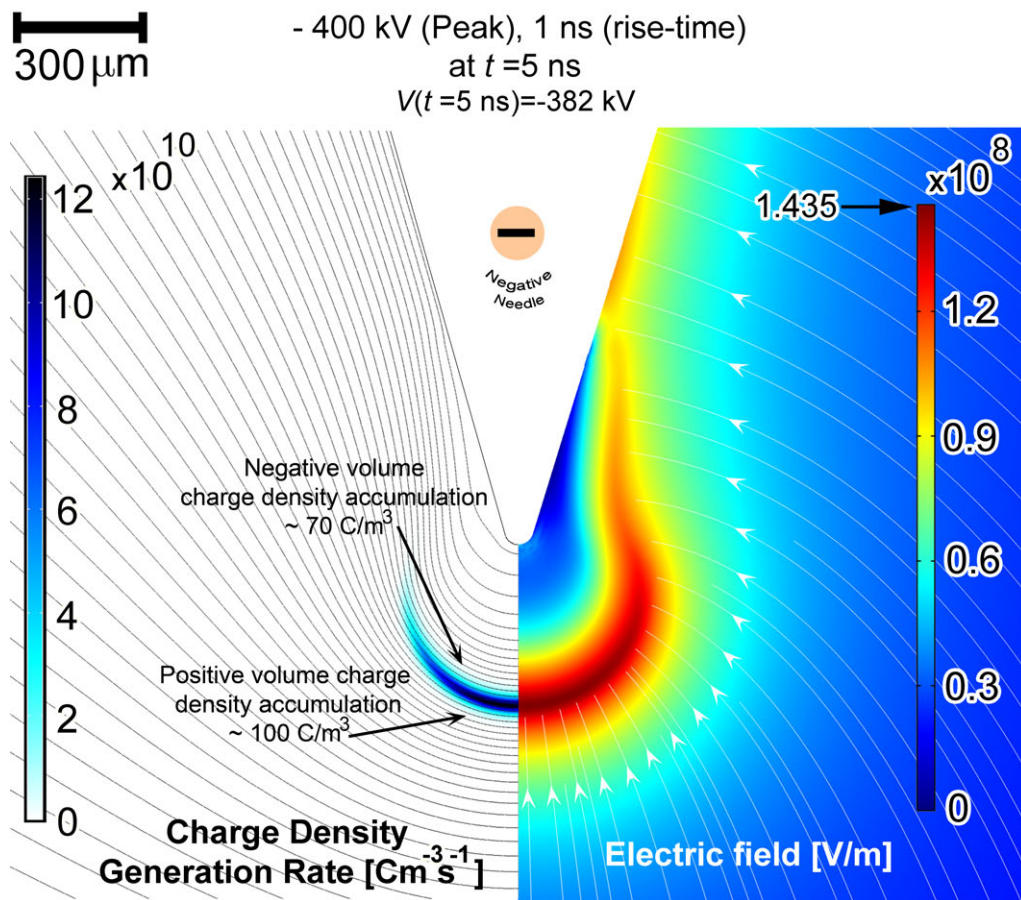


Figure 5.7: Electric field magnitude and lines (right side) with the charge density generation rate and equipotential lines (left side) for a negatively applied lightning impulse voltage with -400 kV peak and 1 ns rise-time at $t=5 \text{ ns}$.

As can be seen in Figures 5.7 and 5.8, the negative streamers occupy much more volume since the highly mobile electrons are repelled by the negative needle electrode and migrate into the liquid bulk. On the other hand, applied positive impulse voltage extracts the electrons from the ionization zone back to the needle electrode creating a positive space charge region that reduces the electric field near the needle electrode and enhances the electric field ahead of the positive space charge region. The field enhancement makes the positive streamer initiation possible at lower applied voltage peak amplitudes compared to the negative streamers.

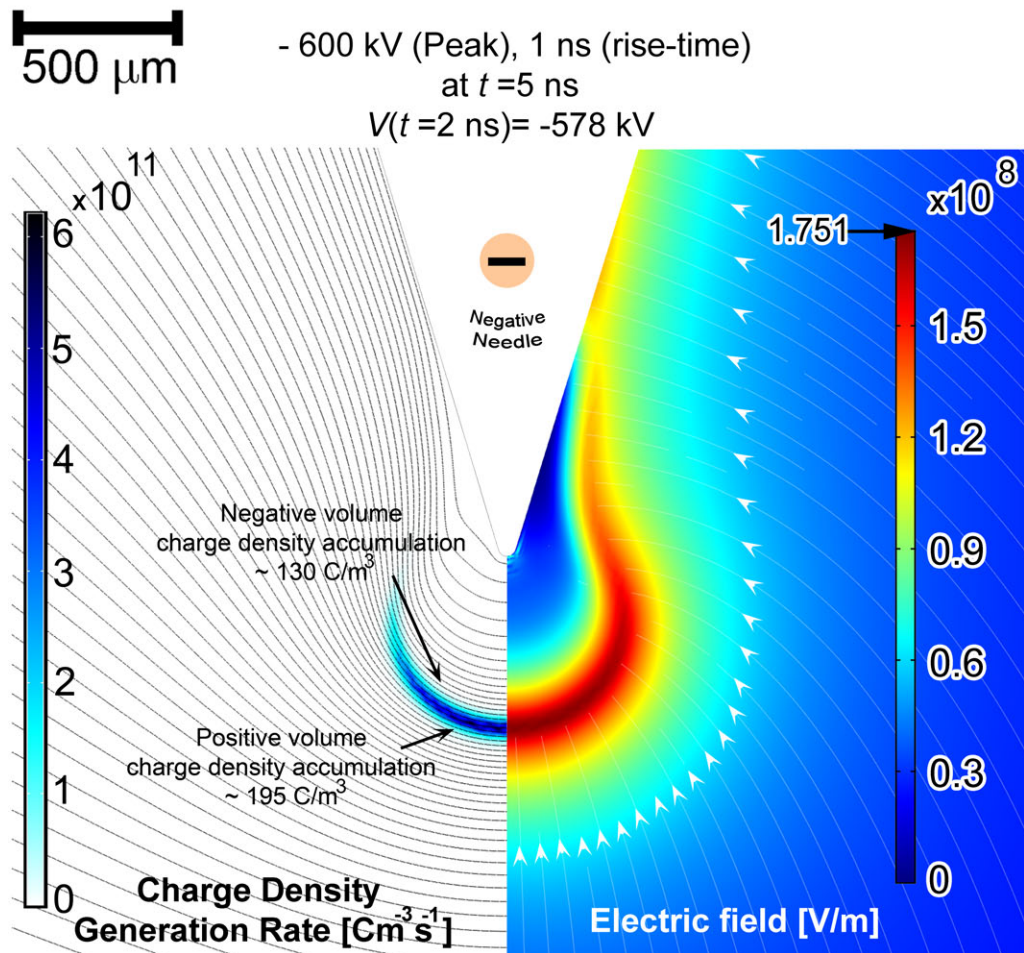


Figure 5.8: Electric field magnitude and lines (right side) with the charge density generation rate and equipotential lines (left side) for a negatively applied lightning impulse voltage with -600 kV peak and 1 ns rise-time at $t=5$ ns.

The model reveals that the velocity and the shape of positive streamers are approximately insensitive to the changes in electron mobility as long as it is about two orders of magnitude greater than the ion mobilities. The experimental results confirm this prediction of the model as

reported in [17]. However, the shape and the velocity of negative streamers are quite sensitive to the electron mobility.

The main difference in the effects of the higher applied voltage peak amplitudes between positive and negative streamers is that the higher positive applied voltage peaks lead to an increase in streamer velocity and streamer diameter and not the electric field ahead of the ionized region while in negative streamers both electric field ahead of the ionized body and the streamer velocity are increased by higher negative peaks as can be seen in Figures 5.4–5.8.

Ionizing the oil molecules into slow positive and negative ions and fast electrons quickly develops a net volume charge because the highly mobile electrons are swept away from the ionization zone leaving behind the low mobility positive and negative ions. The net charge density at the streamer crust, with the same polarity as the needle electrode, modifies the electric field distribution in the oil such that the electric field close to the needle electrode decreases while the electric field magnitude ahead of the ionized volume in the oil increases. The new enhanced electric field distribution leads to ionization occurring further away from the needle electrode, which in turn causes further modification of the electric field and charge distributions. The ultimate result of these electrodynamic processes is the development of an ionizing electric field front, which is a moving dissipative charge carrier source due to the collisions, raises the temperature to vaporize transformer oil and create a gas phase. The temperature rise in the negative streamers is considerably greater over a larger volume. Experimental results have shown that negative streamers initiated from the needle electrode generate gas bubbles around the needle with diameters on the order of 1 mm in transformer oil [7-9]. These observations support the numerical results of our model obtained for negative streamers, since in the larger ionized body around the negative needle, the temperature is about 5000 K, about one order of magnitude higher than the boiling point of the transformer oil (~500 K) [2]. Therefore, it is reasonable to think of a vapor phase generated inside the bushy ionized body around the negative needle [8,18,48]. On the other hand, since the volume that must be ionized by a negatively applied impulse voltage is much larger, the negative streamers demand more energy to form. As a consequence, negative streamer formation occurs at a higher impulse voltage peak than their positive counterparts.

Figure 5.9 shows the distance of the streamer head from the needle tip for positive and negative streamers initiated by different applied voltage peaks. Error-bars in Figure 5.9 show the range of results obtained by application of different streamline artificial diffusions (anisotropic, compensated streamline upwind Petrov-Galerkin (SUPG) and Galerkin least-square methods) to solve continuity equations and the curves are plotted by taking averages on the results of these artificial stabilization techniques. The streamer velocity under +400 kV is roughly 2 times greater than +200 kV streamer velocity which itself is two times greater than +130 kV streamer velocity.

The velocity of the negative streamers is initially higher than positive streamers, however, the instantaneous velocity of a positive streamer tends to increase after a few tens of nanoseconds, before the streamer reaches ~1.2 mm from the needle, while the negative streamer velocity decreases significantly after the initial bubble formed around the needle.

At the point 1.5 mm from the needle, the streamer velocities are ~2.5 km/s, 5 km/s, 12 km/s, 1 km/s and 3 km/s for streamers formed by applied voltages peaks of +130 kV, +200 kV, +400 kV, -400 kV and -600 kV respectively which correspond well with experimental results of [6,13,104] and [17].

Beyond ~1.5 mm from the needle, both positive and negative streamer velocities gradually drop. The positive streamer velocity falls to ~1 km/s, ~3.5 km/s and ~6 km/s for 130 kV, 200 kV and 400 kV applied voltage peaks respectively, which are again in good agreement with corresponding experimental results of [6,13,104].

It has also been presented in [13,104] that initiation velocities of 3rd mode positive streamers (occurring above 200 kV in a 25 mm gap) are at most 2~3 times greater than 2nd mode. The dramatic rise in positive streamer propagation velocity only appears when the 3rd mode streamer head travels about 8~10 mm from the needle tip [13] which is not covered in Figure 5.9. Our 2-D axisymmetric model is unable to keep track of the streamer head velocity this far, since at these points branching usually happens [7]. The branching phenomenon is one of the most interesting characteristics of the streamers in dielectrics, which is not physically understood. The present 2-D axisymmetric model is not able to keep track of the off-axis branches emanating from the main streamer root, since it forces the entire streamer development process to stay in axial symmetry.

Unfortunately, there is not enough experimental evidence to clarify the effects of the applied voltage rise- and fall-times on the shape and velocity of positive and negative streamers in dielectric liquids. Briels *et al.*, have shown in [32, 33] that the applied voltages with shorter rise-times create streamers with visibly larger diameters in gaseous media. Our model shows that impulses with steeper rises form thicker positive and negative streamer columns in transformer oil as well (see definition of 10%–90% rise-time of applied impulse voltage defined by IEC in [86]).

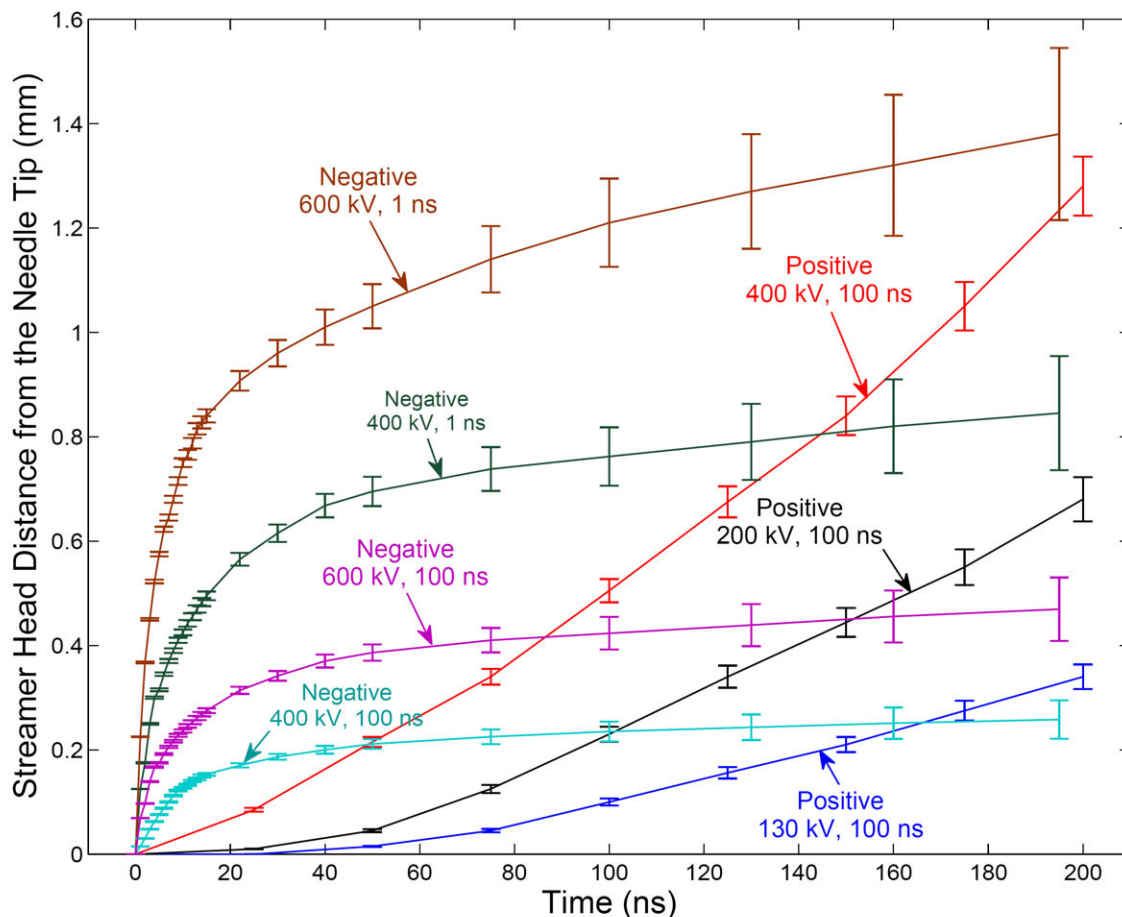


Figure 5.9: Streamer head average distance from needle tip for positive and negative applied voltages with different peak amplitudes. Positive streamer velocity tends to time increases, while a negative streamer decreases significantly after an initial bubble is formed around the needle. Error-bars show the range of results obtained by each of the artificial streamline diffusions (anisotropic, compensated streamline upwind Petrov-Galerkin and Galerkin least-square methods) to solve the charge continuity equations. The streamer velocity under +400 kV is roughly 2 times greater than +200 kV streamer velocity which is itself two times greater than +130 kV. Dissimilar rise-times for positive and negative streamers are shown to ease comparison between positive and negative streamers with velocities on the same order.

It is already shown that increasing the applied voltage magnitude rises both the initial ionized volume and the eventual streamer column diameter (Figures. 5.3–5.9). The effects of applied voltage rise-time on the positive streamer shape can be seen in Figures 5.4, 5.10–5.13 for positive streamers and in Figure 5.14 for negative streamers. The greater streamer diameter formed by steeper applied voltages is caused by the fact that shorter rise-times (higher rate of rise of electric field intensity) impose a stronger electrical ionization shock, especially around the needle. A

faster rising electric field prevents the highly mobile electrons to diffuse into the bulk oil and by capturing more electrons over a larger volume forms a bulkier initial ionized volume, which ends up with a greater streamer column diameter. We have observed such phenomena in different polarities and peak amplitudes. For conciseness, the effects of the rise-time are shown only on the positive streamers formed by applied voltages with +200 kV peak amplitudes in Figures 5.4, 5.10-5.13 and for the negative streamers formed by applied voltages with -400 kV and -600 kV peak amplitudes in Figure 5.14. The positive streamer shown in Figure 10 is slightly thicker compared to the one that is formed with longer rise-time as shown in Figure 5.4. The difference between streamer diameters is more evident for the positive streamers formed by +200 kV impulse voltages with 10 ns and 1 ns rise-times shown in Figures 5.11 and 5.12, respectively. Comparing Figures 5.4, 5.10, 5.11 and 5.12 also suggests that the maximum electric field at the streamer head is slightly less ahead of the streamers formed by steeper applied voltages. Such drops in electric field magnitude are mainly caused by greater radii of curvature of the streamer heads formed by shorter rise-times. The other fact that contributes to the drops in electric field in thicker streamers is that the maximum volume charge density is also less for streamers formed by positive applied voltages with smaller rise-times. Such drops in maximum electric field ahead of the streamer directly lessens the instantaneous streamer velocity, which can lead to lower the chance of total breakdown over the gap if the pulse width (fall time) is not sufficiently long. Our model predicts relatively similar positive streamer behavior for other positive applied voltage magnitudes, such as +130 kV and +400 kV.

Decreasing the applied voltage rise-time, also broadens the distribution of the highly ionized volume close to the needle which can be considered as increasing the chance of branching. For instance a streamer formed by an impulse applied voltage with +200 kV peak and 1 ns rise-time occupies much more radial space than the positive streamer shown in Figure 5.4. The model must be extended to a full three-dimensional geometry to involve the physics of streamer branching and at this point, based on 2-D axisymmetric models we can only evaluate the branching possibility which seems to be more for applied voltages with greater peak amplitudes and/or shorter rise-times.

It is usually tricky to measure the streamer column diameter in experiments. One of the most effective approaches is the optical measurement [18]. The streamer branch diameters from optical measurements is estimated to be about half of the electrodynamic diameters, as the model describes (shown in Figures 5.3–5.6 and 5.10–5.12) [29,51]. Considering this assumption, the streamer column diameters shown in this chapter for both polarities are in agreement with some of the experimental images of [3], [14], [105] and especially [18].

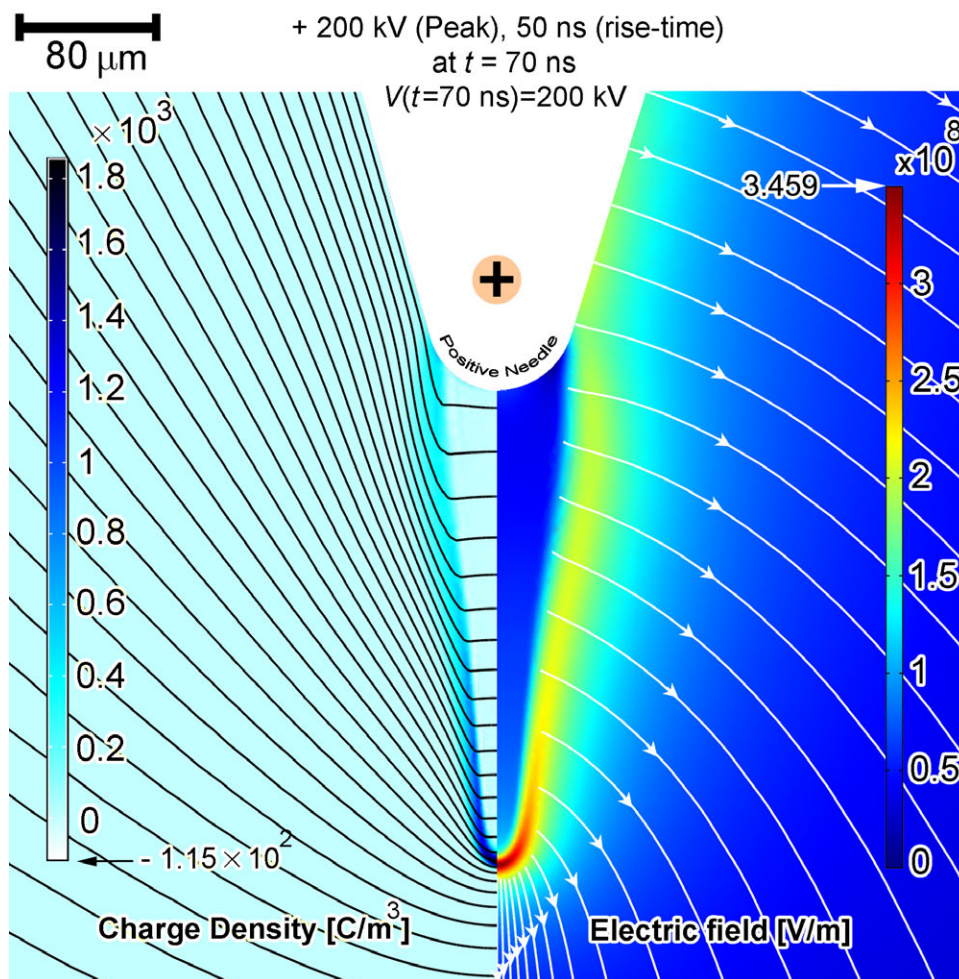


Figure 5.10: Electric field magnitude and lines (right side) and the net charge density and equipotential lines (left side) for a positively applied lightning impulse voltage with +200 kV peak and 50 ns rise-time at $t=70$ ns.

One of the fundamental differences between positive and negative streamers is the temperature inside the streamer column. The temperature within the positive streamers does not exceed a few hundred K, even at extremely high voltages (Figure 5.6), while the temperature tends to rise quickly in the bubble shaped negative streamers even beyond the evaporation point of most liquid dielectrics such as transformer oil. This means negative streamers are mostly associated with gas bubble development, if they initiate. Experimental evidence agrees this finding of the model as imaging of streamers clearly shows that some bubbles develop within the negative streamers [8,18].

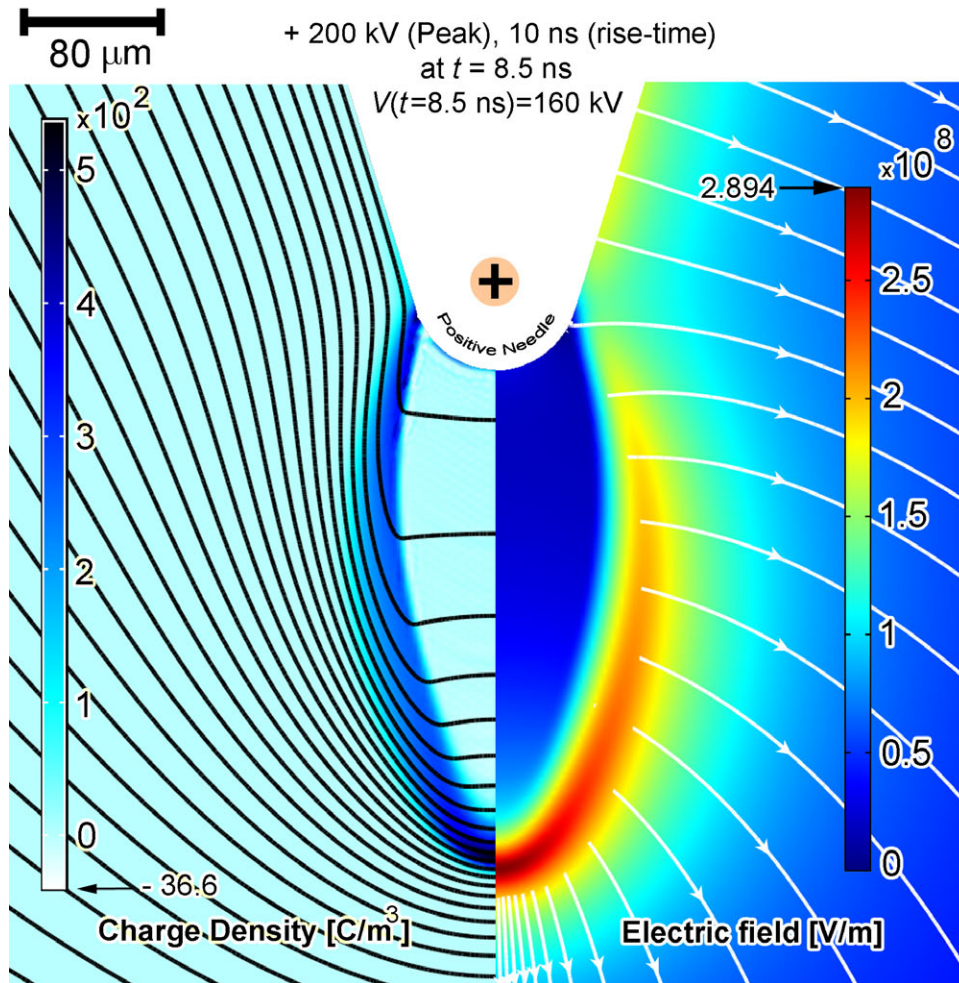


Figure 5.11: Electric field magnitude and lines (right side) and the net charge density and equipotential lines (left side) for a positively applied lightning impulse voltage with +200 kV peak and 10 ns rise-time at $t=8.5$ ns.

Steep rise of applied voltage (short rise-time) makes the positive needle electrode absorb the electrons in a larger area and create a more radially expanded ionized region (Figure 5.12) where the electric field is low. The ionized region acts like a conductor and affect the distribution of free net charge and electric field around and outside of it. In Figure 5.12, the area of ionization is larger (greater radius of curvature) and consequently the electric field ahead of the ionized region is smaller than Figures 5.10 and 5.11. Because ionized region in Figure 5.12 has a larger volume (greater radius of curvature), electric field ahead of ionized region is weaker (analogy of ionized body and a conductive body). Similar argument can be made for negative streamers where the negative needle affects large volume by repelling electrons in a larger space around the needle under steeper applied voltages (shorter rise-times) as can be seen in Figure 5.14.

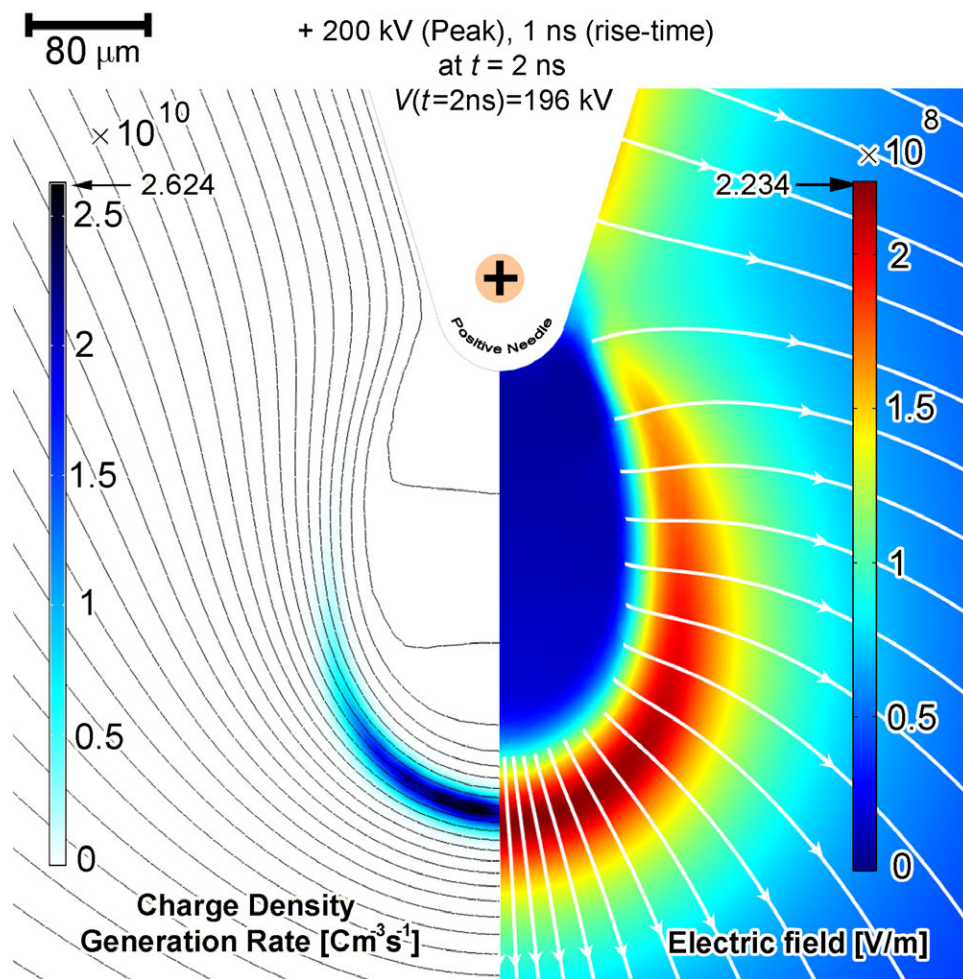


Figure 5.12: Electric field magnitude and lines (right side) and the net charge density and equipotential lines (left side) for a positively applied lightning impulse voltage with +200 kV peak and 2 ns rise-time at $t=2$ ns.

As shown in Figures 5.3–5.6 and 5.10–5.12, the diameter of the positive streamers gradually decreases when it elongates. The diameter reduction rate clearly depends on the applied voltage peak amplitude and rise-time. Figure 5.13 compares the positive streamer head radii of curvatures when the streamers travel a half-millimeter from the positive needle tip. It must be realized that the streamer head velocities, time instants, the instantaneous voltages are different for the cases shown in Figure 5.13, however, the positions of the streamer heads are identical.

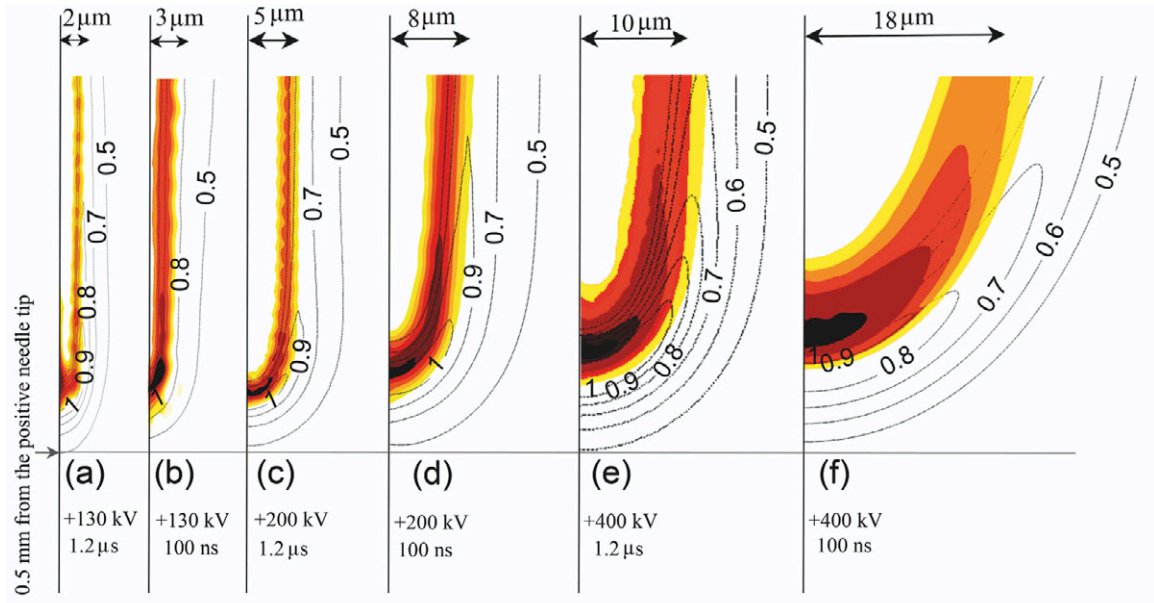


Figure 5.13: Volume charge densities and electric field distributions for different positively applied voltage peak amplitudes and rise-times. The pictures are shown for the instant times that the streamer heads travel half a millimeter from the needle tip. Space charge densities are shown as filled contours from $0.5|\rho_{max}|$ (the brightest color) to $|\rho_{max}|$ (the darkest color). Electric field contours are shown as black solid lines from $0.5|E_{max}|$ to $|E_{max}|$. The value of each contour is labeled on the curve as a fraction of $|E_{max}|$. The streamer head curvatures can be compared between streamers formed by (a): 130 kV with 1.2 μs rise-time: $|E_{max}|=3.1 \times 10^8$ V/m, $|\rho_{max}|=4.25 \times 10^3$ C/m³; (b): 130 kV with 100 ns rise-time: $|E_{max}|=2.9 \times 10^8$ V/m, $|\rho_{max}|=3.94 \times 10^3$ C/m³; (c): 200 kV with 1.2 μs rise-time: $|E_{max}|=2.9 \times 10^8$ V/m, $|\rho_{max}|=3.12 \times 10^3$ C/m³; (d): 200 kV with 100 ns rise-time: $|E_{max}|=2.8 \times 10^8$ V/m, $|\rho_{max}|=2.43 \times 10^3$ C/m³; (e): 400 kV with 1.2 μs rise-time: $|E_{max}|=2.6 \times 10^8$ V/m, $|\rho_{max}|=1.54 \times 10^3$ C/m³; and (f): 400 kV with 100 ns rise-time $|E_{max}|=2.4 \times 10^8$ V/m, $|\rho_{max}|=0.93 \times 10^3$ C/m³.

Similar comparisons are also performed for the negative streamers in Figure 5.14. Like positive streamers, increasing the applied voltage rise-time decreases the streamer volume over the same course of time. Comparing the right and left sides of Figure 5.14 also shows that increasing the negatively applied voltage rise-time also decreases the radial velocity of the ionized bubble, which decreases the chance of branching. It also can be seen that increasing the applied voltage peak amplitude has a similar effect on the negative streamer volume as decreasing the applied voltage rise-time.

Increasing rise-time of the negatively applied voltages also decreases the maximum ionization rate, G_{max} and its gradient. It is visible for streamers formed by -400 kV peak and 100 ns rise-time. Regarding the streamers formed by -600 kV and 100 ns rise-time, it must be noted that the ionization rate is slightly less than $0.5|G_{max}|$ for points closer than 0.1 to the needle which are not shown in Figure 5.14 to prevent confusion with a -400 kV, 100 ns negative streamer.

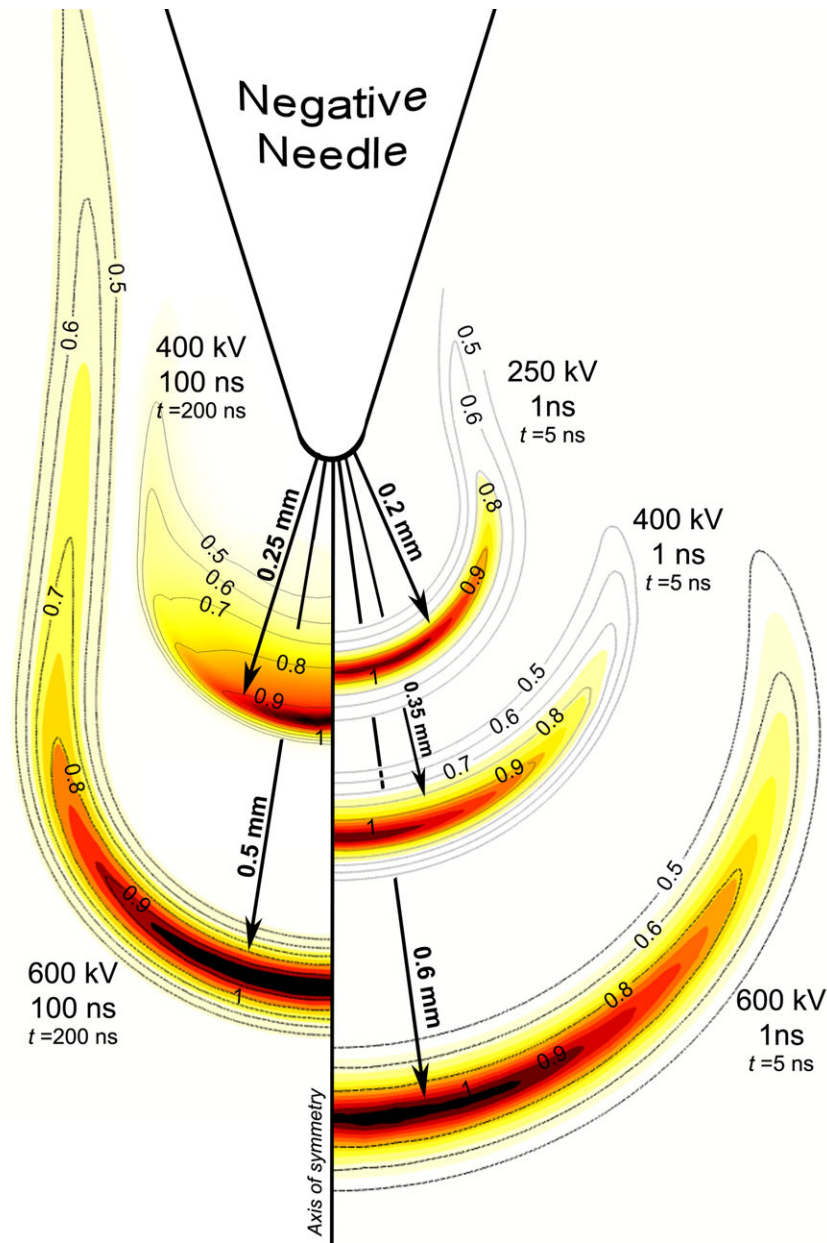


Figure 5.14: Electric field distributions and charge density generation rates for different negatively applied voltage peak amplitudes and rise-times. Space charge density generation rate, G_M are shown as filled contours from $0.5|G_{max}|$ (the brightest color) to $|G_{max}|$ (the darkest color). Electric field contours are shown as black solid lines from $0.5|E_{max}|$ to $|E_{max}|$. The value of each contour is labeled on the curve as a fraction of $|E_{max}|$. The approximate radius of an ionized bubble can be compared between different applied voltage peaks and rise-times: -250 kV with 1ns rise-time (upper right): $|E_{max}|=1.01\times 10^8$ V/m and $|G_{max}|=0.7\times 10^{11}$ $\text{Cm}^{-3}\text{s}^{-1}$; -400 kV with 1ns rise-time (middle right): $|E_{max}|=1.42\times 10^8$ V/m and $|G_{max}|=1.2\times 10^{11}$ $\text{Cm}^{-3}\text{s}^{-1}$; -600 kV with 1ns rise-time (bottom right): $|E_{max}|=1.75\times 10^8$ V/m and $|G_{max}|=6.21\times 10^{11}$ $\text{Cm}^{-3}\text{s}^{-1}$; -400 kV peak with 100 ns rise-time (upper left): $|E_{max}|=0.95\times 10^8$ V/m and $|G_{max}|=0.84\times 10^{11}$ $\text{Cm}^{-3}\text{s}^{-1}$; and -600 kV peak with 100 ns rise-time (bottom left): $|E_{max}|=1.15\times 10^8$ V/m and $|G_{max}|=1.21\times 10^{11}$ $\text{Cm}^{-3}\text{s}^{-1}$.

5.5.2 Streamer Initiation: Effects of Electrode Geometries

Once we started modeling different gap distances of needle sphere electrode geometry, we realized that the electric field maximum in the vicinity of the needle electrode is not determined by the gap distance, despite the intuitive expectations that come from simple calculation in the uniform gap. This fact, which has also been verified in the experimental records [15], suggests that the streamer initiation is not influenced by the gap distance [22]. Our model shows that the streamer initiation stage depends on applied voltage and the positive electrode geometry, not the gap length (in the gaps longer than 1 mm). Figure 5.15 shows the simulation results along with the data obtained from experiments [15]. This figure shows that the model agrees well with experimental records for the same gap distance. The results of the model for other gap lengths (i.e., 2 mm, 4 mm and 10 mm) are essentially within a narrow deviation from the results of a 6 mm gap, which shows that the gap distance does not play a key role in determining the streamer initiation voltage.

As can be seen in Figure 5.15, there is a lack of experimental data especially in the range between 200 μm and 500 μm tip radius of curvature in the work of Lesaint and Top [15] which leaves some of our modeling results not validated. They have also been unable to accurately measure the initiation delay and location [15].

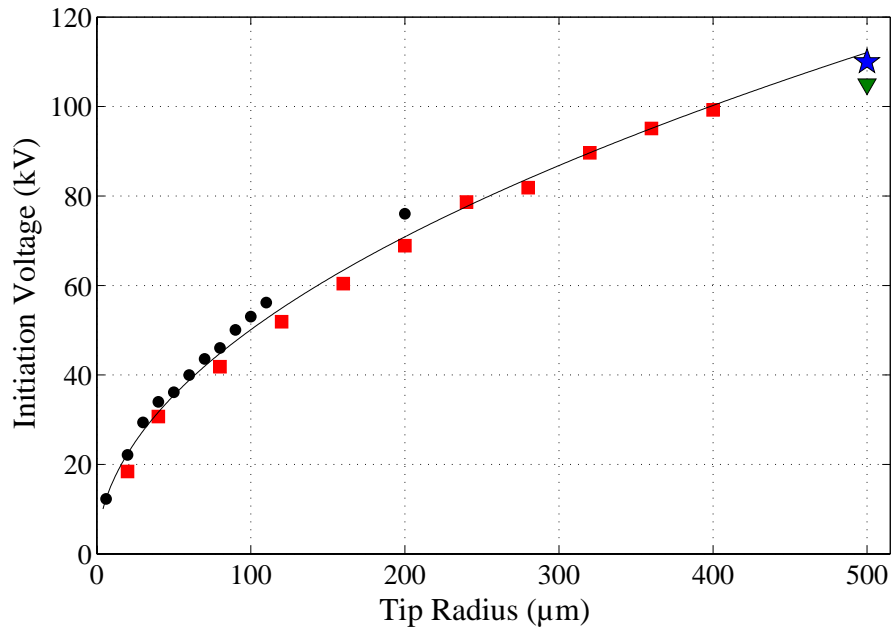


Figure 5.15: Experimental data for a 6 mm gap (\bullet), a 20 mm gap (\blacktriangledown), and a 50 mm gap (\star), all obtained from [15]. Modeling results for a 6 mm gap distance (\blacksquare). The solid curve, which is fitted to the modeling results, is $V_i = 10^{2.2} \sqrt{r_t}$, where r_t is the positive electrode tip radius in millimeters and the initiation voltage, V_i , is in kilovolts.

Although velocity and streamer head shape changes dramatically near the electrodes, streamers travel most of the electrode gap with an approximately constant head shape and velocity. We call this interval of streamer propagation the "stable interval". The velocity and the shape of the streamer in the stable interval are determined by the applied voltage and the gap distance, and the needle tip plays a minor role.

Figure 5.16 shows a set of different positive electrode tip sizes with the same gap distances and applied voltages. In Figure 5.16, although streamers arrive at the same distance from the needle tip at different times, the shape and the velocity of the streamers are almost identical. This shows that positive electrode tip radius does not affect the breakdown delay and voltage appreciably, unless it is either smaller than a few micrometers or larger than a tenth of the gap distance.

The effects of positive electrode radius of curvature, on time to breakdown and average streamer velocity are not appreciable since the eventual streamer column diameter and head curvature in the stable interval does not depend on the needle electrode size as can be seen in Fig. 5.16.

For the same gap distance and the same applied voltage, the streamer acceleration occurs at a farther point from the needle tip and after a longer delay with higher tip radii. This is particularly reasonable, since the electric field is weaker around a tip with higher radius of curvature. However, the electric field in the middle of the gap (far from the needle electrode) is relatively smaller with sharper needle, which reduces the streamer velocity in the stable propagation interval. In general, the breakdown delay, if available, is longer with sharper needle electrodes.

Grounded –or negative– electrodes do not contribute effectively in streamer initiation voltage. However, they play a major role in determining breakdown delay and breakdown voltage, as they are the eventual streamer targets. When the streamer reaches these electrodes, the breakdown is complete meaning that the current passing the electrode gap increases abruptly and dramatically. After this point, the plasma channel forms inside the electrode gap and the current streamer model is no longer valid to describe the dynamics of the produced arc.

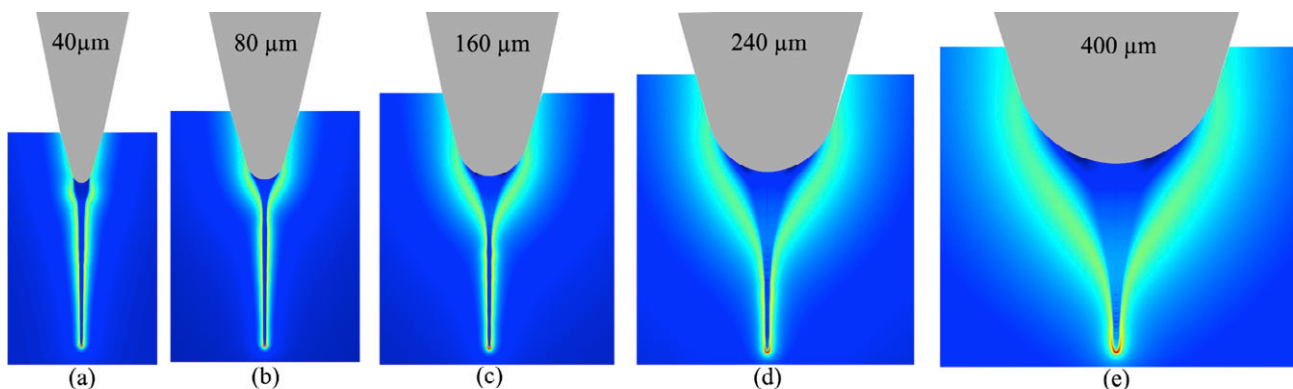


Figure 5.16: A set of different positive needle electrode tip sizes with the same gap distance and applied voltage, which is slightly above the initiation voltage for all of the positive electrode radii of curvature.

Figure 5.17 shows the electric field distribution at the grounded electrodes with different radii of curvature right after positive streamers (formed at the breakdown voltages) reach them. Smaller grounded electrodes collect higher currents before the breakdown occurs, since a small radius of curvature results in a higher electric field amplification and consequently higher ionization rate. Therefore, the grounded electrode can collect products of ionization around the grounded electrode even before the streamer reaches there. In addition, higher electric field at the grounded electrode, means a relatively lower electric field intensity exists in the middle of the gap. This is caused by the fact that the line integral of the electric field between electrodes is equal to the voltage drop across the electrodes. Since the electric field is extremely high near sharp electrodes, it has to be lower in the halfway point between electrodes. The lower electric field in the halfway point between electrodes decreases the streamer acceleration, which consequently reduces the breakdown probability. Therefore, breakdown occurs at higher voltages if the grounded electrode radius of curvature is relatively small. Velocity of the streamers in two different electrode geometries is reported in [49]. Unlike the positive electrode, the grounded electrode size does affect the streamer thickness. Especially at extra high voltages at which ionization rate is also significantly high near the grounded electrode. At breakdown voltage however, the effect of the grounded electrode is not significant as can be seen in Figure 5.17. The thickness of positive streamers, formed at breakdown voltage, when they reach the grounded electrodes is almost identical for different grounded electrode sizes.

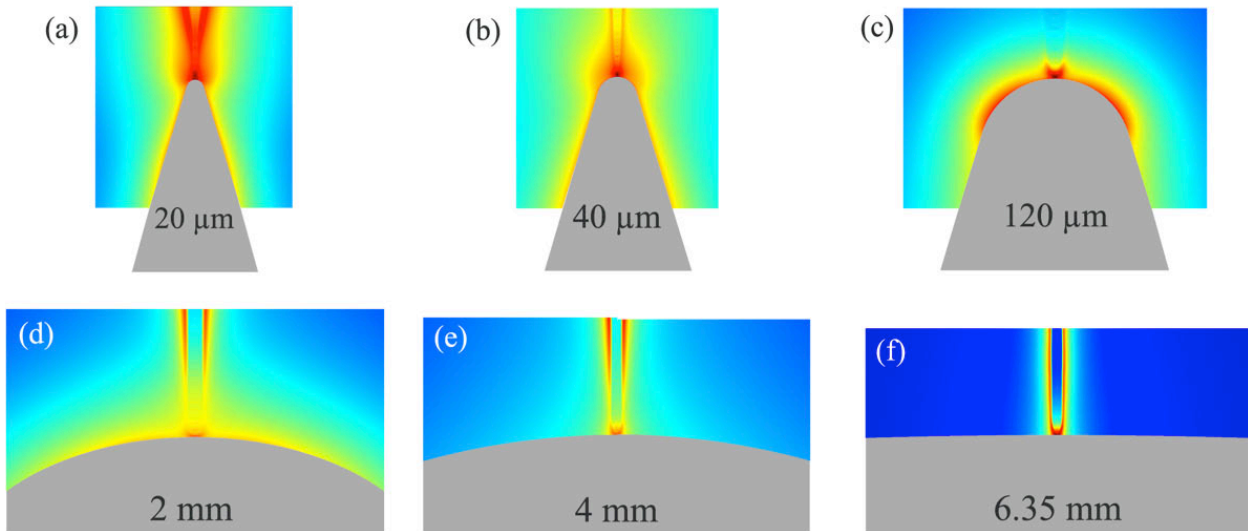


Figure 5.17: A set of different grounded tip sizes with the same gap distances and applied voltages. Ionization (high electric field) region is larger at sharper grounded electrodes.

5.5.3 Streamer Acceleration due to Re-ignition from Needle Electrode

Figure 5.18 shows the ESV, modeled as a rational function of electric field intensity that is adopted from semiconductor models [39, 96]. Field dependent ionization potential [48,49] is also

shown in Figure 5.18 as implemented in the model. The constant mobility model anticipates slower and faster electrons at lower and higher fields than 4 MV/cm, respectively, compared to the ESV model. Constant mobility of electrons, which is derived from measurements performed only at intense uniform electric fields [11,100], has been also used for low electric fields and highly divergent fields in the previous versions of the model [23,25,48] due to the lack of a comprehensive experimental record. The results of the ESV model match the empirical data of higher mode streamers in the literature more closely than the constant mobility model. Therefore, we argue that the ESV model describes the electron behavior at applied voltages above 400 kV more accurately.

Multiple values for the electron velocity saturation field, E_0 , have been tested to study the effects of this factor on streamer re-ignition phenomena. To keep velocity of the streamers formed at 4 MV/cm equal to 40 km/s, which has been experimentally observed [104], we changed the electron saturation velocity, v_0 , accordingly, for any value of E_0 as shown in Figure 5.18. The results indicate that the re-ignition does not occur unless the saturation field is smaller than a certain value, $E_0 = 0.651$ MV/cm (applied voltages up to 10 MV are examined). For saturation fields above this threshold, the higher applied voltage peak is required to reignite a positive streamer in a medium with higher saturation field, E_0 .

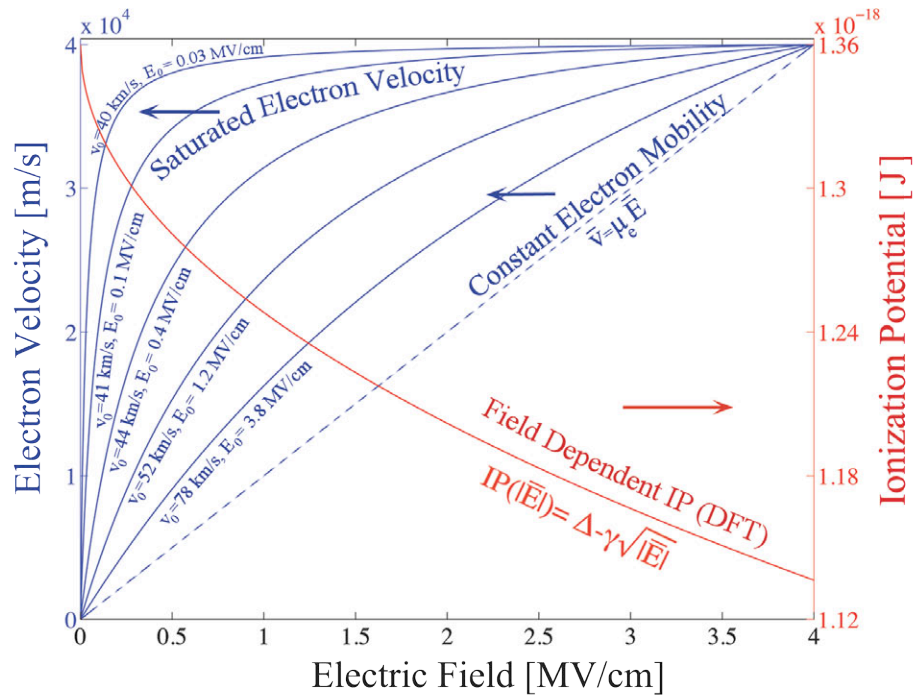


Figure 5.18: Electron velocity models and ionization potential (derived by Density Functional Theory) as functions of electric field intensity, $v_e = v_0 |E| / (|E| + E_0)$. The numerical values of parameters of the saturated electron velocity are labeled on the curves and ionization potential constants are set as $\Delta = 1.36 \times 10^{-18}$ J, $\gamma = 1.118 \times 10^{-22}$ Jcm^{1/2}V^{-1/2}. Values $v_0 = 41$ km/s, $E_0 = 0.1$ MV/cm is used in [2,3].

Since the electron velocity is limited at intense electric fields (ESV model), electrons are no longer capable of keeping the volume within the streamer column almost electrically neutral as the electric field intensity increases near the needle electrode. Therefore, a secondary ionization front initiates from the needle electrode and propagates at a much higher speed compared to the main streamer front in the track of the streamer column until it catches up with the main front when the collision happens. After the collision of the fronts, the streamer velocity increases approximately by a factor of two, since the volume charge density at the streamer head becomes about two times higher after collision. Figure 5.19 compares the results obtained from the ESV and the constant mobility models. The ESV model predicts lower streamer velocity compared to the constant mobility model for the applied voltage amplitudes lower than 400 kV.

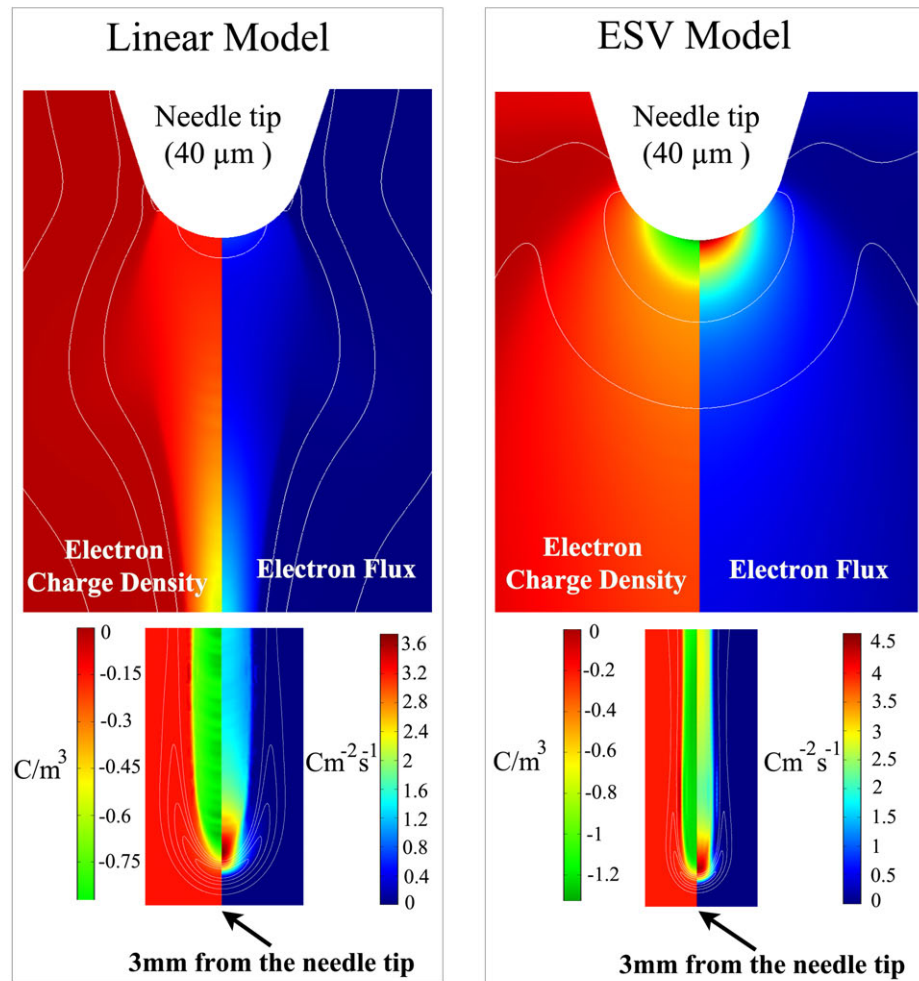


Figure 5.19: Electron charge density and flux distributions obtained by the ordinary model with constant electron mobility (left panel) and the ESV model (right panel) under a similar applied voltage with 500 kV peak and 100 ns rise-time. Each panel shows two frames of the streamer, i.e., the stem of the streamer (which attaches to the needle electrode tip) and the streamer head. Both streamer heads are at the same distance from the needle tip, but at slightly different time instants (after 0.6 μs for the linear model with constant electron mobility and after 0.57 μs for the ESV model).

For applied voltage magnitudes above 400 kV, a great amount of charge density forms inside the main streamer column caused by the high electric field due to the lack of electron velocity outside the streamer column. Figure 5.20 shows that this significant amount of charge propagates inside the streamer column towards the original streamer head. An abrupt jump occurs in the streamer velocity for 400 kV applied voltage amplitude after about half a microsecond due to the collision of the main and secondary streamer fronts (as seen in Figure 5.21).

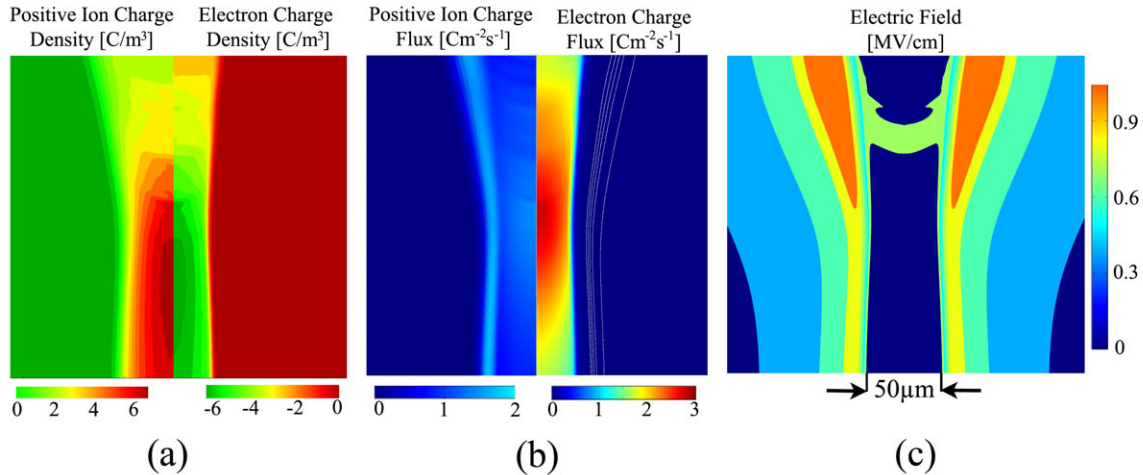


Figure 5.20: Charge carrier density (a), flux (b) and electric field distribution (c) obtained from the ESV model approximately 2 mm from the needle electrode tip while the streamer head is 5 mm from the needle tip under an applied voltage with 500 kV and 100 ns rise-time. Due to the electron velocity saturation, the electron and ion charge density do not quite cancel. Therefore, a secondary frontier of electric field is created inside the streamer column. In the case of $E_0=0.1$ MV/cm, this secondary frontier propagates at a slow pace, however, for smaller E_0 , the secondary frontier can propagate much faster and even collide with the main frontier (streamer head front).

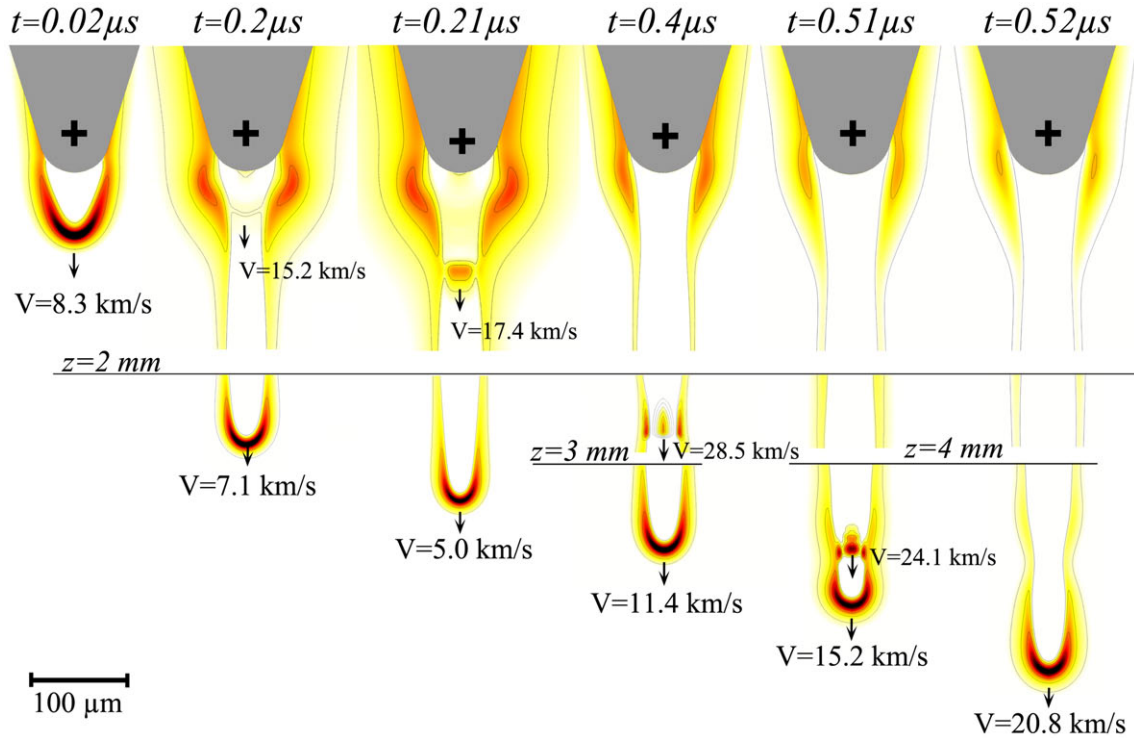


Figure 5.21: Electric field distributions in the range of $0.5|E_{\max}|$ as the brightest color to $|E_{\max}|$ as the darkest color for positively applied impulse voltages with $0.1\mu\text{s}$ rise-time and 400 kV peak amplitude. The values of $|E_{\max}|$ at $z=0$, $z=2\text{ mm}$ and $z=3\text{ mm}$ are 3.24 MV/cm , 3.46 MV/cm and 3.58 MV/cm (except at $t=0.52\mu\text{s}$ that is 4.27 MV/cm), respectively. The velocity of the streamer front is approximately doubled after collision.

Figure 5.22 compares the normalized length of the streamers for different applied voltage amplitudes, through which the significant jump in streamer velocity is evident. Error-bars in Figure 5.22 show the range of results obtained by each of the artificial streamline diffusions (anisotropic, compensated streamline upwind Petrov-Galerkin and Galerkin least-square methods) to solve the charge continuity equations.

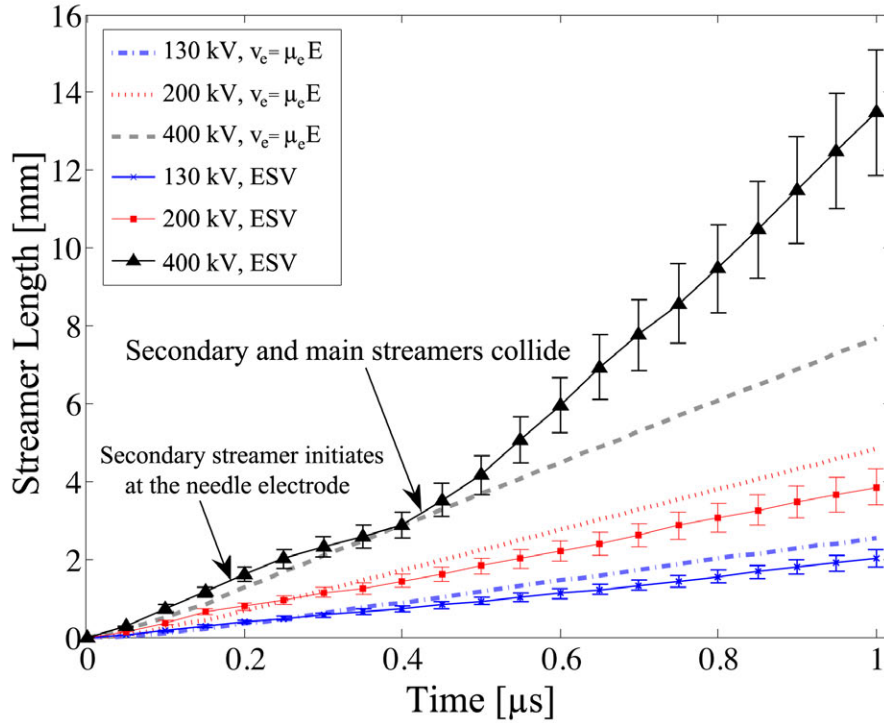


Figure 5.22: Normalized length of the streamers for different applied voltage amplitudes. Dashed lines show the results of the constant electron mobility model adapted from the reference [48] and the solid lines show the ESV model results. Streamers accelerate abruptly under impulse voltages with higher amplitudes than 400 kV in the ESV model. The sudden acceleration happens exactly when the main and secondary streamer fronts collide. Error-bars show the range of results obtained by each of the artificial streamline diffusions (anisotropic, compensated streamline upwind Petrov-Galerkin and Galerkin least-square methods) to solve the charge continuity equations.

As stated earlier, the re-ignition does not occur unless the saturation field is smaller than a certain value, $E_0 = 0.651$ MV/cm (applied voltages up to 10 MV are examined). For saturation fields above this threshold, the higher applied voltage peak is required to reignite a positive streamer in a medium with higher saturation field, E_0 as shown in Figure 5.23.

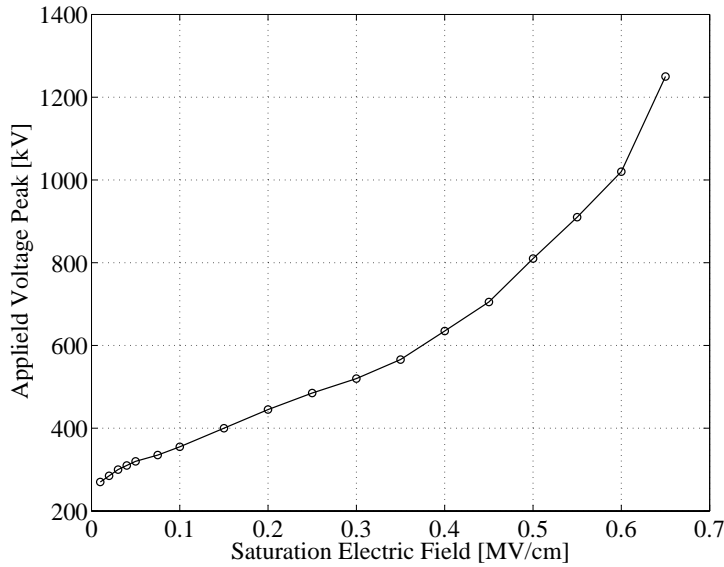


Figure 5.23: Minimum applied voltage peak required for reigniting a positive streamer from the needle electrode placed 25 mm from a grounded sphere electrode against saturation electric field, E_0 . For saturation fields above 0.651 MV/cm no re-ignition is observed (applied voltage peaks up to 10 MV are examined).

5.5.4 Breakdown Completion: Effects of Gap Distance and Electrode Geometries

Streamers, as the main cause of electric breakdown, emanate from an electrode, propagate through a transformer oil based liquid dielectric volume and eventually reach a grounded electrode. The electric field intensity just close to the electrode surface is higher around the points with smaller radius of curvature that is particularly true for a needle electrode defined by the IEC 60897 [66]. This does not necessarily mean that the streamer breakdown occurs at lower voltages in a needle-needle gap rather than the needle-sphere electrode geometry. A positive sharp needle electrode assists the streamer initiation. However, if both electrodes are needles, the electric field in the middle of the gap will be relatively lower than what would be the case for the corresponding needle-sphere electrode gap distance. This is caused by the fact that the line integral of the electric field between electrodes is equal to the voltage drop across the electrodes. Since the voltage distributions across the two electrode configurations are different, and the electric field is extremely high near the needle electrode, it has to be lower in the halfway point between needle electrodes. The lower electric field in the region around the halfway point between two needle electrodes decreases the streamer acceleration, which consequently reduces the breakdown probability. Hence, the breakdown in the needle-needle electrode geometry occurs at higher voltages compared to the needle-sphere electrode geometry as shown in Figure 5.24. The velocity of the streamers in different electrode geometries and gap distances can be derived from the streamer head trajectories along the shortest line that connects electrodes (on the axis of symmetry) as shown in Figure 5.24. For the same applied voltages and gap distances, the average velocity is higher in the needle-sphere geometry. Specifically, the streamer velocity and acceleration toward the grounded sphere electrode increases earlier than in the grounded needle. On the other hand, the maximum instantaneous velocity and acceleration of the streamer is higher

when it propagates toward the grounded needle electrode. The trajectories of streamers in gaps ranging from 1 mm to 10 mm fit closely to polynomial and exponential functions for needle-sphere and needle-needle geometries, respectively, as shown in Figure 5.24.

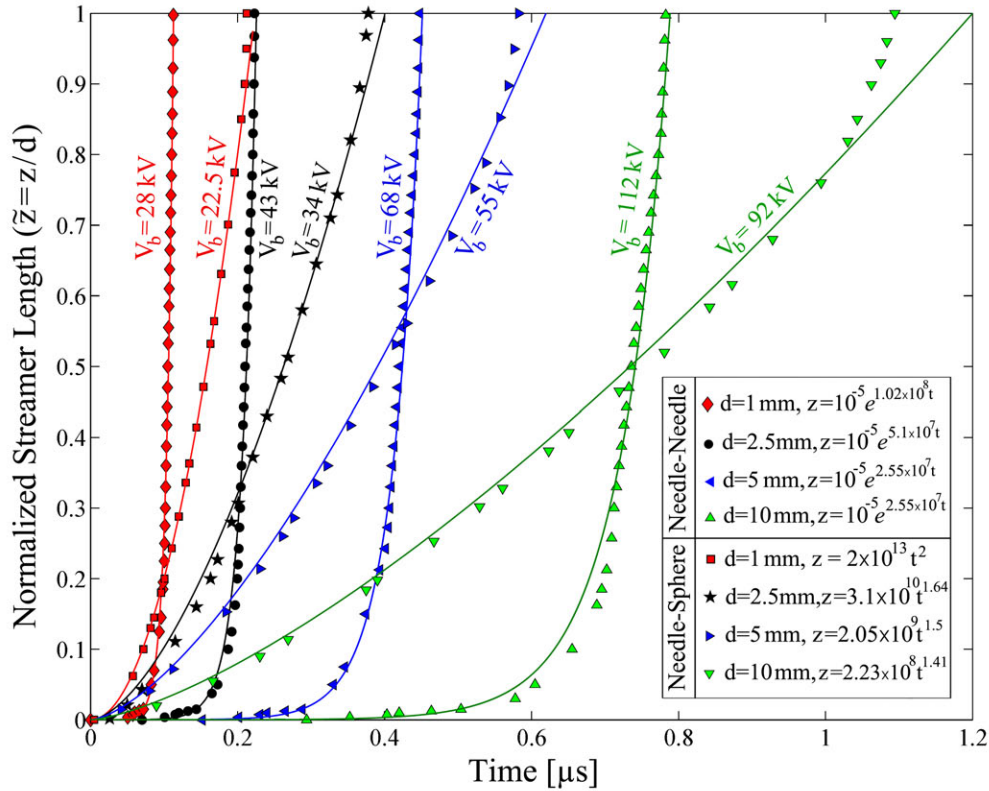


Figure 5.24: Normalized length of the streamers for different electrode geometries and gap distances at breakdown voltages. Breakdown voltage is the minimum impulse voltage amplitude at which the streamer is able to reach the ground electrode and consequently breakdown occurs. The streamer lengths are fitted with exponential and single term polynomial curves for needle-needle and needle-sphere geometries, respectively. Streamers require higher impulse voltage amplitudes to reach the grounded needle electrodes. The streamer velocity clearly increases when the streamer approaches the grounded electrode at $z=d$.

Results show that the probability of breakdown will increase significantly if the applied impulse voltage is able to elongate the streamer within the last ~10% of the gap from the grounded sphere electrode and the last 20% of the gap from the grounded needle electrode. The reason is that the streamer acceleration respectively increases within the 10% and 20% of the gap distance from the grounded sphere and needle electrodes (as shown in Figure 5.24).

Figure 5.25 shows the streamer head shapes and positions until they reach the grounded sphere electrode (panels a, b, c, d) and the grounded needle electrode (panels e, f, g, h) for a 10 mm gap distance. The minimum applied voltage amplitude at which a streamer initiates from the positive needle (initiation voltage) is 11 kV for the needle-sphere and 17 kV for the needle-needle electrodes, 10 mm apart. Streamers formed by the initiation voltage do not necessarily reach the grounded electrode, and therefore, do not lead to breakdown. If the applied voltage amplitude is greater than the initiation voltage but lower than the breakdown voltage, it creates streamers whose accelerations drop at some point (depending on the voltage amplitude) before it reaches the grounded electrode. As soon as the streamer slows down, the volume charge created by ionization along the streamer path starts to diffuse through the oil bulk. However, at voltages higher than the breakdown voltage, the streamer eventually reaches the grounded electrode as shown in Figures 5.24 and 5.25.

The streamer column diameter and head radius of curvature are about 50% higher in the needle-sphere geometry than the needle-needle geometry (Figure 5.25). From the experimental point of view, it is difficult to visualize the streamer head position to find out when it hits the grounded electrode. Instead, it is much easier to measure the current passing through the electrodes [2,102] that can be considered as another good criteria of breakdown occurrence [1,2]. Therefore, determining the terminal current greatly facilitates the validation of modeling results. To calculate the conduction current, we integrate and algebraically add up the total fluxes of all charge carriers on the grounded electrode surface, i.e., $\int(\rho_p\mu_pE_{\perp}+\rho_e\mu_eE_{\perp}+\rho_n\mu_nE_{\perp})ds$. The displacement current is essentially equal to the time derivative of the total surface charge on the grounded electrode that is evaluated over time by integrating the perpendicular component of the displacement field on the surface, i.e., $\partial/\partial t(\int D_{\perp}ds)$.

Displacement and conduction currents at the grounded electrodes are shown against time in Figure 5.26. The displacement component of the current is larger than the conduction current before the streamer reaches the grounded electrode. However, after breakdown occurs, the conduction current dominates.

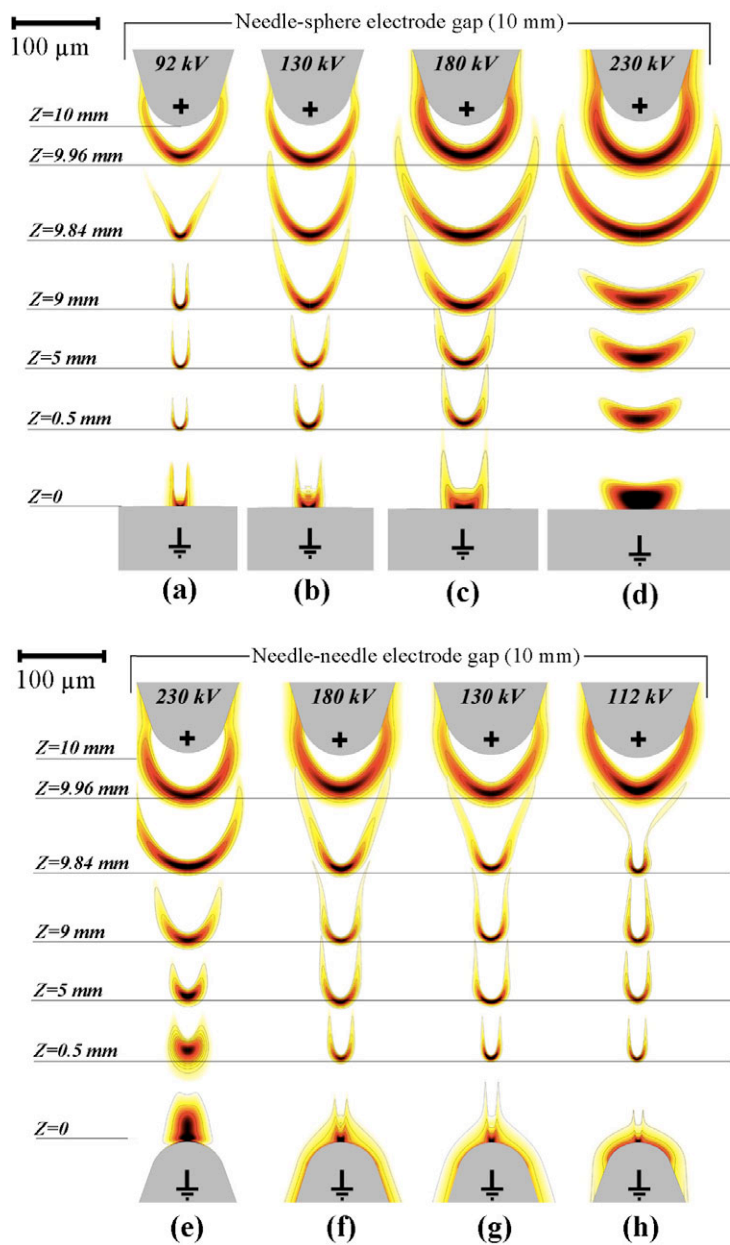


Figure 5.25: Streamer breakdown in needle-sphere (a, b, c, d) and needle-needle (e, f, g, h) electrode gaps, 10 mm apart. Streamers always emanate from the positive needle and eventually hit the grounded electrode. Electric field distributions are shown in the range of $0.5|E_{\max}|$, as the brightest color to $|E_{\max}|$, as the darkest color for positively applied impulse voltages with $0.1\mu\text{s}$ rise-time and different peak amplitudes. The values of $|E_{\max}|$ (for $0.1 < z < 9.9$ mm) and breakdown time are (a): 3.24 MV/cm, $1.092\mu\text{s}$; (b): 3.06 MV/cm, $0.564\mu\text{s}$; (c): 2.98 MV/cm, $0.328\mu\text{s}$; (d): 2.56 MV/cm, $0.212\mu\text{s}$; (e): 3.48 MV/cm, $0.244\mu\text{s}$; (f): 3.47 MV/cm, $0.377\mu\text{s}$; (g): 3.46 MV/cm, $0.648\mu\text{s}$; and (h): 3.48 MV/cm, $0.782\mu\text{s}$. The maximum electric field, $|E_{\max}|$, within 0.1 mm of electrodes is about 30% less. The trajectories of streamers are reasonably similar to Figure 5.25 and can be approximately scaled by the applied voltage amplitude (considering the time to breakdown).

The streamer charge flux and displacement field distribution determine the conduction and the displacement currents, respectively. The rising electric field cannot influence the conduction current if no charge carrier reaches the ground electrode. On the other hand, free charge carriers can indirectly affect the displacement current by changing the electric field (displacement field) distribution between electrodes. The electric field increases at the tip of the grounded electrode as the streamer approaches. However, the area at which electric/displacement field is increased by the approaching streamer is a small portion of the entire electrode surface (roughly, 0.01% and 0.1% of the grounded sphere and needle electrodes, respectively). In addition, while the electric field at the tip of the grounded electrode is increasing dramatically, the perpendicular component of the displacement field is slightly decreasing on other points of the grounded electrode surface particularly at distant points from the electrode tip. Therefore, the rise of the electric field at tip of the grounded electrode hardly affects the displacement current that decays semi-exponentially over time.

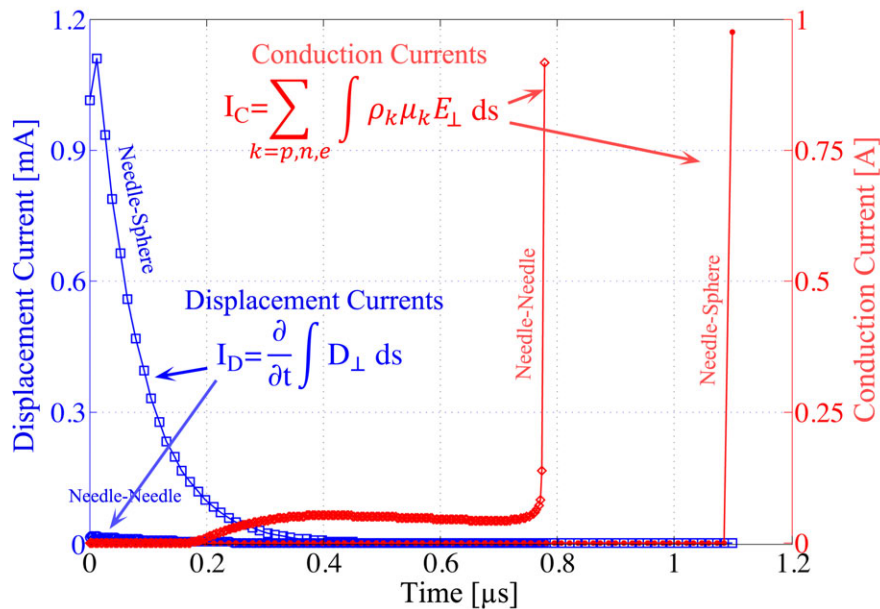


Figure 5.26: Grounded electrodes' displacement and conduction currents, through needle-needle and needle-sphere electrodes 10 mm apart at their own breakdown voltages, i.e., 112 kV and 92 kV, respectively. The displacement current rises abruptly just after application of an impulse voltage by the background electric field while conduction currents increase dramatically when the streamer hits the ground electrode at the times corresponding to $z/d=1$ in Figure 5.24 (for $d=10$ mm). The streamer charge influences displacement current indirectly, by changing the electric field distribution inside the gap. However, the effect of the streamer charge on the displacement current is not appreciable since the streamer engages a negligible portion of the electrode surface. An initial rise in the conduction current of needle-needle geometry is due to the intense electric field near the grounded needle that causes an appreciable ionization leading to a limited conduction current (~ 100 mA) until the streamer reaches the grounded needle.

Figure 5.27 shows the total current passing through the different gaps at breakdown voltages that are the sum of displacement and conduction currents. The time variations of total terminal current in Fig. 4 correspond to the streamer trajectories shown in Fig. 5.24. The dramatic rise of the breakdown current starts exactly at the instantaneous time that the streamer heads reach the grounded electrodes. As supporting evidence of breakdown, the current increases more than 10^8 fold in less than 30 ns for the needle-sphere electrode geometries and more than 10 fold in less than 20 ns for the needle-needle geometries.

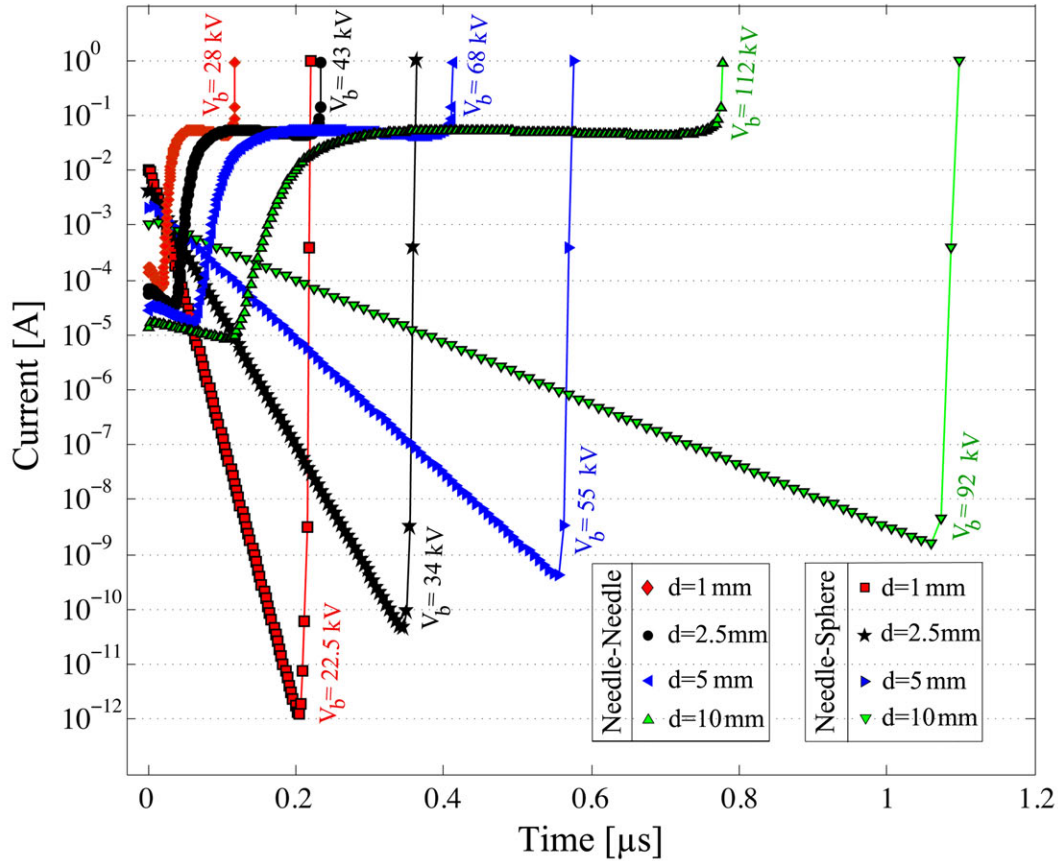


Figure 5.27: Grounded electrodes' total current (conduction plus displacement), through different gaps and geometries at their own breakdown voltages. The current rises dramatically when the streamer hits the ground electrode at the times corresponding to $z=d$ in Figure 5.24. Displacement current dominates the total current just after application of the impulse voltage. Semi-exponential attenuation of the displacement current suggests that the displacement current decay obeys the dielectric relaxation time dictated by the electrode geometry and dielectric properties. Both the initial magnitude and the decay rate of the displacement current toward the grounded needle electrode are smaller than the sphere electrode. This is consistent with their geometries since the area of the needle surface electrode is ~ 10 times smaller than the sphere electrode surface area. The conduction current dominates the total current as the streamer reaches the grounded electrode that leads to breakdown (dramatic rise of current).

The model is no longer complete when the current rises beyond a few amperes, since due to high power dissipation along the streamer path, the streamer will be replaced by a high current arc, which requires additional physics such as plasma formation, thermal, impact and photo ionization and fluid convection to be modeled. Figure 5.28 shows the breakdown voltage for different gaps and electrode shapes.

The equations of charge conservation for electrons and different ions have been numerically stabilized using three types of artificial streamline diffusions: anisotropic, compensated streamline upwind Petrov-Galerkin and Galerkin least-square in combination with crosswind diffusion artificial diffusion [71,75-78]. Error-bars in Figure 5.28 show the upper and lower bounds of the results obtained by each the artificial streamline diffusions. The breakdown voltage is always higher when the streamer travels towards a needle ground electrode compared to sphere electrode for the same electrode gap distances. At similar applied impulse voltage peak amplitudes, the breakdown delay is slightly lower in the needle-sphere electrode geometry.

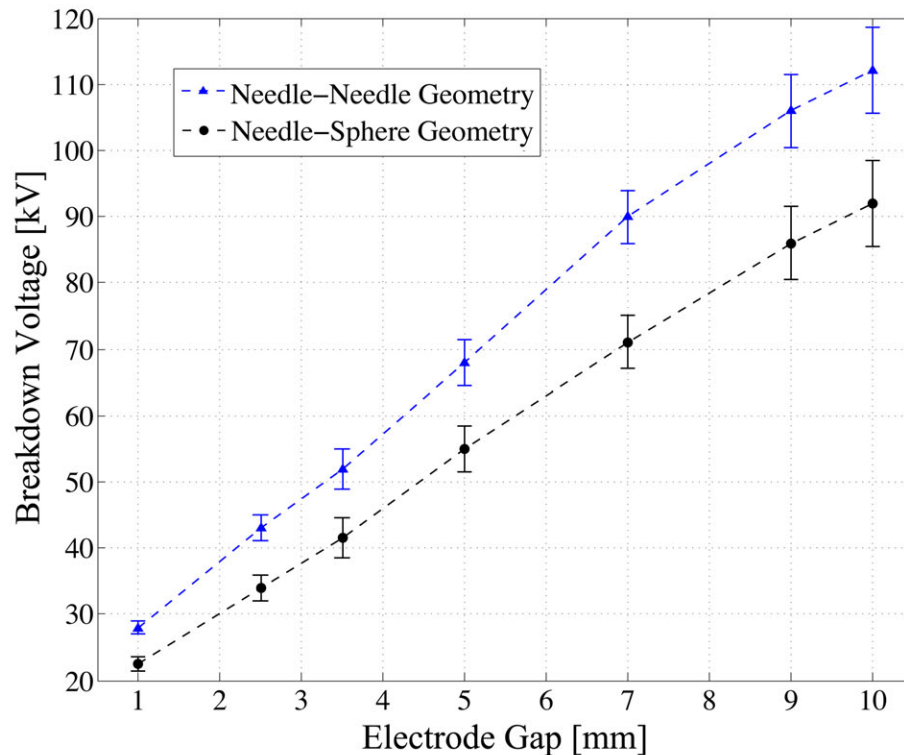


Figure 5.28: Predicted breakdown voltage for different gap distances. Error-bars show the range of results obtained by each of the artificial streamline diffusions (anisotropic, compensated streamline upwind Petrov-Galerkin and Galerkin least-square methods) to solve the charge continuity equations.

5.6 Summary

Mechanisms behind the positive and negative streamers formed by standard impulse voltages with different peak amplitudes and rise-times have been compared using an electro-thermal hydrodynamic model. Simulation results indicate that negative streamers demand higher peak voltages to initiate from a needle electrode.

Including the electric field dependence of ionization potential (derived using DFT) and electron velocity enabled the presented model to physically describe the higher streamer velocity and streamer column diameter under higher applied voltages. The model confirms that higher mode velocities do not take place until the streamer travels beyond 8~10 millimeters from the needle electrode as already observed in experiments.

Our model also indicates that the applied voltages with smaller rise-times form thicker streamer columns in liquid dielectrics, while applied voltages with longer rise-times create thinner streamers. Such effects have been reported from experiments on the streamer formed in gaseous media.

The effects of the electrode shapes on the streamer initiation, propagation and breakdown have been studied in this thesis. The modeling results indicate that the breakdown voltage is mainly dependent on the electrode gap length, while the needle electrode radius of curvature mostly determines the streamer initiation voltage. Accurate results have also been presented in this chapter for the pre-breakdown current flowing through the electrode gap.

The 2-D axisymmetric model is quite efficient and accurate. The major weak point of the presented model is the lack of data about effective electron mass, electron mobility and number of ionizable species in most liquid dielectrics, especially, in electrically stressed transformer oil.

Three-dimensional Electrohydrodynamic Modeling of Streamer Development and Branching in Dielectric Liquids

Streamer branching is driven by stochastic and deterministic factors. So far, all the discussions presented in this thesis have dealt with deterministic attributes of streamers. In this chapter, it is explained how stochastic parameters are also included in the model for completeness. Inevitable stochastic causes of streamer branching, such as inhomogeneities inherited from noisy initial states, impurities and charge carrier density fluctuations, are added to a three-dimensional version of the streamer model introduced in Chapter 5.

Streamer branching plays a significant role in streamer propagation as it dramatically changes the streamer velocity magnitude and direction. Since after branching more streamer branches are born with usually higher velocity (in different directions), it reasonably increases the risk of breakdown. Therefore, stochastic branching cannot be ignored in the dynamics of streamer propagation.

A fully three-dimensional (3-D) streamer modeling presented in this chapter indicates that the deterministic origins of branching are also intrinsic attributes of streamers, which in some cases make the branching inevitable, depending on shape and velocity of the volume charge at the streamer front. Based on the modeling results for streamers propagating in a liquid dielectric, a gauge on the streamer head configuration is introduced that determines whether the branching occurs under particular inhomogeneous circumstances. Estimated number, diameter and velocity of the born branches agree qualitatively with published experimental images of the streamer branching.

6.1 Spatial Inhomogeneities: Stochastic Origins of Branching

It is traditionally thought that stochastic inhomogeneities inherited from noisy initial states, impurities or charge carrier fluctuations are the main cause of streamer branching [1,2]. Our fully three-dimensional model of streamers, however, shows that the branching also has deterministic origins, which in some cases make the branching inevitable depending on shape and velocity of the volume charge at the streamer head. Specifically, if the volume charge layer at the streamer head is thin and slow enough, even an infinitesimal inhomogeneity can effectively trigger the branching. On the other hand, if the streamer head is stable enough, even relatively large perturbations cannot grow instabilities from the streamer head.

Initiation of streamer branching requires a finite perturbation [19,29,30]. If there is absolutely no perturbation around the streamer head, which is practically unlikely, in some situations, the propagation of the streamer in a single column becomes impossible, i.e., the streamer head becomes bushy and the propagation velocity drops significantly due to the shielding effect of the volume charge [25,48]. This has been observed in the presented two-dimensional (2-D) model (described in chapter 5), as 2-D models of streamer with cylindrical symmetry normally suffer from a lack of asymmetric perturbations especially at a high level of applied voltage peak [25]. In such cases, a 2-D streamer model simply fails to evaluate the streamer development accurately. Required perturbations in practice can be inherited from inhomogeneous initial states (such as an initial electron density fluctuation [29]), macroscopic impurity perturbations (such as dust particles, air bubbles, water droplets, or other macroscopic objects [19,37]), or variations of dielectric densities or molecule alignment [60].

6.1.1 *Visible Macro-Inhomogeneities*

Visible (macroscopic) perturbations as causes of streamer branching in liquid dielectrics are less interesting than microscopic inhomogeneities from a modeling point of view for two main reasons. First, macroscopic perturbations essentially modify the extent of the streamer by strongly attracting the streamer towards the inhomogeneities, and second, in industrial applications (as well as laboratory environments declared by standards) any kind of macroscopic impurities is avoided. In these circumstances, the cause of the branching is definitely not the macroscopic perturbations, since laboratory experiments for instance are undertaken in degassed chambers in which the liquid dielectric is filtered several times to eliminate any ionized traces and gas bubbles. In these experiments, the streamers grow in a continuously refreshed body of liquid dielectrics. A similar scenario is the case for transformer oil insulated large devices such as power transformers [3,18,60].

Our 3-D modeling results show that macroscopic inhomogeneities (larger than 10 μm) dominantly determine the branches' structure and velocity. Macroscopic perturbations, which are rare in practice [60], appreciably decrease the sensitivity of branching dynamics to the applied voltage and even geometry of the electrodes. Most of the experimental references of this thesis do not include large inhomogeneities, therefore the results obtained from the microscopic inhomogeneities reasonably match better with respective experimental records.

6.1.2 *Stochastic Micro-Inhomogeneities*

Our 3-D modeling results show that microscopic inhomogeneities (smaller than 10 μm) initiate streamer branches in liquid dielectrics whose characteristics clearly resemble their parents. Verification of the modeling results presented in this chapter with experimental images indicate that the inhomogeneities smaller than 10 μm accurately predict the streamer branching in the laboratory environment. Therefore, throughout this chapter, the streamer branching driven by microscopic inhomogeneities (smaller than 10 μm) is presented.

6.2 Three-Dimensional Modeling of Streamer Initiation and Branching

The complex nature and structure of liquids has inhibited the development of a comprehensive streamer theory in the liquid state. Understanding of basic processes (e.g., ionization, electron transport) and the complex phenomena (e.g., streamer branching) in liquids is derived by utilizing theories from both the solid-state or compressed gas-state [31-36]. Streamer research in the gas-state, in particular, is usually one step ahead of the liquid-state. For instance, the ionization mechanisms are well known in a gas state (both low and high pressure gases) [88], while in liquids, due to lack of independent research, we have to incorporate a solid-state ionization theorem [87]. Specifically, over the last two decades, the research on gaseous dielectrics has determined the mechanisms behind streamer propagation and branching [31-36].

Significant improvements in advanced stereo-photography of streamers [32] have also been used as an enabling tool to investigate the main origins of streamer propagation and branching in gases. Experimental photography of streamers in liquid dielectrics, on the other hand, has proven more difficult over the years [3,10,60]. Therefore, numerical modeling seems to be an appropriate alternative for rendering understandable three-dimensional images that reveal the main causes of streamer branching as they have been successfully used for gaseous media before [31].

As seen in Chapter 5, streamers in liquid dielectrics are thin fast elongating structures with semispherical heads that form in regions of dielectric that are ionized by intense electric fields (on the order of 1 MV/cm for transformer oil) [3,10]. It was also shown in Chapter 5 that streamer heads propagate as ionization waves with velocities much higher than the maximum drift velocity of electrons [48]. Therefore, the inherently three-dimensional streamer structure makes them easily branch out and become asymmetric once they encounter any spatial perturbation. This section presents the developed 3-D streamer modeling approach, which is capable of incorporating spatial inhomogeneities (explained in section 6.3)

Modeling of streamer branching is attractive amongst many different disciplines due to its complexity and importance in discharge physics [19, 29-40, 60]. Some of the examples of the most effective modeling and analytical approaches are fractal morphology of streamer trees [17], conformal mapping [30], electro-hydrodynamic modeling with or without cylindrical symmetry [19,37], a moving boundary approximation [30], particle models [31], macroscopic inhomogeneities [19], realistic fluctuations [29], slow branching in deterministic fluid models [31,32], multiphase fingering driven by small signal interfacial waves [84,85]; each revealing important aspects of the streamer branching. However, none of these studies is capable of giving a thorough answer to the question of how and to what extent deterministic and stochastic elements contribute to the streamer branching. This paper presents a fully three-dimensional (3-D) model that enables us to investigate stochastic and deterministic causes of the streamer branching. Figure 6.1 compares a properly taken experimental image of a streamer tree formed in a liquid dielectric [16], with a corresponding result of our model, obtained under reasonably similar conditions of dielectric medium, gap distance, electrode geometry and the applied voltage. The streamer branch diameters from optical measurements is estimated to be about half of the electrodynamic

diameters, as the model describes [6]. The calculated streamer column diameters, number of branches and the angle between branches meaningfully resemble the experimental image.

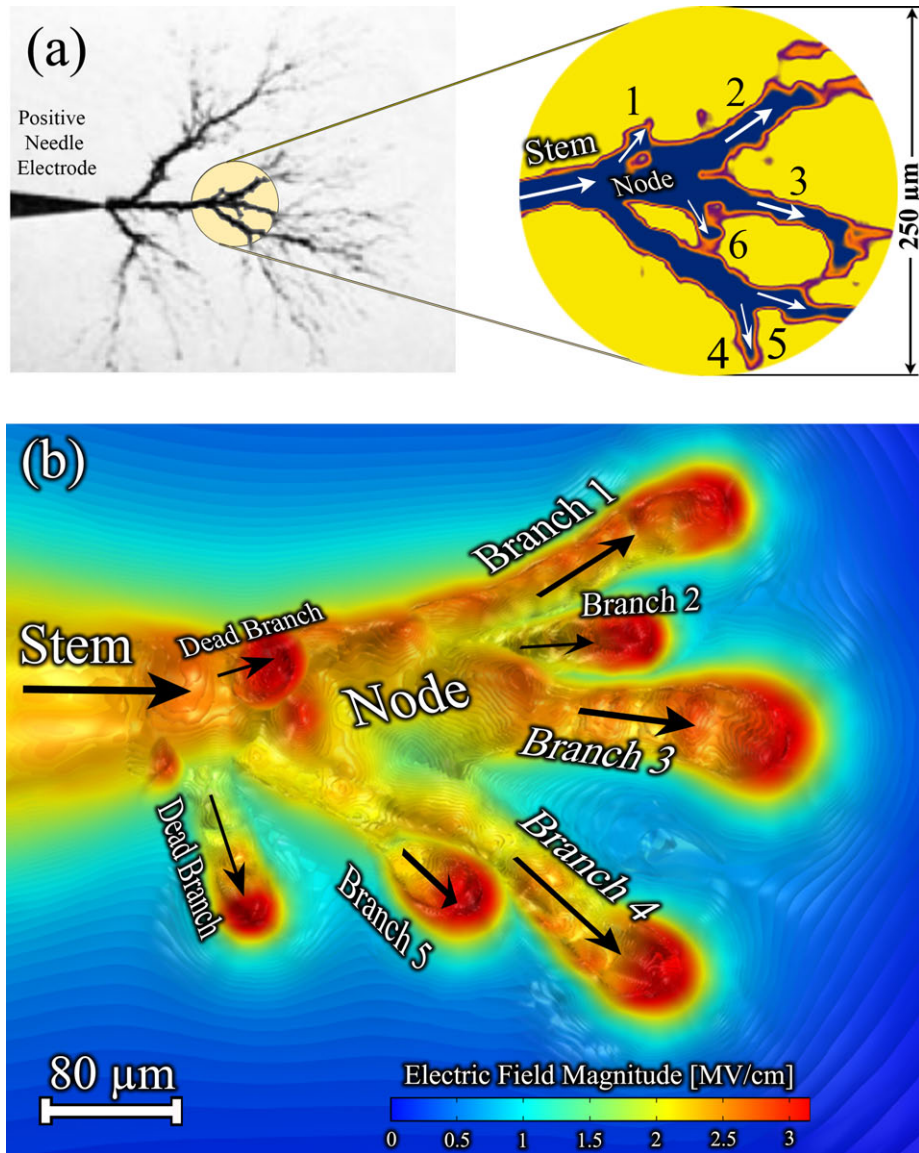


Figure 6.1: Typical view of positive streamer branching in a liquid dielectric, (a) experimental image of a positive streamer initiated from a needle electrode [16] and, (b): 3-D modeling result of a corresponding case (iso-surface plot of the electric field distribution). The streamer structures are qualitatively similar in experiments and simulations. The fractal structure of the streamer tree in the experimental image makes it possible to compare the modeling result also with other nodes of the tree including the one at the needle electrode tip.

The focus of this chapter is on the streamer branching in transformer oil; however, the model and its results can be generalized to other dielectric media. The effects of the applied voltage peak (up to five times larger than 50 percent breakdown voltage, U_{BD} [48]), rise-time (from 1 ns to 0.1 μ s),

the electrode geometry and gap distance are investigated on the shape of the streamer tree, the number, diameter, and velocity of the branches in the IEC needle-sphere electrode geometry (as shown in Figure 5.1). Post processing of the results indicates that there is a clear correlation between the characteristics of the main streamer stem (also known as leader in the literature) just before branching and the attributes of the born branches. This correlation is discussed with details in section 6.5 as deterministic causes of branching.

Theoretically, streamers can branch in fully deterministic models through Laplacian instability that resembles the underlying mechanism of viscous finger branching of a two-fluid Hele-Shaw flow [29] or in an electro-hydrodynamic version of Rayleigh-Taylor instability with superposed charge layers [84,85]. Such instabilities can develop when the volume charge layer ahead of the streamer front is much thinner than the streamer head radius of curvature. In the extreme case of a planar ionization front, an infinitesimal perturbation is enough to initiate a branching instability [6], but for a semi-spherical streamer head with a finite radius of curvature, a minimum magnitude of perturbations is required to trigger a self-sustaining streamer branch.

In practice, even in a carefully filtered ambient, microscopic perturbations are still present. Most of these microscopic inhomogeneities can be categorized into two main classes: 1) perturbations on the spatial properties of material (presumably permittivity) and 2) fluctuations of the charge carrier density or the ionization potential [48]. We have incorporated both of these inhomogeneous cases into the modeling. In applications that are of interest in industry, the macroscopic inhomogeneities inside dielectrics are usually avoided unless breakdown is desirable. Previous studies show that the macroscopic perturbations such as air bubbles or water droplets certainly deviate the streamer paths and most probably initiate the branching. In this thesis, we focus on microscopic inhomogeneities, which are more complex and also are much harder to avoid even in extremely purified media used for electric power insulation, such as transformer oil or SF₆.

Our 3-D electro-hydrodynamic model is built upon the previously developed two-dimensional (2-D) streamer model [41-53], which successfully explained numerous aspects of streamers, except for the branching phenomena (see Chapter 5). The governing equations are based on the drift-dominated charge continuity equations (5.1)-(5.3) for positive ion (ρ_p), negative ion (ρ_n) and electron (ρ_e) charge densities, coupled through Gauss' law (5.4). The thermal diffusion Eq. (5.5) is included to model temperature variations (T) in oil due to Ohmic dissipation. The negative ion and electron charge densities in the governing equations are both negative quantities. The governing equations have been solved using a finite element approach [71].

The same representative values for transformer oil as listed in Table 5.1 have been used in the 3-D modeling (throughout this chapter). Similar boundary conditions as the 2-D model (Chapter 5) are applied to the 3-D model. For instance, the electrode potential is defined by subtracting two exponential functions that create the standard lightning impulse voltage according to IEC 60060-1 [27] (see Figure 5.2).

Since diffusion of the charged species is assumed negligible in equations (5.1)-(5.3), the conservative form of the general convection and diffusion equations have been solved with 3-D

triangular quartic elements [71]. Numerical solutions of the charge continuity equations usually include spatial instabilities rather than expected smooth solutions [75-78]. These spurious oscillations have been avoided by using the artificial nonlinear crosswind diffusion (CWD) along with different types of streamline diffusion (SD) such as anisotropic, compensated streamline upwind Petrov-Galerkin (SUPG) and Galerkin least-square methods to stabilize the charge continuity equations [71]. It has been shown in [48], that CWD is more stable than other over-diffusive discontinuity-capturing techniques and leads to better numerical behavior, although it is computationally expensive due to its non-linear nature [71]. On the other hand, SD techniques effectively stabilize the system and accelerate the solution. We have applied minimal SD and CWD at the same time to optimally stabilize the numerical solution. Minimal artificial diffusion techniques are tuned to balance a tradeoff between removing nonphysical local oscillations (due to SD) and excessively smooth results just next to the walls (due to CWD). An average has been taken whenever any discrepancy is observed between results of different SD techniques mentioned above.

Two direct solvers, MUMPS and PARDISO implemented in COMSOL Multiphysics are employed separately to solve the streamer model. These solvers are well known to be robust and memory efficient tools in parallel high performance computing [71]. These direct solvers have the advantage of more accuracy compared to iterative solvers, although they are computationally much more expensive. Since the present model contains nonsymmetrical matrices and nonlinear equations, combinations of direct and iterative solvers have been applied to speed up the solution. Three computers with a total 48 cores (~3.4 GHz) and 188 GB RAM are used in parallel to solve equations (5.1)-(5.8) for the 3-D electrode geometry.

Figure 5.1 shows the discharge chamber geometry for which we performed the streamer modeling. To verify our modeling results, we have used experimental results from a needle-sphere electrode geometry with other different gap distances. As discussed in [49], with the same electrode geometry, if the ratio of the applied voltage peak over the gap distance is similar, the characteristics of streamers will be comparable.

6.3 Numerical Implementation of Stochastic Inhomogeneities

The stochastic aspect of the streamer branching pertains to the spatial distribution, size and intensity of the inhomogeneities. Therefore, the key role of stochastic inhomogeneities has to be included in the model in order to observe the streamer branching.

As discussed earlier, macroscopic inhomogeneities are avoided in industrial applications and laboratory environments. Therefore, in this chapter, implementation of microscopic inhomogeneities in the 3-D streamer model is described, as they are usually considered more interesting from a modeling point of view.

The stochastic nature of the streamer branching cannot be expressed in equations (5.1)-(5.8), as they only cover macroscopic quantities and processes. Rather, we define and add a finite number of spherical regions (particles) whose stochastic location and intensity convert the equations (5.1)-(5.8) into a stochastic model.

To implement stochastic perturbations in the model, we have used continuous uniform distribution functions (rectangular probabilistic functions) and Gaussian functions to determine the location and intensity of individual perturbations, respectively. Specifically, a set of spherical regions with certain radii (R_p in the range of 1 μm -10 μm) is placed in random locations inside the discharge chamber. The selected inhomogeneity density determines the number of spheres. Each of these spherical regions, which contains a volume charge perturbation, is placed at a stochastic position with coordinates located by three separate uniform distribution functions. These spherical regions have the same permittivity as the rest of the dielectric medium.

Theoretically, charge carrier density fluctuations can be originated by either the discrete nature of electrons at the leading edge of an ionization front where the electron density is low [29] or many external sources such as cosmic rays or other sources of ionizing radiation.

As a major source of volume charge fluctuations, when the background electric field increases, the field ionization generates more discrete free electrons at different locations of the dielectric that can gain enough energy to cause microscopic local ionizations. These local ionizations, occurring at background electric fields much weaker than the critical breakdown field, produce local charge densities that can be regarded as microscopic inhomogeneities.

In the presented model, we simulate these inhomogeneities by adding a stochastic amount of charge generation rates inside spherical regions, which generates a bias charge density in them. The intensity of the perturbation charge density generation rates is determined by continuous Gaussian functions. The minimum perturbation charge generation rate (G_{Mp}) is zero and maximum generation rate of carrier charge densities is $10^{10} \text{ Cm}^{-3}\text{s}^{-1}$, which is roughly one order of magnitude smaller than the generation rate at the typical positive streamer head in transformer oil (see Chapter 5) [1-4]. This stochastic perturbation rate generates inhomogeneous charge densities (ρ_{ps}) that are in agreement with results of [29] for a gaseous environment exposed to intense electric field. The result of the stochastic perturbation rate in the range of zero and $10^{10} \text{ Cm}^{-3}\text{s}^{-1}$ in transformer oil, considering the parameter values of Table 5.1, generates a maximum additional perturbation in charge density of $\sim 10^4 \text{ Cm}^{-3}$ inside the microscopic inhomogeneities.

The density of the microscopic inhomogeneities (C_p) is set to 10^{11} m^{-3} . Considering the volume of the oil in the breakdown chamber, this distribution means that we have to place $\sim 10^6$ spheres inside the chamber which makes the number of required mesh elements too high, since the mesh inside these spheres have to be dense enough. Therefore, we chose to only place the inhomogeneities inside the pillbox close to the streamer head at which we have refined the mesh. Modeling results prove that inhomogeneities farther than 1 mm from the streamer head do not affect the streamer branching.

6.4 Modeling Results: Streamer Stochastic Branching Driven by Micro-Inhomogeneities

A vast variety of inhomogeneous distributions of perturbations has been applied to study the streamer branching specifically in transformer oil. The qualitative shape of the streamer tree, number and diameters of the branches and their velocities are clearly sensitive to the applied voltage (and by a lesser extent, to the nonsymmetrical inhomogeneities). The time it takes for the streamer to branch out since the initiation of the streamer (branching time) decreases as the applied voltage and/or the rate of rise of the voltage increase. For the same inhomogeneity, the applied voltage peak essentially determines the number of branches, while for the same applied voltage peak, the average angle between the propagation directions of the branches is determined by the applied voltage rate of rise. The modeling results show that the deterministic causes of branching such as electrode geometry and applied voltage characteristics are as influential as stochastic origins on the propensity of streamers to branch out.

Using ten different inhomogeneity distributions and densities obtained by ten different sets of Gaussian functions and continuous uniform distribution functions, the model has been run to study the effects of the stochastic parameters on the attributes of the just born branches. The results of these ten different sets indicate that the deterministic roots of the streamer branching are dominant when the stochastic parameters vary within the boundaries described in section 6.3 (i.e., $|G_{Mp}| < 10^{10} \text{ Cm}^{-3}\text{s}^{-1}$, $|\rho_{ps}| < 10^4 \text{ Cm}^{-3}$, $C_p = 10^{11} \text{ m}^{-3}$, $1 \mu\text{m} < R_p < 10 \mu\text{m}$). The qualitative shape of the streamer tree, number and diameters of the branches and their velocities are clearly sensitive to the applied voltage (and by a lesser extent, to the inhomogeneities).

Among the simulation results, 13 cases have been selected to be compared with experimental images as shown in Figures 6.2-6.15. The modeling parameters are not identical to the circumstances of the experiments, however they are reasonably similar. Specifically, the medium in which streamers propagate and branch out is the same for both modeling and experimental results; the maximum electric field sensed in the gap is almost equal for pairs in each figure.

Currently, no approach is known to determine the distribution of inhomogeneities inside the oil. Any measurement of inhomogeneity structure would be extremely difficult since these inhomogeneities are not only functions of position, but they depend on time and electric field intensity as well. Although, the inhomogeneities are not known in experimental images found in the literature, as can be seen in all the panels of Fig. 4, the structure of the streamer node and branches are qualitatively similar which suggests that density, size and intensity of inhomogeneous perturbations in the oil have been properly chosen on realistic orders.

The streamer branch diameters from optical measurements is estimated to be about half of the electrodynamic diameters, as the model describes [29]. It should also be noted that the modeling results are electric field magnitudes and they do not show the structure of charge build up within the streamer. Therefore, the electrodynamic diameter of the streamer stem and branches are slightly smaller than what it looks like in the modeling images.

In Figures 6.2-6.15, the applied voltages are expressed in terms of U_{BD} (50% breakdown voltage peak), which is the impulse peak at which the dielectric breaks down in half of the discharge tests. U_{BD} is equal to 95 kV for the modeling geometry.

Figure 6.2 shows a streamer formed by an applied voltage with 85 kV peak, traveling in single column mode, even with presence of microscopic inhomogeneities. As can be seen in this figure, the inhomogeneities have been able to slightly deviate the streamer from its path on the axis of the electrode geometry. The inhomogeneities also evidently perturbed the surface of the streamer, however they are still unable to grow active branches from the main streamer head, which remains stable regardless of the scattered inhomogeneities. It should be noted that the relatively low applied voltage peak usually generate slow and thin streamers that are reluctant to branch out even in severely inhomogeneous media, due to the thick volume charge concentrated at the streamer head. At applied voltage peaks as low as the case shown in Figure 6.2, the rise-time does not appreciably affects the shape of the streamer head, which is always traveling as a single column.

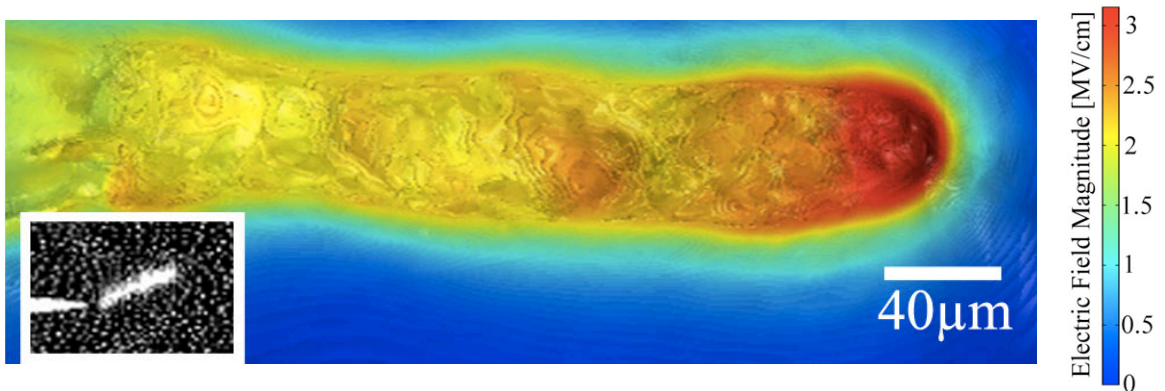


Figure 6.2: Iso-surface plot of electric field distribution as modeling result of streamer is compared with corresponding experimental image in the inset image. Definite breakdown voltage, U_{DBD} , for the modeling geometry (gap length, $d=25$ mm, and the electrode tip radius, $r_i=40$ μm) is equal to 95 kV. The initiation voltage for the modeling geometry is 30 kV. In the experimental data, the applied voltages are expressed in terms of streamer initiation voltage, V_i , and 50% breakdown voltage, U_{BD} , which is the impulse peak at which the dielectric breaks down in half of the discharge tests:

<i>Modeling (peak, rise time)</i>	<i>Experiment (Photography method and applied voltage peak)</i>
2.85 V_i (0.9 U_{DBD}), 1 ns	Streak image of streamer formed by 2.18 V_i (0.33 $U_{50BD} = 327$ kV) in a 150 mm gap with $r_i = 1$ mm ($U_{50BD} \approx 970$ kV) [13,15]

Figure 6.3 shows a streamer formed at 180 kV branching out in a 25 mm long gap, with 40 μm needle electrode tip radius. As can be seen in this figure, there are four branches coming out of the node after the branching. However, only two of the branches remain active after a few nanoseconds. These inactive branches (as called in Figure 6.1, dead branches) do not continue growing towards the electric field lines like active branches, mainly due to lack of volume charge at their heads. Active branches usually carry significant volume charges mostly at their heads.

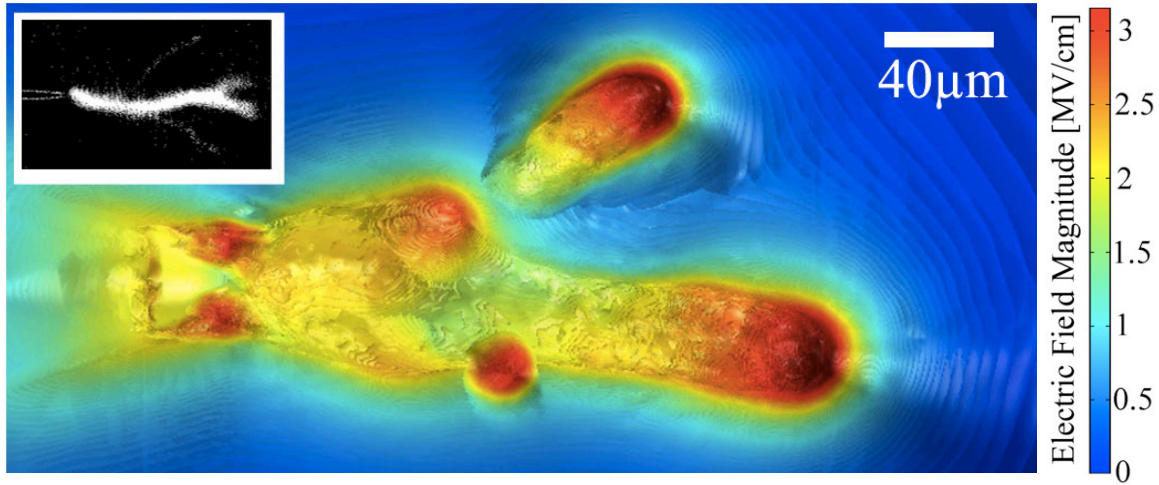


Figure 6.3: Iso-surface plot of electric field distribution as modeling result of streamer is compared with corresponding experimental image in the inset image. Definite breakdown voltage, U_{DBD} , for the modeling geometry ($d=25$ mm, $r_i=40$ μ m) is equal to 95 kV. The initiation voltage for the modeling geometry is 30 kV. In the experimental data, the applied voltages are expressed in terms of streamer initiation voltage, V_i , and 50% breakdown voltage, U_{BD} , which is the impulse peak at which the dielectric breaks down in half of the discharge tests:

<i>Modeling (peak, rise time)</i>	<i>Experiment (Photography method and applied voltage peak)</i>
$6 V_i (1.9 U_{DBD}), 100$ ns	Streak image of streamer formed by $4.88 V_i (1.57 U_{50BD}=583$ kV) in a 100 mm gap with $r_i=1$ mm ($U_{50BD}\approx 370$ kV) [13,15]

Figure 6.4 shows a streamer tree with three active branches with almost equal angles from each other formed by an applied voltage with 230 kV peak. The location and the angle of the streamer branches depend on the inhomogeneity position and intensity. However, this does not necessarily mean that the branches form right at the inhomogeneities, or inhomogeneities directly determine the propagation direction of the branches, which is true for the macroscopic inhomogeneities. In fact, microscopic inhomogeneity effect is only disrupting the symmetry of the streamer head. Once the symmetry is broken, the branches develop based on the energy that the accumulated charge at the streamer head has absorbed from the applied voltage.

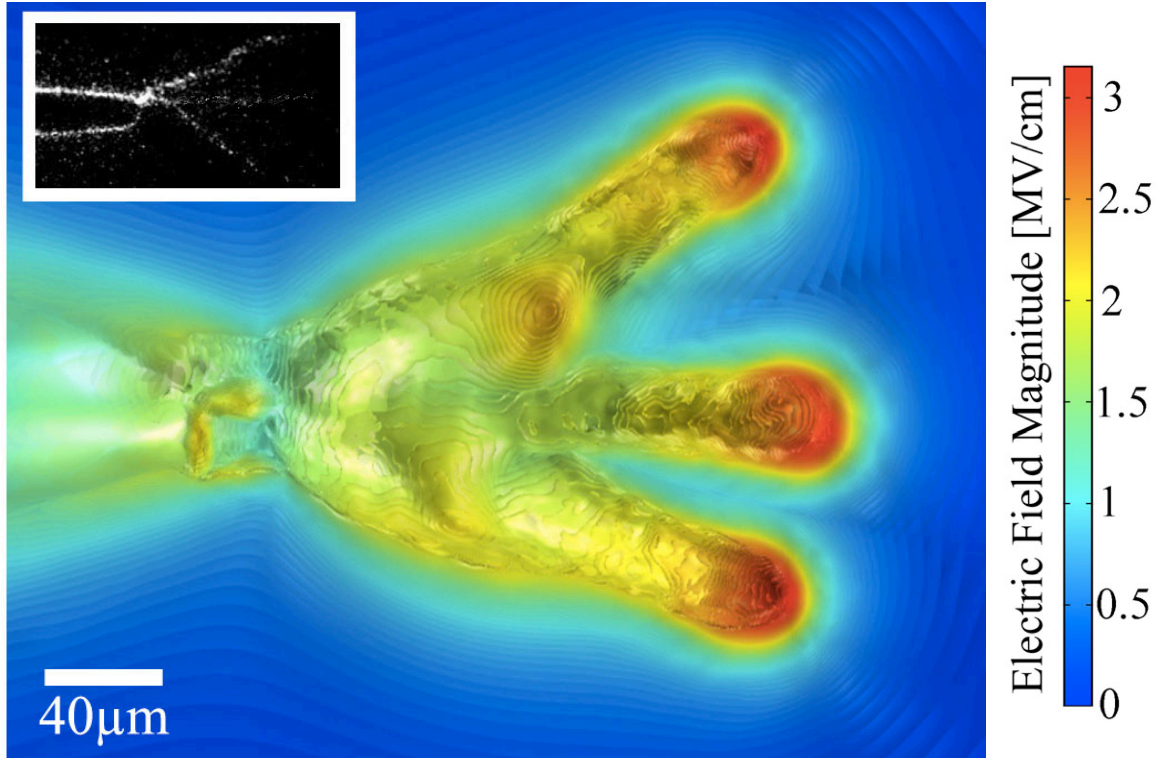


Figure 6.4: Iso-surface plot of electric field distribution as modeling result of streamer is compared with corresponding experimental image in the inset image. Definite breakdown voltage, U_{DBD} , for the modeling geometry ($d=25$ mm, $r_f=40$ μ m) is equal to 95 kV. The initiation voltage for the modeling geometry is 30 kV. In the experimental data, the applied voltages are expressed in terms of streamer initiation voltage, V_i , and 50% breakdown voltage, U_{BD} , which is the impulse peak at which the dielectric breaks down in half of the discharge tests:

Modeling (peak, rise time)	Experiment (Photography method and applied voltage peak)
7.66 V_i (2.42 U_{DBD}), 10 ns	Schlieren images of streamer formed by 7.25 V_i (100 kV=5.55 U_{50BD} , 30 ns) in a 2.5 mm gap with $r_f=25$ μ m ($U_{50BD} \approx 18$ kV) [15,18]

Figure 6.5 shows a streamer tree with five active branches formed by an applied voltage with 260 kV peak. These five branches are interestingly different in terms of velocities and shapes. They can be classified into three types. The thickest branch which is also the fastest one stands alone. This branch is accompanied with two almost identical smaller and slower branches which form equal angles with this branch. Two late branches leave the streamer node with thin structures, which propagate much slower than the other three branches. The electric field generated by the branches, which propagate ahead of these two branches are responsible for their slow development as they cancel out the background electric field (of electrodes) significantly. Once again, it should be noted that all positive streamer branches carry positive volume charge and generate outgoing electric field lines (see Chapter 5). Figure 6.5 shows an interesting case study that indicates based on the applied voltage waveform, the configuration of the volume charge at the streamer head and of course the situation of the microscopic inhomogeneities, different active streamer branches can emanate from the streamer node at different times with different characteristics. The inset experimental image of the streamer tree in Figure 6.5 shows many

secondary branching after the first streamer branching at the electrode tip. It is definitely interesting to determine the required time and space for a just born streamer branch to reach another node and become a parent streamer (also known as leader) through a secondary node. Accomplishing this numerical task requires the mesh to be refined over a larger space which means that it requires a higher computation power. Although, this task remained beyond the scope of this thesis, it could be an interesting future research work. The present 3-D modeling of streamer branching indicates that after the first branching, velocities of the branches increase which makes the secondary branching unlikely at least until the streamer branch travels over hundreds of microns from the original node. The ratio of branching length over streamer diameter is about 12 to 15, reported in [6]. Unfortunately, this ratio cannot be verified through the current version of the model due to computational limitations.

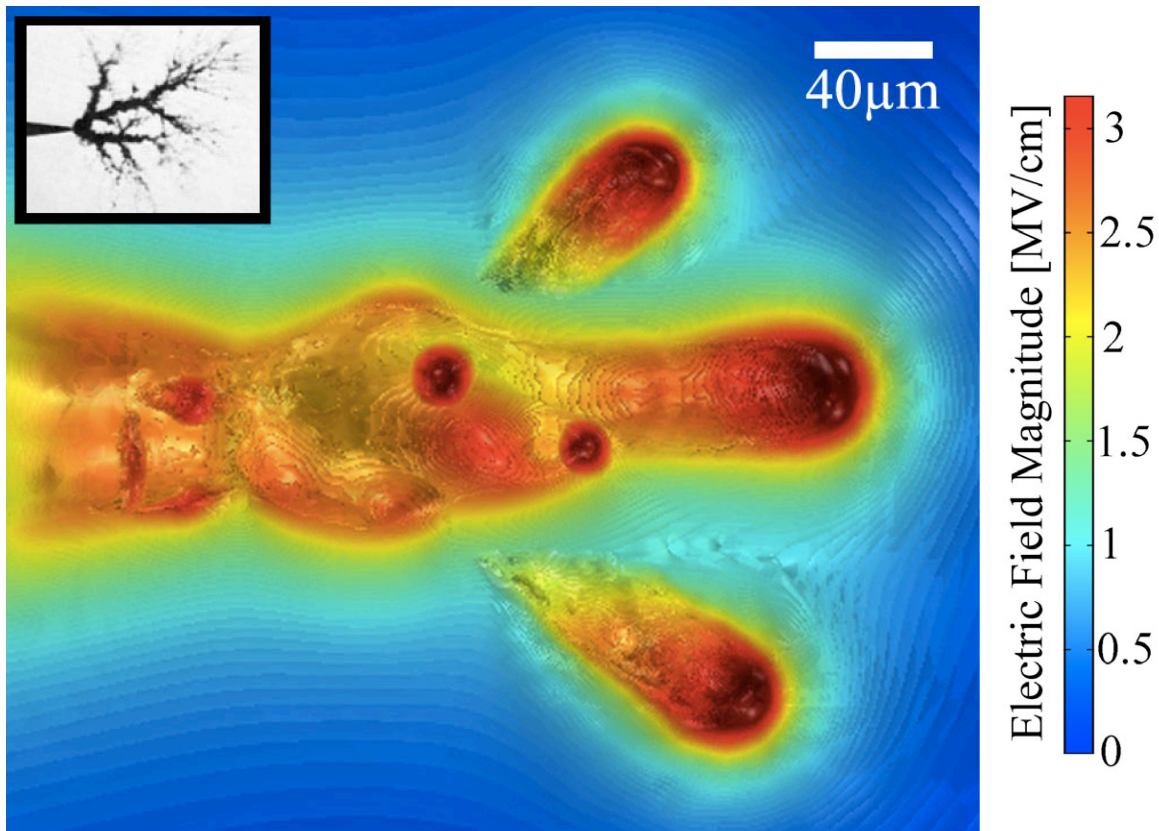


Figure 6.5: Iso-surface plot of electric field distribution as modeling result of streamer is compared with corresponding experimental image in the inset image. Definite breakdown voltage, U_{DBD} , for the modeling geometry ($d=25$ mm, $r_i=40$ μm) is equal to 95 kV. The initiation voltage for the modeling geometry is 30 kV. In the experimental data, the applied voltages are expressed in terms of streamer initiation voltage, V_i , and 50% breakdown voltage, U_{BD} , which is the impulse peak at which the dielectric breaks down in half of the discharge tests:

<i>Modeling (peak, rise time)</i>	<i>Experiment (Photography method and applied voltage peak)</i>
8.66 V_i (2.74 U_{DBD}), 100 ns	Streak images of streamer formed by 8.2 V_i (0.8 $U_{50BD}=24$ kV) in a 3 mm gap with $r_i=5$ μm ($U_{50BD}\approx 30$ kV) [15,105].

Figure 6.6 shows that an applied voltage, with 270 kV peak, creates four active branches with different characteristics, as each branch picks up a different amount of volume charge from the main streamer stem. The repelling force between the branches due to different volume charge of the same polarity inherited from the parent streamer head mainly determines the angle between growing branches.

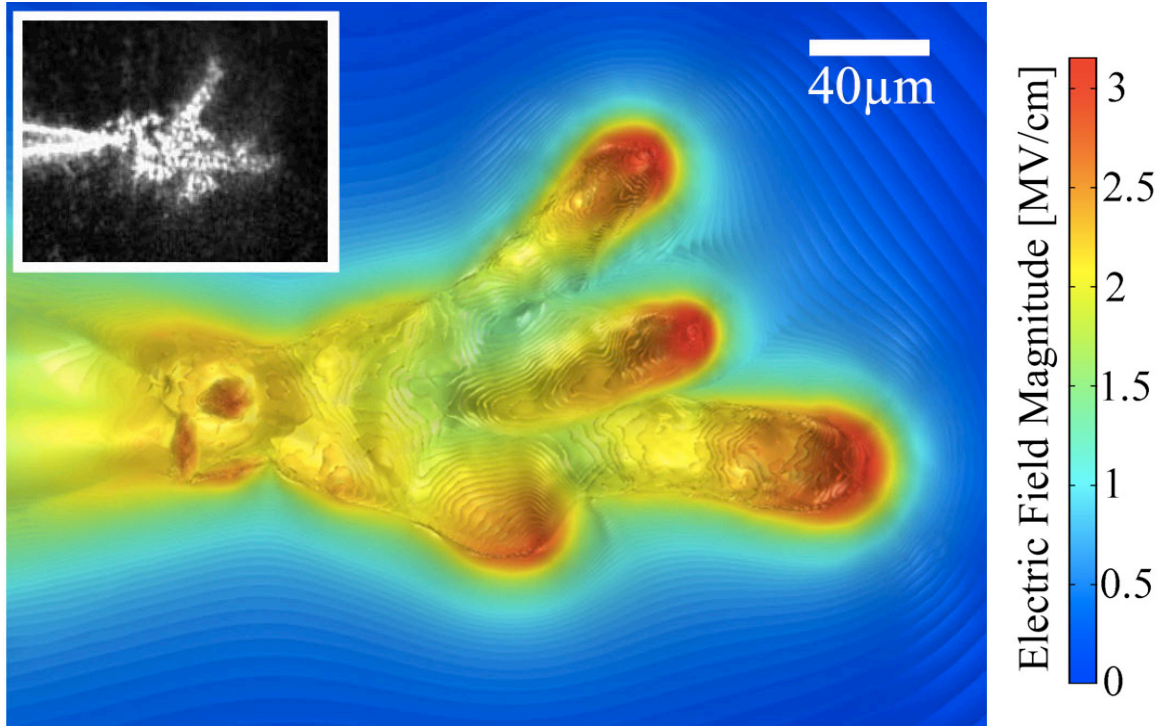


Figure 6.6: Iso-surface plot of electric field distribution as modeling result of streamer is compared with corresponding experimental image in the inset image. Definite breakdown voltage, U_{DBD} , for the modeling geometry ($d=25$ mm, $r_i=40$ μ m) is equal to 95 kV. The initiation voltage for the modeling geometry is 30 kV. In the experimental data, the applied voltages are expressed in terms of streamer initiation voltage, V_i , and 50% breakdown voltage, U_{BD} , which is the impulse peak at which the dielectric breaks down in half of the discharge tests:

<i>Modeling (peak, rise time)</i>	<i>Experiment (Photography method and applied voltage peak)</i>
$9 V_i$ ($2.84 U_{DBD}$), 10 ns	Schlieren images of streamer formed by $2.77 V_i$ (47 KV = $1.88 U_{50BD}$, 20 ns) in a 5 mm gap with $r_i=25$ μ m ($U_{50BD} \approx 25$ kV) [15,18]

Figure 6.7 shows an example of this case. In this figure, a streamer tree is shown which has been formed by an applied voltage with 300 kV peak and 100 ns rise-time. Even though this streamer tree is formed by a higher voltage peak than the streamer shown in Figure 6.9, the streamer branches are slightly thinner due to the shorter rise-time.

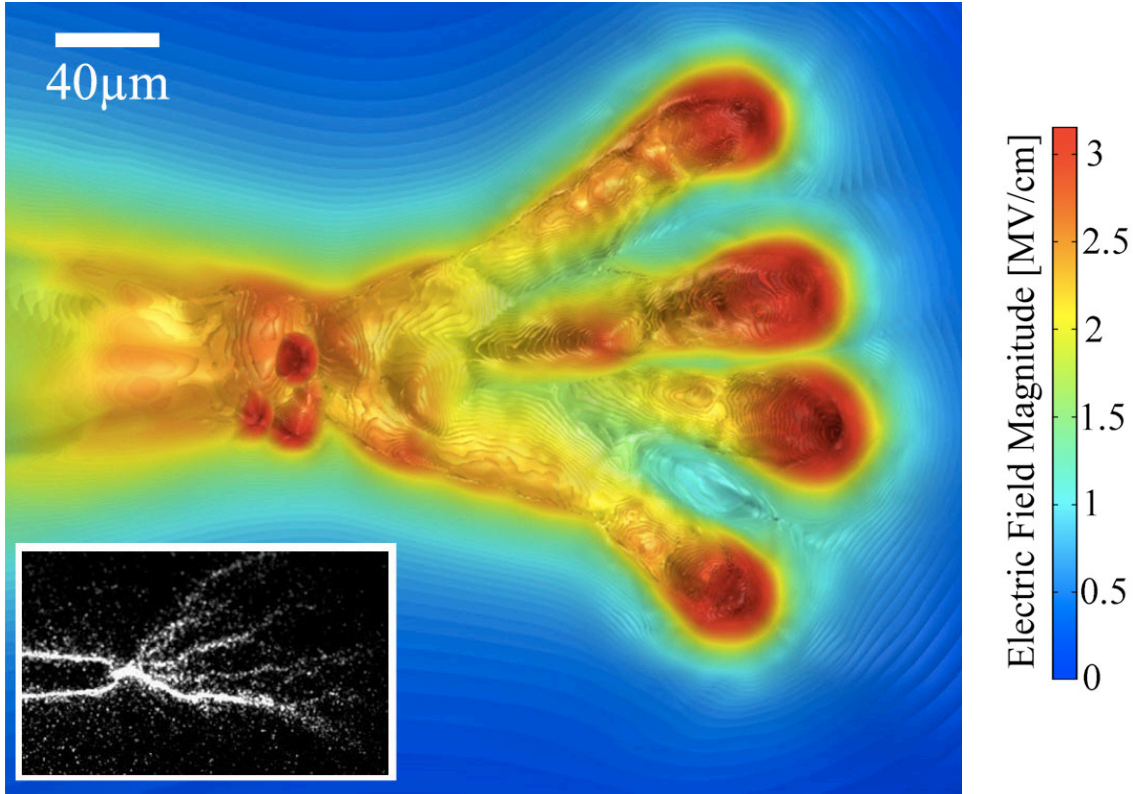


Figure 6.7: Iso-surface plot of electric field distribution as modeling result of streamer is compared with corresponding experimental image in the inset image. Definite breakdown voltage, U_{DBD} , for the modeling geometry ($d=25$ mm, $r_i=40$ μm) is equal to 95 kV. The initiation voltage for the modeling geometry is 30 kV. In the experimental data, the applied voltages are expressed in terms of streamer initiation voltage, V_i , and 50% breakdown voltage, U_{BD} , which is the impulse peak at which the dielectric breaks down in half of the discharge tests:

<i>Modeling (peak, rise time)</i>	<i>Experiment (Photography method and applied voltage peak)</i>
$10 V_i (3.16 U_{DBD}), 100$ ns	Schlieren images of streamer formed by $7.25 V_i (5.55 U_{50BD} = 100$ kV, 300 ns) in a 2.5 mm gap with $r_i=25$ μm ($U_{50BD} \approx 18$ kV) [15,18]

Streamer branches formed by macroscopic inhomogeneities usually have similar characteristics, which are dictated by the inhomogeneity. However, microscopic inhomogeneities only disrupt the symmetry and the streamer dynamics and the applied voltage mainly determine the structure of the streamer tree. An example of streamer branches with different shapes (thicknesses) and velocities formed at 320 kV is shown in Figure 6.8.

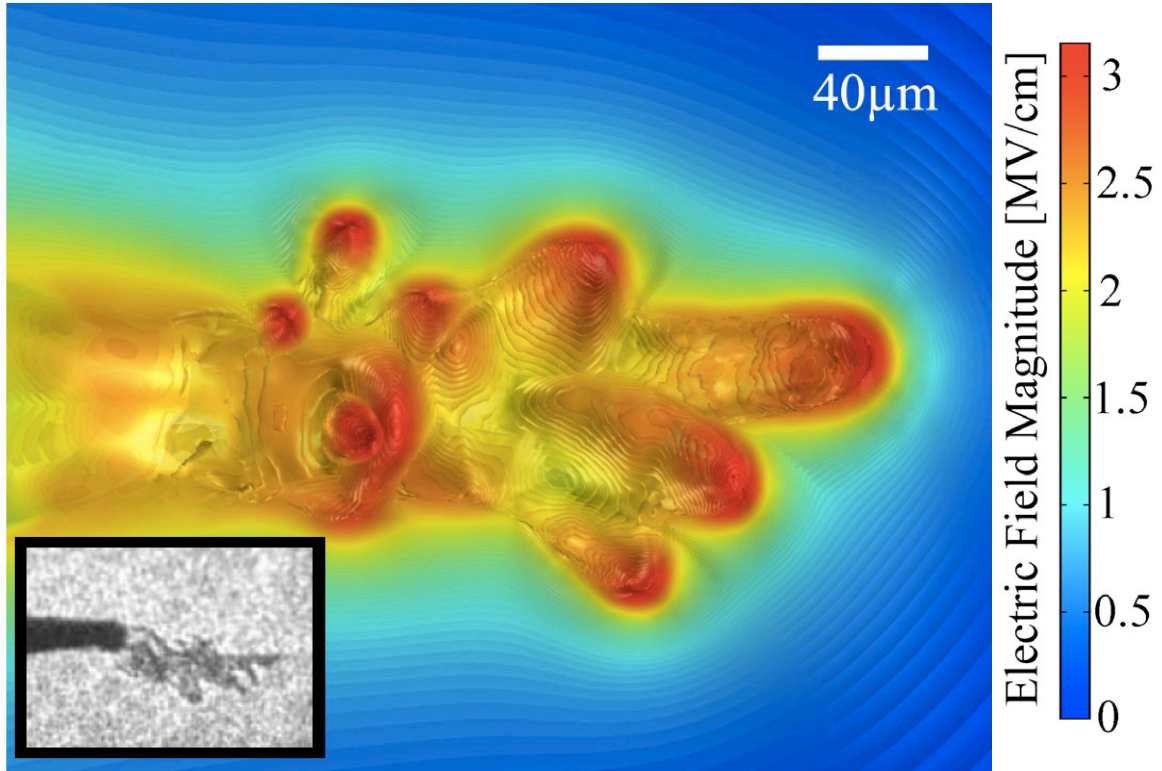


Figure 6.8: Iso-surface plot of electric field distribution as modeling result of streamer is compared with corresponding experimental image in the inset image. Definite breakdown voltage, U_{DBD} , for the modeling geometry ($d=25$ mm, $r_i=40$ μm) is equal to 95 kV. The initiation voltage for the modeling geometry is 30 kV. In the experimental data, the applied voltages are expressed in terms of streamer initiation voltage, V_i , and 50% breakdown voltage, U_{BD} , which is the impulse peak at which the dielectric breaks down in half of the discharge tests:

<i>Modeling (peak, rise time)</i>	<i>Experiment (Photography method and applied voltage peak)</i>
10.66 V_i (3.37 U_{DBD}), 100 ns	Shadowgraphy images of streamer formed by 11.1 V_i (5.55 $U_{50BD}=100$ kV, 1.2 μs) in a 2.5 mm gap with $r_i=30$ μm ($U_{50BD} \approx 14$ kV) [2,15]

Figure 6.9 shows a streamer tree formed by an applied voltage 340 kV peak and 10 ns rise-time. As the rate of rise of the applied voltage increases the cylindrical streamer branch shapes become more of pyramid shapes due to the significant velocity of the streamer branch head.

In general, the streamer velocity drops just before branching begins and rises again once the branching happens. For applied voltages under 300 kV in the electrode geometry of Figure 5.1, each individual branch accelerates with clearly different velocities. One of the streamer branches usually picks up the maximum velocity, which is appreciably higher than the other branch velocities. This maximum velocity agrees with experimental evidence found in the literature, even closer than the 2-D axisymmetric modeling results (Chapter 5). However, streamers formed by applied voltage peaks higher than 300 kV, almost all of the child branches propagate with roughly similar velocity which is slightly lower than the velocities reported in experimental records.

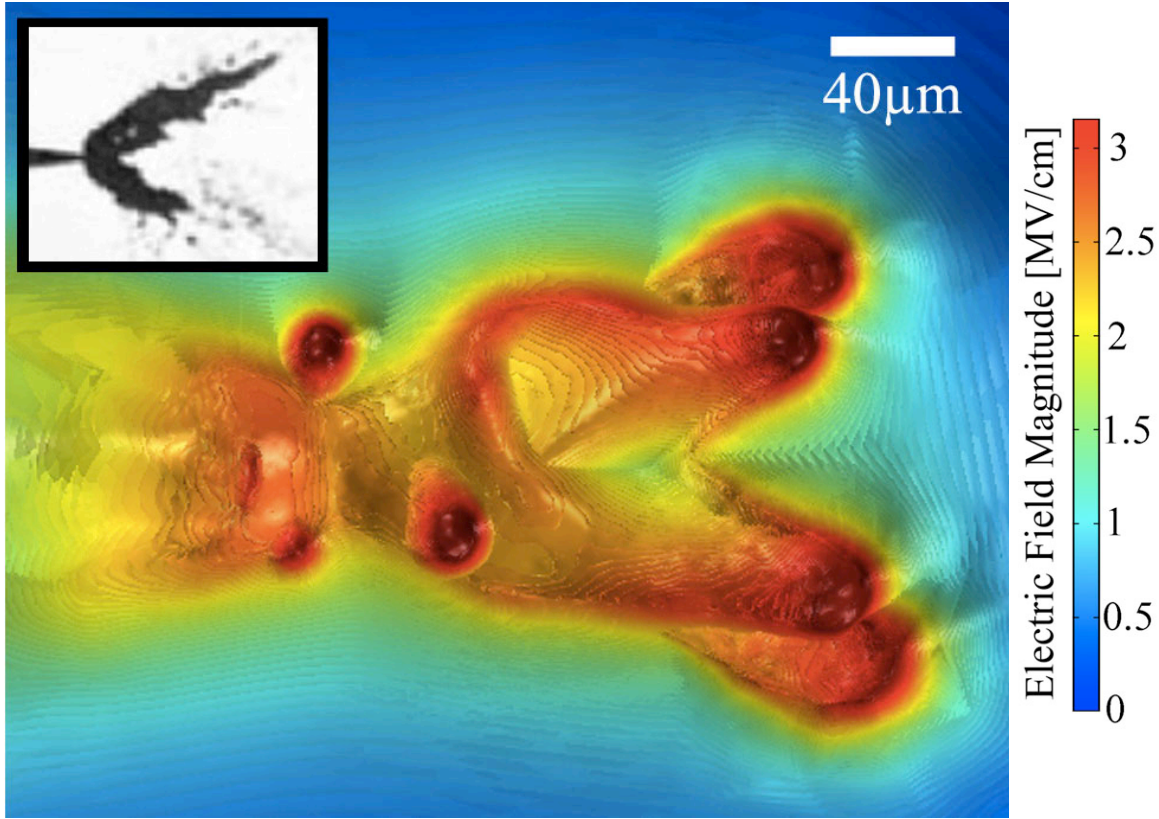


Figure 6.9: Iso-surface plot of electric field distribution as modeling result of streamer is compared with corresponding experimental image in the inset image. Definite breakdown voltage, U_{DBD} , for the modeling geometry ($d=25$ mm, $r_i=40$ μ m) is equal to 95 kV. The initiation voltage for the modeling geometry is 30 kV. In the experimental data, the applied voltages are expressed in terms of streamer initiation voltage, V_i , and 50% breakdown voltage, U_{BD} , which is the impulse peak at which the dielectric breaks down in half of the discharge tests:

<i>Modeling (peak, rise time)</i>	<i>Experiment (Photography method and applied voltage peak)</i>
11.33 V_i (3.58 U_{DBD}), 10 ns	Streak images of streamer formed by 10.23 V_i (1.14 U_{50BD} =30 kV) in a 2 mm gap with $r_i=5$ μ m ($U_{50BD}\approx 30$ kV) [15,105].

Figure 6.10 shows a streamer tree with five active branches formed by an applied voltage with 360 kV peak. Streamers formed by applied voltages higher than 350 kV tend to form a high number of branches due to a high velocity thin crust of the streamer head. Again, the short rise-time of the applied voltage makes the streamer branches bushier (as expected from the results of Chapter 5) and vulnerable to secondary branching as they are more sensitive to the inhomogeneities near the streamer branch head formed at a high rate of rise of voltage.

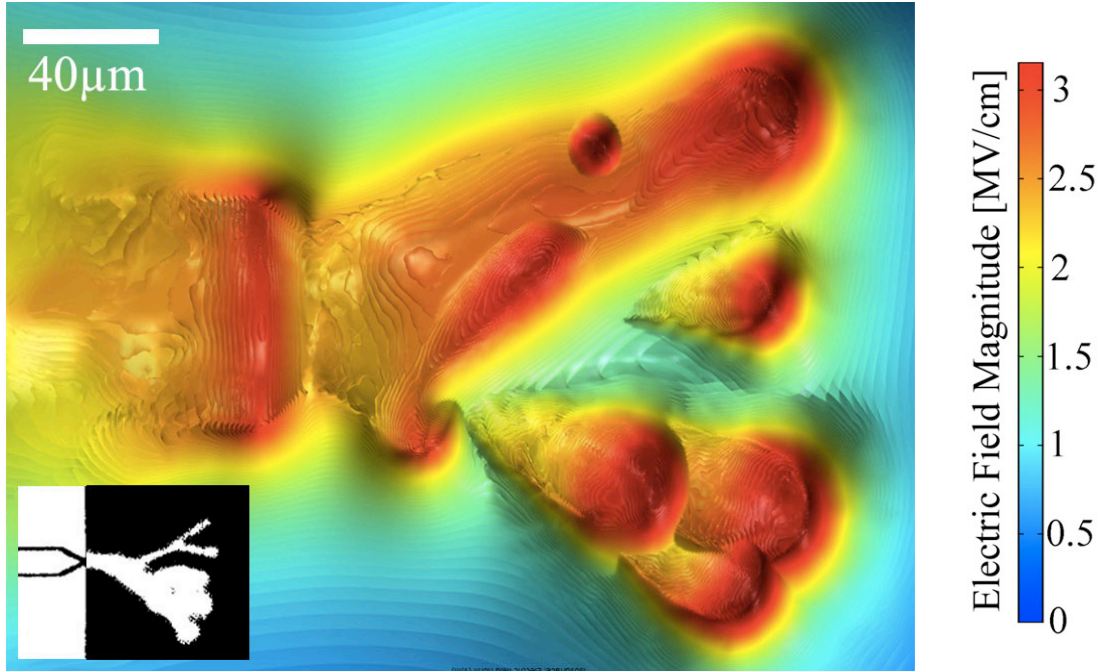


Figure 6.10: Iso-surface plot of electric field distribution as modeling result of streamer is compared with corresponding experimental image in the inset image. Definite breakdown voltage, U_{DBD} , for the modeling geometry ($d=25$ mm, $r_i=40$ μm) is equal to 95 kV. The initiation voltage for the modeling geometry is 30 kV. In the experimental data, the applied voltages are expressed in terms of streamer initiation voltage, V_i , and 50% breakdown voltage, U_{BD} , which is the impulse peak at which the dielectric breaks down in half of the discharge tests:

Modeling (peak, rise time)	Experiment (Photography method and applied voltage peak)
$12.6 V_i$ ($4 U_{DBD}$), 10 ns	Intensifier gate photographs of streamer formed by $13.2 V_i$ ($0.9 U_{50BD} = 304$ kV) in a 200 mm gap with $r_i = 40$ μm ($U_{50BD} \approx 340$ kV) [14,15]

On the other hand, trees of streamers with relatively long and thin branches are usually formed by longer rise-times (as expected from the results in Chapter 5). Such streamer branches show more stability when they confront microscopic inhomogeneities in their flight compared with bushy branches formed at shorter rise-times.

Figure 6.11 shows an exceptional case in which a multiple branching occurs in a short distance (within one millimeter from the needle). There are two secondary branching happening at both upper and lower colonies of branches shown in Figure 6.11. As shown in the inset of this figure, the observed phenomena in the modeling can be seen in practice as well (although it is rare). Once again, there is a combination of the high applied-voltage-peak, short rise-time and high density of inhomogeneities near the streamer.

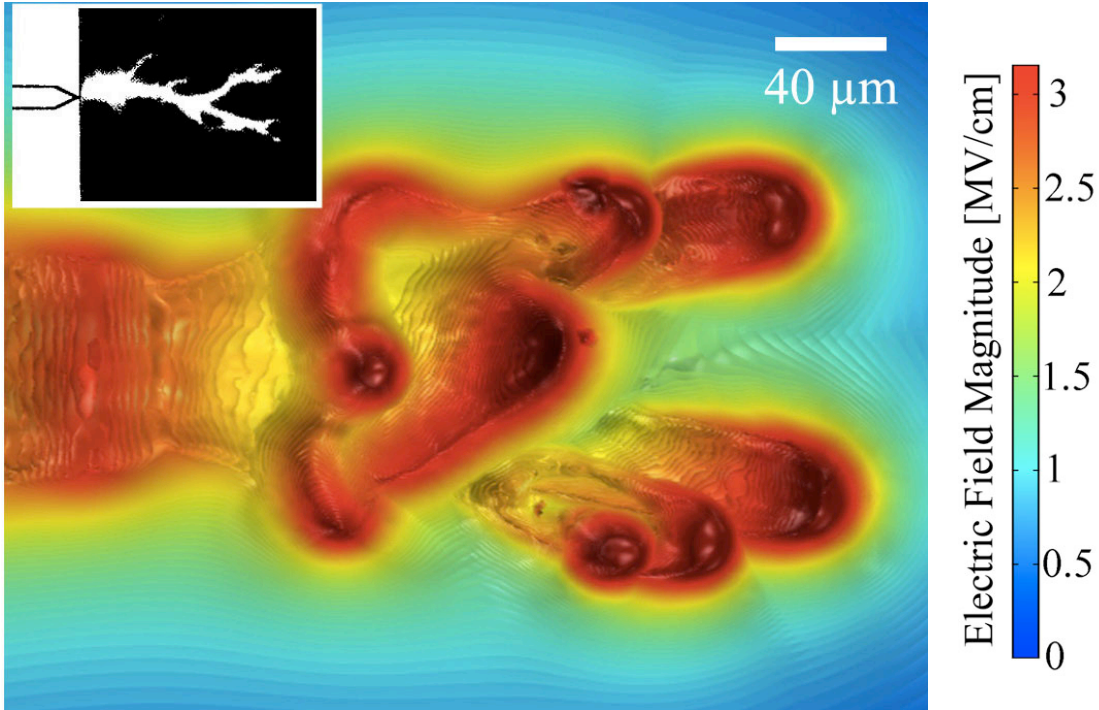


Figure 6.11: Iso-surface plot of electric field distribution as modeling result of streamer is compared with corresponding experimental image in the inset image. Definite breakdown voltage, U_{DBD} , for the modeling geometry ($d=25$ mm, $r_i=40$ μm) is equal to 95 kV. The initiation voltage for the modeling geometry is 30 kV. In the experimental data, the applied voltages are expressed in terms of streamer initiation voltage, V_i , and 50% breakdown voltage, U_{BD} , which is the impulse peak at which the dielectric breaks down in half of the discharge tests:

<i>Modeling (peak, rise time)</i>	<i>Experiment (Photography method and applied voltage peak)</i>
15.2 ($4.8 U_{DBD}$) 10 ns	Intensifier gate photographs of streamer formed by $16V_i$ ($0.87 U_{50BD}=304$ kV) in a 200 mm gap with $r_i=3$ μm ($U_{50BD}\approx 350$ kV) [14,15]

Figure 6.12 shows a streamer tree formed by an applied voltage with 475 kV peak and 100 ns rise-time. For applied voltage peaks above $5 U_{BD}$ the branching occurs immediately at the needle electrode and it becomes difficult to even count the number of branches as every point of the streamer shell becomes vulnerable to branching. The thickness of the streamer volume charge density is significantly narrow for applied voltages over $5 U_{BD}$.

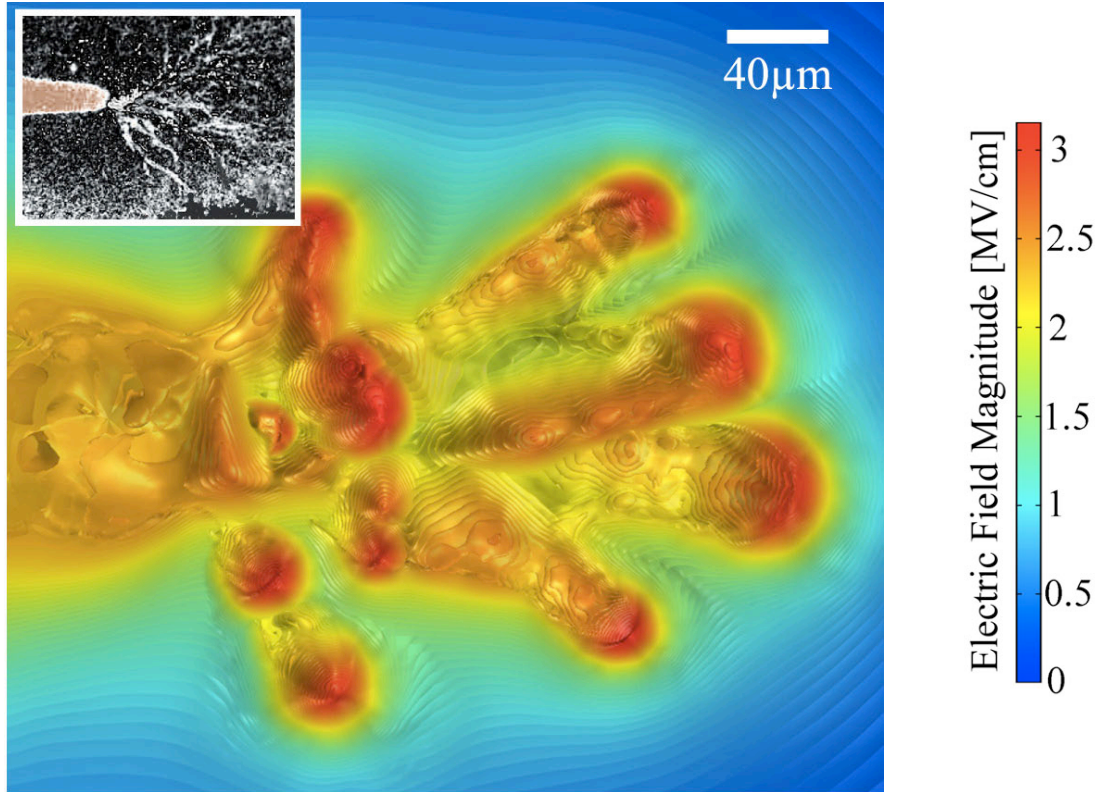


Figure 6.12: Iso-surface plot of electric field distribution as modeling result of streamer is compared with corresponding experimental image in the inset image. Definite breakdown voltage, U_{DBD} , for the modeling geometry ($d=25$ mm, $r_i=40$ μ m) is equal to 95 kV. The initiation voltage for the modeling geometry is 30 kV. In the experimental data, the applied voltages are expressed in terms of streamer initiation voltage, V_i , and 50% breakdown voltage, U_{BD} , which is the impulse peak at which the dielectric breaks down in half of the discharge tests:

<i>Modeling (peak, rise time)</i>	<i>Experiment (Photography method and applied voltage peak)</i>
15.83 V_i ($5 U_{DBD}$), 100 ns	Shadowgraphy images of streamer formed by 14.44 V_i ($9.28 U_{50BD} = 130$ kV, 1.2 μ s) in a 2.5 mm gap with $r_i=30$ μ m ($U_{50BD} \approx 14$ kV) [2,15]

Figure 6.13 shows a streamer tree formed by an applied voltage with 530 kV peak and 10 ns rise-time. As can be seen in this figure, the modeling result indicates that there are two or even more clearly separate streamer branch heads sharing a stem for a significant distance and time. In fact several distinct streamer heads carry the same body of mixed ionized species until they divide the body into different streamer branch stems. Since these small branch heads are formed by such a high rate of rise of voltage, they are not allowed enough amounts of time and space to be segregated successfully at the branching node. Therefore, they travel together like –part of- an umbrella and after a while, as the electric field and charge velocity drop, they eventually become independent branches.

Another interesting point, which can be seen in Figure 6.13, is that many active streamer branches are still emanating from the needle electrode tip, even after the streamer tree has developed about half a millimeter from the streamer initiation point. This indicates that, in addition to inhomogeneities in the dielectric volume, the small cracks and perturbations on the needle

electrode should be included in the streamer branching studies especially if the electrode gap is relatively small. Some of experimental images show that branching has started right at the needle itself [30].

In this figure, the modeling result has been compared with an experimental results with significantly different applied voltage peak in terms of U_{BD} (almost an order of magnitude difference). However, if we compare the gap length of the simulated case with the experiment we realize there is an order of magnitude difference. Since the behavior of streamer within millimeters of the needle electrode is studied in this case, it can be concluded that for extra long gaps, the branching can happen at much lower applied voltage peaks. As discussed in Chapter 5, when the grounded electrode is far enough from the needle electrode (above 25 mm), the 50% breakdown voltage is not the appropriate measure for determining similarities in streamer dynamics between different gap lengths.

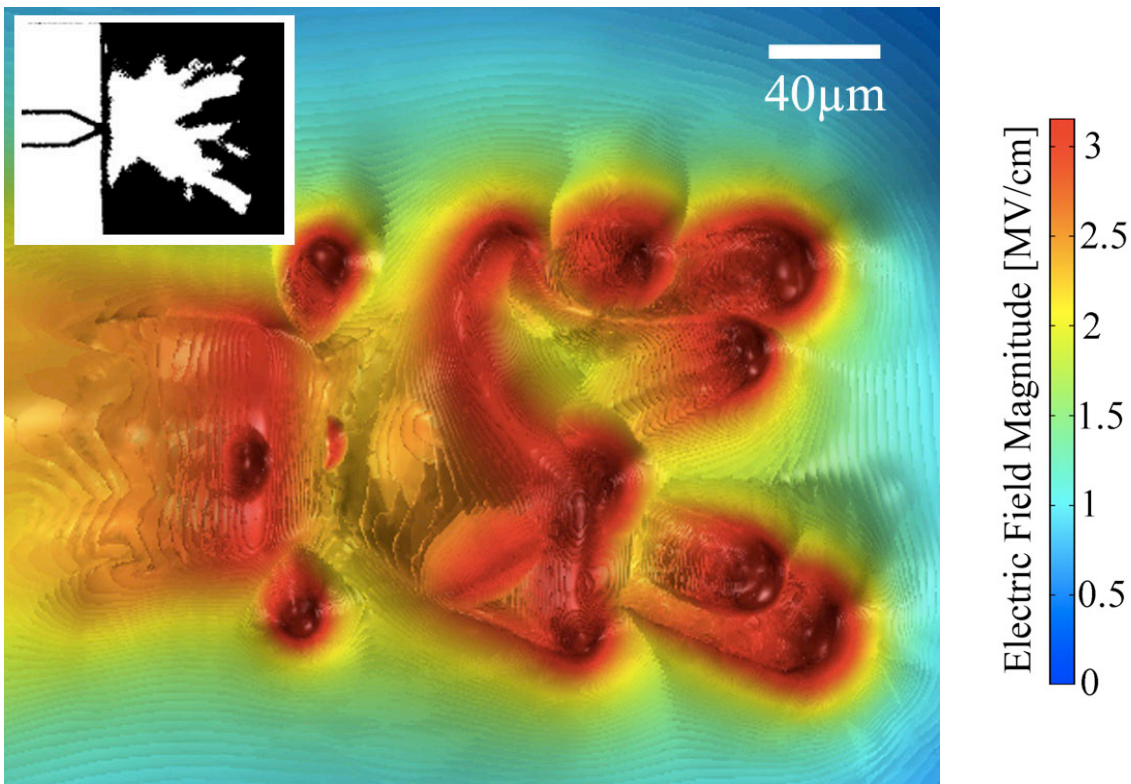


Figure 6.13: Iso-surface plot of electric field distribution as modeling result of streamer is compared with corresponding experimental image in the inset image. Definite breakdown voltage, U_{DBD} , for the modeling geometry ($d=25$ mm, $r_i=40$ μm) is equal to 95 kV. The initiation voltage for the modeling geometry is 30 kV. In the experimental data, the applied voltages are expressed in terms of streamer initiation voltage, V_i , and 50% breakdown voltage, U_{BD} , which is the impulse peak at which the dielectric breaks down in half of the discharge tests:

<i>Modeling (peak, rise time)</i>	<i>Experiment (Photography method and applied voltage peak)</i>
16.1 (5.1 U_{DBD}), 10 ns	Intensifier gate photographs of streamer formed by 18.62 V_i (1.38 $U_{50BD}=304$ kV) in a 50 mm gap with $r_i=3$ μm ($U_{50BD}\approx 220$ kV) [14,15]

Figure 6.14 shows the modeling result for a streamer tree formed by an applied voltage with 550 kV peak and 100 ns rise-time. As can be seen the streamer branches are running away from the needle electrode in almost all possible directions. Such an explosion type of branching occurs for all applied voltage peaks above $5.8 U_{BD}$. The shape and number of branches remain similar, but the velocity of the branches progressively rises as the applied voltage peak increases.

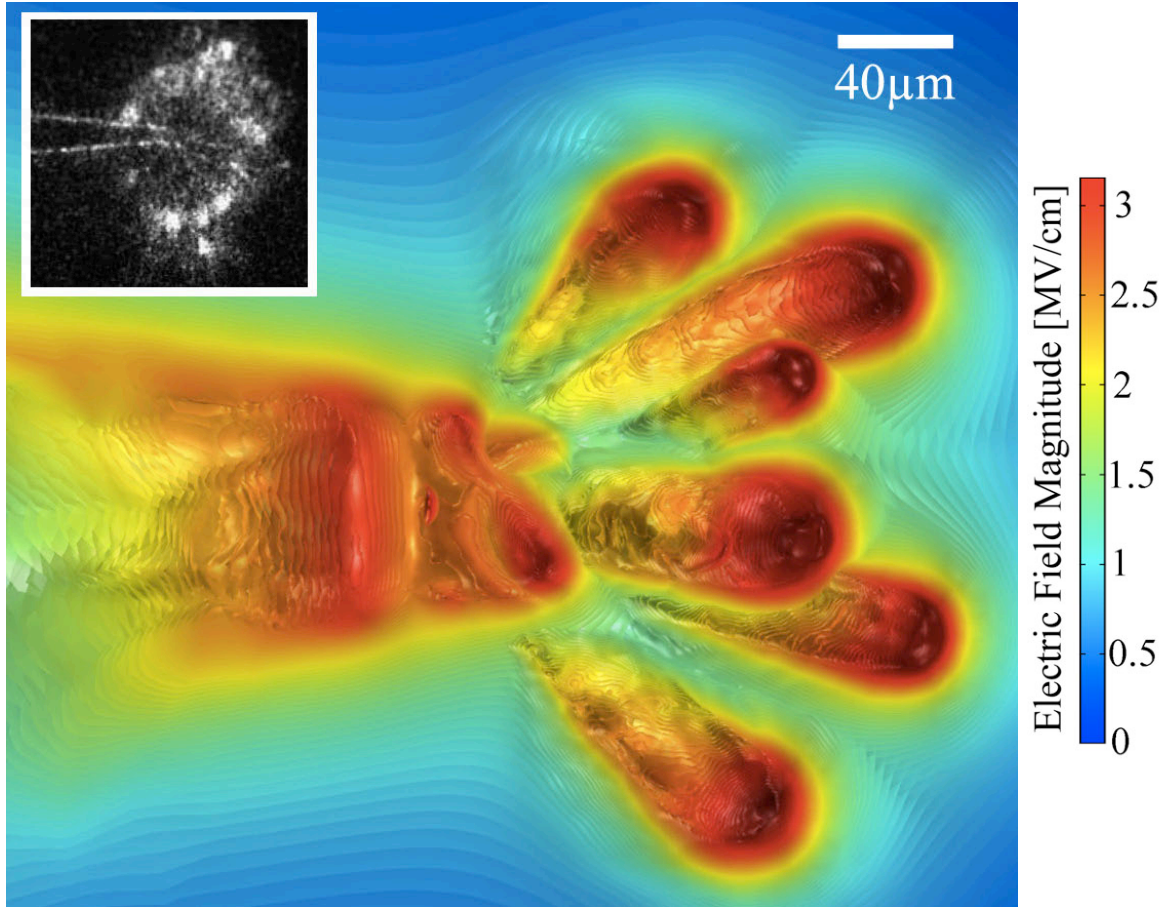


Figure 6.14: Iso-surface plot of electric field distribution as modeling result of streamer is compared with corresponding experimental image in the inset image. Definite breakdown voltage, U_{DBD} , for the modeling geometry ($d=25$ mm, $r_i=40$ μm) is equal to 95 kV. The initiation voltage for the modeling geometry is 30 kV. In the experimental data, the applied voltages are expressed in terms of streamer initiation voltage, V_i , and 50% breakdown voltage, U_{BD} , which is the impulse peak at which the dielectric breaks down in half of the discharge tests:

<i>Modeling (peak, rise time)</i>	<i>Experiment (Photography method and applied voltage peak)</i>
18.3 V_i ($5.8 U_{DBD}$), 100 ns	Schlieren images of streamer formed by 20.1 V_i ($4.3 U_{50BD}=28$ kV, 1 μs) in a 1 mm gap with $r_i=5$ μm ($U_{50BD} \approx 6.5$ kV) [3,18]

In an explosion type of streamer branching (shown in Figure 6.14), even an infinitesimal perturbation can drive a branching, as the original streamer head sheath is extremely narrow and unstable. In the case of absolutely no asymmetric perturbation, this streamer cannot propagate [25]. Therefore, it progressively slows down with a cone-shaped structure (like an umbrella) and eventually stops growing which is clearly not a physical result [48]. Such non-physical observations, known as bell-shaped streamers [25], are common in 2-D modeling of streamers (Chapter 5) especially when the rate of rise of the applied voltage is considerably high.

Regarding the validity of the numerical modeling of instabilities (streamer branches can be considered as kind of a surface instability) there is always a major concern. The question is how can we ensure that the streamer branches are physical, not originating from the numerical instabilities (e.g., due to inappropriate meshing or residual errors). At the end of this section, a verification study that has been applied in this thesis is briefly introduced. Then, in the next section, a gauge will be devised that enables prediction of whether the branching occurs at an instantaneous time based on the geometry of the volume charge distribution at the streamer head, and if it happens, how many branches will be born.

In numerical modeling, the actual branching triggered by the physical perturbations must be distinguished from the artifacts developed by numerical instabilities. Several sanity checks are performed to ensure that the physical elements are the only initiators of the observed branching in the model. For instance, as a sanity check that is performed for every case reported in this thesis, we have studied the effect of many symmetric inhomogeneous charge densities in oil on the streamer branching. If the mesh is refined enough to avoid misinterpreting numerical artifacts as streamer branches, the branching must be symmetric as well as the inhomogeneities.

Figure 6.15 shows a representative case of symmetric sanity check studies in which the spatial distributions on the charge carrier densities are symmetrical to the plane, $y=0$. As can be seen in the left part of Figure 6.16 the streamer branching has followed the symmetry of the inhomogeneities, meaning that numerical instabilities are not amplified by the system. It should be noted that the three-dimensional mesh of the model is not symmetric to the planes of symmetry (e.g., $y=0$ in Figure 6.15). Therefore, the symmetrical branching of the streamer guarantees that the numerical errors are effectively dampened and the results are physical. If there were significant numerical noise amplifications in the system, they would appear and disrupt the symmetry of the results since nothing is symmetrical in the system except the perturbing inhomogeneities.

In addition, as shown in Figures 6.1–6.14, the modeling results have been verified with experimental images wherever available and remarkable similarity between them also suggests that the results are physically valid.

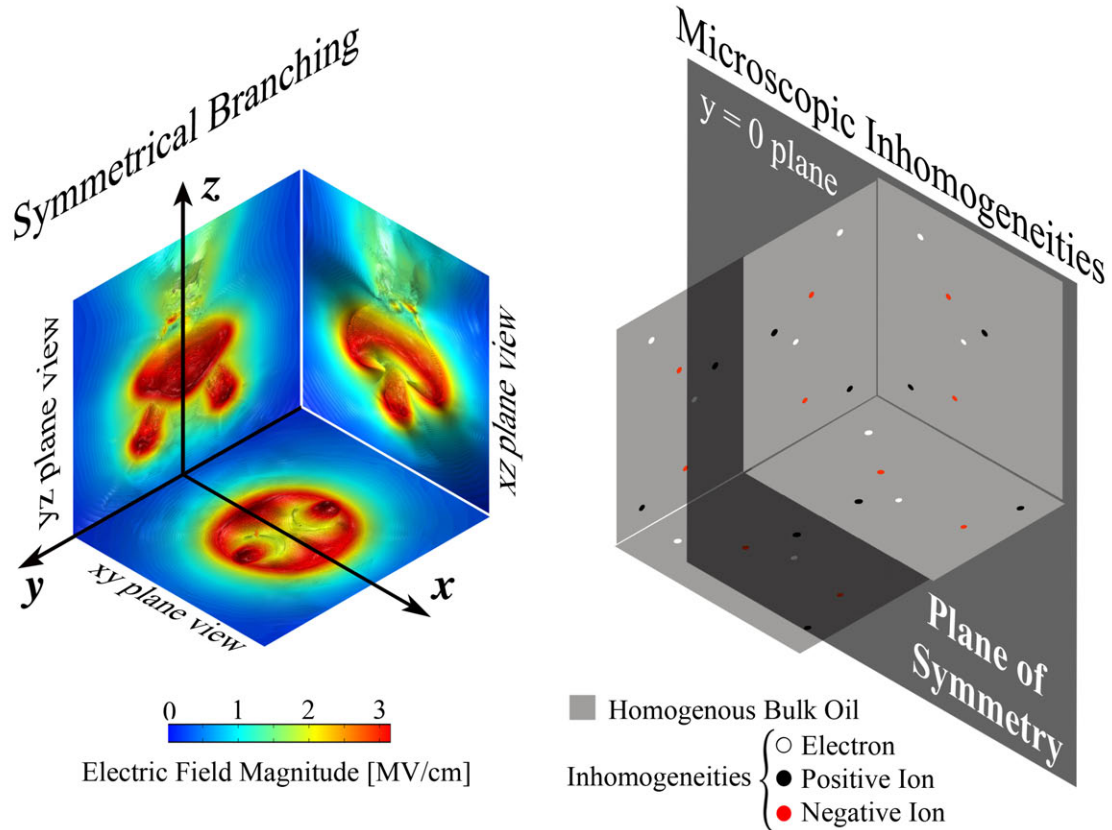


Figure 6.15: Symmetrical streamer branching due to symmetric initial electron disturbance distribution (planes of symmetry are $x=0$ and $y=0$) showing that the numerical instabilities are minor enough to guarantee that the branching occurs due to physical inhomogeneities. The propagation direction of the main streamer column is in $-z$ direction. The left panel shows iso-surface plots of the electric field generated by streamer branching from different view planes (*xy*, *xz* and *xy* plane views).

6.5 Geometry of Streamer Head: Deterministic Causes of Branching

Streamer branching occurs due to both deterministic and stochastic origins in low and high density gases, liquids and even solids [4-12]. To better understand the underlying deterministic causes that make the streamer shell tear apart at the streamer head, it is interesting to study the relationship between the branching dynamics and the structure of the streamer head to realize whether branching occurs, and if yes, how many propagating branches come out of the main streamer stem (also known as a leader). To be able to quantify this relationship, we have defined three characteristic lengths: r_a , r_b and d based on the volume charge density distribution ($0.5\rho_{max}$ to ρ_{max}) and the head curvature ratio, $\alpha=r_a/d$, as shown in Figure 6.16.

These characteristic lengths can be easily measured at any time of streamer flight from the calculated instantaneous distributions of the volume charge density. Specifically, the

characteristic lengths have been measured right before the streamer branching instant. In the case that no branching is observed, the characteristic lengths are measured when the streamer head spatial structure stabilizes as it propagates towards the grounded electrode (see Chapter 5 for streamer head stabilization).

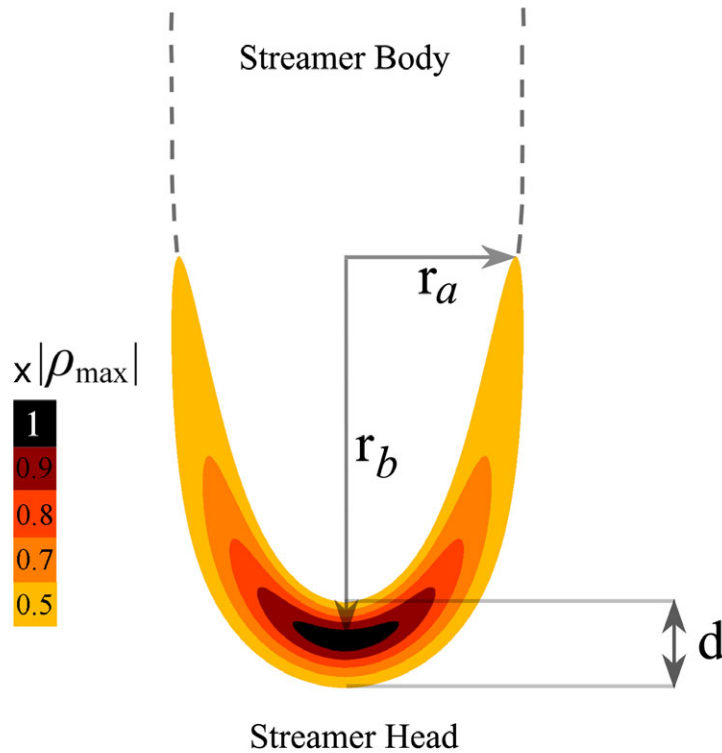


Figure 6.16: Streamer head configuration defined based on distribution of volume charge density. Three characteristic lengths, r_a , r_b and d are defined based on the distribution of charge density magnitude ($0.5\rho_{max}$ to ρ_{max}) to study the streamer head instability growth, which ultimately cause the branching. Numerical modeling shows that the chance of branching increases as the head curvature ratio $\alpha=r_a/d$ increases. Our previous studies on the 2-D streamer model (Chapter 5) show that increasing either applied voltage peak or applied voltage rate of rise would increase α .

The streamer characteristic lengths are measured from the modeling results of 280 simulation case studies and classified based upon the number of propagating branches as shown in Figure 6.17. The values shown in Figure 6.17 are averages that have been taken in each case (10 individual simulations with different inhomogeneities in each case).

The actual span of data can be seen in Figure 6.18, which shows the variation of each normalized characteristic length with an error bar.

Thin streamers usually have a relatively thick shell of streamer head, which makes the propagating streamer unable to branch out even in inhomogeneous media for two main reasons:

1. Small r_a : The streamer head is $\sim 10\text{-}20\ \mu\text{m}$ thick which increases the probability that the streamer is not influenced by microscopic inhomogeneities unless the inhomogeneity density is extremely high. At the current inhomogeneity size, $5\ \mu\text{m}$, and density, $10^{11}\ \text{m}^{-3}$, the streamer takes some detour from its main path, rather than branching out, even if a spherical inhomogeneity is close to the streamer head, since the head is strongly stable.
2. Large d : The charge density at the streamer head is relatively high which considerably increases the streamer velocity. Since the higher the streamer velocity, the lower the branching probability, relatively large d along with small r_a assists the streamer not to branch out.

As the streamer column becomes thicker (r_a increases) and the streamer head crust (d) becomes thinner (as a result of higher applied voltage peak and/or rate of rise of voltage), there are some cases in which branching does not occur even though d and r_a are fairly small and large, respectively. This indicates that neither r_a nor d is able to individually determine whether branching occurs and if it occurs how many branches come out of the original stem.

Comparing the results plotted in Figure 6.17 suggests that the important geometrical parameter which ultimately determines the occurrence of branching and the number of just born branches is the head curvature ratio $\alpha=r_a/d$, not merely r_a , r_b , or d . This ratio seems to be controlled with the applied voltage characteristics and number density and intensity of the inhomogeneities. For a given inhomogeneity, before running the 3-D model, if we know the steady streamer head geometry, α approximately determines the number of the propagating branches. In Figure 6.17, the separation lines between single column, two/three-column and multi-column streamers roughly show the critical head curvature ratio.

The value of critical curvature ratio is controlled by density and intensity of the microscopic inhomogeneities. Particularly, if either density or intensity of the inhomogeneities increases, the critical streamer head curvature ratio will decrease (slope of the separation lines in Figure 6.17 increase). Based on the results obtained from cases having different inhomogeneity densities and intensities, the critical head curvature is more sensitive to the perturbation density rather than the perturbation intensity.

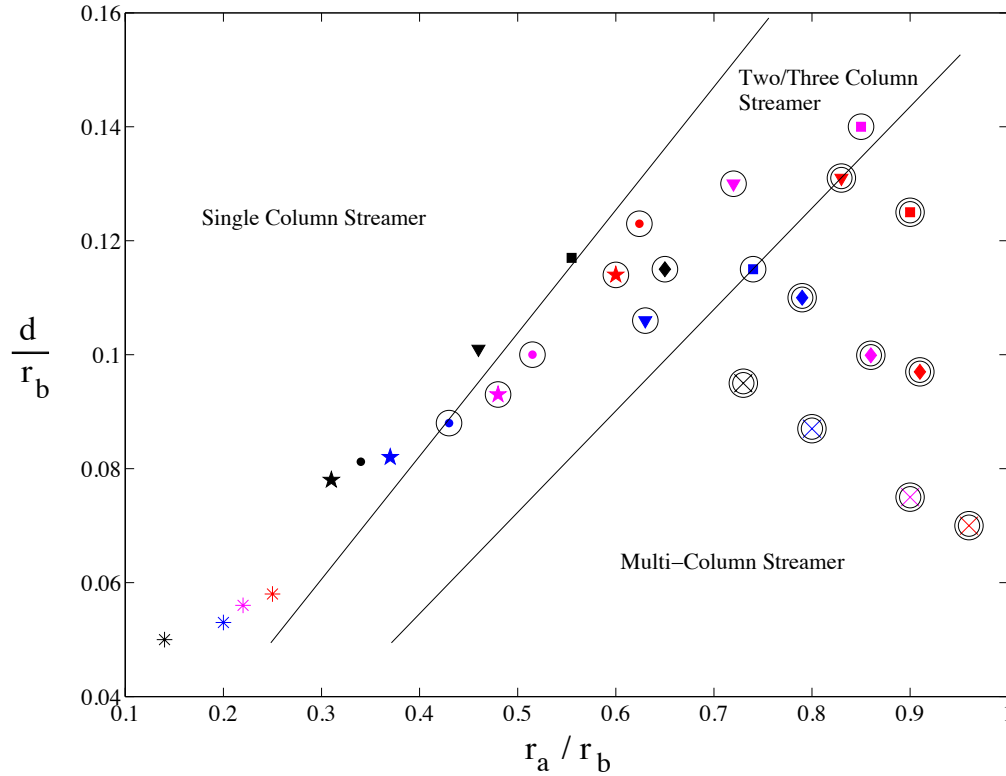


Figure 6.17: Identification of streamer tree number of branches based on the streamer head geometry (characteristic lengths defined in Figure 6.16). Colors show the applied voltage rise-times: black (1 μ s), blue (100 ns), purple (10 ns) and red (1 ns). Marker shapes indicate the applied voltage peaks: 130 kV (*), 200 kV (★), 250 kV (●), 300 kV (▼), 350 kV (■), 400 kV (◆), and 500 kV (×). The points are obtained by taking an average from ten different inhomogeneity distributions, but with the same inhomogeneity radius, maximum intensity and density of $5 \mu\text{m}$, 10^4Cm^{-3} and 10^{11}m^{-3} , respectively.

To plot Figure 6.17, the models have been re-run with ten different inhomogeneity distributions and densities obtained by ten different sets of Gaussian functions and continuous uniform distribution functions for each case study, which is shown by a point in Figure 6.17 (total 280 simulations).

The small variations of the streamer head structure (as shown in Figure 6.18) and more importantly the occurrence of branching and the ultimate number of propagating branches in these ten different sets indicate that the deterministic origins of streamer branching are dominant (within the boundaries of $|G_{Mp}| < 10^{10} \text{Cm}^{-3}\text{s}^{-1}$, $|\rho_p| < 10^4 \text{Cm}^{-3}$, $C_p = 10^{11} \text{m}^{-3}$, $1 \mu\text{m} < R_p < 10 \mu\text{m}$). The qualitative shape of the streamer tree, numbers and diameters of the branches and their velocities are slightly sensitive to the inhomogeneity density and intensity.

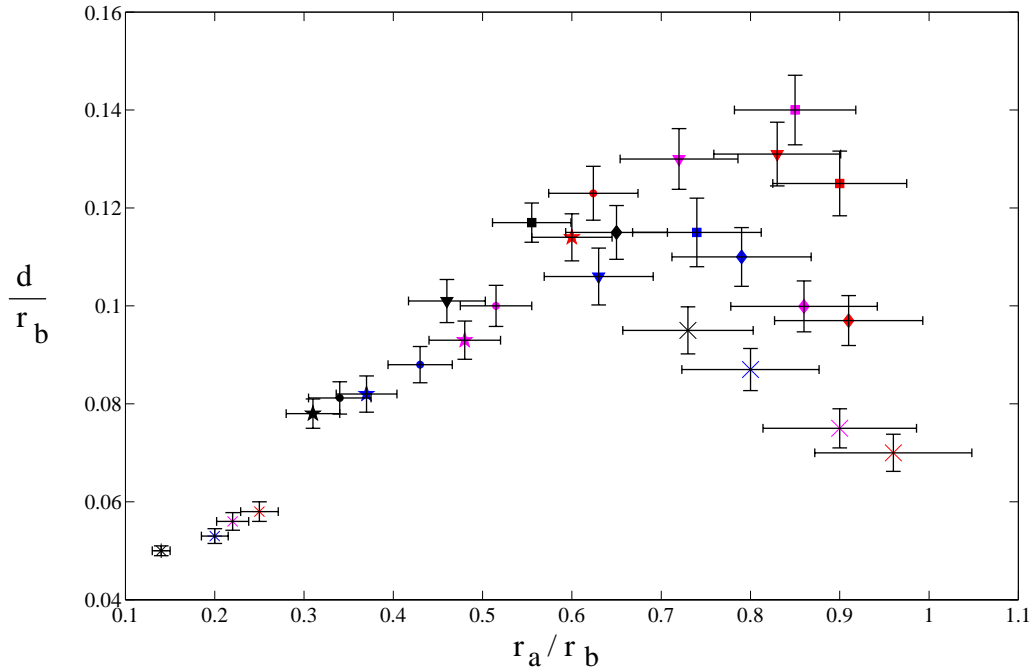


Figure 6.18: Actual span of data of each normalized characteristic length indicated with error bars. The streamer characteristic lengths are measured from 280 simulation cases (10 individual simulations with different inhomogeneities in each case) modeled within the parameter boundaries of $|G_{Mp}| < 10^{10} \text{ Cm}^{-3}\text{s}^{-1}$, $|\rho_p| < 10^4 \text{ Cm}^{-3}$, $C_p = 10^{11} \text{ m}^{-3}$, $1 \mu\text{m} < R_p < 10 \mu\text{m}$. The values shown in Figure 18 are midpoints in each case. Colors show the applied voltage rise-times: black (1 μs), blue (100 ns), purple (10 ns) and red (1 ns). Marker shapes indicate the applied voltage peaks: 130 kV (*), 200 kV (\star), 250 kV (\bullet), 300 kV (\blacktriangledown), 350 kV (\blacksquare), 400 kV (\blacklozenge), and 500 kV (\times).

There are a number of additional interesting discussions raised by observations made on the 3-D geometrical attributes of a streamer right at branching:

- Streamer velocity drops just before branching begins. After branching, each individual branch accelerates again. In the two/three column streamer region (Figure 6.18), one of the streamer branches usually picks up the maximum velocity, which is clearly higher than other branch velocities. This maximum velocity agrees with experimental evidence found in the literature, even closer than the 2-D axisymmetric modeling results. However, for multiple column streamers (especially for four streamer branches or more), almost all of the child branches propagate with roughly similar velocity, which is lower than the velocities reported in experimental records [3,18,60].
- For a given perturbation intensity, the number and thickness of the streamer branches are determined by the applied voltage, unless its diameter is larger than a certain value. This threshold size in the presented perturbation density and intensity is $10 \mu\text{m}$. In other words, for inhomogeneity sizes above $10 \mu\text{m}$, different applied voltages create almost similar streamer trees. This is particularly reasonable, since macroscopic inhomogeneities dominantly determine the streamer behavior. In terms of the visual resemblance between

modeling results and experimental images, as presented in Figure 6.1, $5 \mu\text{m}$ inhomogeneities with a density of 10^{11} m^{-3} for the charge carriers is the optimal combination.

- Modeling results show that the spherical inhomogeneities (containing maximum charge perturbations of 10^4 Cm^{-3}) that are farther than 1 mm from the path of the streamer do not effectively cause streamer deflections or branching. Therefore, as mentioned earlier, the inhomogeneities are limited to be distributed only inside the pillbox close to the streamer tip, and spherical inhomogeneities beyond those boundaries are ignored to avoid numerical difficulties (excessive simulation time).
- After the first branching, velocities of the branches increase which makes the secondary branching unlikely at least with the current magnitude of the perturbations. It has also been observed in experiments [4,30] that the secondary branching does not happen unless the streamer branch travels over a certain distance from the original node. The ratio of branching length over streamer diameter of about 12 to 15, reported in [6], cannot be verified through the current version of the model due to computational limitations.
- Some of the case studies presented in this paper are repeated with inhomogeneities in oil permittivity with almost identical results. No significant difference was found in the branching triggered with the inhomogeneities on permittivity compared to those driven by inhomogeneities on charge density. We have examined water droplets, air bubbles (with higher, 80, and lower, 1, relative permittivities than oil, 2.2, respectively), and conductive dust particles as microscopic perturbations [19]. The streamer crust is attracted to the bubbles with high conductivities or higher permittivities (than oil), while low permittivity inhomogeneities repel the streamer head. A full discussion on the forces on the streamer head applied by the immersed objects in the liquid can be found in [45,50].
- The streamer diameters in the experimental images can be estimated to be about half of the electrodynamic diameter [29]. Therefore, the modeling results describe the streamer branch's column diameters precisely. In general, streamer photography using different approaches such as Charge Coupled Device photography, Schlieren and Shadowgraphy [13,60], is extremely difficult to use for study of streamer branching due to small dimensions and high velocities of streamers. An interesting stereo-photographic approach to resolve streamers in air is presented in [33]. In most of these studies, the scientific goal is to capture streamer trees with the most possible branches. Therefore, the applied voltage and camera shooting times have been set to guarantee a high number of branches, which makes it difficult to find the branching threshold through the images. In addition, what the streak cameras capture are not the ionized body of the streamer, but the path of the emitted light, which is most probably the path of dissipated energy (via joule heating for instance). Experimental photography is more useful to understand the fractal structure of the streamer tree not the branching phenomena itself [19]. Therefore, it seems the 3-D modeling is currently the best practical way to study the branching phenomena.

- This chapter focuses on the streamer branching in liquids. In other media, other processes may become critically important in streamer acceleration and branching. For instance in gaseous environment, other than stochastic charge density fluctuations, in intense electric field, run-away electrons can contribute to accelerating and branching of streamers [38]. A 3-D gaseous hybrid model is developed in [31] that couples a particle model for single electrons in the region of high fields and low electron densities with a fluid model in the rest of the domain.
- In addition to inhomogeneities in the dielectric volume, the small cracks and perturbations on the needle electrode should be addressed in the future. Some of the experimental images show that branching has started right at the needle itself [18].

6.6 Summary

A fully three-dimensional model of streamers is presented in this chapter to investigate the dynamics of streamer branching, which is an asymmetric phenomenon by its nature. The modeling results show that the streamer branching has deterministic origins, as well as stochastic roots. Specifically, if the volume charge layer at the streamer head is thin and slow enough, even an infinitesimal inhomogeneity is sufficient to trigger the branching. On the other hand, if the streamer head is stable, even relatively large perturbations do not grow instabilities from the streamer head.

A quantitative gauge has been derived for the streamer head geometry that determines whether branching occurs under specific inhomogeneous circumstances. The critical ratio of the streamer charge sheath thickness over the streamer width, at which branching occurs, is found for the specific density and intensity of inhomogeneities.

Comparing the modeling results with corresponding experimental images indicates that the model predicts the branching phenomena both quantitatively and qualitatively. In terms of the visual resemblance between modeling results and experimental images, 5 μm spherical inhomogeneities with a spatial number density of 10^{11} m^{-3} is an optimal combination in transformer oil.

Surface Flashover Formation and Growth on Liquid Immersed Dielectrics

In this chapter, flashover formation and expansion mechanisms on the interfaces of different Liquid Immersed Dielectrics (LIDs) has been numerically analyzed. The immersed dielectrics including solid dielectrics, such as Polytetrafluoroethylene (PTFE) and pressboard, and a gaseous dielectric, Sulfur hexafluoride (SF_6) in transformer oil are addressed in this chapter.

It has been reported in the literature that streamer propagation in oil is greatly affected by the permittivity mismatch between the bulk liquid (transformer oil) and the immersed dielectric (pressboard). As shown in Figure 7.1, the experimental records show that the system has the optimum electrical performance and the least breakdown damage in the case that the liquid and solid permittivities are as close as possible [63].

Significant effort has been taken to understand the effects of immersed barriers on the streamer propagation with a focus on the permittivity difference between the liquid and the immersed dielectric. An extended version of the model introduced in Chapter 5 is used in this chapter with appropriate boundary conditions on the interfacial surfaces, to simulate formation of surface flashovers from approaching streamers along the immersed dielectric interface.

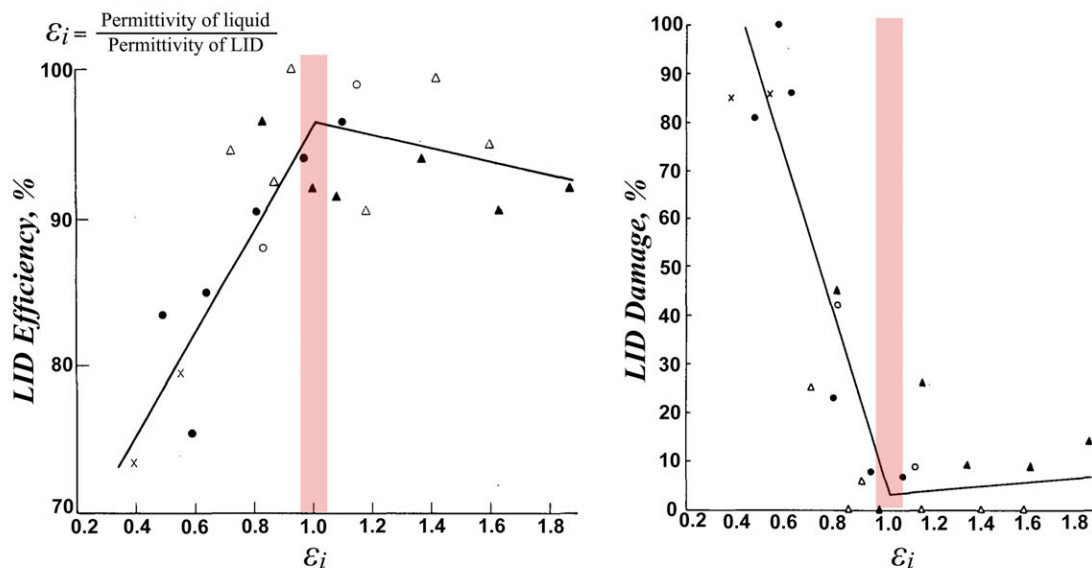


Figure 7.1: Efficiency (left) and damage percentage (right) of liquid immersed solid LID versus interfacial permittivity ratio, ϵ_i , which is the ratio of liquid permittivity over the LID permittivity, for different pressboard materials (different plotted symbols), as reported in [63]. The dielectric efficiency is maximum and the damage on the immersed dielectric is minimum where the permittivities are equal, $\epsilon_i = 1$.

Streamers emanating from the needle electrode tend to transform to surface flashovers, if the immersed dielectric permittivity is higher than the liquid permittivity and/or the dielectric interfacial surface cuts the path of the streamer.

The behavior of streamers near the LID interface is predominantly rationalized by forces applied by LID to the streamer volume charge due to permittivity differences of the liquid and immersed dielectrics. The perpendicular interface of the immersed dielectric impedes the breakdown by deflecting the streamer and slowing down the surface flashover. The parallel dielectric interface, however, assists the breakdown by regulating the surface flashover velocity to an approximately constant value (~ 10 km/s).

7.1 Streamer Interaction with Perpendicular and Parallel Liquid Immersed Dielectric Interfaces

In practice, liquid dielectrics are not used without immersed solid insulation systems as their insulation properties in long electrode gaps are not quite satisfactory [2,13,50]. Solid dielectrics used in high voltage apparatus provide both electrical and mechanical support for the entire insulation system [1,2,107]. Presence of solid dielectrics between the high voltage sections and low voltage and grounded sections of the equipment means that the streamers forming within the liquid dielectric usually have to confront the surface of liquid immersed barriers in their flight inside the high voltage equipment. In general, streamers approaching a second dielectric with different characteristics from the bulk liquid intensify electric field on the interface of the dielectrics [50,107]. In extreme cases, streamers can punch the solid dielectric and cause the breakdown. However, in most cases, streamers hit the LID surface, accumulate free surface charge on the interface and eventually cause an accelerated charge transport on the interface (called surface flashover) leaving conducting traces that can result in further degradation of the surface dielectric strength. A surface flashover can creep along a Liquid Immersed Dielectric (LID) interface for long distances (even faster than streamers [13,25,50]) under about two orders of magnitude lower electric field intensities compared to the streamers forming in the liquid-only system [50,108]. For instance, streamers usually initiate at 1MV/cm in transformer oil [22,50], while surface flashovers on the transformer oil/pressboard interface initiate at 10-20 kV/cm [106-109].

The three-carrier continuum model, described in Chapter 5, is extended in two-dimensional axisymmetric geometry to describe the surface flashover formation and expansion along the LID interface. The governing equations that contain the physics to model streamer/flashover developments (quite similar to the streamer model) are based on the drift-dominated charge continuity equations for positive ion, negative ion and electron charge densities, coupled through Gauss' law. The thermal diffusion equation is also included to model temperature dynamics, predict phase conversions and model the temperature dependent mobility of different charge species [48]. The ionization function, recombination terms and all of the boundary conditions on

the electrodes are set similar to a model previously used for streamers initiated from a sharp needle electrode in the oil-only system [22,48]. At LID interfaces, a set of boundary conditions accounts for the surface charge density, $\sigma_s(t)$, which is always equal to the local jump in the normal (perpendicular) component of the displacement field across the interface. The tangential electric fields on either side of the surface also must be equal at any point of the interface.

$$\begin{cases} \varepsilon_{LID} E_{\perp LID}(t) \Big|_{\text{interface}} - \varepsilon_l E_{\perp liquid}(t) \Big|_{\text{interface}} = \sigma_s(t) \\ E_{\parallel LID}(t) \Big|_{\text{interface}} = E_{\parallel liquid}(t) \Big|_{\text{interface}} \end{cases} \quad (7.1)$$

At the same time, the time derivative of the surface charge density must be equal to the difference in the normal component of current density on either side of the interface.

$$\frac{d\sigma_s(t)}{dt} = J_{\perp LID}(t) \Big|_{\text{interface}} - J_{\perp liquid}(t) \Big|_{\text{interface}} \quad (7.2)$$

As mentioned before, the current density in the liquid region is calculated by migration currents as shown in equation (5.4), while the governing equation in the LID is defined by Ohms' law:

$$\vec{J}_{LID}(t) = \sigma \vec{E}_{LID}(t) \quad (7.3)$$

where σ is the Ohmic conductivity of the LID. The underlying assumption for our two-phase model is that the LID has zero conductivity. In practice, the conduction through LID cannot contribute to the charge transport between electrodes in the sub-microsecond time-constants of interest in this paper, since conductivity of the LID is negligible (less than $10^{-13} \Omega^{-1} \text{m}^{-1}$). Therefore, the governing equation for the perfect insulator model of the LID is merely Gauss' Law with zero space charge (i.e., Laplace's equation). The relative permittivity (ε_r) of the liquid is set to 2.2 that represents the transformer oil, while LIDs are examined having permittivities 2.1, 4.4 and 1.1 that represent Polytetrafluoroethylene (PTFE), pressboard and Sulfur hexafluoride (SF_6) at 5-bars, respectively, (Table 7.1). As shown in Figure 7.2, LID interfacial surfaces are oriented in parallel (an axial concentric cylindrical bore in LID bulk with 0.1-mm diameter) and in perpendicular (a 10-mm thick LID disk placed 1-mm from the needle) to the primary streamer propagation direction.

Table 7.1: Parameters of investigated transformer oil-immersed dielectrics

Dielectric	Parameter	Symbol	Value
Pressboard	Permittivity	ε_{pb}	$4.4 \varepsilon_0$
	Conductivity	σ_{pb}	$\sim 0 \Omega^{-1} \text{m}^{-1}$
Polytetrafluoroethylene (PTFE)	Permittivity	ε_{PTFE}	$2.1 \varepsilon_0$
	Conductivity	σ_{PTFE}	$\sim 0 \Omega^{-1} \text{m}^{-1}$
Sulfur hexafluoride (SF_6)	Permittivity	ε_{SF_6}	$1.1 \varepsilon_0$
	Conductivity	σ_{SF_6}	$\sim 0 \Omega^{-1} \text{m}^{-1}$

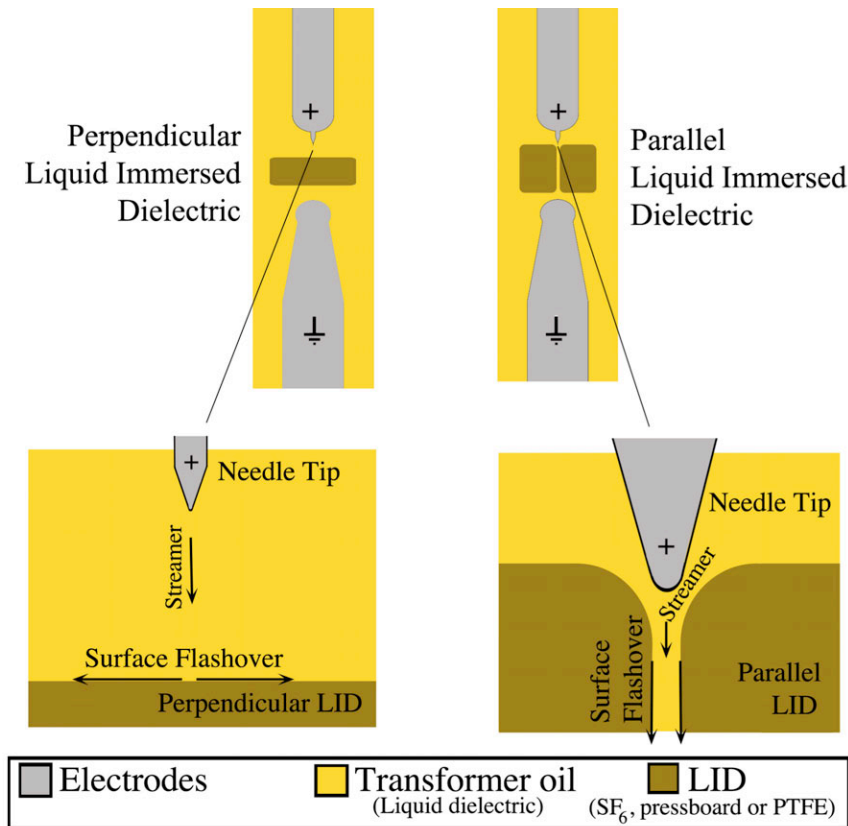


Figure 7.2: Perpendicular (left) and parallel (right) liquid immersed dielectric (LID) configurations in 25 mm apart needle-sphere electrode geometries. Two bottom panels show closer views of the perpendicular (left) and parallel (right) immersed dielectrics just next to the needle electrodes. Streamers initiate from the positive needle electrode, elongate through the oil bulk and possibly settle on the LID surface as shown by arrows in the bottom panels. The distance of the perpendicular interfacial surface from the needle electrode tip varies in the range of 1- 4 mm and the diameter of the parallel bore varies between 100-400 μm .

Figure 7.3 shows the typical streamer behavior in transformer oil as it reaches the LID interface. The pressboard whose permittivity is higher than transformer oil tends to attract the streamer crust to the interface (Fig. 7.3 (b) and (d)), while lower permittivity SF_6 repels the streamer crust (Fig. 7.3 (a) and (c)). Therefore, the streamer becomes slower and thicker when approaching the perpendicular SF_6 surface and becomes faster and thinner close to the perpendicular pressboard interface compared to streamers propagating in an oil-only system [22,48]. Streamers are pulled and become surface flashovers by settling alongside the parallel pressboard interface, while a parallel SF_6 interface squeezes streamers by repelling them in the concentric parallel bore (compare panels (c) and (d) in Fig. 7.3). Volume charge density and surface charge density remain constantly high along the track of the surface flashover even if the flashover edge is millimeters away. In the next sections of this chapter, the behavior of the streamers and surface

flashovers will be studied at interfacial surfaces of pressboard, PTFE and SF₆ with parallel and perpendicular orientations.

The behavior of a streamer at the LID interface can be explained using the method of images [52,64] for interfaces with different permittivities. Since a streamer carries a significant amount of free charge, the force on the streamer due to the LID interface can be assumed to be produced by the electric field from the image charge in the LID that is proportional to the permittivity difference between transformer oil and LID, $\epsilon_{LID} - \epsilon_{Oil}$. If the LID permittivity is higher than oil ($\epsilon_{LID} - \epsilon_{Oil} > 0$), then the electrical force pulls the free charge (streamer) towards the interface (attraction). On the other hand, if the LID permittivity is lower than oil ($\epsilon_{LID} - \epsilon_{Oil} < 0$), the surface (image charge) repels the free volume charge in the oil (streamer), regardless of the free charge's polarity [64,50].

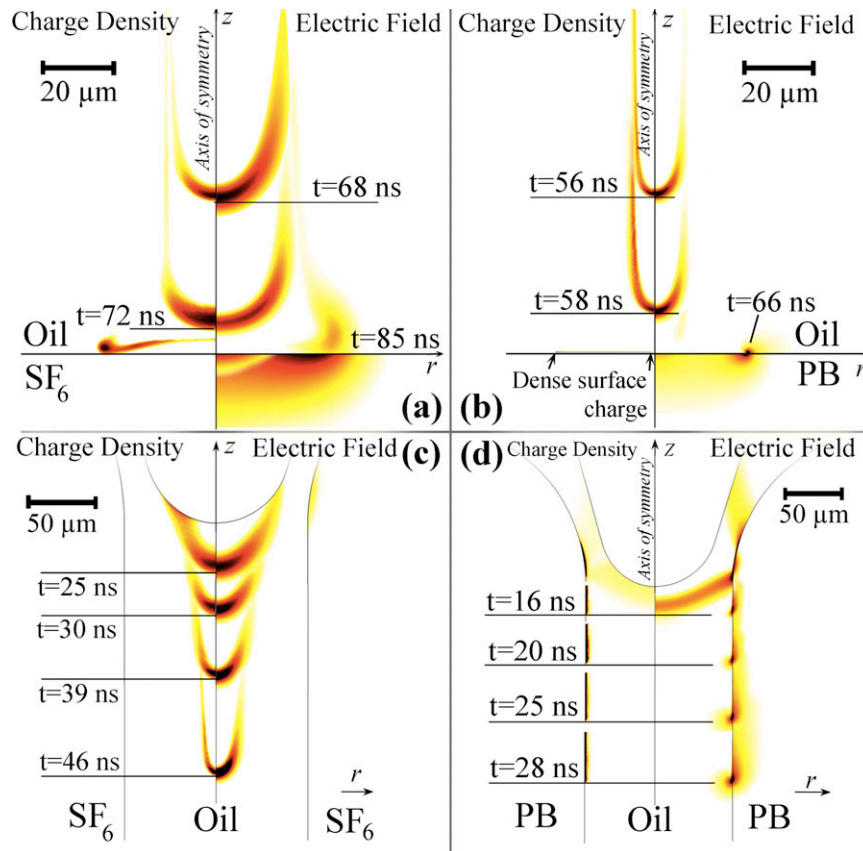


Figure 7.3: Streamer/surface flashover initiation on the perpendicular [panels (a), (b)] and parallel [panels (c), (d)] LID interfaces. The streamer formed in oil emanates from a needle under an impulse voltage with 400 kV peak and 0.1 μ s rise-time hits the SF₆ surface [panels (a), (c)] and the pressboard surfaces [panels (b), (d)]. In each panel, the left hand side picture shows the normalized volume charge density (from $0.5|\rho_{max}|$ (the brightest color) to $|\rho_{max}|$ (the darkest color)) and the right hand side picture shows the normalized electric field magnitude (from $0.5|E_{max}|$ to $|E_{max}|$). Values of $|E_{max}|$ and $|\rho_{max}|$ are (a): $|E_{max}|=2.2 \times 10^8$ V/m, $|\rho_{max}|=7.71 \times 10^2$ C/m³, (b): $|E_{max}|=2.9 \times 10^8$ V/m, $|\rho_{max}|=1.85 \times 10^3$ C/m³, (c): $|E_{max}|=2.8 \times 10^8$ V/m, $|\rho_{max}|=2.31 \times 10^3$ C/m³ and (d): $|E_{max}|=3.21 \times 10^8$ V/m, $|\rho_{max}|=4.88 \times 10^3$ C/m³ respectively.

For a point-charge placed in the liquid next to a semi-space with a different permittivity, the image charge, and the resulting force from it is calculated in [64]. In particular, for the point charge, q , placed in the oil region, at the distance d from the barrier, the image charge in the barrier, q' , and the force applied by the barrier, f , are

$$q' = q \frac{\epsilon_{Oil} - \epsilon_{PB}}{\epsilon_{Oil} + \epsilon_{PB}} \rightarrow \vec{f} = \frac{qq'}{4\pi\epsilon_1(2d)^2} \hat{x} = \frac{q^2(\epsilon_{Oil} - \epsilon_{PB})}{16\pi\epsilon_1 d^2 (\epsilon_{Oil} + \epsilon_{PB})} \hat{x} \quad (7.4)$$

Therefore, the streamer force applied by the surface charge accumulated on the barrier interface is proportional to $([\epsilon_{Oil} - \epsilon_{PB}] / [\epsilon_{PB} + \epsilon_{Oil}])$, meaning that the greater the permittivity difference across the interface, the stronger the force. In addition, since streamers carry significant amounts of free charge, the force on the streamer applied by the barrier interface (equal to the force due to the image charge in the barrier) is usually strong enough to either settle the streamer on the surface or deflect it away from the surface. In the limiting case, the force on the streamer head goes to infinity as the streamer head reaches the surface (i.e., d goes to zero).

On the other hand, if the barrier and oil permittivities are equal ($\epsilon_{PB} - \epsilon_{Oil} = 0$), there will be no image charge in the solid dielectric and consequently, the force is zero. This is particularly true for those solid dielectrics that have permittivities of $\sim 2.2\epsilon_0$ such as PTFE [50,109].

By substituting the point charge q with an arbitrary volume charge density, ρ , such as that of the approaching streamer (Figure 7.4), the polarization force can be determined by calculating the volume integral of equation (7.4). In particular for the streamer shown in Figure 7.4, regardless of the polarity of the charge which the streamer carries, the force on differential sections of the free charge will be upward (repelling) if the permittivity of LID is smaller than the liquid and downward (attracting) if the permittivity of LID is greater than the liquid.

Comparing right and left sides of Figure 7.3 shows that the streamers close to barrier with relative permittivity of 4.4 become narrower and faster due to the attractive force, while they become slower and bushier when approaching the barrier with relative permittivity of 1.1 due to the repelling force applied by the image charge.

Using equations 7.1-7.3, the intensity and direction difference across the interfacial surface of two dielectrics due to the difference of permittivity can be determined. Figure 7.5 shows a typical situation at the interfacial surface of oil and pressboard before the streamer reaches there. The left side of the figure shows that the electric field magnitude, in the absence of surface charge density, is greater in low permittivity pressboard (lighter color) and field lines are deflected inward. The reason is that the pressboard permittivity is smaller than the oil and the normal component of the displacement field has to be continuous due to lack of surface charge density. The right hand side shows the electric field lines that are deflected outward since the pressboard permittivity is greater than the oil and there is no surface charge on the surface (surface flashover has not arrived yet).

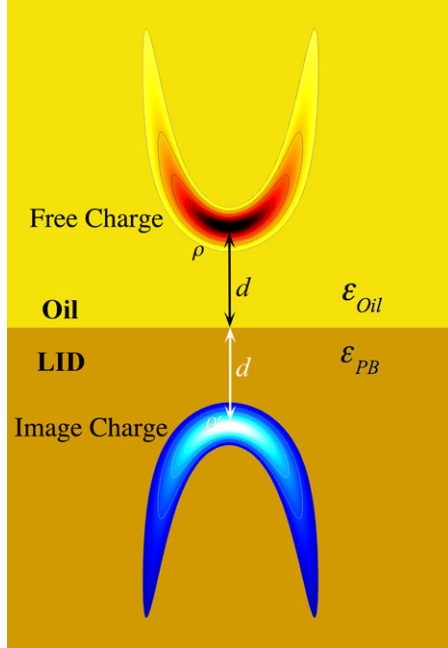


Figure 7.4: Free volume charge in the oil region and its image charge in pressboard region close to the oil immersed barrier interface. The direction and magnitude of the force on the free volume charge caused by permittivity mismatch can be calculated using the method of images [15].

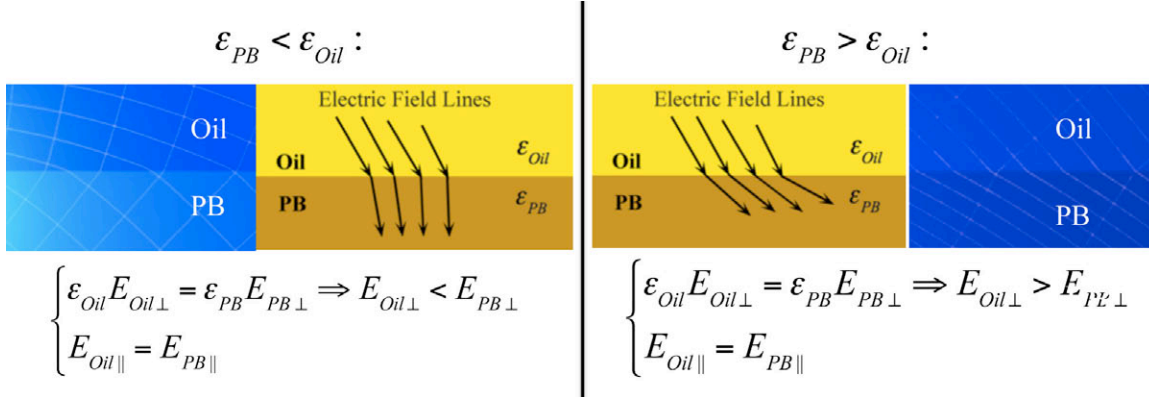


Figure 7.5: Intensity and direction difference across the interfacial surface of two dielectrics due to the difference of permittivity. Left side of the figure shows the reason that the electric field magnitude is greater in the pressboard region (in absence of surface charge density) and field lines deflect inward when the pressboard permittivity is smaller than the oil. The right hand side shows the reason that the opposite is true when the pressboard permittivity is greater than the oil.

7.2 Surface Flashover Development on Parallel Liquid Immersed Dielectric Interface

Experimental evidence has shown that streamer propagation is dramatically altered when the streamer comes in contact with a parallel immersed-dielectric interface [10,13,104,108]. The modeling results show that the parallel LID interface assists streamer/surface propagation regardless of the LID permittivity. If the permittivity of the pressboard is greater than the liquid, the streamer usually transforms into a surface flashover due to the attracting force. On the other hand, if the LID permittivity is smaller than the liquid, the repelling force squeezes the streamers and helps them remain in streamer propagation mode [50].

The surface flashover velocity on the parallel LID interface depends strongly on the applied voltage peak, while the shape of the flashover is not appreciably affected by the voltage peak. Instead, the flashover shape is more influenced by LID permittivity as shown in Figure 7.5. The streamer is reluctant to attach to parallel LIDs whose permittivities are lower than oil, even if it propagates through an extremely narrow bore. The main difference between parallel PTFE and SF₆ interfaces is that the streamer does attach to the PTFE surface under applied voltages with peaks higher than 250 kV in a bore with diameters smaller than 0.1 mm (Fig. 7.4, part (b)). If the applied voltage peak is not high enough, the flashover dissociates from the PTFE surface and returns to streamer mode after initial attachment (Figure 7.6, part (a)). Streamers immediately attach to the parallel pressboard surface and remain in surface flashover mode steadily keeping a similar shape over time for different applied voltage peaks (Fig. 7.4, part (c)).

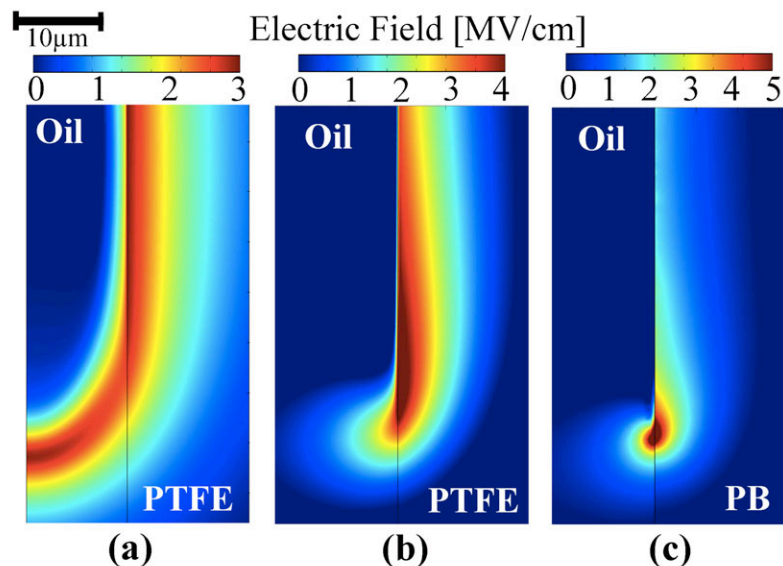


Figure 7.6: Electric field distribution for flashovers expanding on the parallel LID surface under positive applied impulse voltage with (a): 200 kV peak and (b,c): 400 kV peak all with 0.1 μ s rise-time. Panels (a) and (b) show surface flashover on PTFE and panel (c) shows surface flashover on a pressboard interface. At all panels, the flashover edge is about 1 mm from the needle tip.

7.2.1 Liquid Immersed Dielectrics with Greater Permittivity than the Liquid

Attracting polarization force applied by the LID due to its greater permittivity quickly makes the streamer charge density settle down on the surface of the interface as shown in Figure 7.7. The force also keeps flashover shape narrow on the surface by attracting the volume charge near the surface into the interface. This significantly increases the volume charge density next to the surface and the surface charge density sitting on the surface which consequently escalates the resulting electric field ahead of the surface flashover and accelerates the surface flashover expansion.

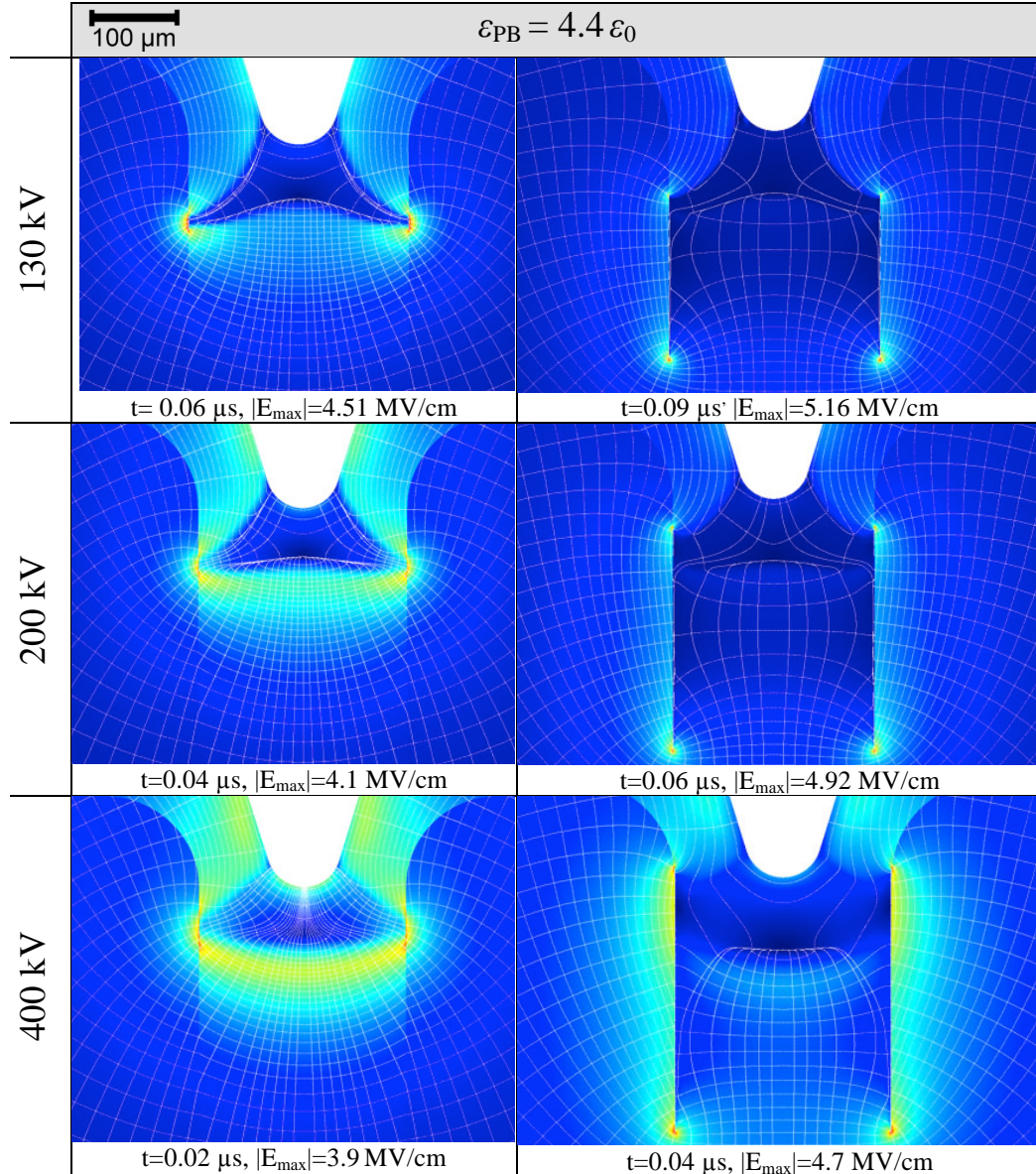


Figure 7.7: Electric field magnitude distribution for parallel pressboard (PB) interface. The streamers are formed by impulse voltages with 130 kV (first row), 200 kV (second row) and 400 kV (third row) peak amplitudes, all with $0.1 \mu\text{s}$ rise-time. $E_{\text{min}} \approx 0$ and E_{max} is given in each panel. E_{min} E_{max}

7.2.2 Liquid Immersed Dielectrics with about the Same Permittivity as the Liquid

Based on the method of images, it is expected that a LID with approximately similar dielectric constant as the liquid would impose negligible force on the free volume charge of the streamer. In this case, since the force applied by the dielectric is negligible, the surface flashover is not likely to form unless the interfacial surface somehow cuts the path of the streamer, which is not the case in the parallel LID interface shown in Figure 7.8.

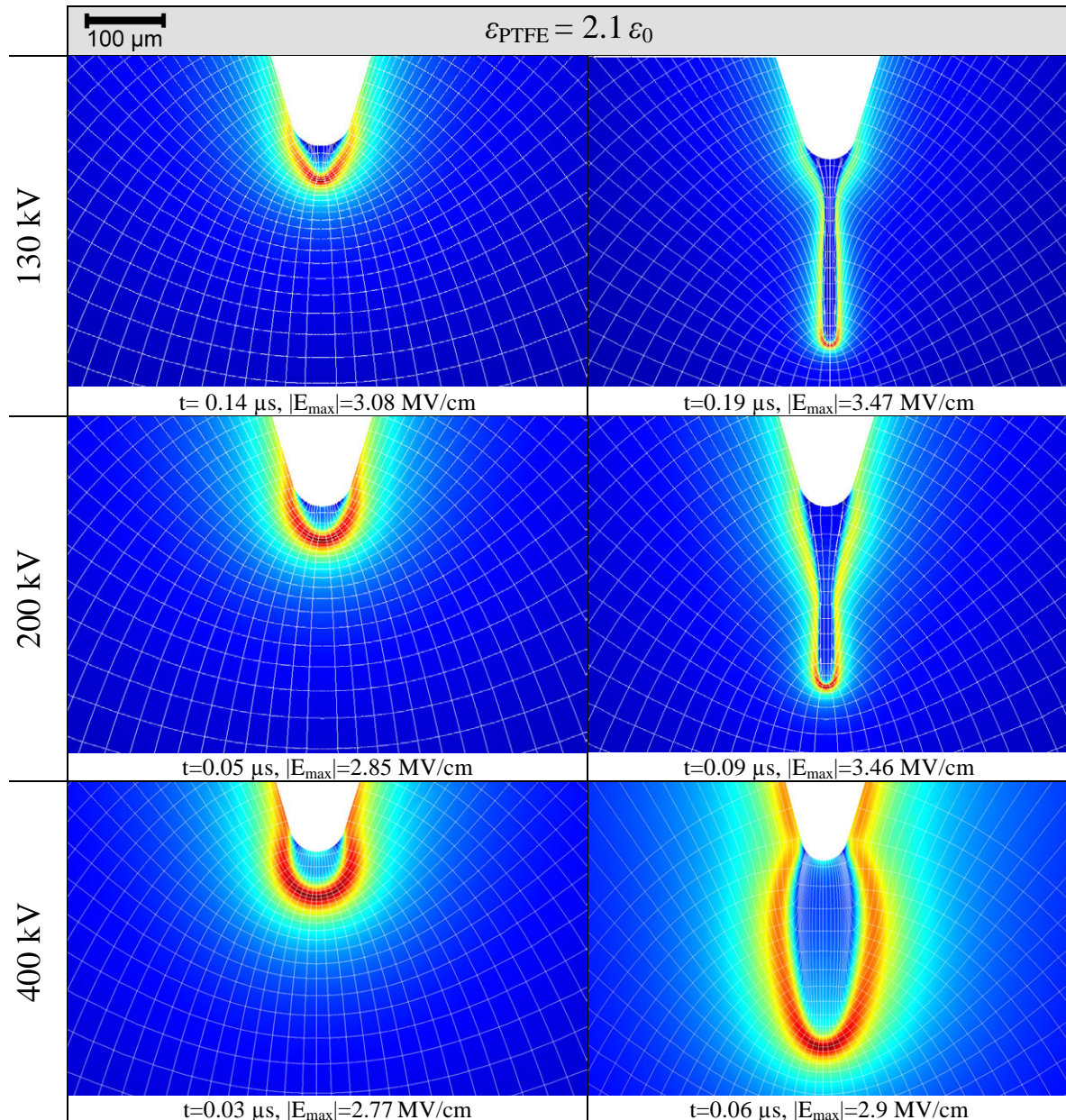



Figure 7.8: Electric field magnitude distribution for a parallel PTFE interface. The streamers are formed by impulse voltages with 130 kV (first row), 200 kV (second row) and 400 kV (third row) peak amplitudes, all with 0.1 μs rise-time. $E_{\min} \approx 0$ and E_{\max} is given in each panel. E_{\min}  E_{\max}

In Figure 7.8, although the relative permittivity of PTFE (2.1) does not quite match the relative permittivity of the oil (2.2) there is no visible change in the intensity and direction of the electric field in the panels of the figure. In fact, the interface cannot be recognized in any of panels in Figure 7.8 due to the continuity in electric field line direction and the smoothness in the electric field intensity variation.

When the LID permittivity matches the liquid dielectric constant, although the polarization force is about zero, the accumulated charge on the interfacial surface (if available) still can put some force on the streamer volume charge. The modeling results indicate that this force is much smaller than the polarization force.

7.2.3 *Liquid Immersed Dielectrics with Smaller Permittivity than the Liquid*

Compared to Figure 7.8 (where there is almost zero force on the streamers), the repelling force on streamers is evident in all panels of Figure 7.9, which shows the streamer propagation within the liquid filled bore inside a low permittivity LID. As explained in Figure 7.5, the higher intensity of the electric field in the LID region is because the LID permittivity is smaller than the liquid in Figure 7.9.

As can be seen in Figure 7.9, there is no flashover formed on the LID surface even at higher peaks. It is particularly interesting to compare the thickness of the streamers of Figure 7.9 with streamers formed by similar applied voltages in Chapter 5.

The experimental records show that the low permittivity immersed barriers are as dangerous as high permittivity barriers in terms of the electric breakdown [106-109]. Based on modeling results, these two types of dielectrics increase the risk of breakdown in completely different ways. High permittivity immersed barriers tend to transform streamers into rapidly growing flashovers, while low permittivity parallel increase streamer volume charge density by compressing them. Compressed streamers intensify the electric field ahead of them, which consequently increase the average velocity of streamer and the chance of breakdown.

In addition to the modeling results it can also be proven, using the method of images, that parallel high permittivity LIDs accelerate the charge transport between the two electrodes by attracting the streamers into the interface and make them settle on the surface. The parallel low permittivity barriers, on the other hand, intensify the volume charge density of the streamer and the electric field around them by squeezing the streamer crust. Accelerating the charge transport between high voltage electrodes increases the risk of a successful breakdown. This justifies the fact that the most popular industrial pressboards have approximately similar dielectric constant as the liquid dielectric. The great industrial interest in LIDs with matched permittivity is due to the larger breakdown voltages recorded for composite insulation systems containing liquid dielectric and LIDs with similar permittivities [62,110,111].

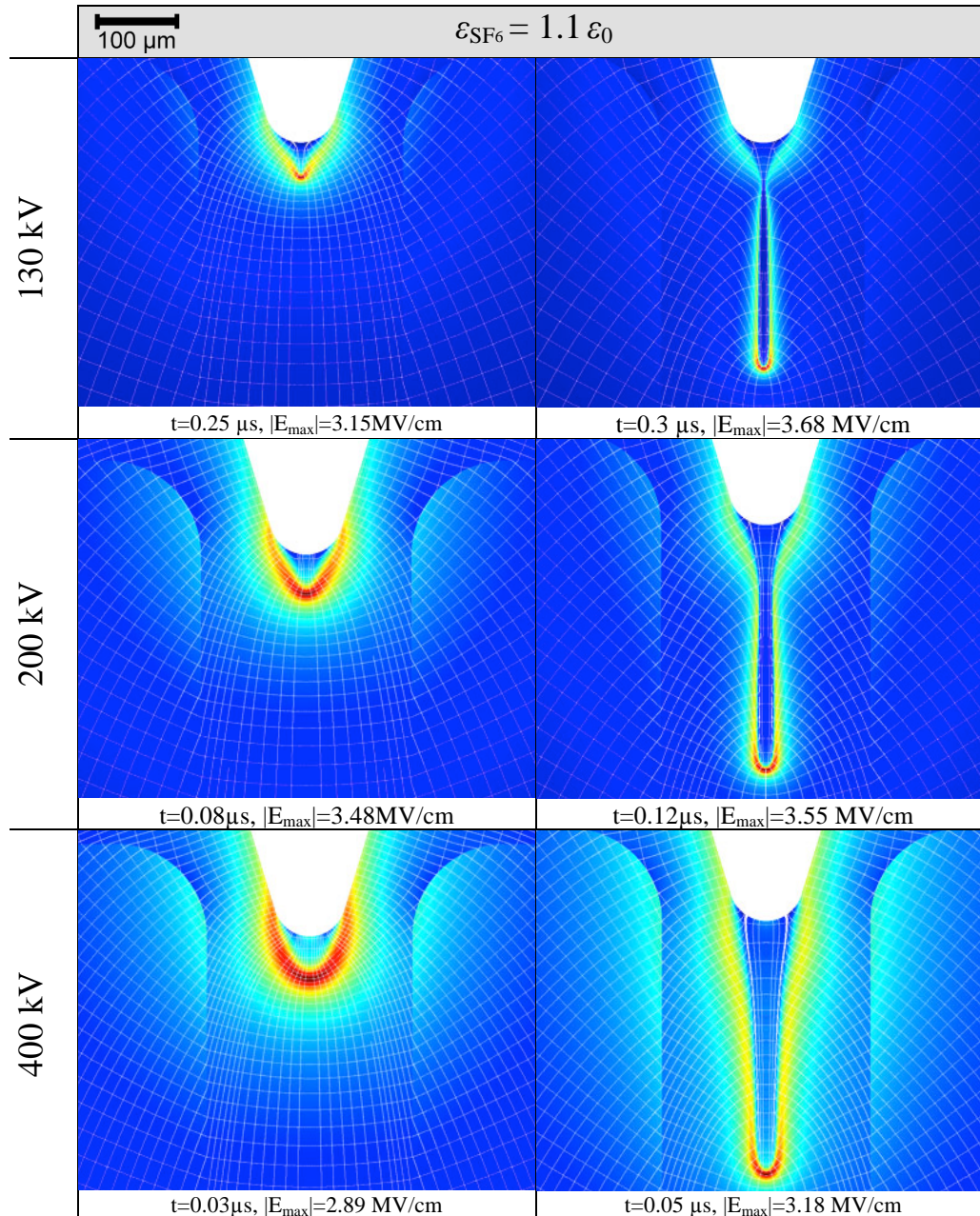


Figure 7.9. Electric field magnitude distribution for parallel SF₆ interface. The streamers are formed by impulse voltages with 130 kV (first row), 200 kV (second row) and 400 kV (third row) peak amplitudes, all with 0.1 μs rise-time. $E_{min} \approx 0$ and E_{max} is given in each panel. E_{Min} E_{Max}

As shown in Figure 7.10, the velocity of streamers on all parallel interfaces is regulated such that the surface flashover expands with approximate constant velocity along the interface, regardless of the extent of the LID. In the oil-only system, however, the streamer velocity is subject to dramatic changes [48,49] as shown in Figure 7.10 (the slope of the streamer trajectory in oil-only

system is not constant). The streamers, in oil-only systems, become continuously narrower as they propagate toward the sphere electrode that results in higher local electric fields, higher charge generations and eventually higher velocities that are continuously increasing. Despite streamer mode, in the surface flashover mode, the charge density at the surface flashover edge remains almost constant as it propagates along the parallel interface, which results in an approximately constant surface flashover velocity. This is particularly true for those cases that secondary electron emission can be ignored (i.e., most of solid LIDs) [107]. Secondary electron emission plays an important role in surface flashover propagation on solid dielectric interfaces with gaseous dielectrics and especially vacuum [103,107]. The constant velocity of the surface flashover on the parallel LID interface slightly increases as the applied voltage peak increases. The LID permittivity has small effects on the flashover velocity especially at higher voltages (greater than 200 kV). According to Figure 7.10, even if the streamer never attaches to the parallel LID interface, it still travels with approximately constant velocity within the concentric bore (constant velocity region) under the influence of the charge build up on the LID surface. In other words, if the streamer is forced to travel within a bore in the LID, whether it attaches to LID or not, the streamer velocity is regulated. The constant velocity of streamer trapped in the bore is caused by the fact that the streamer head retains its radius of curvature and the surface charge distribution pattern on the adjacent parallel LID interfaces also remains the same. The constant velocity region within the concentric parallel bore can be used as an interesting feature to design low jitter closing switches.

7.3 Surface Flashover Development on a Perpendicular Liquid Immersed Dielectric Interface

It has been shown that for the case where the LID surface orientation is parallel to the primary direction of the electric field component, the interface accelerates streamer propagation and aids in breakdown (compare the slope of the surface flashover and streamer trajectories in Figure 7.10) [10,13,104,108]. Perpendicular LIDs usually slow down the streamer propagation unless the LID fails (hitting streamer punches the LID and penetrates it).

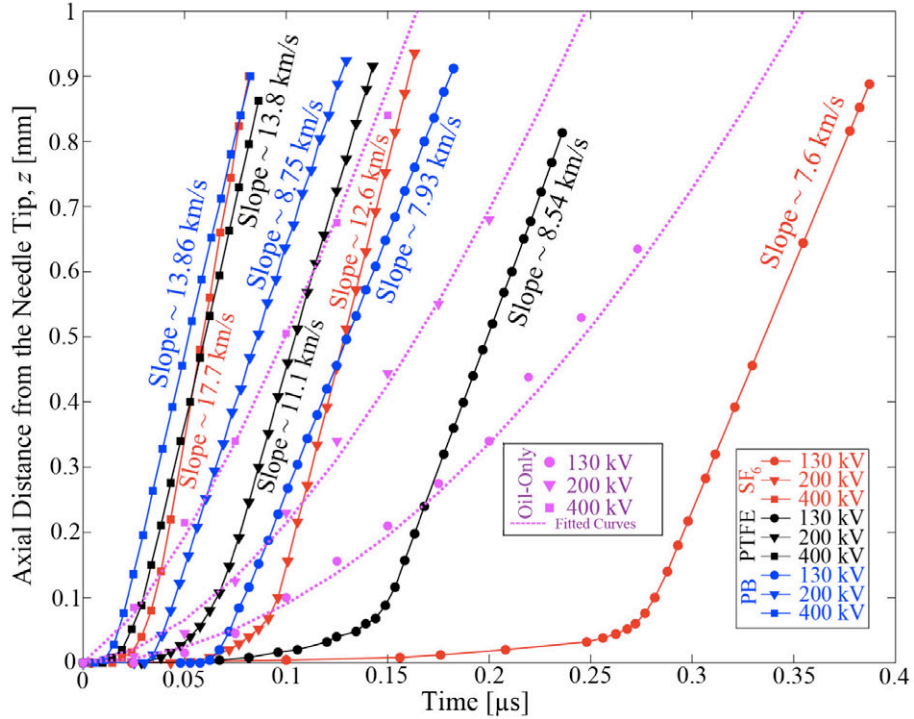


Figure 7.10: Surface flashover edge trajectories on the parallel LID surface against time under applied impulse voltage with 130 kV, 200 kV and 400 kV peaks and 0.1 μs rise-time. Purple markers and dashed curves show streamer head positions in oil-only system adapted from ². Time $t=0$ corresponds to the time that streamer reaches the parallel LID interface. Purple dotted curves are fitted polynomial expressions as $1.8 \times 10^{12} t^{1.9}$, $1.7 \times 10^{11} t^{1.7}$ and $2.3 \times 10^9 t^{1.38}$ [mm] for streamers formed by 130 kV, 200 kV and 400 kV, respectively in oil-only systems which are valid for $t < 1 \mu\text{s}$.

Figure 7.11 shows the electric field magnitude distribution at the perpendicular LID surface 1 mm from the needle tip under applied impulse voltage peaks of 130 kV (top), 200 kV (middle) and 400 kV (bottom) for pressboard (left panel) and SF_6 (right panel). The surface flashover is faster and thicker at higher applied voltages for different LIDs. In oil-only systems, the streamer column diameter is prominently sensitive to the applied voltage amplitude [48,49]; however, the thickness of the flashover formed at 400 kV is only about 2-3 times thicker than the 130 kV surface flashover developing on the surface of perpendicular LIDs as can be seen in Figure 7.11. Instead, like the parallel LID interface, the surface flashover thickness and expansion velocity on the perpendicular LID interface are also mainly influenced by the permittivity difference across the interface such that the flashovers on the SF_6 interface are approximately five times thicker and five times slower than the flashovers that propagate on the pressboard surface formed by the same applied voltage amplitudes (Figure 7.11). These are again caused by the fact that different LIDs apply different forces (due to $\epsilon_{LID} - \epsilon_{Oil}$) to the free volume and surface charge densities.

At those points on the interface that the surface flashover has not reached yet, the electric field must be determined by the difference in permittivity, meaning that the electric field has to be

higher at regions with lower permittivity [64] simply because there is no significant surface charge build up on the interface yet, which usually dominates the distribution of the electric field magnitude. This is in agreement with results shown in Figures 7.7 and 7.11, since the electric field magnitude is appreciably higher in the oil region at the pressboard interface and is higher in the LID region at SF_6 interfaces. However, at the surface flashover track (points where the surface flashover edge has already passed), the electric field in the near field is dominated by oil volume and LID surface charge densities. The electric field generated by the surface charge superposes with the background electric field and results in a higher electric field on the perpendicular LID surface.

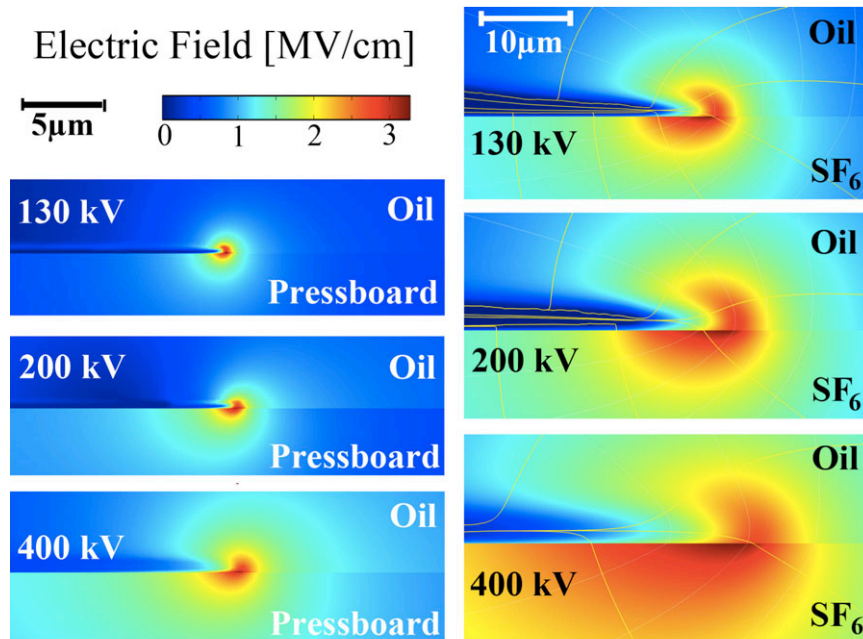


Figure 7.11: Electric field distributions at the perpendicular interfacial LID surfaces 1 mm from the needle tip for applied voltages with 130 kV (top), 200 kV (middle) and 400 kV (bottom) peaks and 0.1 μs rise-time. Left panel shows the oil-pressboard interface with size scale of 5 μm for all three sections. Right panel shows oil-SF₆ interface with size scale of 10 μm for all three sections. All surface flashover edges are 0.25 mm from the axis of symmetry. Again, it should be noted that the spatial scale of the left column is different from the right column.

7.3.1 Liquid Immersed Dielectrics with Greater Permittivity than the Liquid

Perpendicularly oriented oil immersed barriers apply polarization forces on the streamers, proportional to the permittivity difference across the interface, $\epsilon_{\text{SB}} - \epsilon_{\text{Oil}}$ [45,50,52]. In general, if the LID itself does not fail, perpendicular barriers prevent breakdown over the electrode gap. Streamers become surface flashovers (even if the barrier permittivity is smaller than the oil

permittivity) when they confront the perpendicular LIDs since the interfacial surface obstructs the streamer propagation. Perpendicular LID interfaces (with respect to axis of symmetry), in spite of parallel interfaces, which assist the breakdown by regulating the surface flashover velocity to an approximately constant value (~ 10 km/s), impede the breakdown by deflecting the streamer and slowing down the surface flashover.

Figure 7.12 shows the behavior of streamers, formed by different voltage peaks, reaching the perpendicular pressboard, having higher permittivity ($4.4 \epsilon_0$) than the oil permittivity ($2.2 \epsilon_0$).

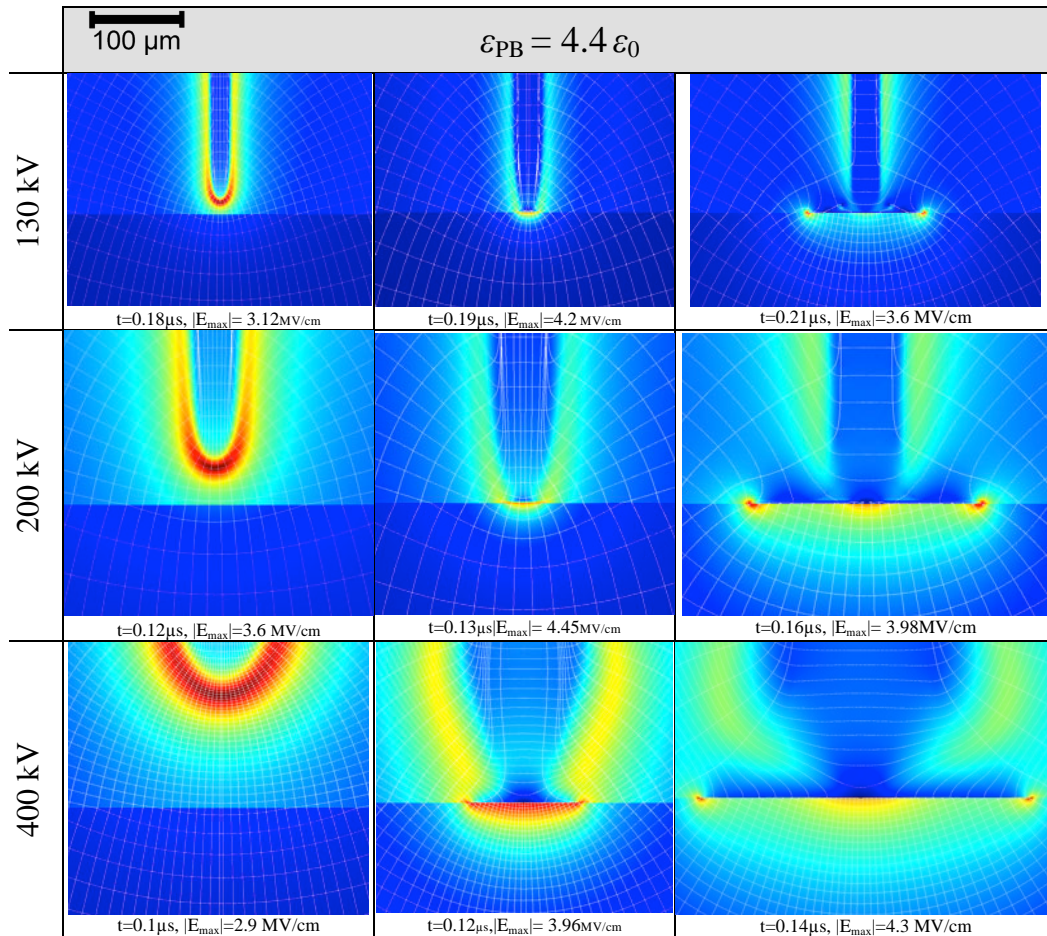



Figure 7.12: Electric field magnitude distribution for perpendicular pressboard interface. The streamers are formed by impulse voltages with 130 kV (first row), 200 kV (second row) and 400 kV (third row) peak amplitudes, all with $0.1 \mu\text{s}$ rise-time. $E_{\min} \approx 0$ and E_{\max} is given in each panel. E_{\min}  E_{\max}

As can be seen in Figure 7.12, in spite of streamers, the shape of the surface flashover does not significantly depend on the applied voltage peak. The thickness and velocity of the surface

flashovers are mainly dependent on the permittivity jump across the perpendicular interface as shown in Figure 7.11. Once more, comparing the column diameter of the streamer near the perpendicular pressboard interface (shown in Figure 7.12) with a similar case in oil without presence of the pressboard (streamer head 1 mm from the needle tip) indicates that the streamer becomes appreciably thinner. The strong attracting force from the perpendicular pressboard makes the streamer head thinner pulling the streamer volume charge towards the interface.

7.3.2 *Liquid Immersed Dielectrics with about the Same Permittivity as the Liquid*

As discussed in section 7.2, a LID with equal permittivity to the liquid dielectric does not apply any polarization force on the streamer charge. Therefore, the perpendicular interface transforms the hitting streamer into surface flashover only because it obstructs the path of the streamer.

Figure 7.13 shows the behavior of streamers, formed by different voltage peaks, reaching the perpendicular PTFE having approximately equal permittivity ($2.1 \epsilon_0$) compared to the oil permittivity ($2.2 \epsilon_0$). Comparing to Figure 7.12 both streamer and surface flashover velocities are smaller in presence of PTFE rather than the pressboard, simply because there is much smaller polarization force. Since the shape and the velocity of the streamers in presence of perpendicular PTFE resemble streamers in oil only systems, it is reasonable to assume that presence of PTFE does not affect the dynamics of streamers unless its interface cuts the path of the streamer.

7.3.3 *Liquid Immersed Dielectrics with Smaller Permittivity than the Liquid*

As expected, the perpendicular low permittivity LID repels the approaching streamer and makes it slower. It also flattens the streamer head appreciably since the streamer volume charge is maximum at its tip and the applied polarization force is proportional to the permittivity difference and the charge magnitude (therefore the applied force is maximum at the streamer tip). Figure 7.14 shows the behavior of streamers, formed by different voltage peaks, reaching the perpendicular SF₆, having lower permittivity ($1.1 \epsilon_0$) than the oil permittivity ($2.2 \epsilon_0$). It is interesting to see that in spite of the streamer velocity, which becomes smaller as the LID permittivity decreases (see Figure 7.12-7.14), the surface flashover velocity is minimum when the LID permittivity is approximately equal to the liquid dielectric constant.

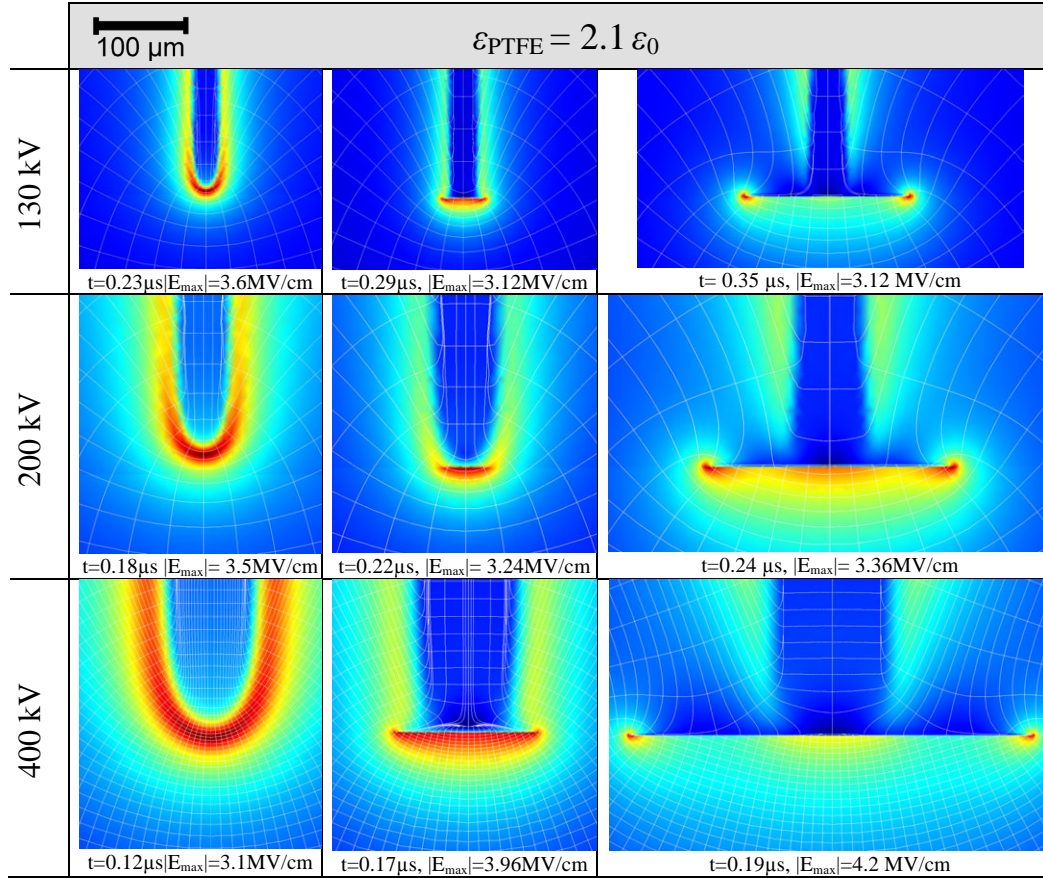


Figure 7.13: Electric field magnitude distribution for perpendicular PTFE interface. The streamers are formed by impulse voltages with 130 kV (first row), 200 kV (second row) and 400 kV (third row) peak amplitudes, all with 0.1 μs rise-time. $E_{\text{min}} \approx 0$ and E_{max} is given in each panel. E_{min} E_{max}

Figure 7.15 shows the space (volume) charge density of surface flashover on the surface of different LIDs. The force applied to the streamer charge due to the permittivity difference across the interface determines the thickness of the free space charge layer and the density of it. As it can be seen in this figure, the higher the LID permittivity, the thinner the charge layer and the higher the charge density of the surface flashover, which is caused by the polarization force and can be explained by the method of images.

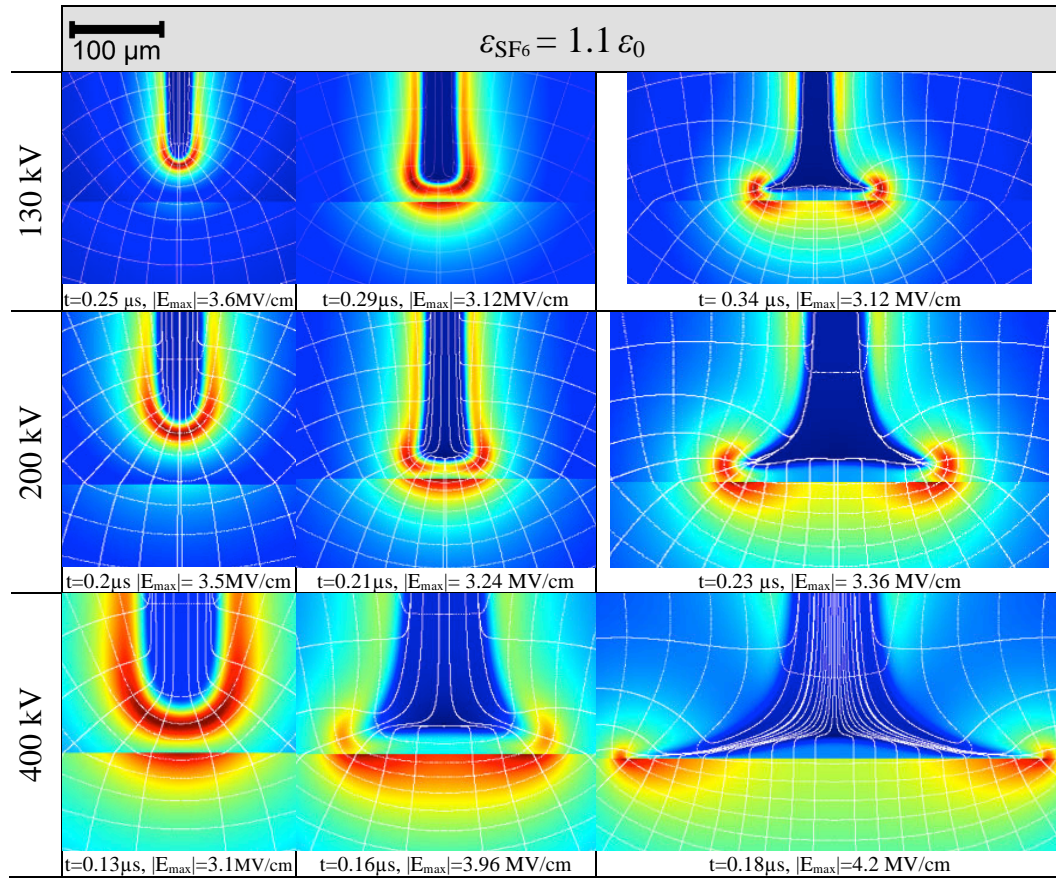


Figure 7.14: Electric field magnitude distribution for perpendicular SF₆ interface. The streamers are formed by impulse voltages with 130 kV (first row), 200 kV (second row) and 400 kV (third row) peak amplitudes, all with 0.1 μs rise-time. $E_{min} \approx 0$ and E_{max} is given in each panel. E_{Min} E_{Max}

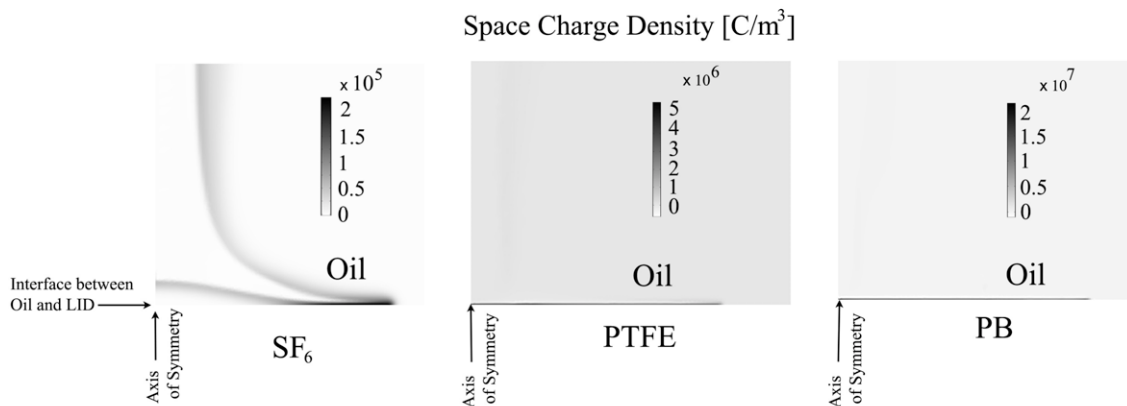


Figure 7.15: Electric field magnitude distribution for perpendicular LID interfaces. The streamers are formed by impulse voltages with 130 kV (first row), 200 kV (second row) and 400 kV (third row) peak amplitudes, all with 0.1 μs rise-time. $E_{min} \approx 0$ and E_{max} is given in each panel.

Figure 7.16 shows the surface flashover edge trajectories on the perpendicular SF₆ and pressboard surfaces. Generally, regardless of configuration of LID, the line integral of the electric field on any path connecting the electrodes has to be constant, equal to the potential drop across the electrodes. Therefore, the higher the LID permittivity, the higher the electric field and the higher the ionization rate in the oil region. Consequently, in the presence of perpendicular pressboard, volume charge formed in the oil increases (even though the streamer is narrower, the volume charge density is still much higher). An increase in the streamer total volume charge density results in the streamer acceleration. On the other hand, a smaller LID permittivity lowers the electric field and ionization rate in the oil and creates less volume charge and smoother streamer heads, which result in slower streamers hitting the SF₆ surface. Furthermore, based on the method of images, LIDs with lower and higher permittivities than oil repel and attract the streamer head, respectively [50], which is an additional cause of the difference in streamer head velocity towards different perpendicular LID interfaces. Accordingly, the higher the perpendicular LID permittivity, the greater the surface flashover velocity as shown in Figure 7.16 (a) and (b). Surface flashovers on the perpendicular LID interfaces formed by higher voltages require much longer times and larger distances from the point that the streamer hits the interface (on the axis of symmetry) to slow down and eventually stop as shown in Figure 7.16.

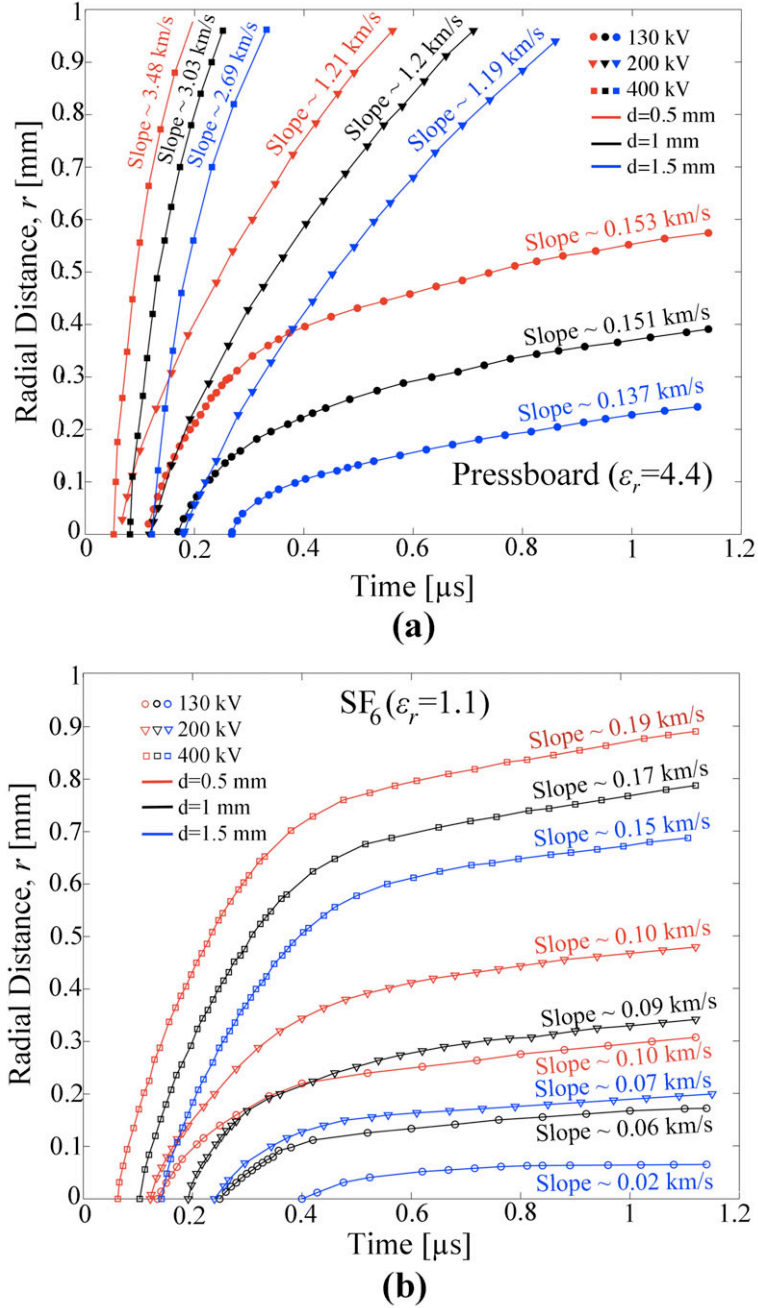


Figure 7.16: Surface flashover edge trajectories on the perpendicular LID surface against time for (a): pressboard with $\epsilon_r = 4.4$ and (b): SF_6 at five bar with $\epsilon_r = 1.1$ (b). “ d ” is the distance of the perpendicular interface from the needle tip.

7.4 Sanity Checks

One of the critical concerns about theoretical modeling in general and simulation of streamer/surface flashover behavior is always to find an approach to verify the results through experiments or analysis.

Modeling results presented in this chapter can be verified with both electrical and optical measurements. Specifically, the model gives the streamer current as well as the streamer trajectory, which can be measured in experiments using circuit current measurement and fast photography. The procedure to calculate the streamer current and the streamer head trajectory is explained in [49]. Interpreting physical results of the model such as electric field distribution and velocity profile of the streamers into the parameters that can possibly be measured in an ordinary high voltage laboratory enables the future experimental results of the same electrode geometries and applied voltages to be compared to the presented results.

Before experimental verification of the results, extensive sanity checks have been performed on the results in time and space domains, boundary conditions, etc. to make sure that the results reasonably satisfy the governing equations and boundary conditions. For instance, here one of the trickiest modeling results to physically verify is presented. The difficulty is due to the harsh numerical data oscillation on the surface of the liquid and LID interface, which is caused by use of streamline artificial diffusion to solve the charge continuity equations. Particularly, normal components of electric field have been presented in oil and pressboard regions as well as the surface charge density on the interfacial surface. It is known that the normal component of electric field should be higher in the medium that has the lower permittivity if there is no surface charge build up. Therefore, in the oil/pressboard composition, the normal component of electric field must be higher in oil, unless we have significant surface charge density on the oil/pressboard interface. In streamer propagation, both situations always exist on the interface (having and not having surface charge). Specifically, the interfacial surface charge density is negligible until the streamer touches the interface and starts to propagate along it. Simulation results show that after the streamer passes along the interface, the surface charge density remains high at the points left behind. Surface charge densities delivered by the streamer dominate the magnitude and direction of the electric field (in near field) in both regions. The electric field generated by surface charge density superposes with the background electric field (generated by the potential difference of the electrodes); meaning that in positively applied electric field, it cancels a portion of the electric field in the oil region (closer to positive needle electrode) and boosts up the electric field in the pressboard region (closer to grounded sphere). Therefore, the electric field is lower in the pressboard region before the streamer reaches the interface (no available surface charge density) and is higher in the pressboard region after the streamer hits the interfacial surface (strong positive surface charge density build up). The electric field magnitude at the interface is higher in oil for those points the streamer has not reached yet. For the point that a streamer has already passed, the electric field in the near field is dominated by volume (in oil) and surface charge density (on the interface), which results in an even higher electric field in the LID region.

Figure 7.17 shows the distribution of normal component of the electric field near the interface. Upper region is occupied with oil having a relative permittivity of 2.2, while the region below the interface is pressboard with a relative permittivity of 4.4. The distribution of the normal electric field is especially of interest for our numerical sanity checks of the magnitude of surface charge density accumulation.

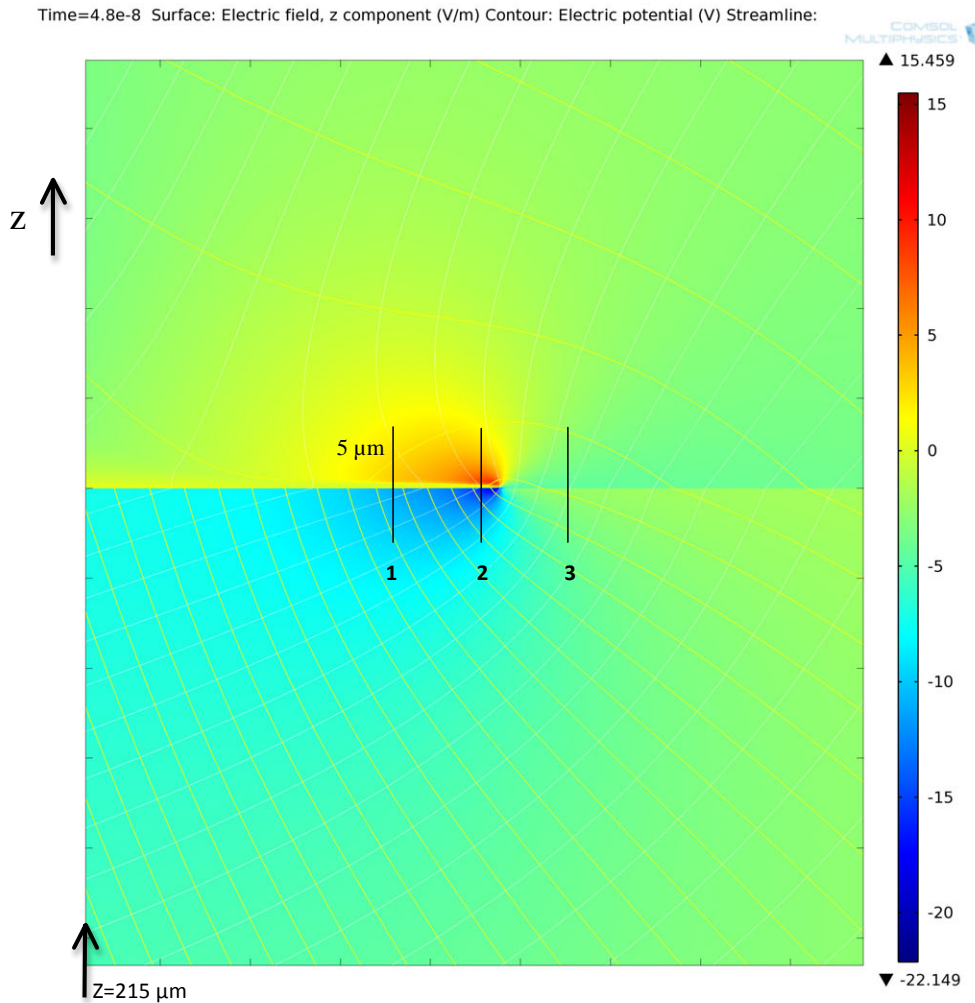


Figure 7.17: Normal component (z-direction) electric field distribution at the interfacial surface of oil/pressboard at $z=250 \mu\text{m}$ distance from the needle having 200 kV peak and 100 ns rise-time at $t=200 \text{ ns}$. The electric field strength is normalized to $1.2 \times 10^7 \text{ V/m}$. The tangential component (r-direction) of electric field is continuous across the interface. Three perpendicular $5 \mu\text{m}$ segments have been chosen (using “cross-sectional plot parameters, line/extrusion”) to plot E_z , and ρ on. Yellow lines show electric field streamlines and white lines show equipotential lines.

Figures 7.18, 7.19 and 7.20 show the magnitude of the normal component of the electric field (in z-direction) on segments 1, 2 and 3, respectively, shown in Figure 7.17.

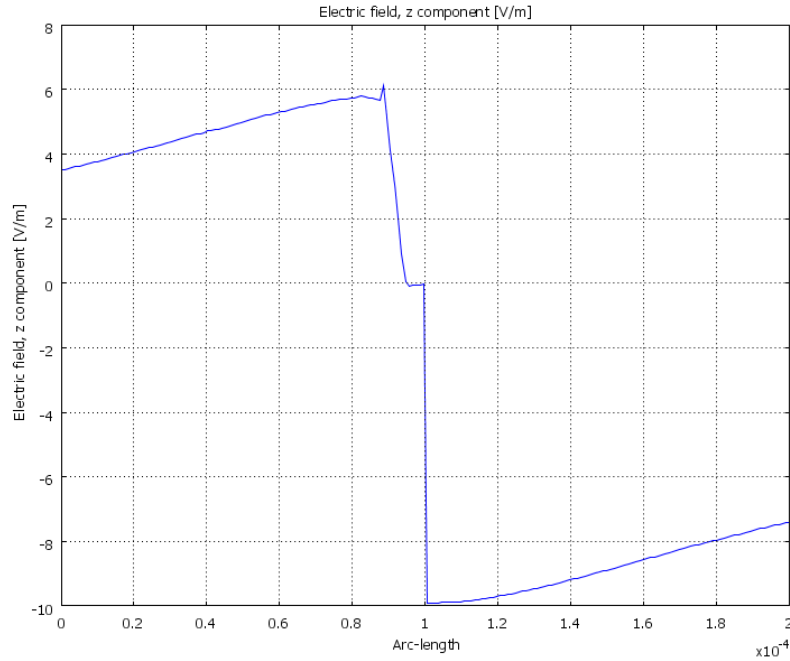


Figure 7.18: Normal component (z-direction) electric field distribution on *segment 1* shown in Fig. 7.17 at the oil/pressboard interfacial. The electric field strength is normalized to 1.2×10^7 V/m. The distance is normalized to 25 mm.

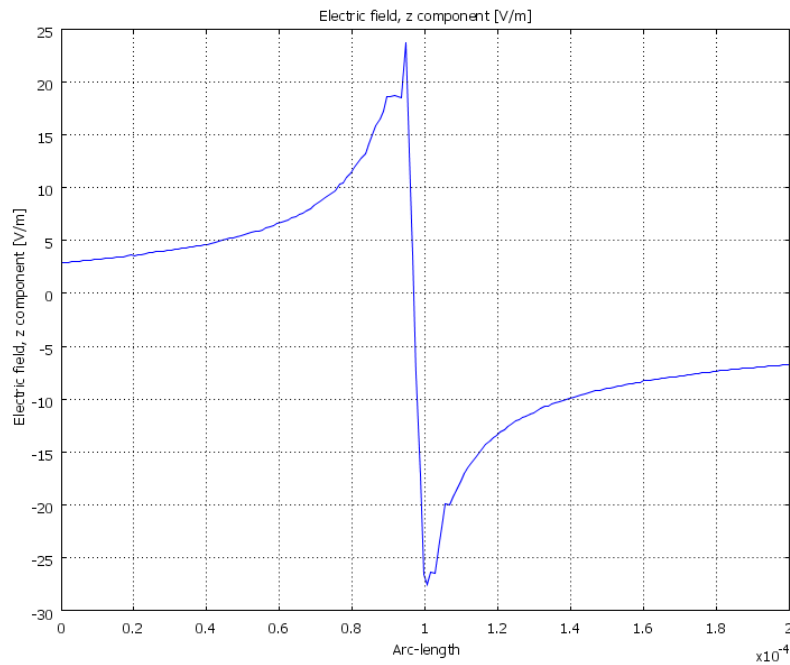


Figure 7.19: Normal component (z-direction) electric field distribution on *segment 2* shown in Fig. 7.17 at the oil/pressboard interfacial surface 250 μm far from the needle having 200 kV peak and 100 ns rise-time at $t=200$ ns. The electric field strength is normalized to 1.2×10^7 V/m. The distance is normalized to 25 mm.

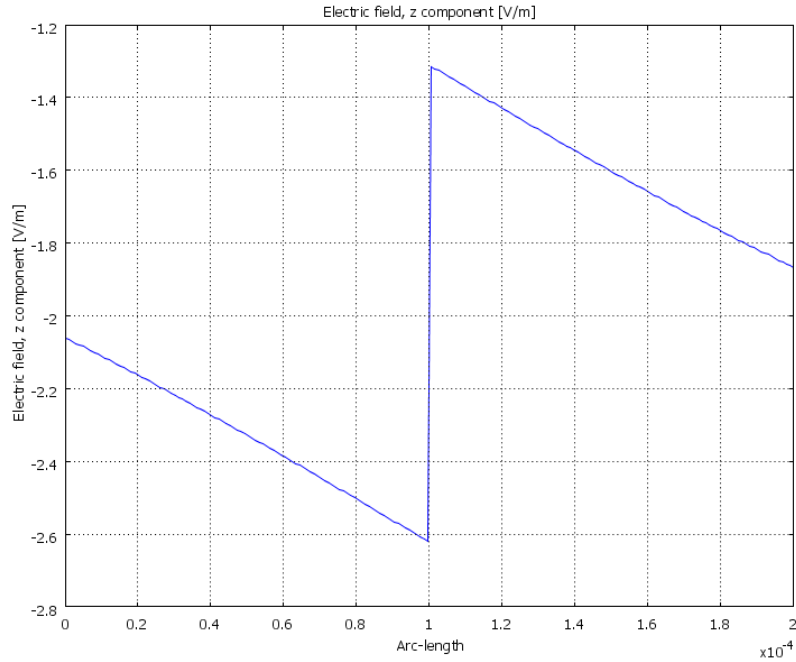


Figure 7.20: Normal component (z-direction) electric field distribution on *segment 3* shown in Fig. 7.17 at the oil/pressboard interfacial surface 250 μm far from the needle having 200 kV peak and 100 ns rise-time at $t=200$ ns. The electric field strength is normalized to 1.2×10^7 V/m. The distance is normalized to 25 mm

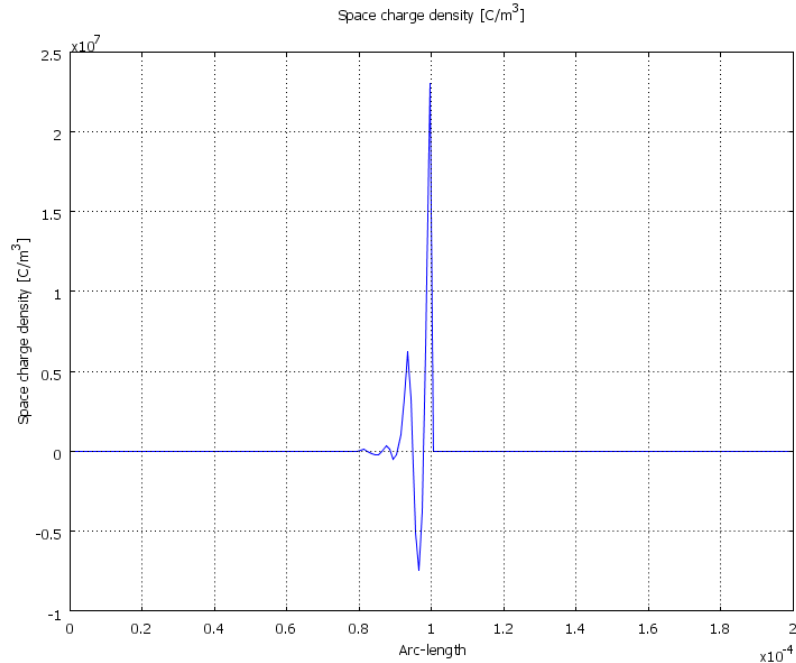


Figure 7.21: Space charge density on the *segment 1* shown in Fig. 7.17 at the oil/pressboard interfacial surface 250 μm from the needle having 200 kV peak and 100 ns.

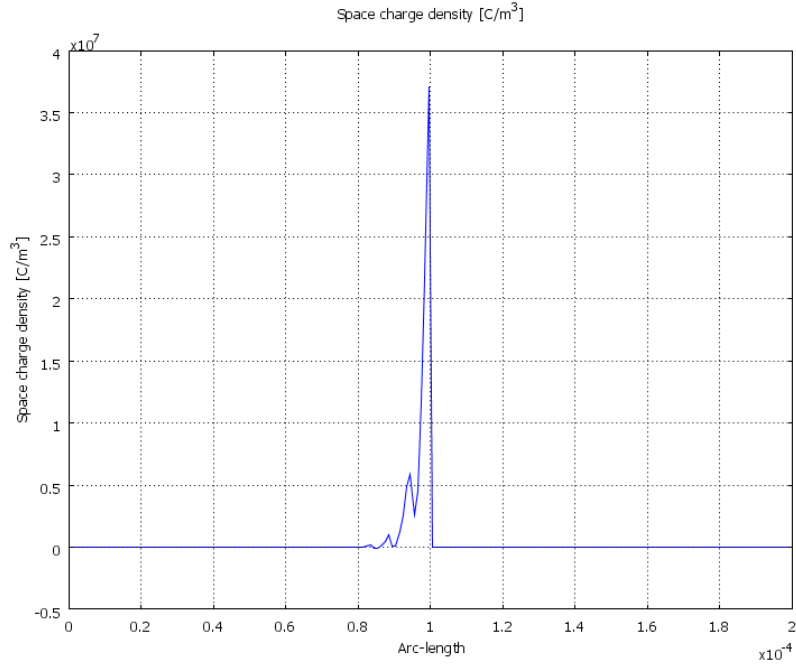


Figure 7.22: Space charge density on the *segment 2* shown in Fig. 7.17 at the oil/pressboard interfacial surface 250 μm from the needle having 200 kV peak and 100 ns.

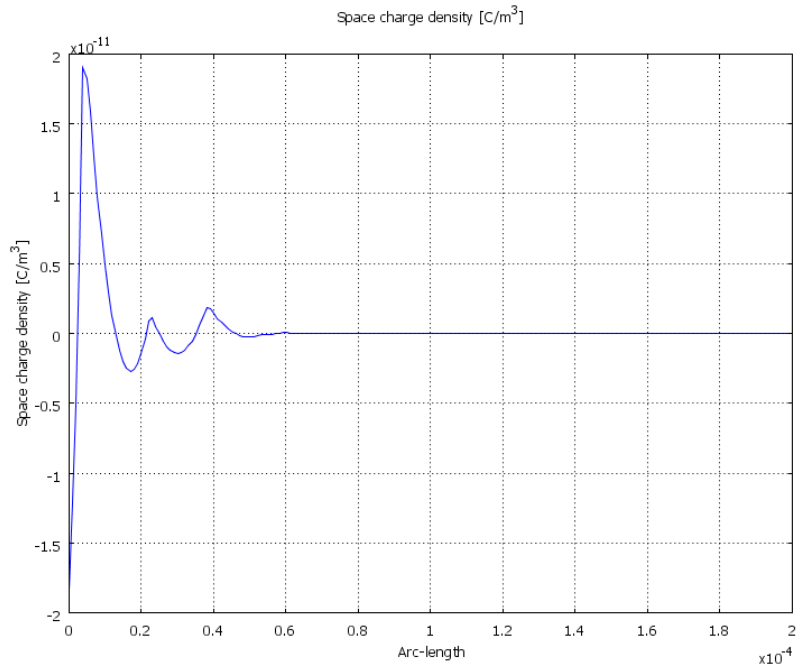


Figure 7.23: Space charge density on the *segment 3* shown in Fig. 7.17 at the oil/pressboard interfacial surface 250 μm from the needle having 200 kV peak and 100 ns. Space charge density is almost zero at this segment.

Figure 7.24 shows the raw data of the calculated surface charge density on the interfacial surface (in r-direction). As can be seen significant and harsh oscillations exist on the calculated surface charge density along the interface which is not likely to be physical. These oscillations are considered to be caused by the streamline artificial diffusion used in solving charge continuity equations of charge carriers.

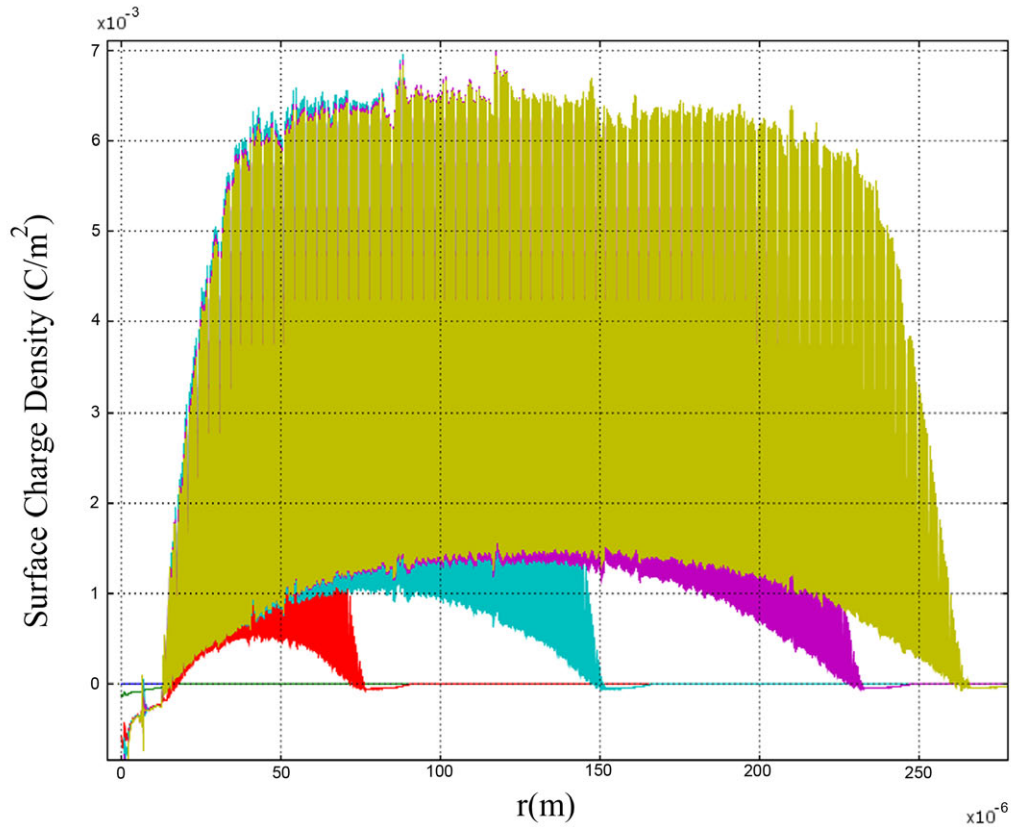


Figure 7.24: Surface charge density at the oil/pressboard interfacial (shown in Fig. 7.17) surface 250 μm far from the needle having 200 kV peak and 100 ns at different time instants. The harsh oscillations observed in this plot is usual when we are using the weak form boundary conditions and streamline artificial diffusion. These fluctuations are minimized using different arbitrary functions and weak constraints. However, these oscillations are inevitable when streamline artificial diffusion is applied.

Therefore, to find a reasonable value that can be used in the sanity checks of the modeling results, MATLAB Gaussian fitting function has been employed to take the best fitted graph of surface charge density versus position which is plotted in Figure 7.25.

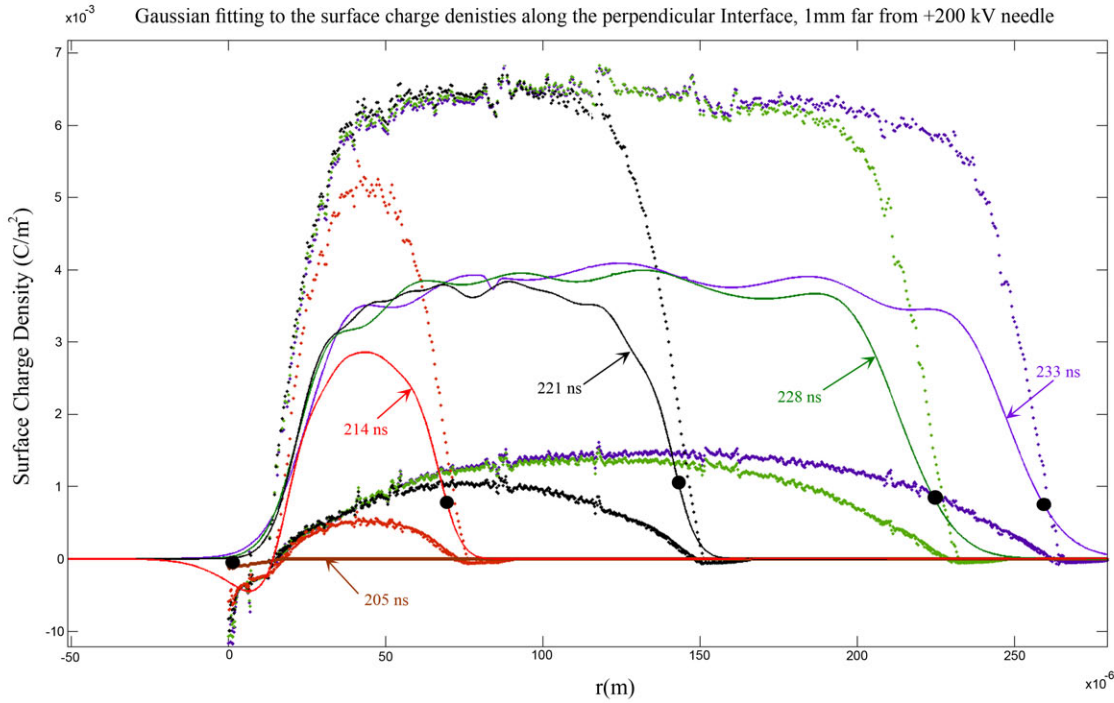


Figure 7.25: Surface charge density at the oil/pressboard interfacial surface 250 μm from the needle having 200 kV peak and 100 ns rise-time at $t=200$ ns. Fitting is also provided using MATLAB parameters Gaussian fit. Dotted data shows the envelopes of the raw data and the solid lines show the fitted curve with similar colors for each data.

Comparing Figures 7.21–7.25 show that the surface charge boundary condition is approximately satisfied over the interface (the charge density is equal to the difference of normal component of the displacement field on either side of the interface: $\sigma_s = \epsilon_{PB} E_z(\text{PB}) - \epsilon_{Oil} E_z(\text{Oil})$). Particularly on the regions that the surface charge density is negligible, $\epsilon_{PB} E_z(\text{PB}) = \epsilon_{Oil} E_z(\text{Oil})$ meaning that $2 E_z(\text{PB}) = E_z(\text{Oil})$ which can be seen in Figure 7.17 (exactly at interface) and more clearly in Figure 7.20.

7.5 Summary

Compared to the streamers propagating in the oil-only system, the streamer becomes slower (thicker), and faster (thinner) when it approaches the perpendicular low and high permittivity perpendicular barrier, respectively. Similarly, the streamers convert to surface flashovers by propagating alongside the parallel high permittivity barrier interface, since the strong attractive force causes the streamers to immediately follow the barrier interface and remain a surface

flashover with approximately constant shape and velocity over time. However, the repelling force applied by the low permittivity parallel barrier squeezes the streamers in the concentric parallel bore. The squeezed streamers propagate with higher velocity and smaller column diameters, compared to streamers in oil only systems.

Therefore, both low and high permittivity LIDs increase the risk of breakdown. The parallel high permittivity LIDs accelerate the charge transport between the two electrodes by attracting the streamers into the interface and make them settle on the surface. The parallel low permittivity LIDs, on the other hand, intensify the volume charge density of the streamer and the electric field around them by squeezing the streamer crust. Accelerating the charge transport between high voltage electrodes always increases the risk of breakdown. This explains the fact that the most popular industrial pressboards match dielectric constant of the liquid dielectric.

Concluding Remarks and Suggestions for Future Work

This chapter presents a summary of the thesis, highlighting the main contributions of this work to the understanding of dielectric breakdown in insulating liquids, with and without microscopic inhomogeneities, and liquid immersed solid and gaseous dielectrics. The chapter concludes by discussing the possible future modeling work that would help deepen the current theoretical understanding of the liquid dielectric breakdown. Any experiment with similar parameters as the modeling cases of this thesis will surely help validate main conclusions from this thesis research.

8.1 Streamer Initiation

Mechanisms behind the positive and negative streamers initiated by impulse voltages (defined by IEC standard) with different peak amplitudes and rise-times have been explained using a 2-D axisymmetric electrohydrodynamic model. Simulation results presented in Chapter 5 indicate that the negative streamers require higher voltage peak amplitudes to initiate from a needle electrode. The bushy negative streamer initially occupies a larger volume around the needle electrode compared to the filamentary positive streamer. An initial ionized body formed by a negatively applied impulse voltage propagates at a slower pace due to the lower electric field enhancement ahead of its bushy ionization front. When the ionized body grows a few millimeters from the negative needle, the 2-D axisymmetric model fails to track the physical velocity of the negative streamer, since in spite of positive streamers, as experiments also confirm, the negative streamers cannot propagate in a stable single on-axis streamer column (especially for the large electrode gaps) and the formation of the off-axis branches are inevitable for negative streamer propagation beyond a few millimeters. Off-axis phenomena cannot be studied in a 2-D axisymmetric model.

Geometrical effects of electrodes on the streamer initiation are investigated in transformer oil using the 2-D axisymmetric streamer model. Modeling results indicate that for a given applied voltage, the positive electrode size affects the initiation voltage and the grounded electrode size affects the breakdown voltage and delay. The model, presented in this thesis, also indicates that the applied voltages with smaller rise-times form thicker streamer columns in liquid dielectrics, while applied voltages with longer rise-times create thinner streamers. Such effects have been

reported by the experimental research on the streamers formed in gaseous media, where the streamer imaging is more convenient.

8.2 Streamer Propagation

Inclusion of electric field dependence of the ionization potential derived from DFT and electric field dependent electron velocity (electron velocity saturation) enables the presented 2-D axisymmetric model to physically describe the higher streamer velocities and streamer column diameters under extremely high-applied voltages, also known as higher modes of streamer propagation. The model confirms earlier experimental observations that the higher mode velocities do not take place until the streamer travels beyond ~ 10 millimeters from the needle electrode (almost at the middle of the gap).

As explained in Chapter 5, the velocities of the streamer propagation in different electrode geometries and gap distances have been derived from the streamer head trajectories along the shortest line which connects electrodes (on the axis of symmetry). For the same applied voltages and gap distances, the average velocity is higher in electrode geometries with greater radius of curvature. Specifically, the streamer velocity and acceleration toward the grounded sphere electrode increases earlier than toward the grounded needle electrode, and the streamer average propagation velocity is higher when it propagates toward a sphere electrode. On the other hand, the maximum instantaneous velocity and acceleration of the streamer is higher when it propagates towards the grounded needle electrode. As discussed in Chapter 5, the trajectories of streamers in gaps ranging from 1 mm to 10 mm fit closely to polynomial and exponential functions for needle-sphere and needle-needle, respectively.

8.3 Streamer Branching

A fully three-dimensional model of streamers is employed in Chapter 6 to investigate the dynamics of streamer branching, which is an asymmetric phenomenon by its nature. The modeling results show that the streamer branching has deterministic origins, as well as stochastic roots. Specifically, if the volume charge layer at the streamer head is thin and slow enough, even an infinitesimal inhomogeneity is sufficient to trigger the branching. On the other hand, if the streamer head is stable, even relatively large perturbations do not grow instabilities from the streamer head. We have derived a quantitative gauge for the streamer head geometry that determines whether branching occurs under specific inhomogeneous circumstances. The critical

ratio of the streamer charge sheath thickness over the streamer width, at which branching occurs, is found for the specific density and intensity of inhomogeneities. Comparing the modeling results with corresponding experimental images indicates that the model predicts the branching phenomena both quantitatively and qualitatively. In terms of the visual resemblance between modeling results and experimental images, 5 μm spherical inhomogeneities with spatial number density of 10^{11} m^{-3} is an optimal combination in transformer oil.

8.4 Streamer Interaction with Immersed Dielectrics

Incorporating different liquid immersed barrier orientations in the model shows that the polarization forces from the barrier dielectrics on the charge carrying streamers are proportional to the permittivity difference between liquid (transformer oil) and the immersed dielectric (pressboard). If the pressboard permittivity is greater than the oil permittivity, the attractive force turns the streamer into a surface flashover. On the other hand, a low permittivity pressboard interface repels the approaching streamer. A mismatch in permittivities of the liquid dielectric and the liquid immersed barrier usually increases the chance of the breakdown, as the polarization force on the free volume charge inside the liquid applied by the immersed barrier is nonzero if the permittivities are not equal.

Compared to the streamers propagating in the oil-only system, the streamer becomes slower (thicker), and faster (thinner) when it approaches the perpendicular low and high permittivity perpendicular barrier, respectively. Therefore, it is preferred to use a low permittivity material for perpendicular immersed barriers (spacer), if its dielectric strength is high enough (it does not fail against approaching streamers).

Similarly, the streamers convert to surface flashovers by propagating alongside the parallel high permittivity barrier interface, since the strong attractive force causes the streamers to immediately settle on the interface and remain a surface flashover with approximately constant shape and velocity over time. However, the repelling force applied by the low permittivity parallel barrier squeezes the streamers in the concentric parallel bore. The squeezed streamers propagate with higher velocity and smaller column diameters, compared to streamers in oil only systems. Therefore, both low and high permittivity Liquid Immersed Dielectrics (LIDs) increase the risk of breakdown. Parallel high permittivity LIDs accelerate the charge transport between the two electrodes by attracting the streamers into the interface and make them settle on the surface. The parallel low permittivity LIDs, on the other hand, intensify the volume charge density of the streamer and the electric field around them by squeezing the streamer. Accelerating the charge transport between high voltage electrodes always increases the risk of breakdown. This explains the fact that the least damage is reported on pressboards that have a matched dielectric constant with the liquid dielectric.

8.5 Streamer Breakdown

The streamer model presented in this thesis indicates that the breakdown voltage is mainly a function of gap distance. A breakdown voltage is determined using the modeling results for any gap distance as long as the needle electrode radius of curvature and the electrode gap distance do not exceed 1 mm and 12 mm, respectively. The constraint on the gap distance is due to the computational capacity limitation and the constraint on the needle radius of curvature is because the breakdown voltage becomes sensitive to the needle electrode tip radius of curvature as well as the electrode gap distance for needle electrode radius of curvatures beyond 1 mm.

The electric field intensity near the electrode surface is higher around the points with smaller radii of curvature, which is particularly true for a needle electrode. This does not necessarily mean that the streamer breakdown occurs at lower voltages if both electrodes are needle-shaped rather than the needle-sphere electrode geometry. A sharp needle shape of the positive electrode assists the streamer initiation. If both electrodes are needles, the electric field in the middle of the gap will be relatively lower than what would be the case for the corresponding needle-sphere electrode geometry. This is caused by the fact that the line integral of the electric field between electrodes is equal to the voltage drop across the electrodes. Since the voltage distributions across the two electrode configurations are different, and the electric field is extremely high in the vicinity of the needle electrode, it has to be lower in the halfway point between needle electrodes. The lower electric field in the region around the halfway point between two needle electrodes decreases the streamer acceleration, which consequently reduces the breakdown probability. Therefore, the breakdown in the needle-needle electrode geometry occurs at higher voltages compared to the needle-sphere electrode geometry.

The model is able to show that the total current passing through electrode gap at the breakdown voltage dramatically rises exactly at the instantaneous time at which the streamer head reaches the grounded electrode (breakdown completion). As a sign of breakdown, the current increases more than 10^8 fold in less than 30 ns for the needle-sphere electrode geometries and more than 10 fold in less than 20 ns for the needle-needle geometries.

The modeling results such as breakdown current, streamer initiation voltage, time to breakdown and breakdown current agree with the experimental data extracted from the literature.

8.6 Sanity Checks

In addition to comparing the modeling results obtained in this thesis research, the results have been validated by the following approaches:

- Different element types (Lagrange linear, quadratic, cubic, quartic and quintic) have been examined to ensure the accuracy and consistency of the results.
- Different direct solvers (such as PARDISO and MUMPS) and iterative solvers (such as GMRES, FGMERS and Conjugate gradients) have been used and the comparison of the results shows that there is no major differences between the results that could possibly warn the correctness of the results.
- A Finite Difference analysis (using MATLAB codes) has been implemented to check the results of the FEM COMSOL modeling. Although the results obtained by this finite difference method modeling lack accuracy and simulation speed, the results are essentially identical to the FEM results presented in Chapter 5.
- Finite Volume Method: A research performed at ABB Corporate Research [74] using OpenFOAM confirms identical results of the FEM approach developed in COMSOL Multiphysics.

8.7 Future Work

The molecular structure and behavior of liquid dielectrics is more complex than gases and solids and even in the purest liquids there exists trace amounts of impurities that make it difficult to isolate the mechanisms behind electrical breakdown. In particular, transformer oil is a mixture of many different aromatic, naphthenic, and paraffinic molecules with complex molecular structures. The major weak point of the presented model is the lack of data about effective electron mass, electron mobility and number of ionizable species in electrically stressed transformer oil. Future theoretical studies should address these areas of research to enable the numerical modeling of streamer better explain the streamer breakdown dynamics.

According to the current thermal simulations and experimental evidence, more realistic models of streamers in transformer oil must include the addition of a gas phase (vapor) and low temperature collisional plasma over a temperature range from 300 to 2000 K. However, previous experience [102] in simulating plasmas in COMSOL indicates that it is extremely difficult to combine the

entire plasma equation set with the pre-breakdown equations (presented in Chapter 5) with an acceptable convergence.

Figure 8.1 shows a simplified schematic view of the plasma-gas-liquid combined 2-D axisymmetric model. To reduce the number of elements and the complexity of the model, one could ignore the needle electrode geometry by assuming the electric field to be uniformly distributed in the inter-electrode area. The multiphase model of the streamer propagation shown in Figure 8.1 can also use the current model results as the initial conditions. Initial conditions of the problem (shape of the streamer head, distribution of electron and ion density, heat flow, etc.) can be derived from a separate pre-breakdown model, which includes the needle-sphere geometry (streamer initiation). In fact, Figure 8.1 shows a model of the streamer propagation mode. In the propagation mode, when the streamer head has traveled a few millimeters from the needle, the effect of the gas and plasma phases are more dominant, since we will have considerable heat flow.

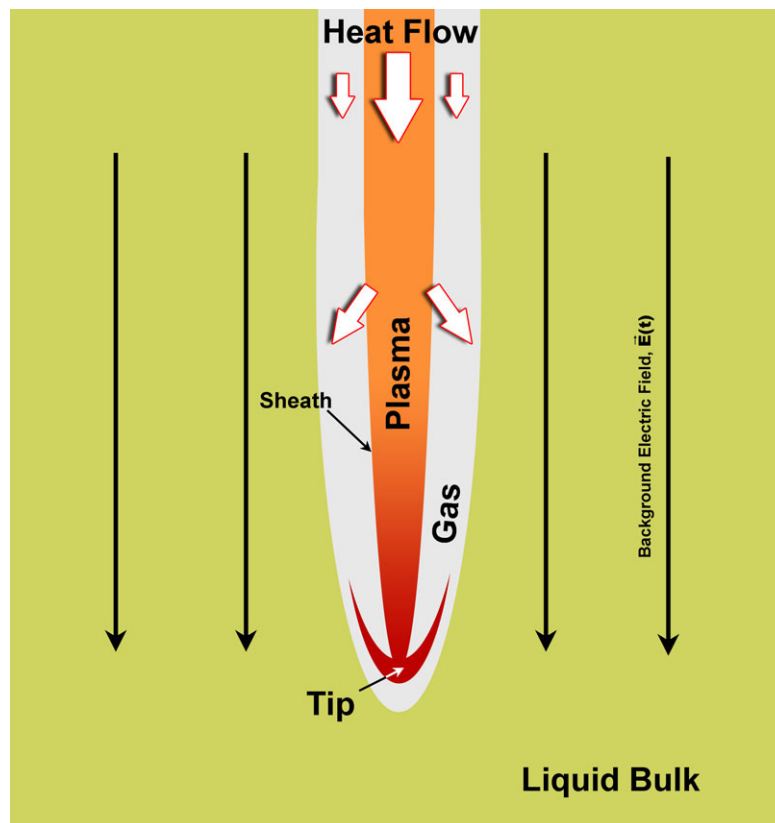


Figure 8.1: Schematic view of the multiphase model of streamer propagation. There are three distinct physical phases: liquid, gas and plasma. For each phase one would have to solve different sets of equations, which also have to be interrelated. To reduce the number of elements and complexity of the model, one can assume the background electric field to be uniformly distributed in the inter-electrode area.

The model presented in Chapter 5 is no longer valid after breakdown of the liquid dielectric (when the streamer reaches the opposite electrode and the current rises beyond a few amperes), since due to high power dissipation along the streamer path, the streamer will be replaced by a high current arc, which requires additional physics such as plasma formation, thermal, impact and photo ionization and fluid convection to be modeled. Implementation of a multiphase streamer model of Figure 8.1 may enable the model to describe post breakdown consequences as well (electric arc model). Developing such a model requires a consistent definition of proper boundary conditions, complete gas phase properties (mostly hydrogen for transformer oil), charge injection governing equations from the needle electrode (especially after breakdown and formation of the arc) and effective and complete heat generation and transfer equations.

Apart from the ambitious goal of a multiphase streamer model, the presented work in this thesis can be continued in many other directions.

For instance the branching of negative streamers still remains open. Using the model introduced in Chapter 6, it is convenient to develop a 3-D negative streamer branching model, only it requires more computational capacity as negative streamers are bulkier and require larger volume with refined mesh. In addition, the secondary branching of the streamers have not been addressed in this thesis. Secondary branching means the branching that occurs on a streamer branch that itself comes off the original streamer column. Longer pillboxes with refined mesh will be required to perform this task.

In the streamer/surface flashover model of liquid immersed insulation system, the possibility of the streamer penetration into the LID (known as immersed dielectric punching) is ignored. To include such a situation (streamer formation inside LID), the LID itself can be considered as a dielectric with specific electron and ion mobility, which is essentially a similar model to the liquid phase.

This section presents five appendices of this thesis. Appendix A1 explain an optimized combination of artificial diffusion techniques to stabilize a drift dominated streamer discharge model which includes COMSOL Multiphysics' Transport of Diluted Species modules for positive ion, negative ion, and electron charge densities, in the streamer/surface flashover model presented in Chapters 5–7. Several combinations of streamline diffusions and crosswind diffusion with different tuning parameters are applied to the charge continuity and the thermal equations with different mesh element size distributions to determine the ideal combination. Appendix A2 introduces the 2-D axisymmetric and 3-D mesh schemes, which have been employed in Chapters 5–7 to effectively solve the numerical problems. Appendix A3 presents a simple illustration of the physical differences between positive and negative streamer formation in dielectric liquids. This appendix particularly answers the question, why negative streamers propagate with slower pace compared to positive streamers. Appendix A4 explains how the microscopic inhomogeneities are implemented in Chapter 6. Finally, Appendix A5 compares the finite element method that is employed in this thesis with other suggested simulation methods for streamer development modeling.

A1 Optimized Combination of Artificial Diffusion Stabilization Techniques for Finite Element Modeling of Drift Dominated Transport of Charge Carriers

Stabilization techniques are required for solving conservation equations of charge (mass continuity equations) for electron and different ions. Different artificial diffusions are provided in COMSOL Multiphysics (versions 3.5a–4.3a). The performance of different consistent stabilization techniques is investigated in this thesis. Diffusion of the charged species is assumed negligible in equations (5.1–5.3). Numerical solutions of the charge continuity equations usually include spatial instabilities rather than expected smooth solutions. These spurious oscillations can be avoided by using nonlinear CWD in addition to different types of SDs such as anisotropic, compensated streamline upwind Petrov-Galerkin (SUPG) and Galerkin least-square methods, to stabilize the charge continuity equations. It has been shown that CWD is more stable than other over-diffusive discontinuity-capturing techniques and leads to better numerical behavior, although it is computationally expensive due to its nonlinear nature. On the other hand, SD techniques effectively stabilize the system and accelerate the solution. We have applied minimal SD and CWD at the same time to optimally stabilize the numerical solution. Minimal artificial diffusion techniques are tuned to balance a tradeoff between removing nonphysical local oscillations (due to SD) and excessively smooth results just next to the walls (due to CWD).

Including CWD effectively dampens oscillations in the charge number densities and prevents them from becoming negative which is nonphysical [43]. It also increases the streamer diameter and decreases the streamer velocity and the maximum electric field ahead of the streamer compared to the results obtained using SD only. This is reasonable since CWD adds some artificial diffusion terms orthogonal to the flow of species to stabilize the numerical solution. The CWD also provides extra diffusion in the region of sharp gradients.

In spite of COMSOL 3.5a, SD is sometimes not enough to converge the streamer model in COMSOL 4.2a and 4.3a, which makes it harder to compare results of the SD only cases. In addition, COMSOL 4.3a employs only one SD type without any tuning parameters. COMSOL recommends that “Both artificial diffusions should be selected for optimal performance” [71].

The CWD method specifies the smallest allowable concentration change across an element. As the concentration gradient appears in the denominator in the equations describing CWD, the gradient ensures that unreasonable values do not occur in the regions with small to negligible concentration changes. Figure A1 compares a pair of results obtained from two identical cases with the only difference being the applied artificial diffusion method.

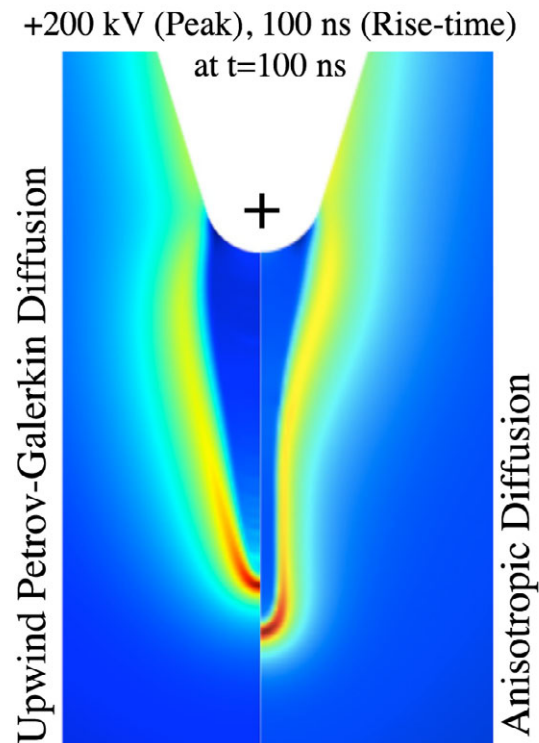


Figure A1: Different streamer propagation mechanisms under two different artificial diffusions: electric field magnitude distribution solved by (left): upwind Petrov-Galerkin diffusion and (right): anisotropic diffusion. The applied voltage peak magnitude to the positive needle is 200 kV peak and the rise-time is 100 ns.

A2 Optimal Mesh Element Density Distribution for Streamer Development Finite Element Modeling

In fact it is impossible to optimize the artificial diffusions without the proper mesh distribution scheme. Particularly, if the applied voltage is steep enough to form an initial charge volume wider than 0.2 mm diameter, nonphysical off-axis branching is likely to appear in the 2-D axisymmetric geometry. Based on experimental observations, the cone-shaped instability shown in Figure A2 is assumed to be a consequence of inappropriate element size distribution especially in the vicinity of the needle electrode. Such off-axis deflections of the streamer head will not disappear even if we add either excessive CWD or large inconsistent isotropic diffusion terms to the equations. The off-axis growth of the ionized structure in our streamer model is worsened by the nature of the SD concept. In fact, this artificial stabilizer adds greater diffusion terms at those points where electric field lines are denser (convergent or divergent). As described earlier, the SD term is in the direction that strengthens the particle velocity in the particle motion streamline direction. Since electrons are very mobile, the SD based model is vulnerable to any spatial noise. This is even worse in our model since such excessive diffusions can accumulate the charge off the axis of symmetry, which itself increases the electric field intensity in those directions and consequently generates more charge based on the Zener molecular ionization equation. In some cases, the off-axis instabilities disappear if we remove SD. It has been known that the charge conservation equations never converge without a consistent stabilization method. Thus, the only option to prove that these branches is not a direct consequence of artificial diffusions in FEM, is to use FVM in which the artificial diffusions are not required. Results of a FVM streamer modeling in [74] show that such off-axis instabilities can also appear in FVM as well. Therefore, nonphysical off-axis instabilities should be regarded as a shortcoming of the 2-D axisymmetric modeling, not a flaw in FEM.

Removing SD is not a desirable option in the presented model in this thesis, since it decreases the streamer velocity, which does not agree with experimental observations. Therefore, it is an obligation to deal with SD sensitivities. To overcome these off-axis instabilities we tested several dense mesh distributions in the needle-sphere geometry shown in Chapter 5. It has already been proven that only refining the mesh around the needle tip cannot solve the problem as, for example, shown in Figure A2 for a box with an excessively dense mesh (maximum mesh element of 0.5 μm).

Figure A3 shows simulation results of a smoothly distributed element size. In this mesh scheme, we have successfully removed off-axis instability; instead, an axial high-speed streamer column evolves from the initially ionized volume. In this case, we have employed an extremely dense mesh on the axis of symmetry and a larger rectangular area for a fine mesh around the needle tip (not visible in this figure with maximum element size of 2 μm) while the total number of elements is almost the same as Figure A2. The main difference between these two cases is that we have avoided any jump in element size in the critical area fore the result shown in Figure A3. The position and dimensions of this critical area are mainly determined by the applied voltage

waveform and the molecular properties of bulk oil. For a +200 kV, 100 ns impulse, the critical zone is up to one millimeter from the needle. For a given case, the optimal area should be determined after trying a few fine mesh areas.

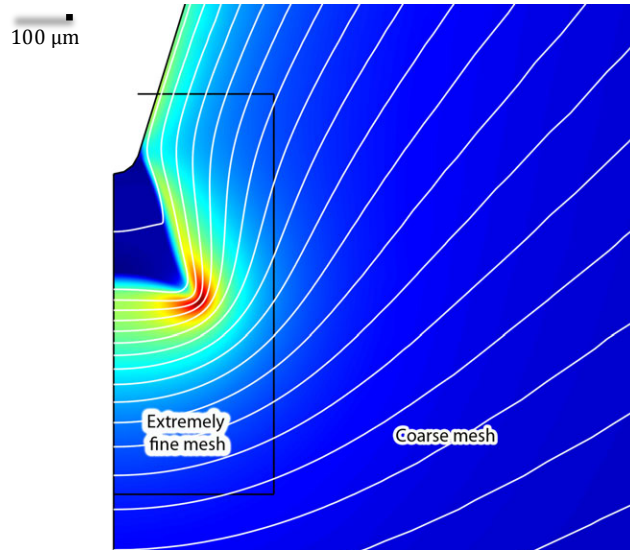


Figure A2: Off-axis branching in a streamer formed by a positive impulse with 200 kV and 1 ns rise-time still appears even with an extremely fine mesh around the needle (colors and white lines depict electric field and equipotential lines, respectively).

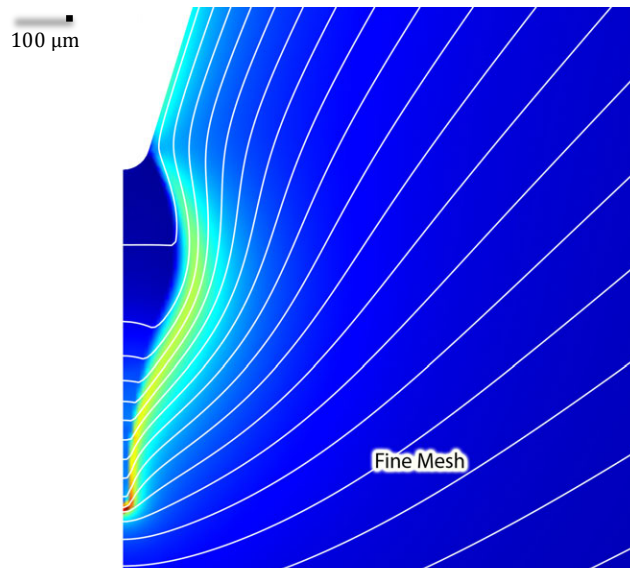


Figure A3: Off-axis branching in a positive streamer formed by a positive impulse with 200 kV and 1 ns rise-time disappears even with a fine mesh over a larger box around the needle (colors and white lines depict electric field and equipotential lines, respectively).

Increasing the mesh density in the vicinity of the needle electrode generally decreases the streamer velocity. If we refine the mesh more smoothly over the space around the needle (left side of Figure A4), the result is more consistent to the physical expectations compared with an extremely dense mesh over a smaller rectangle around the needle tip (right side of Figure A4). For instance, the number of streamlines deflected in the off-axis direction for the left hand side picture of Figure A4 is increased and consequently a deflection is formed on the streamer surface. We have also confirmed this idea with adapted mesh feature of COMSOL 4.3a. Similar results to the left side of Figure A4 have been obtained by activating the adapted mesh feature of COMSOL 4.3a which takes about 10 times longer simulation time to converge. The importance of this comparison is that the conclusion of superiority of smoothly changing element size is consistent with the COMSOL 4.3a adapted meshing policy that uses smoother mesh element size change over the space (Fig. A4 left side).

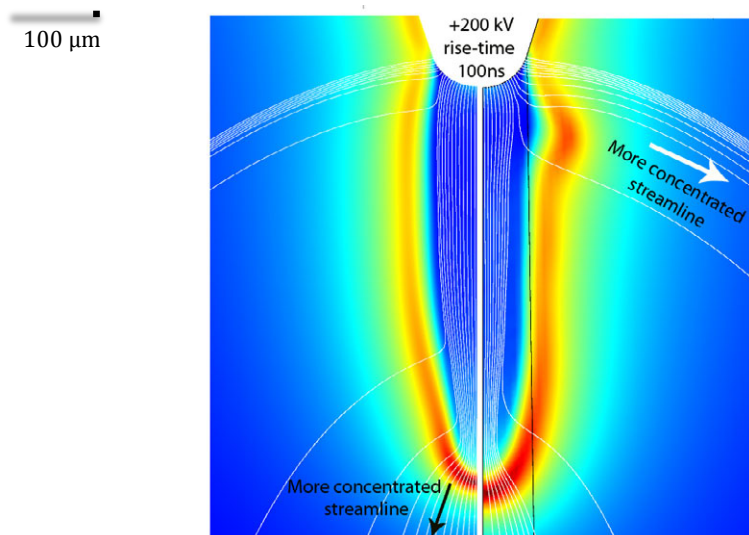


Figure A4: Electric field magnitude (color) and streamlines (white lines) for two different mesh element size distributions under a positively applied voltage (200 kV peak and 100 ns rise-time at time 85 ns). The two simulations are separately computed with the left side plot having a smooth fine mesh while the right side plot has a fine mesh within 40 μm and for the outer area beyond this box it has been freely meshed. Both SD and CWD are applied.

Our numerical experiments show that a big jump in element size distribution over space may cause a sort of positive feedback effect and form nonphysical branching especially when the electric field is extremely divergent (which is the case in applied voltages with higher peaks and smaller rise-times). Such big jumps create small numerical perturbations that grow due to a SD accumulative effect in our model. Figure A5 conceptually compares different cases of element size change over space and spatial disturbances that they may produce. Part (a) of Figure A5 shows a critical case in which a big jump can produce disturbances that form large enough

deflections on the electric field lines to add an excessive SD, and consequently deflect the main axial steamer branch. An example of this case can be seen in Figure A2. Excessive SD in the off-axis (radial) direction deflects the streamer and accumulates the charges away from the axis of symmetry. Such big jumps in mesh density must be avoided if the non-physical "radial bump" has to be eliminated from the results. Part (b) shows minor disturbances that can form off-axis instability, however, they are not large enough to deflect the main axial steamer branch. An example of this case can be seen in the right side of the Figure A4. The problem with this approach is that the number of elements is too high which leads to a long simulation time.

Part (c) of Figure A5 shows one of the possible options to minimize the effect of spatial disturbances due to element size alteration. It seems that a gradual rise in element size is the optimum approach to keep the accuracy high enough and decrease the number of elements at the same time. This approach can be realized by determining an appropriate "element growth rate" in COMSOL Multiphysics meshing section. Considering the fact that SD adds artificial diffusion in the streamline direction (electric field or particle velocity), these numerical results can be explained as a keen sensitivity of SD to spatial disturbances that are caused by sudden large changes in element sizes over space.

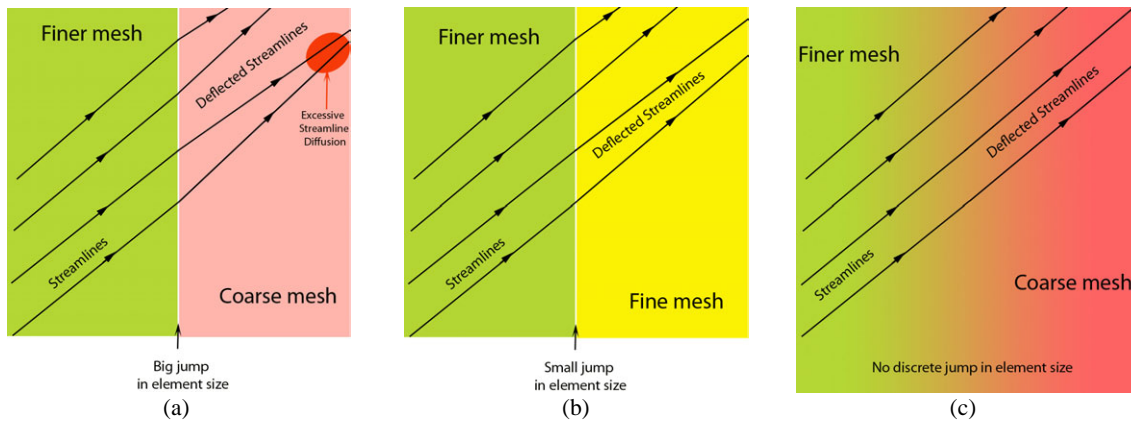


Figure A5: Different cases of element size transformation over space and spatial disturbances that they may produce, (a): critical disturbance over a big jump in element size; (b): negligible disturbance over a small jump in element size; (c): a gradual rise in element size minimizes the effect of numerical disturbances due to element size variation.

For the 3-D model we have studied the effect of symmetric perturbations on the streamer branching as a sanity check (see Chapter 6). If the mesh is fine enough to avoid misinterpreting of numerical artifacts as streamer branches, the branching must be symmetric also. Then we have applied a vast variety of inhomogeneous initial conditions and perturbations to study the branching. The qualitative shape of the streamer tree, numbers and diameters of the branches and their velocities are clearly sensitive to the applied voltage and the extent of the nonsymmetrical inhomogeneities. For the same inhomogeneity, number of the branches in a positive streamer is

determined by the applied voltage peak, while at the same applied voltage peak, the average diameter of branches is determined by both applied voltage rise-time and peak voltages. We have examined water droplets and air bubbles (with higher and lower permittivities than oil, respectively), and conductive and nonconductive dust particles as macroscopic perturbations. In addition, spatial variation of oil molecule composition/density (e.g., due to locally increased temperature) and inhomogeneous initial electron density (due to external radiation sources or previous discharges) is investigated as microscopic fluctuations. The average magnitude of the perturbations is set to the minimum value required for branching. From the numerical simulation point of view there are a few interesting points in the 3-D simulations. First, predefined plasma mesh in COMSOL Multiphysics greatly accelerates the model solution compared to the other types of meshing with the same meshing scheme. Second, the CWD cannot be avoided in the 3-D simulations due to the convergence issues.

Based on the modeling results, it has been concluded that the plasma, general physics, and fluid dynamics mesh calibrations in COMSOL Multiphysics 4.3a, which simply correspond to different default mesh sizes used by the “mesher,” result in significantly different performances. A turbulent flow problem, for instance, will require a much finer mesh than a structural mechanics problem. The streamer/surface flashover problem, which comprises three convection equations coupled through the quasi-electrostatic equation (Gauss’ law), will definitely require a finer mesh than predefined values. Therefore, the plasma calibration, which corresponds to the finest mesh on the boundaries and a high rate of rise of mesh size, performs well enough.

In general, COMSOL recommends running a convergence study with each of the mesh calibration (with refining the mesh manually until we reach a converged solution) and then select the optimal calibration for similar cases. Thus, we used the plasma mesh with fine meshes for Boxes 1, 2, and the predefined “extremely course” mesh size for outer space (out of Boxes 1 and 2 as shown in Figure A6) without jeopardizing the convergence to reduce the degrees of freedom to save simulation time.

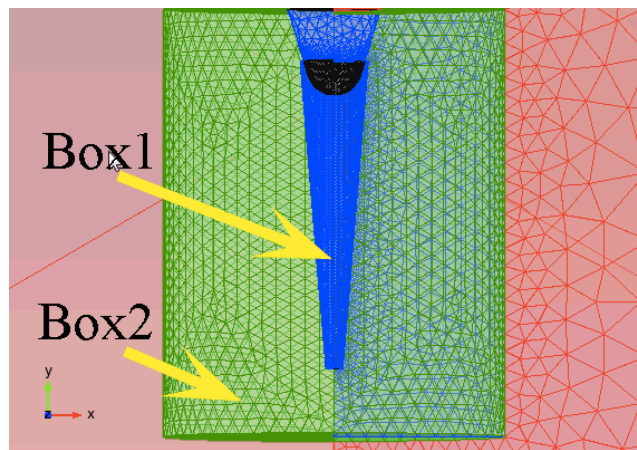


Figure A6: Mesh refinement policy in the 3D model in the vicinity of the needle. Mesh refinement data is given in Table A1.

Figures A7 and A8 show the effect of refining the mesh in the accuracy of the 3-D results compared to the presumably accurate 2-D result. The mesh data is given in Table A1 for each solution.

Table A1: Mesh Data in Figure A6

<i>Mesh Calibration</i>	<i>Maximum element size in the Box 1</i>	<i>Maximum element size in the Box 2</i>	<i>Predefined element size everywhere else</i>	<i>Number of elements</i>	<i>Degrees of freedom</i>	<i>Time to finishing all time steps</i>
Plasma Mesh 1 (Figure A7)	4 μm	20 μm	Extremely Course	701645	1319082	~115 h
Plasma Mesh 2 (Figure A8)	1 μm	Extremely Course	Extremely Course	1594329	3012502	~218 h

Finer mesh in the streamer column (Box 1) has improved the streamer velocity and the maximum electric field compared to 2-D result as shown in Figure A7. Specifically, the maximum electric field is improved by $\sim 3.5\%$ compared to results of mesh 2. The distribution of the electric field is also (qualitatively) more similar to 2-D result in terms of numerical fluctuations around the streamer column and the streamer head's radius of curvature, as can be seen in Figure A7 by inspection compared to Figure A8. The streamer head at $t=84$ ns is slightly ahead of the 2D streamer meaning that the velocity is slightly closer in 3-D simulation using mesh 2.

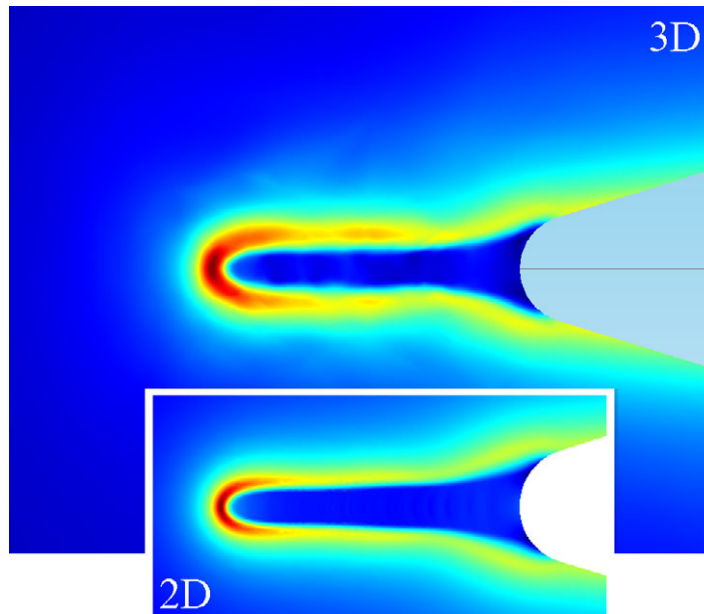


Figure A7: Comparison of 3-D model result and 2-D model result for plasma mesh calibration for an applied impulse voltage with 200 kV peak and 100 ns rise-time after 80 ns (2-D model) and 84 ns (3-D model). The maximum electric fields are 3.54 MV/cm (2-D model) and 3.42 MV/cm (3-D model). The streamer heads are at almost equal distances from the needle tip. No post-processing smoother function is used on the 3-D simulation result.

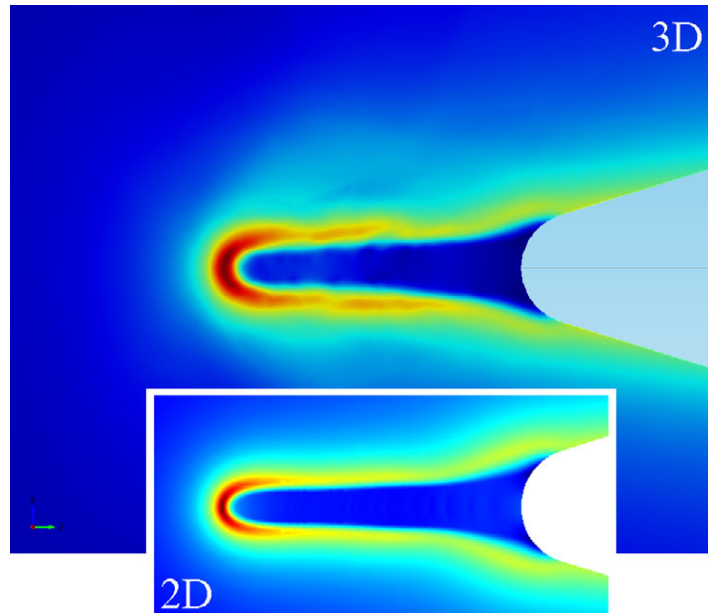


Figure A8: Comparison of 3-D model result and 2-D model result for plasma mesh calibration for an applied impulse voltage with 200 kV peak and 100 ns rise-time after 80 ns (2-D model) and 84 ns (3-D model). The maximum electric fields are 3.54 MV/cm (2-D model) and 3.36 MV/cm (3-D model). The streamer heads are at almost equal distances from the needle tip. No post-processing smoother function is used on the 3-D simulation result.

Nevertheless, there is still a gap between 2-D and 3-D results even if the size of the mesh is almost the same for the streamer column (Box 1). The reasons for this can be classified to

1. The dense mesh area is much wider in 2-D simulations (a cylinder with radius of ~ 200 μm around the axis of symmetry). However, in the 3-D simulations (mesh 2), Box 1 radius is smaller than 50 microns. Other than that the space out of Box 1 is meshed with predefined “extremely course” while in 2-D simulation, the outer area is meshed by normal size.
2. The artificial diffusion coefficients are minimized for 2-D simulations (to reach the most accurate result), which is not possible to do for 3-D simulations. Therefore, to keep the convergence in a reasonable time, the CWD coefficient (COMSOL 4.3a) is slightly increased (less than doubled). The slight overdiffusive results (e.g., thicker walls of the streamer) are caused by the excessive CWD that cannot be avoided. The smaller streamer velocity is another consequence (~ 5 -10% slower).
3. The 3-D mesh is not symmetrical; therefore, the numerical fluctuations can never be avoided. However, as long as such perturbations do not grow and the maximum electric field and the streamer velocity agree with 2-D results, these fluctuations can be tolerated.

As a conclusion, we have gained ~3.5% and ~2% improvements in maximum electric field and streamer velocity results, respectively, by almost doubling the simulation time.

For all of the results presented in this thesis, the absolute possible maximum has been set for the number of elements (with a limit of one-week to be the maximum simulation time). However, it is not possible to do every modeling case with such mesh densities. Therefore, a mesh selection process like one that is shown in Figure A9 has been applied for each case study considered during this thesis research. In this process, we start the simulation with a coarse mesh. Then we compare the modeling results while continuously increase the mesh density. Usually, there is a point that the results are accurate enough and increasing the mesh density does not actually add enough accuracy when we look at the computational expanse we pay for it. In this thesis, we have been working with this optimal mesh density for each case (shown with a circle in Figure A9) to understand the dynamics, since it usually takes many preliminary modeling cases to see a trend in the dynamics of the streamer/surface flashover development. Then to represent the results, we have rerun the model with the absolute maximum mesh density. It should be noted here that, if the mesh were not configured well, the modeling results would not converge as shown in Figure A9. In such cases, the modeling results change significantly as we increase the mesh density. If such a situation occurs, it shows that the mesh distribution scheme is not an effective one, meaning that it is most likely that there is an important position in the simulation geometry that is not meshed fine enough. To solve the problem, the scheme has to be changed and the validation process similar to the one shown in Figure A9 has to be repeated until the results converge.

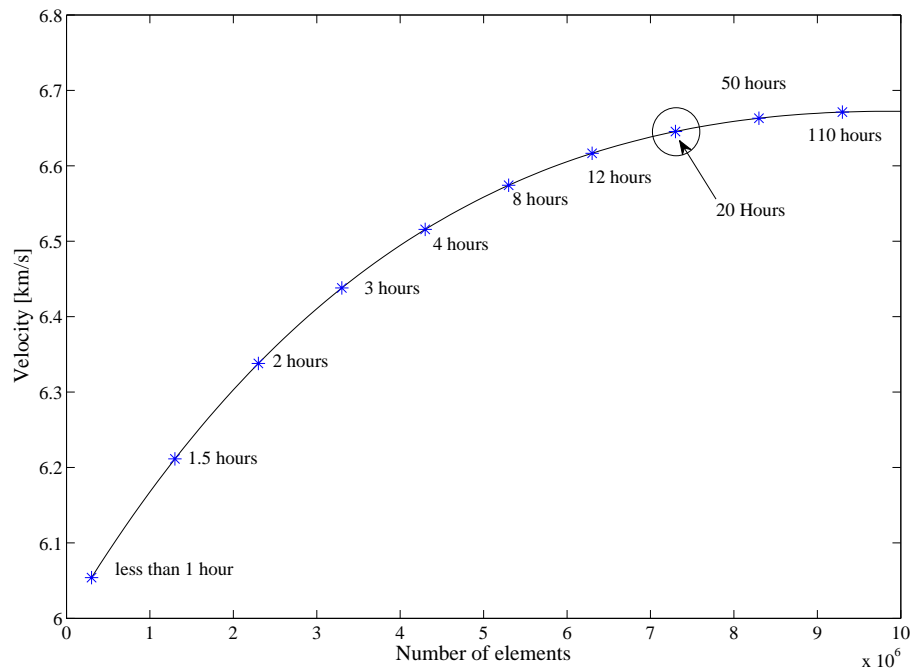


Figure A9: An exemplary mesh selection process for a 2-D axisymmetric modeling. Similar processes have been employed for each cases presented in this thesis.

A3 Simple Illustration of the Physical Differences between Positive and Negative Streamer Formation in Dielectric Liquids

In positive streamer propagation, the highly mobile electrons are swept back towards the positive electrode leaving a net positive volume charge region that propagates towards the grounded electrode causing the maximum electric field to move further into the liquid bulk. In negative streamer propagation, it is also the moving electric field and space charge waves that allow ionization to occur further into the oil. However, the difference is that the negative needle and later, the negative streamer head push back the electrons away from the ionization zone, leaving a net negative volume charge region behind. Since the positive ions are slow to shield the strong field generated by negative needle tip, it further affects the bulk oil and the ionization zone becomes larger and wider than positive streamers, which gives more freedom to electrons for moving within the neutral zone (known as ionized body or the low density streamer channel) and generate more heat via thermal dissipation. This explains the higher temperatures observed inside the negative streamer channels as they propagate. In principle, electron velocities in both streamers are the same. However, since the negative streamer has a greater radius of curvature, the field enhancement ahead of it is much smaller than the positive counterparts (about half, see Chapter 5). Therefore, the negative streamer tends to elongate at a slower pace (about half) than the positive streamer.

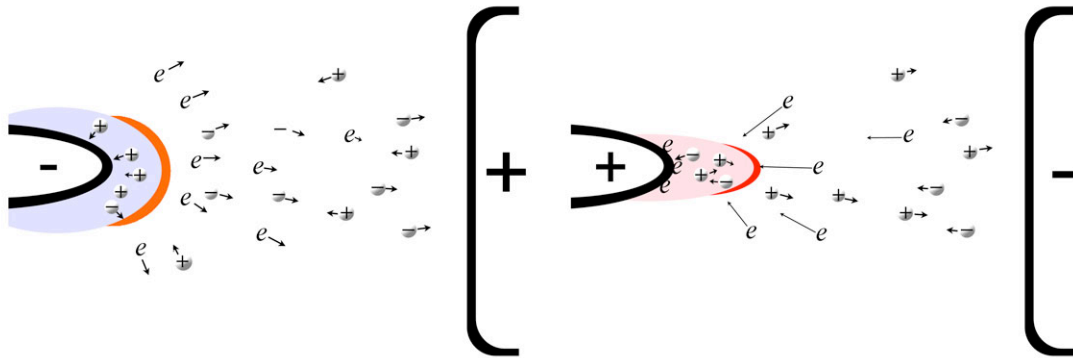


Figure A10: Illustration of a negative streamer (left) and a positive streamer (right) formation and propagation in a needle-plane geometry (which is similar to needle-sphere geometry). The negative streamers initiate with wider front due to the lower mobility of the positive ions. Since positive ions are not as effective as electrons to shield the needle electrode electric field, the needle affects a larger space immediately after the voltage is applied to the electrode; therefore the initial ionized region becomes much bulkier than the positive streamers. This eventually leads to lower field enhancement ahead of negative streamers and decreases the average negative streamer velocity compared to fast positive streamers, which always keep their filamentary shape thanks to the highly mobile electrons constantly forming at the ionization zone near the streamer head.

A4 Implementation of Stochastic Inhomogeneities

The key role of stochastic inhomogeneities has to be included in the 3-D model in order to observe the streamer branching. The cause of the branching is definitely not the macroscopic perturbations in experiments that are undertaken in degassed chambers in which the liquid dielectric is filtered repeatedly to eliminate any ionized traces and gas bubbles. In these experiments, the streamers grow in a continuously refreshed body of liquid dielectric. The models described in Chapter 5 cannot express the stochastic nature of the streamer branching, as they only cover macroscopic quantities and processes. Instead, we have defined and added a finite number of spherical regions (micro-particles) whose stochastic location and intensity convert the governing equations into a stochastic model (Chapter 6). To implement the stochastic perturbations in the model, we have used continuous uniform distribution functions (rectangular probabilistic functions) and Gaussian functions to determine the location and intensity of the individual perturbations, respectively. Specifically, a set of spherical regions with certain radii (R_p in the range of 1 μm -10 μm) is placed in random locations inside the discharge chamber. The selected inhomogeneity density determines the number of spheres. Each of these spherical regions, which contains a volume charge perturbation, is placed at a stochastic position with coordinates located by three separate uniform distribution functions. These spherical regions have the same permittivity as the rest of the dielectric medium.

Theoretically, charge carrier density fluctuations can be originated by either discrete nature of electrons at the leading edge of an ionization front where the electron density is low or many external sources such as cosmic rays or other sources of ionizing radiation. As the background electric field increases, the field ionization generates more discrete electrons at different locations of the dielectric that can gain enough energy to cause microscopic local ionizations. These local ionizations, occurring at much weaker electric fields than the critical breakdown field, produce local charge densities that can be regarded as microscopic inhomogeneities. In our model, we simulate these inhomogeneities by adding a stochastic amount of charge generation rates inside spherical regions, which generates a bias charge density in them. The intensity of the perturbation charge density generation rates is determined by continuous Gaussian functions. The minimum perturbation charge generation rate (G_{Mp}) is zero and maximum generation rate of carrier charge densities is $10^{10} \text{ Cm}^{-3}\text{s}^{-1}$, which is roughly one order of magnitude smaller than the generation rate at the typical positive streamer head in transformer oil. This stochastic perturbation rate generates inhomogeneous charge densities (ρ_{ps}) for a gaseous environment exposed to intense electric field. The result of stochastic perturbation rate in the range of zero and $10^{10} \text{ Cm}^{-3}\text{s}^{-1}$ in transformer oil, generates a maximum additional perturbation charge density of $\sim 10^4 \text{ Cm}^{-3}$ inside the microscopic spherical regions.

The density of the microscopic inhomogeneities (C_p) is set to 10^{11} m^{-3} . Considering the volume of the oil in the chamber, this distribution means that we have to place $\sim 10^6$ spheres in the chamber, which makes the number of the mesh elements too high, since the mesh inside these spheres have to be dense enough. Therefore, we chose to place the inhomogeneities only inside the pillbox

close to the needle tip at which we have the most refined mesh. Modeling results prove that the inhomogeneities farther than 1 mm from the streamer head do not contribute to the streamer branching. Figure A11 shows the pillbox (cylinder with 0.65 mm height and a base with 0.5 diameter) containing 12 inhomogeneities with 10 μm radius.

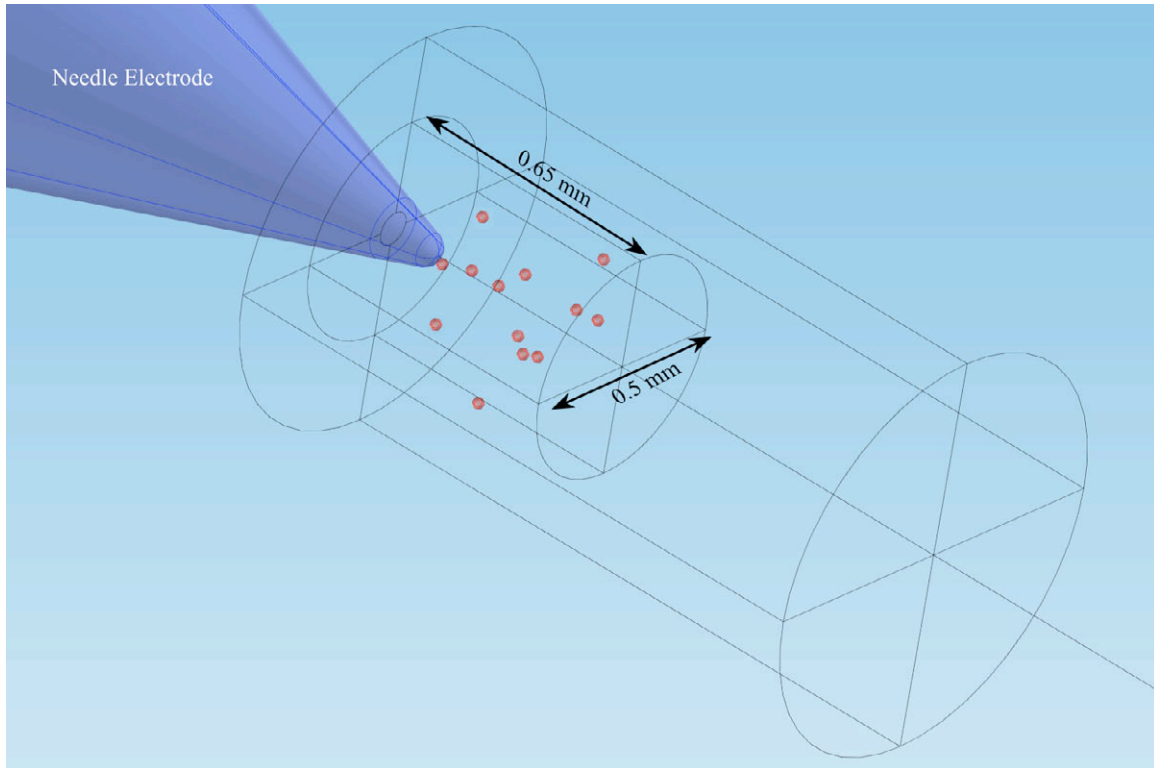


Figure A11: The pillbox adjacent to the needle electrode containing 12 inhomogeneities (red spheres) with 10 μm radius. The streamer branching results obtained with these inhomogeneities (and any other sizes above and below 5 μm radius) show less similarity to the experimental images than those modeling images taken from the results generated using inhomogeneities with 5 μm radius, suggesting that in practice, the effective inhomogeneities should have an average radius of 5 μm .

The streamer branching simulations using the model described in Chapter 6 show that the streamer branching results caused by inhomogeneities having any radii above and below 5 μm lead to less resemblances with experimental images than those modeling images taken from inhomogeneities with 5 μm radius. This observation suggests that in practice, the most effective inhomogeneities in transformer oil that cause branching should have an average radius of 5 μm . Figure A12 shows the pillbox (cylinder with 0.65 mm height and a base with 0.5 diameter) containing 12 inhomogeneities with 5 μm radius. Most of the results presented in Chapter 6 are obtained with an inhomogeneity distribution like Figure A12.

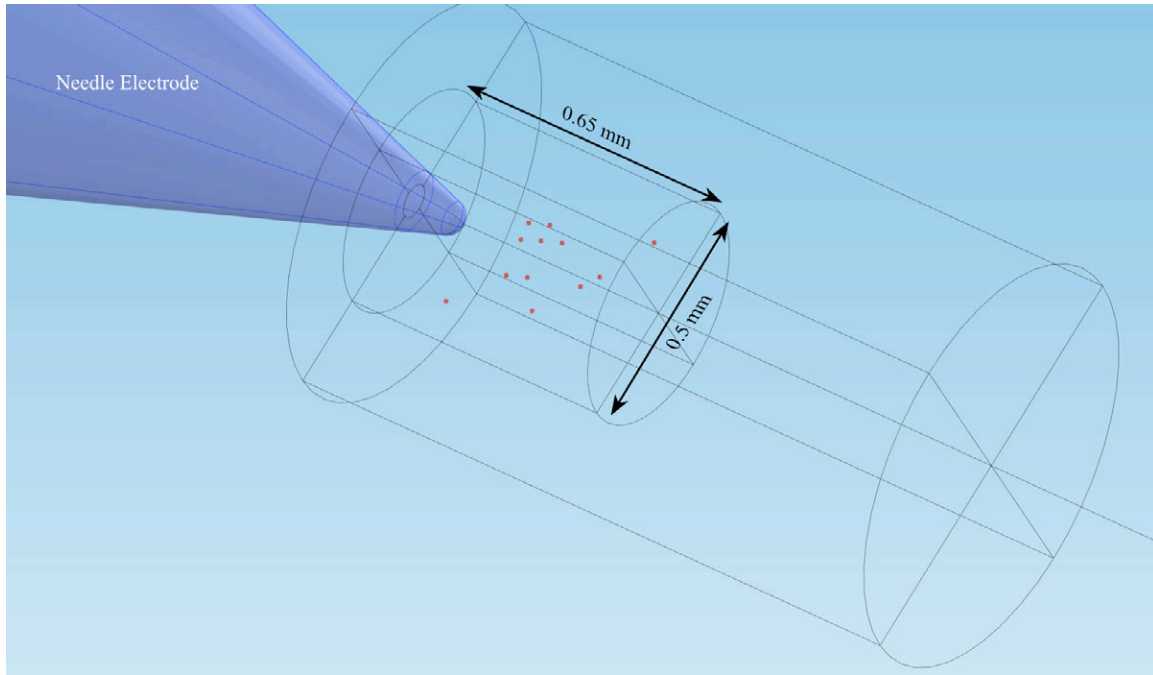


Figure A12: The pillbox adjacent to the needle electrode containing 12 inhomogeneities (red spheres) with $5\ \mu\text{m}$ radius. The streamer branching results obtained using inhomogeneities with $5\ \mu\text{m}$ radius show the maximum resemblance with experimental pictures suggesting that in practice, the effective inhomogeneities should have an average radius of $5\ \mu\text{m}$.

A5 Other Numerical Simulation Methods for Streamer Development Modeling

ABB Corporate Research in Västerås, Sweden, in addition to supporting this thesis research that solved the modeling equations using a multiphysics computational tool based on the finite element method, has implemented a model in a C++ toolbox (OpenFOAM) that uses the finite volume method [74]. This method might be better suited for transport equations than the finite element method used in this thesis, however, it is computationally more expensive and usually needs parallel computing. Fors [74] has analyzed the results from the OpenFOAM solver and has compared them to the results of [23–28]. The model used in [74] is analogous to those used in O’Sullivan [23] and Hwang [25], however a minor change has been made in neglecting thermal effects. This is due to the decoupling of the thermal diffusion equation from the charge carrier

transport equations. Thus, the thermal effects have had no impact on the streamer propagation itself and can be disregarded without significantly influencing the results.

In addition to the FVM approach taken by ABB, some efforts have been made in the early stages of this research to implement the modeling equations in a Finite Difference Method (FDM implemented in MATLAB). The results did not show any superiority over FEM results of COMSOL in terms of both accuracy and speed. Therefore the FDM was ignored early on. Table A2 lists the most important advantages and disadvantages of each of these numerical approaches.

Table A2: Numerical Simulation Methods for Streamer Development Modeling

<i>Method</i>	<i>Advantages</i>	<i>Disadvantages</i>
<p><u>Finite Difference</u> (Series expansion, usually a Taylor series. The series is truncated after 1 or 2 terms between nodes)</p>	<ul style="list-style-type: none"> • Simple • Ideal for electromagnetic field calculations 	<ul style="list-style-type: none"> • Unstable and inefficient • Equations must be transformed for irregular boundaries, before Taylor series expansion.
<p><u>Finite Volume</u> (Domain is divided to boxes with finite volume)</p>	<ul style="list-style-type: none"> • Fast for fluid flow • Based on integral conservation laws in PDEs based on divergence theorem • Works with fluxes (more physical significance) • Ideal for compressive flow 	<ul style="list-style-type: none"> • Usually more computationally expensive • Sensitive to complicated boundaries and boundary conditions (Irregular geometries require far more effort) • More parallelizable
<p><u>Finite Element</u> (Domain is divided to boxes with finite area)</p>	<ul style="list-style-type: none"> • No need to simplify the boundary/geometry • Simpler meshing • usually uses weight residual method (useful to decrease order of PDEs) • a more suitable choice for multiphysics problems • Ideal for incompressible flow problems 	<ul style="list-style-type: none"> • More mathematics involved - less physical interpretation • usually uses weight residual method • (not a good arrangement for nonlinear terms) • Commercial software more single node oriented

Bibliography

- [1] J. Kuffel, E. Kuffel and W. S. Zaengl, *High voltage engineering fundamentals*, Newness, Boston, 2000.
- [2] V. Y. Ushakov, V. F. Klimkin, and S. M. Korobeynikov, *Impulse breakdown of liquids*. Springer-Verlag, Berlin, 2007.
- [3] A. Beroual, M. Zahn, et. al, "Propagation and structure of streamers in liquid dielectrics," *IEEE Electr. Insul. Mag.*, vol. 14, pp. 6–17, 1998.
- [4] C. T. Duy, O. Lesaint, A. Denat, and N. Bonifaci, "Streamer propagation and breakdown in natural ester at high voltage," *IEEE Trans. Dielectr. Electr. Insul.*, vol. 16, no. 6, pp. 1582–1594, 2009.
- [5] F. M. J. McCluskey, A. Denat, and O. Lesaint, "Breakdown and pre-breakdown phenomena in liquids under positive impulse voltages," *IEEE Trans. Dielectr. Electr. Insul.*, vol. 1, no. 3, pp. 377–382, 1994.
- [6] J. C. Devins, S. J. Rzed, R. J. Schwabe, "Breakdown and pre-breakdown phenomena in liquids," *J. Appl. Phys.*, vol. 52, no. 7, 1981.
- [7] K. C. Kao, J. P. C. McMath, "Time dependent pressure effect in liquid dielectrics," *IEEE Trans. Electr. Insul.*, vol. EI-5, no. 3, pp. 64–68, 1970.
- [8] M. Cevallos, M. Butcher, J. Dickens, A. Neuber, H. Krompholz, "Imaging of negative polarity DC breakdown streamer expansion in transformer oil due to variations in background pressure," *IEEE Trans on Plasma Sci.*, vol. 33, pp. 494–495, 2005.
- [9] O. Lesaint, R. Tobazeon, "Streamer generation and propagation in transformer oil under ac divergent field conditions," *IEEE Trans. Electr. Ins.*, vol. 23, no. 6 pp. 941–954, 1988.
- [10] G. Massala and O. Lesaint, "Positive streamer propagation in large oil gaps: electrical properties of streamers," *IEEE Trans. Dielectr. Electr. Insul.*, vol. 5, no. 3, pp. 371–381, 1998.
- [11] W. F. Schmidt. *Liquid state electronics of insulating liquids*, CRC Press, 1997.
- [12] H. S. Smalø, Ø. Hestad, S. Ingebrigtsen, and P. O. Åstrand, "Field dependence on the molecular ionization potential and excitation energies compared to conductivity models for insulation materials at high electric fields," *J. Applied Phys.*, vol. 109, no. 073306, 2011.
- [13] L. Lundgaard, D. Linhjell, G. Berg, and S. Sigmond, "Propagation of positive and negative streamers in oil with and without pressboard interfaces," *IEEE Trans. Dielectr. Electr. Insul.*, vol. 5, no. 3, pp. 388–395, 1998.

- [14] P. Rain and O. Lesaint, "Prebreakdown phenomena in mineral oil under step and ac voltage in large-gap divergent fields," *IEEE Trans. Dielectr. Electr. Insul.*, vol. 1, no. 4, pp. 692–701, 1994.
- [15] O. Lesaint and T. V. Top, "Streamer initiation in mineral oil, Part I: Electrode surface effect under impulse voltage", *IEEE Trans. Dielectr. Electr. Insul.*, vol. 9, pp. 84–91, 2002.
- [16] R. Bartnikas, editor, "Engineering Dielectrics: Electrical Insulating Liquids," *volume 3. American Society for Testing and Materials*, Philadelphia, 1994.
- [17] H. A. Fowler, J. E. Devaney, and J. G. Hagedorn, "Growth model for filamentary streamers in an ambient field," *IEEE Trans. Dielectr. Electr. Insul.*, vol. 10, no. 1, pp. 73–79, 2003.
- [18] M. D. Cevallos, *Phenomenological investigation of breakdown in oil dielectrics*, Ph.D. dissertation (available online), Texas Tech University, Lubbock, TX, USA, 2005.
- [19] N. Y. Babaeva and M. J. Kushner, "Streamer branching: the role of inhomogeneities and bubbles," *IEEE Trans. Plasma Sci.*, vol. 36, no. 4, pp. 892– 893, 2008.
- [20] M. Zahn, "Dynamics of stratified liquids in the presence of space charge," *Physics of Fluids*, vol. 15 , pp. 1408–1417, 1972.
- [21] M. Zahn, "Space charge coupled interfacial waves," *Physics of Fluids*, 17:343–352, 1974.
- [22] P. M. Mitchinson and P. L. Lewin, P. Jarman, "Oil-Gap Discharge in Transformers," *IEEE Electr. Insul. Mag.*, vol. 29, no. 2, 2013.
- [23] F. O'Sullivan, *A model for the initiation and propagation of electrical streamers in transformer oil and transformer oil based nanofluids*, Ph.D. dissertation, Massachusetts Institute of Technology (available online at dspace.mit.edu), Cambridge, MA, USA, 2007.
- [24] F. O'Sullivan, J. G. Hwang, M. Zahn, O. Hjortstam, L. Pettersson, R. Liu, and P. Biller, "A model for the initiation and propagation of positive streamers in transformer oil", *IEEE Int'l. Sympos. Electr. Insul. (ISEI)*, pp. 210-214, Vancouver, BC, Canada, 2008.
- [25] J. G. Hwang, *Elucidating the mechanisms behind pre-breakdown phenomena in transformer oil systems*, Ph.D. dissertation, Massachusetts Institute of Technology (available online at dspace.mit.edu), Cambridge, MA, USA, 2010.
- [26] J. G. Hwang, M. Zahn, F. M. O'Sullivan, L. A. A. Pettersson, O. Hjortstam, and R. Liu, "Effects of nanoparticle charging on streamer development in transformer-oil based nanofluids," *J. Appl. Phys.*, vol. 107, no. 014310, pp. 1–17, 2010.
- [27] J. G. Hwang, M. Zahn, L. A. A. Pettersson, O. Hjortstam, R. Liu, "Modeling Streamers in Transformer Oil: The Transitional Fast 3rd Mode Streamer," *IEEE 9th International Conference on Properties and Applications of Dielectric Materials*, pp. 573–578, 2009.
- [28] J. G. Hwang, M. Zahn, L. A. A. Pettersson, "Mechanisms behind positive streamers and their distinct propagation modes in transformer oil," *IEEE Trans. Dielectr. Electr. Insul.*, vol. 19, no. 1, pp.162–174, 2012.

- [29] A. Luque and U. Ebert, "Electron density fluctuations accelerate the branching of positive streamer discharges in air," *Phys. Rev. E*, 84, 046411, 2011.
- [30] B. Meulenbroek, *Streamer branching: conformal mapping and regularization*, Ph.D. dissertation, Technische Universiteit Eindhoven (available online), Wageningen, Netherlands, 2006.
- [31] C. Li, J. Teunissen, M. Nool, W. Hundsdorfer, U. Ebert, "A comparison of 3D fluid, particle and hybrid model for negative streamers," *Plasma Sources Science and Technology*, vol. 21, no. 055019, 2012.
- [32] T. M. P. Briels, J. Kos, G. J. J. Winands, E. M. van Veldhuizen, U. Ebert, "Positive and negative streamers in ambient air: measuring diameter, velocity and dissipated energy," *J. Phys. D, Appl. Phys.*, vol. 41, no. 234004, 2008.
- [33] E. Hashemi, K. Niayesh, A. A. Shaygani, E. Agheb, J. Jadidian, "Field Emission Enhanced Breakdown Gaseous Spark Gaps In Sub-nano Second Pulsed Regime", *XVII International Conference on Gas Discharge and Their Applications*, pp. 361–364, Wales, 2008.
- [34] E. M. van Veldhuizen, P. C. M. Kemps, and W. R. Rutgers, "Streamer branching in a short gap: the influence of the power supply," *IEEE Trans on Plasma Sci.*, vol. 30, no. 1, pp 162–163, 2002.
- [35] S. Nijdam, *Experimental Investigations on the Physics of Streamers*, , Ph.D. dissertation, Technische Universiteit Eindhoven (available online), Wageningen, Netherlands, 2011.
- [36] S. Nijdam, K. Miermans, E. M. van Veldhuizen, U. Ebert, "A peculiar streamer morphology created by a complex voltage pulse," *IEEE Trans. Plasma Sci.*, vol. 39, pp. 2216–2217, 2011.
- [37] L. Papageorgiou, A. C. Metaxas and G. E. Georghiou, "Three-dimensional numerical modelling of gas discharges at atmospheric pressure incorporating photoionization phenomena," *J. Phys. D: Appl. Phys.*, vol. 44, 045203, 2011.
- [38] K. Niayesh, E. Hashemi, E. Agheb, J. Jadidian, "Sub-nanosecond breakdown mechanism of low pressure gaseous spark gaps," *IEEE Trans. Plasma Sci.*, 36, 930–931, 2008.
- [39] J. Qian, R. P. Joshi, E. Schamiloglu, J. Gaudet, J. R. Woodworth, J. M. Lehr, "Analysis of polarity effects in the electrical breakdown of liquids," *J. Phys. D: Appl. Phys.*, vol. 39, pp. 359–369, 2006.
- [40] L. Niemeyer, L. Pietronero, H. J. Wiesmann, "Fractal dimension of dielectric breakdown," *Phys. Rev. Lett.*, vol. 52, no. 2, pp. 1033–1036, 1984.
- [41] J. Jadidian, J. G. Hwang, M. Zahn, N. Lavesson, O. Widlund, K. Borg, "Streamer initiation and propagation in transformer oil under positive and negative impulse voltages," *13th IEEE Int. Pulsed Power Conference*, pp. 251–256, Chicago, 2011.
- [42] J. Jadidian, J. G. Hwang, M. Zahn, N. Lavesson, O. Widlund, K. Borg, "Streamer dynamics in transformer oil: influence of applied voltage rise-time," *38th IEEE Int. Conf. on Plasma Science*, Chicago, 2011.

- [43] J. Jadidian, M. Zahn, N. Lavesson, O. Widlund, K. Borg, "Effectiveness of different artificial diffusions in charge transport simulations," *COMSOL Conference*, Boston, MA, 2012.
- [44] J. Jadidian, X. Zhang, J. K. Nowocin, M. Zahn, "Numerical modeling of streamer discharges in liquid dielectric materials," Invited Workshop at *2012 Conference on Electrical Insulation and Dielectric Phenomena (CEIDP)*, Montreal, Canada.
- [45] J. Jadidian, M. Zahn, N. Lavesson, O. Widlund, K. Borg, "Surface flashover propagation on transformer oil immersed dielectrics," *IEEE 2012 International Power Modulator and High Voltage Conference*, pp. 39–42, San Diego, CA, 2012.
- [46] J. Jadidian, M. Zahn, "Multiphysics modeling of streamer discharges in transformer oil-pressboard systems," Invited plenary talk at *2012 International IEEE International Conference on Power and Energy in NERIST (ICPEN)*, Arunachal Pradesh, India.
- [47] J. Jadidian, M. Zahn, N. Lavesson, O. Widlund, K. Borg, "Abrupt changes in streamer propagation velocity driven by electron velocity saturation and microscopic inhomogeneities," Invited talk at *2013 Pulsed Power and Plasma Science Conference*, San Francisco, CA.
- [48] J. Jadidian, M. Zahn, N. Lavesson, O. Widlund and K. Borg, "Effects of impulse voltage polarity, peak amplitude and rise-time on streamers initiated from a needle electrode in transformer oil," *IEEE Trans. Plasma Sci.*, vol. 40, no. 2, pp. 909–918, 2012.
- [49] J. Jadidian, M. Zahn, N. Lavesson, O. Widlund, K. Borg, "Impulse breakdown delay in liquid dielectrics," *Appl. Phys. Lett.*, vol. 100, no. 192910, 2012.
- [50] J. Jadidian, M. Zahn, N. Lavesson, O. Widlund, K. Borg, "Surface flashover breakdown mechanism on the liquid immersed dielectrics," *Appl. Phys. Lett.*, vol. 100, no. 172903, 2012.
- [51] J. Jadidian, M. Zahn, N. Lavesson, O. Widlund, K. Borg, "Stochastic and deterministic causes of streamer branching in liquid dielectrics," *J. Appl. Phys.*, Submitted.
- [52] J. Jadidian, M. Zahn, N. Lavesson, O. Widlund, K. Borg, "Effects of electrodes and barrier geometries on streamer discharge in transformer oil," *IEEE Trans. on Dielec. Electr. Insul.*, submitted.
- [53] J. Jadidian, M. Zahn, N. Lavesson, O. Widlund, K. Borg, "Streamer initiation, propagation, branching and breakdown in liquid dielectrics," *IEEE Trans. Plasma Sci.*, submitted.
- [54] M. A. Uman, *Lightning; Advanced Physics Monograph Series*, McGraw-Hill, 1969.
- [55] *Needle-sphere transformer oil breakdown experimental setup* at ABB Corporate Research, Västerås, Sweden. Courtesy of Rongsheng Liu.
- [56] R. Liu, L. A.A. Pettersson, T. Auletta, O. Hjortstam, "Fundamental Research on the Application of Nano Dielectrics to Transformers," *2011 Electrical Insulation and Dielectric Phenomena (CEIDP)*, pp. 423–427, 2011.
- [57] ABB Transformer Handbook. ABB, 2004.
- [58] H. P. Moser, "Transformerboard," H. Weidmann AG, Rapperswil, Switzerland, 1979.

- [59] H. P. Moser and V. Dahinden, "Transformer board II," H. Weidmann AG, Rapperswil, Switzerland, 1987.
- [60] O. Lesaint and M. Jung, "On the relationship between streamer branching and propagation in liquids: influence of pyrene in cyclohexane," *J. Phys. D: Appl. Phys.*, vol. 33, pp. 1360–1368, 2000.
- [61] P. Rozga, "Influence of paper insulation on the pre-breakdown phenomena in mineral oil under lightning impulse," *IEEE Trans. on Dielec. Electr. Insul.*, vol. 18, no. 3, pp. 720–727, 2011.
- [62] M. U. Anker, "Effect of test geometry, permittivity matching and metal particles on the flashover voltage of oil/solid interfaces," *IEEE Trans. Power App. Syst.*, PAS- 102, no. 12, pp. 3796–3802, 1983.
- [63] R. J. Taylor, "Effect of permittivity matching on the flashover of solid/liquid interfaces," *Proc. IEE*, vol. 124, no. 10, pp. 899–904, 1977.
- [64] M. Zahn, *Electromagnetic Field Theory: A Problem Solving Approach*, Robert E. Krieger, Inc., 2003.
- [65] P. Biller, "A simple qualitative model for the different types of streamers in dielectric liquids," *12th International Conference on Conduction and Breakdown in Dielectric Liquids*, pp. 189–192, Baden-Dattwil, Switzerland, 1996.
- [66] IEC Standard #60897, "Methods for the determination of the lightning impulse breakdown voltage of insulating liquids."
- [67] V. Segal and K. Raj, "An investigation of power transformer cooling with magnetic fluids," *Indian J. Eng. Mater. Sci.*, vol. 5, no. 6, pp. 416–422, 1998.
- [68] V. Segal, A. Rabinovich, D. Natrass, K. Raj, A. Nunes, "Experimental study of magnetic colloidal fluids behavior in power transformers," *J. Magn. Magn. Mater.*, vol. 215, pp.513–515, 2000.
- [69] V. Segal, D. Natrass, K. Raj, D. Leonard, "Accelerated thermal aging of petroleum-based ferrofluids," *J. Magn. Magn. Mater.*, 201:70–72, 1999.
- [70] V. Segal, "Colloidal insulating and cooling fluid," *United States Patent 5,863,455*, January 26, 1999.
- [71] Reference guide COMSOL Multiphysics 4.3a.
- [72] J. Jadidian, G. J. Hwang, M. Zahn, N. Lavesson, O. Widlund, K. Borg, "Migration-ohmic charge transport in liquid-solid insulation systems," *IEEE International Conference on Dielectric Liquids (ICDL)*, p. 978-1-4244-7354-0/11, Trondheim, Norway, 2011.
- [73] J. Jadidian, M. Zahn, "Unipolar Charge Transport in Oil-Pressboard Systems with Planar, Coaxial Cylindrical and Concentric Spherical Electrode Geometries," Invited planary talk presented as the Inuishi Memorial Lecture at *International Symposium on Electrical Insulating Materials* (available online at dspace.mit.edu), Kyoto, Japan, 2011.

- [74] J. Fors, *Modeling and OpenFOAM simulation of streamers in transformer oil*, M.Sc. Thesis, Linköping University, Research conducted in cooperation with ABB Corporate Research (Västerås, Sweden), Linköping, Sweden, 2012.
- [75] O. C. Zienkiewicz, R.L. Taylor, P. Nithiarasu, *The Finite Element Method for Fluid Dynamics*, 6th ed., Elsevier, 2005.
- [76] R. Codina, “A discontinuity-capturing cross-wind-dissipation for the finite element solution of the convection-diffusion equation,” *Computer Methods in Applied Mechanics and Eng.*, vol. 110, pp. 325–342, 1993.
- [77] G. Hauke, “A Simple subgrid scale stabilized method for the advection-diffusion-reaction equation,” *Comput. Methods Appl. Mech. Eng.*, vol. 191, pp. 2925–2947, 2002.
- [78] V. John, P. Knobloch, “On spurious oscillations at layers diminishing (SOLD) methods for convection-diffusion equations: Part I - A Review,” *Comput. Methods Appl. Mech. Engrg.*, vol. 196, pp. 2197–2215, 2007.
- [79] <http://graal.ens-lyon.fr/MUMPS/>
- [80] <http://www.pardiso-project.org/>
- [81] <http://www.netlib.org/linalg/spooles/>
- [82] A. Greenbaum, “Iterative Methods for Linear Systems,” *Frontiers in Applied Mathematics*, vol. 17, SIAM, 1997.
- [83] Y. Saad, *Iterative Methods for Sparse Linear Systems*, Boston, 1996.
- [84] M. Zahn, C. F. Tsang and S. C. Pao, “Transient electric field and space-charge behavior for unipolar ion conduction,” *J. Appl. Phys.*, vol. 45, pp. 2432–2440, 1974.
- [85] M. Zahn, B. Fenneman, S. Voldman, T. Takada, “Charge injection and transport in high voltage water/glycol capacitors” *J. Appl. Phys.*, vol. 54, pp. 315–325, 1983.
- [86] IEC Standard # 60060-1, “High-voltage test techniques - Part 1: General definitions and test requirements.”
- [87] C. Zener, “A theory of the electrical breakdown of solid dielectrics,” *Proc. Roy. Soc. A*, pp. 523–529, 1934.
- [88] J. Townsend, “The Theory of Ionization of Gases by Collision,” Constable & Company, London, 1910.
- [89] R. Tobazeon, “Prebreakdown phenomena in dielectric liquids,” *IEEE Trans. Dielectr. Electr. Insul.*, 1(6):1132–1147, 1994.
- [90] W. G. Chadband, “Electrical breakdown - from liquid to amorphous solids,” *J. Phys. D: Appl. Phys.*, 24:56–64, 1991.
- [91] L. Onsager, “Deviations from ohm’s law in weak electrolytes,” *J. Chem. Phys.*, 2:599– 615, 1934.

- [92] S.-H. Lee, I.-H. Park, F. O'Sullivan, M. Zahn, L. Pettersson, R. Liu, O. Hjortstam, A. Jaksts, T. Auletta, and U. Gafvert, "Evaluation of discharge current by generalized energy method and integral ohm's law," *Conference on the Computation of Electromagnetic Fields Compumag*, Florianopolis, Brazil, 2009.
- [93] D. S. Sholl, J. A. Steckel, *Density Functional Theory, A Practical Introduction*, John Wiley & Sons, Inc., New Jersey, 2009.
- [94] G. Giuliani, G. Vignale, *Quantum Theory of the Electron Liquid*, Cambridge University Press, Cambridge-UK, 2005.
- [95] D. Sinitsky, F. Assaderaghi, C. Hu, and J. Bokor, "High field hole velocity and velocity overshoot in silicon inversion layers," *IEEE Electron Device Letters*, vol. 18, no. 2, 1997.
- [96] J. M. Lehr, F. J. Agee, R. Copeland, W. D. Prather, "Measurement of the electric breakdown strength of transformer oil in the sub-nanosecond regime," *IEEE Trans. Dielectr. Electr. Insul.*, vol. 5, pp. 857-861, 1998.
- [97] E. E. Kunhardt, "Electron kinetics in simple liquids at high electric fields," *Phys. Rev. B*, vol. 44, pp. 4235-4244, 1991.
- [98] S.S.Huang and G. R. Freeman, "Electron transport in gaseous and liquid Argon: effects of density and temperature", *Phys. Rev. A*, vol. 24, p. 714, 1981.
- [99] W. E. Spear, G. Le Comber, "A Possible explanation of the observed electron drift velocity saturation in solid Ar, Kr, and Xe," *Phys. Rev.*, no. 178, 1454-1456, 1969.
- [100] R. A. Holroyd and W. F. Schmidt, "Transport of electrons in nonpolar fluids," *Annu. Rev. Phys. Chem.*, 40:439-468, 1989.
- [101] J. K. Baird, "Negative ion photodetachment and the electron effective mass in liquids," *J. Chem. Phys.*, no. 79, pp. 316-320, 1983.
- [102] J. Jadidian, S. Mohseni, M. Jebeli-Javan, E. Hashemi, A. A. Shayegani, K. Niayesh, "Visualization of a Copper Wire Explosion in Atmospheric Pressure Air," *IEEE Transactions on Plasma Science*, vol. 39, no. 11, pp. 2842-2843, 2011.
- [103] J. Jadidian, "A Compact Design for High Voltage Direct Current Circuit Breaker," *IEEE Transactions on Plasma Science*, vol. 37, no. 6, pp. 1084-1091, 2009.
- [104] O. Lesaint and G. Massala, "Positive streamer propagation in large oil gaps: experimental characterization of propagation modes," *IEEE Trans. Dielectr. Electr. Insul.*, vol. 5, pp. 360-370, 1998.
- [105] W. G. Chadband, "On variations in the propagation of positive discharges between transformer oil and silicone fluids," *Phys. D: Appl. Phys.*, vol. 13, pp. 1299-1307, 1980.
- [106] Y. Nakao, H. Itoh, Y. Sakai and H. Tagashira, "Studies of impulse creepage discharge in transformer oil," *IEEE Trans. Dielectr. Electr. Insul.*, vol. 26, no. 4, pp. 732-738, 1991.

- [107] H. Craig Miller, "Surface flashover of insulators," *IEEE Trans. Dielectr. Electr. Insul.*, vol. 17, no. 4, pp. 1327–1335, 2010.
- [108] J. Dai, Z. D. Wang, P. Jarman, "Creepage discharge on insulation barriers in aged power transformers," *IEEE Trans. Dielectr. Electr. Insul.*, vol. 17, no. 4, pp. 1327–1335, 2010.
- [109] P. M. Mitchinson and P. L. Lewin, B. D. Strawbridge, P. Jarman, "Tracking and surface discharge at the oil–pressboard interface," *IEEE Electr. Insul. Mag.*, vol. 26, no. 2, pp. 35–41, 2010.
- [110] R. J. Taylor, "Effect of permittivity matching on the flashover of solid/liquid interfaces," *Proc. IEE*, vol. 124, no. 10, pp. 899–904, 1977.
- [111] L. Lundgaard, H. Forster, and W. Hansen, "Electric breakdown in liquid insulation combined with solid insulation," *Nordic Insulation Symposium*, NORD-IS 1984, pp. 8.1–8.9, Kungälv, Sweden, 1984.
- [112] M. Nozaki, H. Ishizuka, E. Ooe, I. Tani, Y. Kamata, and K. Endo, "Low-dielectric constant press board for oil impregnation insulation," *European Patent EP 0272497 A3*, 1993.
- [113] O. Hjortstam, R. Liu, A. Jaksts, and L. A. Pettersson, "An electrical insulation material, an electric device comprising the insulation material and a transformer," *International Patent WO 2009/083343*, 2009.